# A Study of the Fractional Quantum Hall Energy Gap at Half Filling

Cory R. Dean

Department of Physics
McGill University
Montréal, Québec, Canada
November 2008

A thesis submitted to McGill University
in partial fulfilment of the requirements of the degree of
Doctor of Philosophy

*For Theresa, my closest friend and confidant.*
*Thank you for waiting.*

*'It has been stated above that in the experiments thus far tried the current apparently tends to move, without actually moving, toward the side of the conductor. I have in mind a form of apparatus which will, I think, allow the current to follow this tendency and move across the lines of magnetic force. If this experiment succeeds, one or two others immediately suggest themselves.'*

-Edwin Hall, Am. J. Math, **2**, 287 (1879)

*'Methinks that in looking at things spiritual, we are too much like Oysters observing the sun through the water, and thinking that water the thinnest of air.'*

-Herman Mellville in Moby Dick

*'At every crisis in one's life, it is an absolute salvation to have some sympathetic friend to whom you can think aloud without restraint or misgiving.'*

-Woodrow Wilson

*'On peut rire de tout, mais pas avec n'importe qui.'*

-Pierre Desproges

*'In the mountains, the shortest route is from peak to peak, but for that you must have long legs.'*

-Friedrich Nietzsche in Thus Spoke Zarathustra

# ACKNOWLEDGEMENTS

many incredible opportunities that have come with it; for taking a chance on me, inviting me to Montreal, and having the confidence in me to pursue this research to its end; and perhaps above all else, for truly teaching me the value of "doing whatever it takes" to "just get it done".

## ABSTRACT

A complete understanding of the the $\nu = \frac{5}{2}$ fractional quantum hall effect (FQHE) continues to be among the most exciting problems in semiconductor physics. It is widely believed that this unique electron state is described by the Moore-Read Pfaffian wavefunction, resulting from a BCS-like pairing of composite fermions. In recent years this wavefunction has received special interest owing to its non-abelian quantum statistics which underlies a new paradigm for fault tolerant quantum computation. However, in spite of several theoretical advancements, an unequivocal experimental verification of the Moore-Read description is still missing.

We studied the $\frac{5}{2}$ state in a very high quality 2DEG sample with the lowest electron density reported to date, by nearly a factor of two. We demonstrate that large discrepancies between experimentally measured values of the $\frac{5}{2}$ energy gap, and theoretical calculations based on the Moore-Read theory, can not be trivially attributed to disorder as has conventionally been assumed. Using a tilted field geometry, we investigated the effect of applying an in-plane magnetic field on the $\frac{5}{2}$ state. We observe the $\frac{5}{2}$ energy gap to collapse linearly with the in-plane field, whereas the neighbouring $\frac{7}{3}$ shows a strong enhancement. The opposite behaviour between the two states is in startling contrast to theory which predicts both gaps should be similarly suppressed. Since the early theoretical foundation in support of the Moore-Read interpretation presumed the two states should behave the same, our experimental finding of opposite behaviour may necessitate a fundamental rethinking of the nature of the $\frac{5}{2}$ FQHE.

A crucial step towards verifying the Moore-Read description of the $\nu = \frac{5}{2}$ FQHE will be an unambiguous measurement of its spin state. In an effort to measure the $\frac{5}{2}$ spin directly, we implemented a resistively detected nuclear magnetic resonance (RDNMR) technique. I report on our detailed study of the anomalous RDNMR lineshape around $\nu = 1$, and discuss progress made towards measuring the $\frac{5}{2}$ spin with this technique.

# ABRÉGÉ

Une compréhension complète de l'effet Hall quantique fractionnaire (EHQF) à $\nu = \frac{5}{2}$ continue à faire partie des problèmes les plus passionnants de la physique des semi-conducteurs. On estime généralement que cet état électronique unique est décrit par la fonction d'onde de Moore-Read connue sous le nom de "Pfaffien", résultant d'un appariement de type BCS de fermions composites. Cette fonction d'onde a récemment suscité un intérêt tout particulier en raison de ses statistiques quantiques non-abéliennes qui sous tendent un nouveau paradigme pour le calcul quantique insensible aux défaillances. En dépit de plusieurs avancées théoriques, il manque toutefois une vérification expérimentale définitive de la description Moore-Read.

Nous avons étudié l'état $\frac{5}{2}$ dans un gaz électronique bidimensionnel de très haute mobilité ayant la plus faible densité d'électrons reportée à ce jour, ceci de par un facteur proche de deux. Nous démontrons que les importants écarts entre les valeurs du gap d'énergie à $\frac{5}{2}$ mesurées expérimentalement et les calculs théoriques basés sur la théorie Moore-Read ne peuvent pas être uniquement attribués au désordre, comme cela a traditionnellement été proposé. En utilisant un champ à géométrie inclinée, nous avons étudié l'effet de l'application d'un champ magnétique dans le plan sur l'état $\frac{5}{2}$. Nous observons une décroissance linéaire du gap d'énergie à $\frac{5}{2}$ en fonction du champ magnétique dans le plan, tandis que le gap d'énergie d'état fractionnaire voisin $\frac{7}{3}$ exhibe une forte augmentation. Le comportement opposé des deux états est en contraste avec la théorie qui prévoit que les deux gaps doivent être supprimés par l'application d'un champ magnétique dans le plan, ce qui nécessite un nouvel examen de la nature de l'EHQF $\frac{5}{2}$.

Une étape cruciale vers la vérification de la description Moore-Read de l'EHQF $\nu = \frac{5}{2}$ sera une mesure définitive de son état de spin. Dans un effort visant à mesurer directement le spin de l'état $\frac{5}{2}$, nous avons mis en place une technique de résonance magnétique nucléaire détectée résistivement (RMNDR). Je détaille notre étude de la forme du signal de RMNDR autour de $\nu = 1$, et expose les progrès réalisés en vue de mesurer le spin de l'état $\frac{5}{2}$ à l'aide de cette technique.

# STATEMENT OF ORIGINALITY

The work described in this thesis represents original scholarship by the author, and has not been submitted for a degree or diploma at any other institution. This thesis contains no material previously written or published by any other persons excepted where references are made.

Several physical designs described in the thesis are the authors own ideas, and were constructed and implemented by the author. These are described in detail in Chapter 3 and include, but are not limited to

- Experimental cold finger, designed to achieve maximal sample cooling and retro-fitted to a commercially purchased dilution refrigerator.
- *In-situ* sample rotator that allows transport measurement to be performed in a rotated field geometry.
- Implementation of a resistively detected nuclear magnetic resonance (RDNMR) measurement scheme. While the RDNMR technique was developed previously, our unique design offers several improvements including incorporation of a fixed, rigid, RF coil; design of a custom sample holder highly specialized in several ways; and incorporation of a custom designed AC bridge to improve measurement sensitivity.
- Implementation of all infrastructure for the dilution refrigerator operation and sample measurement.

Chapters 4, 5 and 6 describe experimental results obtained from examination of a unique GaAs 2DEG sample, supplied by Bell Laboratories. Portions of Chapter 4 and 5 were published as original work with the author of this thesis appearing as the first author in each publication [Dean *et al.*, Phys. Rev. Lett., **100**, 146803 (2008) and Dean *et al.*, Phys. Rev. Lett., **101**, 186806 (2008), respectively]. Highlights of this research that represent a significant and important contribution to the study of the quantum Hall effect include

- Observation of the $\frac{5}{2}$ fractional quantum Hall effect in a new low-field regime, by nearly a factor of two smaller than than previously reported.
- Identification that disorder does not trivially account for the reported discrepancy between the measured $\frac{5}{2}$ energy gap and the corresponding theoretically predicted value.

- Observation that the $\frac{5}{2}$ and neighbouring $\frac{7}{3}$ FQHE states behave oppositely in a tilted field geometry, representing a startling contradiction with theoretical predictions.
- First-ever evidence of skyrmion excitation in the second Landau level.
- Experimental demonstration of several important questions regarding the theoretical description of the $\frac{5}{2}$ FQHE state, motivating the need for further theoretical and experimental studies.

Chapter 6 describes implementation and examination of the RDNMR technique. A summary of the author's investigation of the anomalous lineshape near exact filling of the lowest Landau level was published as original work in a conference proceedings [Dean *et al.*, Physica E, **40**, 990 (2008)]. A second publication, featuring the analysis of our first-ever observed current-induced inversion of this lineshape, is in preparation. The observation of an RDNMR response near the $\frac{5}{2}$ FQHE state, presented at the end of Chapter 6, represents an important fist step towards direct measurement of the $\frac{5}{2}$ spin, which so far has not been reported in the literature.

# TABLE OF CONTENTS

# LIST OF TABLES

# LIST OF FIGURES

# CHAPTER 1

# Introduction

T he history of the quantum Hall effect has continually been marked by unexpected new experimental discoveries. The quantum Hall effect (QHE) was first discovered in 1980, when Klaus von Klitzing demonstrated quantization in the Hall resistance of a 2D electron system, at high magnetic fields [1]. Observation of this entirely new quantum phenomenon quickly gave birth to a rich new field of physics. Moreover, von Klitzing's discovery of exact quantization in the Hall resistance in units $h/e^2$, depending only on fundamental constants, gave us a new standard of resistance.

In 1982 Daniel Tsui and Horst Stormer [2] observed the characteristic features of the quantum Hall effect, *i.e.* exact quantization in the Hall resistance together with a zero value in the magnetoresistance, but occurring at $\frac{1}{3}$ *fractional filling* of the lowest Landau level. This surprising discovery called into question early theories of the quantum Hall effect, which described states occurring only at integer values of Landau level filling. It was quickly realized that, while the QHE could be mostly understood in terms of a non-interacting single-electron picture, understanding the fractional quantum Hall effect (FQHE) would require the explicit inclusion of electron-electron interactions [3] into the theory. Studies of these often subtle and complex many-body effects has since been the source of major breakthroughs in our understanding of strongly interacting electrons in two dimensional systems. Chief among these is the composite fermion picture of the incompressible FQH liquid [4,5], extremely successful at explaining both the complete series of fractional quantum Hall states observed in the lowest Landau level, and the absence of such a liquid at precisely half-filling.

In 1987 Willett *et al.* reported the observation of a quantum hall state at even denominator fractional filling $\nu = \frac{5}{2}$ [6–8]. This discovery was later confirmed unambiguously by Pan *et al.* who demonstrated exact quantization in the corresponding Hall resistance to an accuracy better than $2 \times 10^{-6}$ [9]. Remarkably, the $\frac{5}{2}$ state (and equivalently its

particle-hole conjugate at $\frac{7}{2}$ fractional filling) remains the only even-denominator state in the more than 100 unique FQH states that have been identified over the past 25 years. With this singular exception, every other FQH state is found at odd-denominator fractional filling, obeying the so-called "odd-denominator rule". Theoretical models of the fractional quantum Hall effect all reflect this rule giving FQH states that occur at, and only at, odd-denominator rational fractions [3, 4, 10–13]. The otherwise strict adherence to the odd-denominator rule together with the many successes of the theories that describe this rule makes the appearance of a quantum Hall state at *even denominator* a truly surprising and unexpected discovery. In 1991, Moore and Read [14] proposed an elegant many-body wavefunction to explain the appearance of the $\frac{5}{2}$ FQH state. The so called Moore-Read Pfaffian, which describes a condensation of Bosons resulting from a BCS-like pairing of composite electrons at half filling, is now widely believed to be the correct description of the $\frac{5}{2}$ state. However, support for the Moore-Read wavefunction remains mostly theoretical with an unequivocal experimental verification still conspicuously missing.

The Moore-Read Pfaffian has received special interest owing to its predicted exotic (non-Abelian) quantum statistics. On its own, discovery of a new kind of quantum particle would represent an important milestone in physics research. However, the Moore-Read Pfaffian has received particular attention for its potential technological applications. Kitaev proposed [15] that the topology in a system of non-Abelian particles would have a robust and therefore stable quantum property, which could be used to construct a fault-tolerant quantum computer. This represents a new paradigm in the attempt to achieve quantum computation, which so far has not been possible with conventional approaches. In recent years, the possibility that the $\frac{5}{2}$ state possesses the necessary quantum properties to realize the topological quantum computer [16,17] sparked a renewed interest in this state, and now more than ever underlines the importance in verifying whether the Moore-Read description is indeed correct.

Recent experiments [18,19] have measured the $e^* = e/4$ fractional charge expected for excitations from the Moore-Read ground state at $\frac{5}{2}$. However this measurement alone does not rule out other, Abelian, pairing wavefunctions which could also exhibit $e/4$ charged excitations. The key feature that distinguishes the Moore-Read Pfaffian from other proposed theories of the $\frac{5}{2}$ FQHE is its spin polarization. While the Moore-Read Pfaffian describes a fully spin-polarized paired-state, all other candidate wavefunctions result from a spin-unpolarized pairing. Measurement of the spin-polarization therefore remains the most important missing piece of the puzzle in our attempt to understand the origins of the $\frac{5}{2}$ state.

In the following thesis, I describe our efforts to measure experimentally the spin polarization of the $\frac{5}{2}$ FQH state. Our approach was two-fold. First, we investigated the $\frac{5}{2}$ state in a very high quality sample with a remarkably low density. This allowed us to examine the $\frac{5}{2}$ at a much lower magnetic field than previously observed (by nearly a factor of two) which for the first time $i$) allowed observation of the $\frac{5}{2}$ in a region of strong Landau level coupling and $ii$) allowed us to follow up on the first tilted field experiments of Eisenstein *et al.* [7,8] but with much higher sensitivity in the low tilt (*i.e.* low parallel field) regime than previously possible. Secondly, and in parallel, we implemented and characterized a newly developed *resistively detected nuclear magnetic resonance* (RDNMR) measurement technique, which promises to allow direct measurement of the $\frac{5}{2}$ spin by exploiting interactions with the surrounding nuclear spin.

Our investigation of our low density sample lead to several observations [20,21] regarding our understanding of the $\frac{5}{2}$ FQHE state. In particular, our results call into question the usual assumption that disorder effects at $\frac{5}{2}$ explain in a trivial way the large discrepancy between the theoretically predicted energy gap for a Moore-Read state, and the gap measured experimentally [20]. Our tilted field experiment raised further important questions regarding the Moore-Read description where, for the first time, we identify a startling contradiction in the behaviour of the $\frac{5}{2}$ under tilt when compared with neighbouring states [21]. Finally, we obtained a response signal near $\nu = \frac{5}{2}$ using the resistively detected NMR scheme. This preliminary measurement represents an important first step towards a direct measurement of the $\frac{5}{2}$ spin state.

## 1.1  Outline of thesis

I first begin with an introduction to the quantum Hall effect. Here I review important experimental discoveries and theoretical developments in both the integer and fractional quantum Hall effect, leading up to the discovery of the anomalous $\frac{5}{2}$ state. I then give a detailed description of $\frac{5}{2}$ FQHE. After presenting a summary of the Moore-Read theory, I review the theoretical and experimental support in favour of this description. At the end of this chapter, I highlight known shortcomings, and discrepancies of the Moore-Read Pfaffian as it applies to the $\frac{5}{2}$ state and outline the need for further experimentation.

In Chapter 3, I describe in detail the apparatus I designed and constructed in our effort to study the $\frac{5}{2}$ state. I review conventional transport techniques used to study the physics of interacting electrons in 2D, and outline novel approaches that I developed over the course of my studies.

In the remainder of the thesis (Chapters 4 to 6), I present the results of our investigation into the $\frac{5}{2}$ FQHE. First, I discuss our examination of the $\frac{5}{2}$ state in our very high quality, low density, sample. Results from conventional activation energy gap studies [20], and from using a tilted field geometry [21], are presented and discussed in terms of the Moore-Read Pfaffian wavefunction. I then describe our implementation of the newly developed RDNMR measurement technique. We characterized and optimized the RDNMR scheme by first examining the $\nu = 1$ integer quantum Hall effect, where it is easy to obtain strong responsive signals. I present our investigation of the anomalous lineshape obtained at $\nu = 1$ including our discovery of a current induced inversion in the signal shape [22]. Having characterized the technique, we applied RDNMR measurements to the $\frac{5}{2}$ FQHE, which I discuss at the end of the thesis. Finally, I review the current status of a bridge measurement scheme we developed that together with the RDNMR technique should allow for a full analysis of the spin nature of the $\frac{5}{2}$ state. In the final chapter I conclude by summarizing our main findings and propose future studies based on our results.

# References

[1] von Klitzing, K., Dorda, G., and Pepper, M. *Phys. Rev. Lett* **45**, 494 (1980).

[2] Tsui, D. C., Stormer, H. L., and Gossard, A. C. *Phys. Rev. Lett.* **48**, 1559 (1982).

[3] Laughlin, R. B. *Phys. Rev. Lett.* **50**, 1395 (1983).

[4] Jain, J. K. *Phys. Rev. Lett.* **63**, 199 (1989).

[5] Halperin, B. I., Lee, P. A., and Read, N. *Phys. Rev. B* **47**, 7312 (1993).

[6] Willett, R. L., Eisenstein, J. P., Stormer, H. L., Tsui, D. C., Gossard, A. C., and English, J. H. *Phys. Rev. Lett.* **59**, 1776 (1987).

[7] Eisenstein, J. P., Willett, R., Stormer, H. L., Tsui, D. C., Gossard, A. C., and English, J. H. *Phys. Rev. Lett.* **61**, 997 (1988).

[8] Eisenstein, J. P., Willet, R. L., STormer, H. L., Pfeiffer, L. N., and West, K. W. *Surf. Sci.* **229**, 31 (1990).

[9] Pan, W., Xia, J. S., Shvarts, V., Adams, D. E., Stormer, H. L., Tsui, D. C., Pfeiffer, L. N., Baldwin, K. W., and West, K. W. *Phys. Rev. Lett.* **83**, 3530 (1999).

[10] Haldane, F. D. M. *Phys. Rev. Lett.* **51**, 605 (1983).

[11] Halperin, B. I. *Phys. Rev. Lett.* **52**, 1583 (1984).

[12] Zhang, S. C., Hansson, H., and Kivelson, S. *Phys. Rev. Lett.* **62**, 82 (1989).

[13] Read, N. *Phys. Rev. Lett.* **62**, 86 (1989).

[14] Moore, G. and Read, N. *Nucl. Phys. B* **360**, 362 (1991).

[15] Kitaev, A. Y. *Ann. Phys.* **303**, 2 (2003).

[16] Das Sarma, S., Freedman, M., and Nayak, C. *Phys. Rev. Lett* **94**, 166802 (2005).

[17] Freedman, M., Nayak, C., and Walker, K. *Ann. Phys.* **73**, 245307 (2006).

[18] Dolev, M., Heiblum, M., Umansky, V., Stern, A., and Mahalu, D. *Nature* **452**, 829 (2008).

[19] Radu, I. P., Miller, J. B., Marcus, C. M., Kastner, M. A., Pfeiffer, L. N., and West, K. W. *Science* **320**, 899 (2008).

[20] Dean, C. R., Piot, B. A., Hayden, P., Das Sarma, S., Gervais, G., Pfeiffer, L. N., and West, K. W. *Phys. Rev. Lett.* **100**, 146803 (2008).

[21] Dean, C. R., Piot, B. A., Hayden, P., Das Sarma, S., Gervais, G., Pfeiffer, L. N., and West, K. W. *Phys. Rev. Lett.* **101**, 186806 (2008).

[22] Dean, C. R., Piot, B. A., Pfeiffer, L. N., West, K. W., and Gervais, G. *Physica E* **40**, 990 (2008).

CHAPTER 2

# Theory and Historical Context

In the following chapter I give a review of the quantum Hall effect by discussing in parallel important experimental discoveries and theoretical breakthroughs. The overarching aim of this chapter is to provide a theoretical framework for our study of the even-denominator $\frac{5}{2}$ FQHE while simultaneously giving historical context to our findings. Towards this effort, I first give a broad overview of the integer and fractional quantum Hall effect. I then discuss in detail the experimental and theoretical foundations that have lead to our current understanding of the $\frac{5}{2}$ FQHE, with an emphasis on important remaining questions regarding the origin of this enigmatic phenomenon.

## 2.1  Quantum Hall Effect

### 2.1.1  Classical Hall Effect

Nearly 130 years ago, Edwin Hall discovered the now famous Hall effect. Applying current through a thin foil sample in the presence of a large magnetic field, he observed a voltage develop in the direction transverse to the direction of current flow. This so called Hall voltage, $V_H$, was found to vary proportionally with current and with the size of the applied field

$$V_H \propto I,\ B. \tag{2.1}$$

This observation is now easily explained by the Lorentz force interaction which states that a charged particle moving in a magnetic field experiences a torque given by

$$\mathbf{F}_B = e(\mathbf{v} \times \mathbf{B}) \tag{2.2}$$

6

Figure 2–1: Schematic cartoon of the Hall effect. Application of a magnetic field causes a build up of charge on one side of the sample (due to the Lorentz force interaction) resulting in a voltage difference along the transverse (Hall) direction. The charge imbalance however gives rise to an electric field, yielding an electrostatic force that opposes the Lorentz force. The size of the Hall voltage is determined by the equilibrium condition between these forces.(see text).

where $\mathbf{F}_B$ is the Lorentz force, $e$ is the charge of the electron, $\mathbf{v}$ is the electron velocity (in this case the drift velocity defined by the current flow) and $\mathbf{B}$ is the magnetic field vector. The Lorentz force causes electrons to drift in the transverse direction resulting in charge accumulation on one side of the sample. This charge imbalance in turn creates an electric field, giving rise to an electrostatic force, given by

$$F_e = \frac{eV_H}{w} \tag{2.3}$$

where $e$ is the electron charge, $w$ is the width of the sample and $V_H$ is the voltage difference across the sample, *i.e.* the Hall voltage.

The electrostatic force opposes the Lorentz force, so that as the Hall voltage increases equilibrium is quickly established (Fig. 2–1). Equating the two forces (Eqns. 2.2 and 2.3) gives

$$\frac{eV_H}{w} = ev_d B. \tag{2.4}$$

Now, the current flow through the sample is defined by

$$I = Nev_d A \tag{2.5}$$

where $N$ is the electron density, $v_d$ is the electron drift velocity, and $A$ is the cross sectional area through which the current flows, *i.e.* $A = w\,d$ where $d$ is the sample thickness. Rearranging Eqn. 2.5 for the velocity and substituting into Eqn. 2.4 gives the full relationship between the hall voltage and the current and magnetic field to be

$$V_H = \frac{IB}{Ned} \tag{2.6}$$

where $d$ is the thickness of the sample, and $N$ is the electron density per unit volume. If we consider a thin sample, the electron density is mostly defined by the planar density, and so it is useful to instead consider the 2D electron density per unit area, $n = Nd$, which gives the Hall voltage to be

$$V_H = \frac{IB}{ne}. \tag{2.7}$$

Transport in the longitudinal direction (*i.e.* in the direction of the applied current) is unaffected by the B field and so the longitudinal resistance, $R_{xx}$, is given simply by Ohms law relation

$$R_{xx} = \frac{V_{xx}}{I} \tag{2.8}$$

where $V_{xx}$ is the voltage drop across the sample in the longitudinal direction and $I$ is the current flow. While in the transverse direction there is no actual current flow since the system reaches equilibrium (for a given current and magnetic field), it is conventional to define a similar resistance relation, determined by dividing the transverse Hall voltage by the longitudinal current. From Eqn. 2.7 this gives the Hall resistance, $R_H = V_H/I$, to be

$$R_H = \frac{B}{ne}. \tag{2.9}$$

Importantly, the Hall resistance depends only on the size of the magnetic field and the electron density, *i.e.* no other physical parameters such as sample size, geometry, etc. play a role. The Hall resistance (voltage) is often denoted by $R_{xy}$ ($V_{xy}$) reflecting that it is measured in the transverse direction. Throughout this thesis, however, I will use the convention that denotes the Hall direction by a subscript $_H$.

### 2.1.2  Integer Quantum Hall Effect

In 1980, performing a similar experiment to Edwin Hall's but in the quantum regime (very low temperature, and in the 2D limit), Klaus von Klitzing discovered the quantum Hall effect [1]. In von Klitzing's experiment, shown in Fig. 2–2, the basic Hall effect was
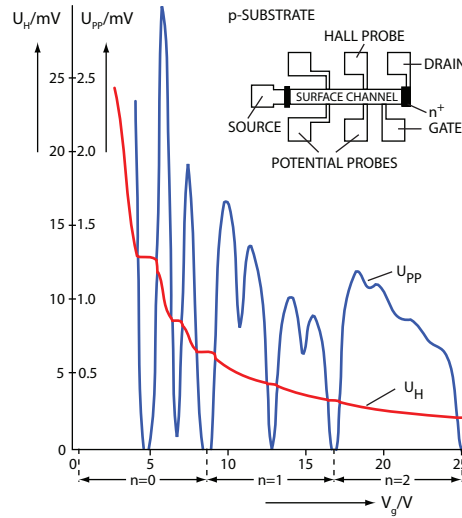
Figure 2–2: Plot from von Klitzing's discovery of the quantum Hall effect [1]. Plateaus in the Hall resistance were observed to be quantized to integer multiples of $h/e^2$, together with vanishing resistance in the longitudinal direction.

observed, namely the Hall resistance varies with magnetic field[1] , however at well defined values of B field, plateaus appear in the hall resistance, together with vanishing resistance measured in the longitudinal direction. The plateaus were found to be exactly quantized at values

$$R_H = \frac{1}{i} \frac{h}{e^2} \tag{2.10}$$

where $i$ is integer valued, $h$ is Plank's constant, and $e$ is the electron charge. Both the quantized plateau in $R_H$ and the zero resistance value in $R_{xx}$ can be understood in terms of Landau levels in a 2D system.

In the presence of a magnetic field, the electron energy states collapse onto quantized circular orbits in the plane transverse to the B field, separated by a well defined gap (Fig. 2–3). In the strictly 2D limit the LL levels represent the only energy levels the electrons can occupy. Note that this differs from the 3D case where electrons are likewise confined to LLs in the x-y plane, but can take on any value in the quasi-continuous energy spectrum

---

[1] In his von Klitzing's experiment he equivalently varied the electron density by applying a gate voltage.

along the z-direction. Solving the Schrodinger equation in 2D for a single electron in the presence of a magnetic field gives the the Landau level (LL) energy to be

$$E_N = (N + 1/2)\hbar\omega_c \tag{2.11}$$

where N=0,1,2... is the LL index and $\omega_c$ is the cyclotron frequency, given by

$$\omega_c = \frac{eB}{m^*} \tag{2.12}$$

where $B$ is the magnetic field and $m^*$ is the effective electron mass ($m^* = 0.067m_e$ in GaAs). In the absence of a magnetic field, the density of states (DOS) in 2D is constant as a function of energy. With a magnetic field turned on however, the density of states collapses onto a series of highly degenerate $\delta$-functions (in the ideal, zero disorder case), corresponding to the Landau Levels. In real samples, the $\delta$-functions are broadened due to disorder scattering. The LL degeneracy, *i.e.* the number of states per LL (per unit area) varies with the size of the $B$ field according to

$$n_B = \frac{eB}{h} \tag{2.13}$$

where the spin degeneracy has not been included, which, for spin degenerate system would contribute an additional factor of two. As the magnetic field is increased, the degeneracy of the LLs, or in other words the size of the LLs (in k-space), increases so that it requires more electrons to fill up each LL. At very low temperatures, electrons fill the lowest available energy states in the usual way so that LLs are filled sequentially up to the Fermi level. At low temperatures and low magnetic fields a large number of LLs will in general be filled. As the magnetic field is increased the LL degeneracy increases resulting in fewer and fewer LLs being occupied until at sufficiently large values of $B$ only the lowest LL contains any electrons. Between these two extremes there exists special cases where an integer number of LLs are exactly filled, occurring at magnetic field values of

$$B_\nu = \frac{1}{\nu}\frac{n\,h}{e} \tag{2.14}$$

where $\nu = \frac{n}{n_B}$ is termed the filling fraction. The filling fraction gives the ratio between the number of electrons and the number of available states per LL. For example $\nu = 1$ indicates the lower spin branch of the lowest LL (N=0) is exactly filled; $\nu = \frac{3}{2}(= 1 + \frac{1}{2})$ indicates the lower spin branch of the lowest LL is completely filled plus exactly half of the
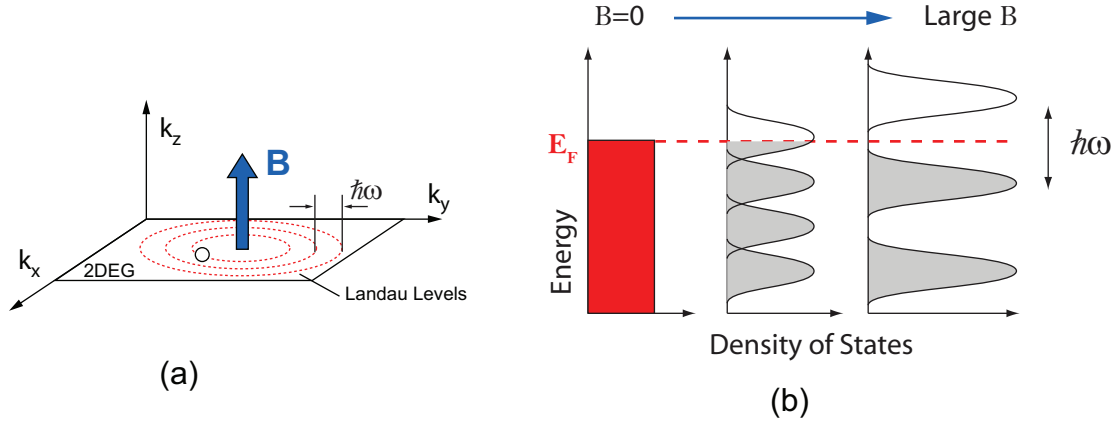
Figure 2–3: (a) Application of a magnetic field causes the electron energy states to collapse onto concentric circular orbits (in k-space), separated by a well defined gap. (b) Increasing the magnetic field increases the size of the LLs so that fewer and fewer LLs are occupied if the electron density remains fixed. At special values of the B field (far right panel) an integer number of LLs are exactly filled, and the Fermi level lies in the gap between adjacent LLs. The LLs are shown as disorder broadened, rather than as ideal (unrealistic) $\delta$-functions in the DOS.

upper spin branch in the lowest LL is filled, while at $\nu = 2$ both spin branches of the LL level are exactly filled, and so on.

It is useful to note that there are several equivalent definitions of the filling fraction

$$\nu = \frac{n}{n_B} = n\frac{h}{eB} = n\frac{\Phi_o}{B} = n\,2\pi l_B^2 \tag{2.15}$$

which can all be derived from the above equations, where $\Phi_o = h/e$ is the definition of the flux quantum, and $2\pi l_B^2$ is simply the area of a Landau level whose radius is the magnetic length, $l_B = \sqrt{\hbar/eB}$. In particular, it can be illuminating to note that from the definition of the flux quantum, the LL degeneracy (per unit area) in Eqn. 2.13 can be rewritten as $n_B = B/\Phi_o$. For a sample of area A, this gives the total number of states per LL to be

$$N_B = AB/\Phi_o = \Phi/\Phi_o \tag{2.16}$$

where $\Phi$ is the *total flux* penetrating the sample. Rewriting the LL degeneracy in this way reveals explicitly that there exists one energy state for each quantum of flux that penetrates the sample.

At exact filling, all lower energy states (LLs) are completely filled while the higher levels are separated by the energy gap between LLs (*i.e.* the cyclotron energy gap, $\Delta = \hbar\omega_c$). Since there are no free energy states within the filled LL level there can be no

scattering as there are no available states to scatter into, provided the temperature is low enough that $k_B T < \Delta$. The transport therefore becomes dissipationless and the resistance falls to zero. Recall from the classical Hall effect (Eqn. 2.9), that the Hall resistance is $R_H = B/ne$. Substituting into this relation the result from Eqn. 2.14, therefore gives the value of the Hall resistance at the condition of exact LL filling to be

$$R_H = \frac{1}{\nu} \frac{h}{e^2} \tag{2.17}$$

which is exactly the quantized resistance values of the plateaus observed in experiment (Eqn. 2.10).

It can be useful to consider the transport in terms of conductance rather than resistance. From the semi-classical Drude model, conductivity is given by

$$\sigma = \frac{ne^2 \tau}{m^*} \tag{2.18}$$

where the conductivity defines the relation between current density and applied electric field ($J = \sigma E$). In this relation $n$ is the electron density, $e$ is the electron charge, $m^*$ is the effective mass, and $\tau$ is the transport (or scattering) lifetime. In zero magnetic field the conductivity is isotropic, and related simply to the resistivity by $\rho = 1/\sigma$. The magnetic field however introduces anisotropy causing the conductivity in the plane perpendicular to the $B$ field to become defined by a 2D tensor relation

$$\sigma = \begin{pmatrix} \sigma_{xx} & \sigma_H \\ -\sigma_H & \sigma_{xx} \end{pmatrix}. \tag{2.19}$$

The corresponding resistivities are then related by the resistivity tensor

$$\rho = \frac{1}{\sigma_{xx}^2 + \sigma_H^2} \begin{pmatrix} \sigma_{xx} & \sigma_H \\ -\sigma_H & \sigma_{xx} \end{pmatrix}. \tag{2.20}$$

For a square 2D sample the resistance equals the resistivity ($\rho = R$) so that the QHE is characterized by

$$\rho_{xx} = 0, \quad \rho_H = \frac{1}{\nu} \frac{h}{e^2}. \tag{2.21}$$

From the relation in Eqn. 2.20 this gives the corresponding conductivities of the QHE state to be
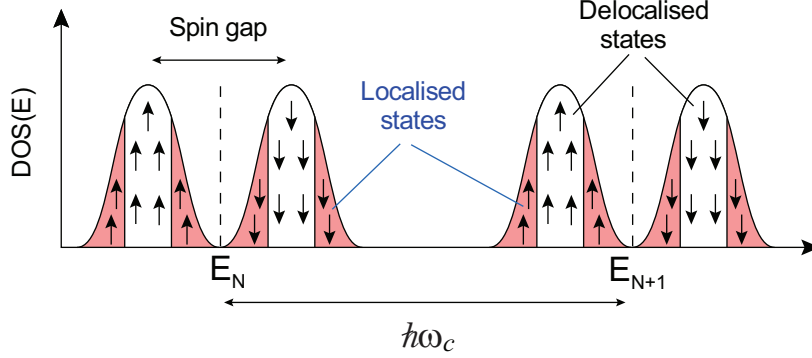
Figure 2–4: Diagram showing the region of localized states versus delocalized states in the disorder broadened LLs. Also illustrated is Zeeman splitting of the upper and lower spin branch of adjacent LLs.

$$\sigma_{xx} = 0, \quad \sigma_H = \nu \frac{e^2}{h}. \tag{2.22}$$

The vanishing longitudinal resistance seen at the QHE can also be understood from the point of view of conductivities by noting that at exact filling the Fermi level lies in the gap between LLs, where the density of states is zero. Since the longitudinal conduction happens at the Fermi level, when the DOS goes to zero the conductivity also goes to zero. From the above relations, $\rho_{xx} \propto \sigma_{xx}$ giving $\rho_{xx} = 0$ at exact filling of the LL as above.

The condition of exact LL filling that is used to explain the QHE is met only at very unique values of the $B$ field. Experimentally however, the plateaus in $R_H$ and corresponding zero resistance in $R_{xx}$ are observed to extend over a wide range of the magnetic field around these values. This is attributed to impurities that cause broadening of the LLs due to scattering. The broadened LLs consist of two types of states, namely *extended states* that occupy the middle of the LL and *localized states* that occupy the tails as shown in Fig. 2–4. The "localized" nature of the states result form impurities in the 2DEG that create potential variations, which trap electrons in tight circular orbits (Anderson localization). These localized states cannot contribute to transport since they do not extend over the whole sample. The QHE can thus be considered as a transition from localized to delocalized states as the Fermi level moves across the density of states [2,3].

Finally, the above description of the QHE assumes an ideal 2D sample of infinite extent in the x and y directions. In a real system, effects of the boundaries and contacts causes the energy bands to bend up at the edges. This gives rise to the edge state picture which
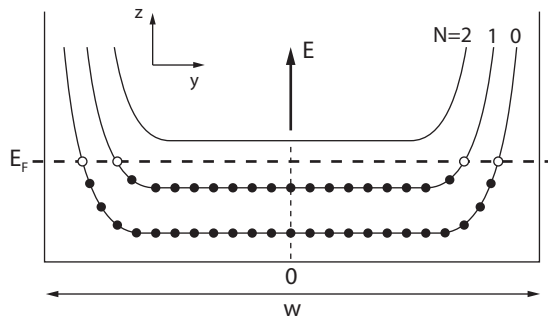
Figure 2–5: Energy spectrum of a 2DEG in a sample of finite width, w, showing only the three lowest LLs. Energy states bend upwards at the edges due to the confining potential. All states below the Fermi level are occupied (solid circles), with the transport edge channels existing only at the intersection of the LLs with the Fermi level (open circles).

interprets the quantum Hall effect in terms of a sequence of incompressible stripes crossing the Fermi level at the edge (Fig. 2–5) [4–6].

### 2.1.3   Fractional Quantum Hall Effect

In 1982, examining 2DEG samples with significantly improved quality than in von Klitzing's earlier experiment, and under the application of much higher magnetic fields, Daniel Tsui and Horst Stormer observed the hallmark characteristics of the quantum Hall effect (quantized plateau in $R_H$ together with vanishing resistance in $R_{xx}$), but occurring at only $\frac{1}{3}$ *fractional filling* of the lowest Landau level [7]. Since in this regime the system was far away from exact filling, the usual filled LL picture could not apply. Instead, understanding the existence of fractional states would require the explicit inclusion of many-body interactions into the theory.

### 2.1.4   Laughlin States

In the earliest theoretical work following the discovery of a quantum Hall state at $\nu = \frac{1}{3}$, Robert Laughlin proposed a ground state wavefunction to describe the FQHE at $\nu = 1/m$ fractional filling [8,9]

$$\Psi_m(z_j, ..., z_k) = \prod_{j<k>}^{N} (z_j - z_k)^m \exp\left[-\frac{1}{4\,l_B^2} \sum_{j}^{N} |z_i|^2\right] \tag{2.23}$$

where $m$ is an odd integer, $z_j = x_i + iy_j$ is the location of the $j^{th}$ particle expressed as a complex number, and $l_B$ is the magnetic length. Laughlin constructed this wave function as a many-body variational ground state for the Hamiltonian
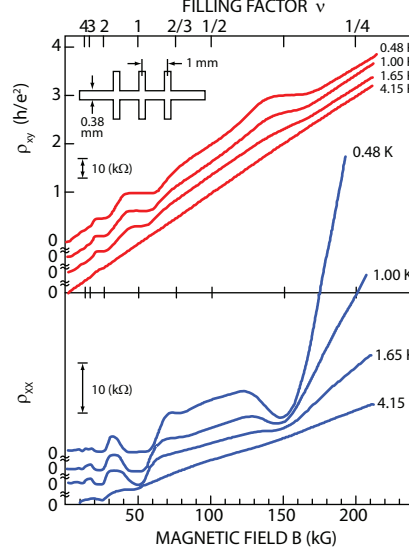
Figure 2–6: Plot from Dan Tsui and Horst Stormer's discovery of the fractional quantum Hall effect [7]. Characteristics of the quantum Hall effect (quantized resistance in $R_H$ together with vanishing resistance in $R_{xx}$) is observed at $\nu = \frac{1}{3}$ fractional filling.

$$\mathcal{H} = \sum_{j}^{N} \frac{1}{2m_e} \left[ \frac{\hbar}{i} \vec{\nabla}_j - \frac{e}{c} \vec{A}(\vec{r_j}) \right]^2 + \sum_{j<k}^{N} v(\vec{r}_j - \vec{r}_k) + \sum_{j}^{N} V_{ion}(\vec{r_j}) \qquad (2.24)$$

where the first term is simply the Hamiltonian for a charged particle moving in a magnetic field where $\vec{A}$ is the vector potential associated with the magnetic field, $\vec{B} = \vec{\nabla} \times \vec{A}$; the second term is the electron-electron Coulomb interaction, $v(r) = e^2/r$; and the third term, called the ion potential, is introduced to describe a background charge density that is necessary to balance out the Coulomb repulsion in order for the system to be stable.

There are several important features of the original Laughlin wavefunction that continue to form the basis of our understanding of the FQHE states, including:

i. The Laughlin ground state wavefunction is a many-body wavefunction constructed to satisfy a Hamiltonian that explicitly includes electron-electron interactions

ii. The electron density is restricted to values $\frac{1}{m} n_B$ where $m$ is an odd integer and $n_B = 1/2\pi l_B^2$ is the LL degeneracy. In other words the wavefunction only applies to *odd-denominator fractional filling* of the LL.

iii. The functional form of the wavefunction necessarily gives rise to an energy gap in the excitation spectrum. The existence of the gap is the basis for the incompressible nature of the states (zero resistance measured in $R_{xx}$), similar to the IQHE.

15

iv. Elementary excitations carry a fractional charge of $e^* = \frac{1}{m}e$

Importantly, while many of the features of Laughlin's wavefunction were essentially required in order to agree with existing experimental observation of the FQH state, the predicted fractional charge was confirmed by later experiments [10–13].

### 2.1.5  Hierarchical model

The original Laughlin formalism only described states occurring at $\nu = \frac{1}{m}$ fractional filling of the lowest LL. After the first discovery of the $\nu = \frac{1}{3}$ fractional state, however, the FQHE was observed at many fractional fillings throughout the first and second Landau levels, occurring in general at $\nu = \frac{p}{q}$ where q is an odd integer. Haldane [14] and Halperin [15] extended the work of Laughlin to explain these other fractional states by introducing the hierarchical model. In the standard hierarchical model, the Laughlin states $(\nu = \frac{1}{m})$ are identified as "primary" fractions. Other fractions are then interpreted as "daughter states", resulting from a Laughlin-like condensation of quasi-particles formed from the parent states of the primary fractions. The process is then repeated to subsequent levels giving the hierarchical sequence

$$\nu = \cfrac{1}{m + \cfrac{\alpha_1}{p_1 + \cfrac{\alpha_2}{p_2 + \cfrac{\alpha_3}{p_3 + \cdot_{\cdot_\cdot}}}}} = \{m, \alpha_1 p_1, \alpha_2 p_2, ...\} \tag{2.25}$$

where $m = 1, 3, 5, ...$, $\alpha_i = \pm 1$ and $p_i = 2, 4, 6....$ The hierarchical states are therefore restricted to rational values of $\nu$ with odd denominators where the $\nu = \{m, p_1, \cdots, p_n\}$ state can exist only if the parent $\nu = \{m, p_1, \cdots, p_{n-1}\}$ state also exists. An important consequence of the hierarchical construction was the identification by Halperin [15] that the quasi-particle excitations in addition to being fractionally charged also exhibit fractional statistics. This was later confirmed in calculations of the Berry phase by Arovas *et al.* [16, 17].

### 2.1.6  Composite Fermion model

Jain proposed [18,19] an alternate model based on the formation of composite particles (CP). In the composite particle picture the parameter of interest is the number of flux quantum present in the sample relative to the number of electrons. For a 2DEG in the presence of a magnetic field, there exists 1 flux quantum for every available particle state in the Landau level (Eqn. 2.16). Therefore, at $\frac{1}{3}$ fractional filling of the lowest LL, for
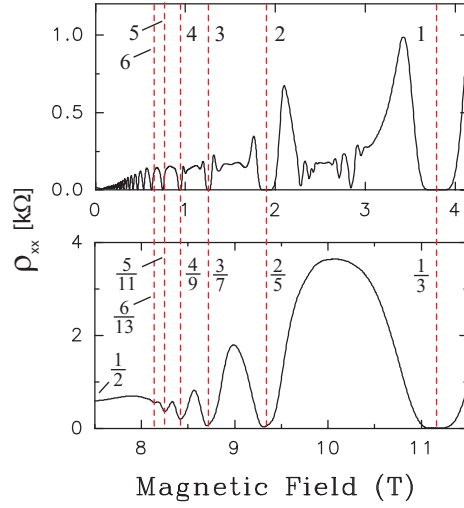
Figure 2–7: (a) Magnetoresistance plotted versus B showing the IQHE for filling fractions greater than $\nu = 1$. (b) Magnetoresistance trace from the same sample showing FQH states in the region $\nu < \frac{1}{2}$. The curve in (b) is plotted on the same scale as in (a) revealing an exact one-to-one correlation (indicated by the dashed lines) between the oscillations in the FQH states around $\nu = \frac{1}{2}$ and the IQH states around B=0. In the composite Fermion model the FQH states around $\nu = \frac{1}{2}$ are interpreted as the IQHE but for composite Fermions. The panels in the figure are reproduced from Ref. [20].

example, there are 3 times as many flux quanta as electrons. At $\frac{1}{2}$ fractional filling there are twice as many flux quanta as electrons, and so on. By attaching these fluxes to the electrons (physically this corresponds to minimizing the Coulomb interaction), the strongly interacting many body electron system can be renormalized as a system of essentially non-interacting "composite particles" (electrons + flux quantum) in the presence of a zero effective magnetic field. The quantum statistics of this process are such that an electron + an even number of flux yields a composite Fermion, while an electron + an odd number of flux gives a composite Boson. Jain used this concept to unify the fractional and integer quantum Hall effects under a single theory by arguing that the FQHE resulting from complicated many-body interactions in the electron system could be understood simply as the IQHE but for non-interacting *composite Fermions* (CF's).

By way of example consider the FQH states around $\nu = \frac{1}{2}$ fractional filling in the lowest Landau level. In the composite particle picture, the system at exactly $\nu = \frac{1}{2}$ can be remapped as a system of independent CF's (each CF comprised of 1 electron + 2 flux), in a zero effective magnetic field. As the real field is increased away from this value, the effective field likewise increases away from zero. The complete series of fractional states observed between $\nu = \frac{1}{2}$ and $\nu = \frac{1}{3}$ can then be reinterpreted as the integer QHE

effect for the electron + 2 flux composite Fermions, with, for example the $\nu = \frac{1}{3}$ FQH state for electrons corresponding to the $\nu = 1$ IQH state of CF's; the $\nu = \frac{2}{5}$ FQH state corresponding to the $\nu = 2$ IQH state in the CF series, and so on (Fig. 2–7). Note that the same result follows from decreasing the B field away from $\nu = \frac{1}{2}$ state since the $\nu = \frac{2}{3}$ is the particle-hole conjugate of the $\nu = \frac{1}{3}$ (*i.e.* $\frac{2}{3} = 1 - \frac{1}{3}$) and is expected to obey the same physics. In the renormalized CF picture, therefore, all quantum hall states around $\nu = \frac{1}{2}$ are interpreted as resulting from sequential filling of quantized CF Landau orbits, with corresponding CF-energy gaps (the CF's being characterized by their own effective mass) etc., in direct analogy to the IQHE for real electrons. This model can be generalized so that all FQHE states are classified according to a composite Fermion series around a $\nu = \frac{1}{2m}$ even denominator fraction (*i.e.* $\nu = \frac{1}{2}, \frac{1}{4}$,...). This gives a general theory that restricts the FQHE to odd denominator fractional fillings according to

$$\nu = \frac{p}{2mp \pm 1} \tag{2.26}$$

where $m, p$ are integer valued.

Several experiments have lent considerable support to the composite Fermion model. For example the CF effective mass and corresponding CF IQHE energy gaps deduced from activation studies, and from examination of the Shubnikov de Haas (SdH) oscillations around $\nu = \frac{1}{2}$ have shown excellent correspondence to the IQHE $B$ field behaviour of electrons around $B = 0$ [21–25]. Similar to the hierarchical construction developed by Haldane [14] and Halperin [15], the CF model likewise predicts excitations to carry fractional charge and fractional statistics. Furthermore, the CF model gives a complete prediction of which fractional fillings are even expected to exhibit FQH states, and with the correct relative strength [18, 19]. A further recent success in the CF model was realized by Pan *et al.* in which it was shown that observed FQH states that do not fit the standard series given by Eqn. 2.26 (*i.e.* $\nu = \frac{4}{11}$ and $\frac{5}{13}$) actually correspond to a second level hierarchy corresponding to a FQHE of composite Fermions, resulting from residual interactions between the CF's [26, 27].
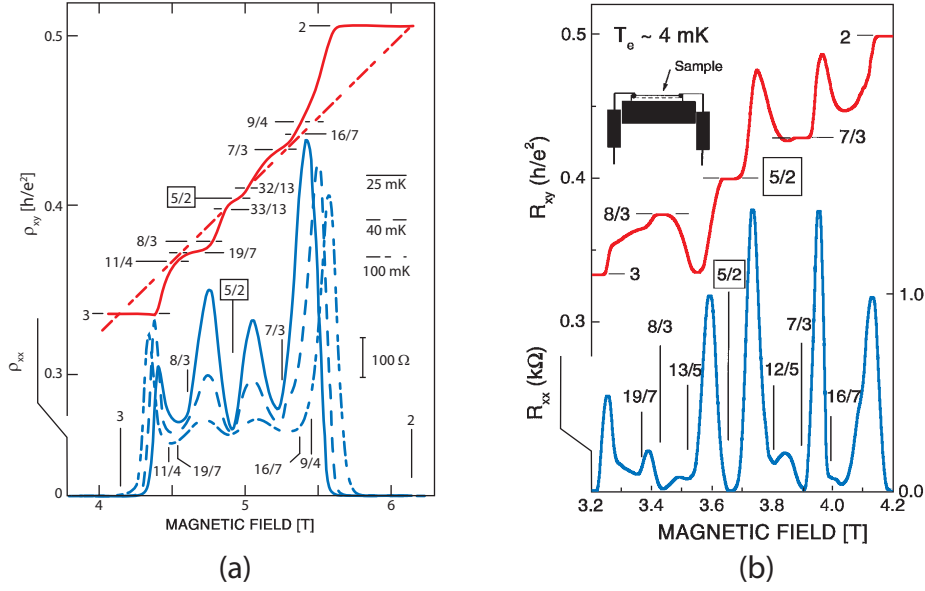
Figure 2–8: (a) Plot from the first discovery of the $\nu = \frac{5}{2}$ state by Willett *et al* [28]. (b) Verification of the FQH effect at $\frac{5}{2}$ by Pan *et al.* [29] showing exact quantization in $R_H$ together with zero resistance measured in $R_{xx}$.

## 2.2   Quantum Hall Effect at $\nu = 5/2$

In 1987 Willett *et al.* reported the observation of a quantum hall state at $\nu = \frac{5}{2}$ even denominator filling fraction [28]. In the more than twenty years since its discovery, the $\frac{5}{2}$ FQHE (and equivalently its particle hole pair conjugate at $\nu = \frac{7}{2}$) remains the only violation of an otherwise strict adherence to the odd-denominator rule[2] . Extensive theoretical work has indicated the $\frac{5}{2}$ state is likely described by the Moore-Read Pfaffian wavefunction, which describes a Laughlin-like condensation of Bosons resulting from a BCS-like pairing of composite Fermions. However, unequivocal experimental support for this theory remains elusive. In this section I give an historical account of the experimental and theoretical efforts that have been made in an attempt to understand the origin of the enigmatic $\frac{5}{2}$ FQHE. I begin with a review of the early work leading up to the proposed Moore-Read Pfaffian and in this context discuss other candidate wavefunctions. I then review in detail the Moore-Read wavefunction, and discuss the theoretical and experimental support for

---

[2] There is some experimental evidence [30–32] of a possible even denominator FQH state at $\nu = 2 + \frac{3}{8}$, however, this has not yet been verified by observation of exact quantization in $R_H$.

19

this theory. Finally I conclude with a summary of the current status of the $\frac{5}{2}$ and outline important remaining questions, motivating the work described in the remainder of this thesis.

### 2.2.1   Discovery and early work on the 5/2 FQHE

An even-denominator FQH state was unexpected according to existing theories and so Willett's surprising discovery of the $\nu = \frac{5}{2}$ FQHE initiated intense investigation of this state. To account for a FQH state at even denominator fractional filling, Haldane and Rezayi [33] proposed a spin-singlet (unpolarized) candidate wavefunction, drawing inspiration from an electron pairing idea first suggested by Halperin [34]. At the same time, Eisenstein *et al.* used a tilted field technique to experimentally measure the spin-polarization nature of the $\frac{5}{2}$ state [35,36]. Eisenstein found that under the application of a parallel field, the $\frac{5}{2}$ was destroyed. This was interpreted as an indication that the $\frac{5}{2}$ state is spin-unpolarized, where the destruction under tilt results from an increasing Zeeman energy that drives the system from a spin-unpolarized $\frac{5}{2}$ state to a spin-polarized compressible Fermi liquid. A linear fit to the activation energy gave support to this interpretation, yielding a value for the effective g-factor of 0.56, in reasonable agreement with the value 0.44 for bulk GaAs [36]. Eisenstein's results therefore seemed to confirm the unpolarized spin-singlet wavefunction proposed by Haldane and Rezayi (HR). However, the pairing mechanism in HR's spin-singlet picture remained unclear. Moore and Read then pointed out [37] that pairing at even denominator filling (*i.e.* 1/2, 1/4...) could be interpreted as a BCS-like pairing [38,39] of composite fermions in zero effective magnetic field. Moore and Read then proposed an alternate spin-polarized (p-wave) triplet wavefunction to describe this pairing, which has since become known as the Moore-Read Pfaffian. Following the work of Moore and Read, Greiter, Wen and Wilczek [40] suggested that the Moore-Read Pfaffian could be applied to describe the $\frac{5}{2}$ state, finding the Moore-Read wavefunction to be the zero energy ground state for a three-body Hamiltonian, and calculating a gap energy. This work was supported by Read and Rezayi [41] who later confirmed the Moore-Read wavefunction to be an exact ground state for a three body interaction Hamiltonian at $\nu = \frac{5}{2}$.

Halperin's original paired wavefunction, the so called 331 state, also remained as a candidate wavefunction to explain the $\frac{5}{2}$ FQHE. However, this state was viewed as an unlikely description. Halperin's $\Psi_{mmn}$ wavefunction was originally proposed in an an early effort to extend the Laughlin formalism to other fractions. In this construction, Halperin suggested that incompressible states at fractional filling could result from electron pairing,

where the paired-electrons could, in principle, form a Laughlin state for Bosons [34]. He further showed that this wavefunction could be extended to even-denominator filling, with the $\Psi_{331}$ describing a pairing of opposite spin electrons at half-filling. The 331 state was later found to be the correct description of the even denominator fractional state observed in *bi-layer* systems [42–45]. However, in single layer systems the 331 state is expected to occur only at very weak magnetic fields where the spin splitting is small [44]. Even more problematic is that the 331 does not belong to the correct symmetry group [33, 44, 46] and vanishes when the opposite spin electrons coincide [33]. It should be noted that Haldane and Rezayi began with the Halperin 331 state when constructing their spin-singlet wavefunction, but explicitly modified it to correct these issues [33].

Since its introduction, the Moore-Read Pfaffian wavefunction received considerable interest due to its exotic, fractionally charged excitations ($e^*=e/4$ at $\nu = \frac{5}{2}$), predicted to exhibit non-Abelian fractional statistics. However, for several years it was believed that the Rezayi-Haldane spin-singlet was the correct description of the $\frac{5}{2}$ state rather than the Moore-Read Pfaffian, largely due to the tilted field results of Eisenstein *et al* [35, 36]. In 1998 Morf challenged this view when he showed by numerics that a spin polarized ground state represents the lowest energy state at $\frac{5}{2}$, and simultaneously demonstrated large overlap of the spin-polarized Moore-Read Pfaffian with the exact small-system numerical wavefunction, *i.e.*, obtained by numerical exact diagonalization for a few particle system. To account for the observations of Eisenstein *et al.* in tilted fields, Morf argued that the destruction of the $\frac{5}{2}$ could be due to magneto-orbital coupling to the parallel field rather than the result of a "simple" Zeeman interaction. This was considered plausible since it was already known that the in-plane field can have several effects in addition to merely increasing the Zeeman energy, such as squeezing the wavefunction in the transverse direction, increasing the disorder induced level broadening, and introducing subband/Landau level mixing [4, 35, 36, 47–51]. Finally, Morf identified the appearance of the $\frac{5}{2}$ as being related to an optimal tuning of the effective interaction between carriers, with even a slight modification away from the optimal value causing a transition to a new state. Rezayi and Haldane subsequently confirmed Morf's findings, reporting similar evidence in favour of the spin-polarized MR Pfaffian being the likely description of the $\frac{5}{2}$ state and rejected their previously proposed unpolarized spin-singlet wavefunction [51].

### 2.2.2   The Moore-Read Pfaffian

The Moore-Read (MR) Pfaffian wavefunction is given by

$$\Psi_{Pf}(z_1, ..., z_N) = Pf\left(\frac{1}{z_i - z_j}\right)\psi_{1/q} \tag{2.27}$$

where $Pf(M)$ is the *Pfaffian* operator. The Pfaffian is *"precisely the sum of products of Fermion pairs, antisymmeterized over all distinct ways of pairing"* [52], defined by

$$Pf(M_{ij}) = \frac{1}{2^{L/2}(L/2)!} \sum_\sigma sgn(\sigma) \prod_{k=1}^{N/2} M_{\sigma(2k-1),\sigma(2k)} \tag{2.28}$$

where $M_{i,j}$ are the elements of an antisymmetric $L \times L$ matrix. The Pfaffian formalism was inspired by the notion that the wavefunction for a spin-polarized p-wave BCS superconductor, written in real space for a definite number of Fermions, takes the form of a Pfaffian [37, 40, 52].

The second term in Eqn. 2.27 is

$$\psi_{1/q} = \prod_{i<j}(z_i - z_j)^q \exp\left[-\frac{1}{4\,l_B^2}\sum_j^N |z_i|^2\right] \tag{2.29}$$

which is just the Laughlin wavefunction, given in (2.23), but with $q$ restricted to *even* integer values. The Laughlin wavefunction was originally defined for odd-denominator fractions only (*i.e.* odd values of $q$). However, in the composite particle picture the Laughlin state can be precisely interpreted as a Bose condensation of composite Bosons (electron plus odd number of flux) [52]. The Laughlin state therefore can equally describe a condensation of Bosons at even denominator filling, but where the existence of Bosons results from electron pairing. In essence therefore, the Moore-Read Pfaffian describes a Laughlin-like condensation of Bosons, where the formation of Bosonic particles results from a BCS-like pairing of composite Fermions. Importantly, Read pointed out that the Moore-Read Pfaffian can be equivalently viewed as describing either pairing of spin-polarized electrons or pairing of composite Fermions [53, 54, 54]. This is because the essential feature of the wavefunction is the Pfaffian construction, which results from the p-wave pairing of polarized Fermions (in a triplet state), independent of whether the Fermions are electrons or composite Fermions (Fermion plus even number of flux quanta).

While the Moore-Read Pfaffian can be viewed in general terms as a Laughlin-like condensation of Bosons, this state has charged excitations that are very different from the Laughlin liquid. In the following the many unique features of the Moore-Read wavefunction are discussed in further detail.

### 2.2.3  $e^* = e/4$ fractional charge

Excitations of the Moore-Read ground state at $\nu = \frac{5}{2}$ carry $e/4$ fractional charge. This results from the Laughlin term in the Moore-Read wavefunction which in general (see section 2.1.4) exhibits excitations at fractional filling, $\nu$, with fractional charge $\nu e$. Recall from Eqn. 2.15 that the filling factor for a system of electrons (Fermions) can be written as

$$\nu = n\frac{h}{eB} \tag{2.30}$$

where $n$ is the electron density and $e$ is the electron charge. Electron pairing transforms this into a system of Bosons, thereby giving half as many particles, $n \rightarrow n/2$, with each particle (Boson) carrying twice the charge $e \rightarrow 2e$. The filling fraction for this system of Bosons therefore becomes

$$\nu_B = \left(\frac{n}{2}\right)\frac{h}{(2e)B} = \frac{1}{4}\left(n\frac{h}{eB}\right) = \frac{1}{4}\nu. \tag{2.31}$$

Ignoring the LLL, the filling fraction for Fermions at $\nu = \frac{1}{2}$ in the SLL (*i.e.* $\nu = \frac{5}{2} = 2 + \frac{1}{2}$) therefore becomes $\nu_B = \frac{1}{8}$ in the system of Bosons. Finally, Laughlin quasi-particle excitations carry charge $\nu q$ where q is the particle charge, and so for the system of charge-2 Bosons at $\nu_B = \frac{1}{8}$ (*i.e.* $\nu = \frac{1}{2}$ for electrons), the Laughlin quasi-particle fractional charge is

$$e^* = (\frac{1}{8})(2e) = \frac{e}{4}. \tag{2.32}$$

Note that in this picture the Hall conductivity remains unchanged. For a system of Fermions, the quantized Hall conductivity, $\sigma_H$, is

$$\sigma_H = \nu\frac{e^2}{h} \tag{2.33}$$

In the system of Bosons $e \rightarrow 2e$ and $\nu \rightarrow \nu/4$, but, substituting these into Eqn. 2.33 just gives back the same result, in agreement with the Hall quantization measured at $\frac{5}{2}$ in experiments [29].

### 2.2.4  Non-Abelian statistics

The quantum statistics of Fermions or Bosons can be distinguished by the symmetry that results when adiabatically exchanging a pair of particles. For example, if $\mid \psi_1\psi_2 \rangle$ is a two-particle wavefunction, then if we interchange the two particles the state becomes

$$| \psi_2 \psi_1 \rangle = \pm | \psi_1 \psi_2 \rangle \qquad (2.34)$$

such that the wavefunction describing the two-particle state is symmetric (antisymmetric) under exchange for Bosons (Fermions). In 2D spatial dimensions, quantum particles are not restricted to only Bosonic or Fermionic behaviour but instead can exhibit more generalized statistics such that interchange results in an arbitrary phase rather than only $\pm 1$, *i.e.*

$$| \psi_2 \psi_1 \rangle = e^{i\theta} | \psi_1 \psi_2 \rangle \qquad (2.35)$$

where the statistical phase angle, $\theta$, can take any values between 0 and $\pi$. Particles that exhibit such statistics are termed anyons ("any"-ons) [17]. The Laughlin quasi-particles are believed to exhibit anyonic fractional statistics [15–17] such that at fractional filling, $\nu$, the corresponding phase is given by

$$\theta = \nu\pi. \qquad (2.36)$$

In their seminal paper, Moore and Read argued, by making connections to conformal field theory, that the Moore-Read Pfaffian gives rise to excitations with even more exotic quantum statistics termed non-Abelian anyonic statistics [37, 41]. Particles exhibiting non-Abelian statistics are not described by a simple phase factor under adiabatic exchange but rather by a matrix operator, which is not commutable. This is perhaps best summarized by Read and Rezayi [41];

> *"...non-Abelian statistics requires that there be degenerate states for well-separated quasiparticles, and, when the quasiparticles are exchanged adiabatically, the effect is not merely a Berry phase representing ordinary fractional statistics, but a matrix acting within the space of degenerate quasiparticle states."*

The possibility that the composite particles comprising the $\frac{5}{2}$ state exhibit non-Abelian statistics, a predicted quantum property that has never been observed experimentally, has excited intense interest. The recent suggestion that non-Abelian particles could be used to realize fault-tolerant topological quantum computation [55–57] has even further extended the urgency to understand the $\frac{5}{2}$ state beyond the study of quantum Hall physics.

### 2.2.5 Short-range interactions

The fractional quantum Hall effect is fundamentally characterized by many-body electron-electron interactions. Haldane showed that the interaction Hamiltonian in a purely

2D system, where the interaction is strictly defined by the Coulomb energy, can be parameterized by an expansion in "pseudopotential" functions [14], *i.e.*

$$\hat{H} = \sum_{i<j}^{N} V(r_{ij}) = \sum_{m}^{\infty} V_m^{(n)} \sum_{i<j}^{N} \hat{P_m}(m_{ij}) \tag{2.37}$$

where $V(r_{ij})$ is the Coulomb interaction potential, and $\hat{P}$ is a momentum operator. The Haldane pseudopotentials, $V_m^{(n)}$, form a complete basis and are defined for electrons with relative angular momentum, $m$, confined to a LL with index $n$. The appearance of the LL index in the pseudopotential reflects a dependence on which LL's are occupied. For example, for the first pseudopotential, $V_1^{(0)} > V_1^{(1)} > V_1^{(2)}$, whereas for the second pseudopotential $V_2^{(0)} < V_2^{(1)} < V_2^{(2)}$ [58].

The subtle differences in these short range interaction terms are important since they are responsible for the different behaviours observed throughout the Landau levels. For example, the vast majority of the FQH states that have been identified are found in the lowest Landau level (n=0, $0 < \nu < 2$), with only a handful identified in the second Landau level (n=1, $2 < \nu < 4$), and with no states convincingly verified at higher filling fractions ($n > 1$, $\nu > 4$) [31, 58, 59]. Morf argued [47] that the $\frac{5}{2}$ FQH state forms in the second Landau level only for a critical range in values of the short range interaction. He further showed through numerics that weakening the short range interaction away from this critical value causes a transition from the $\frac{5}{2}$ incompressible liquid to a compressible state while in the other extreme strengthening the interaction results in a transition to a Fermi-sea state. Rezayi and Haldane subsequently confirmed this result and identified the compressible state in the weak interaction regime as an anisotropic charge density wave state ("stripe phase") [51, 60]. From this perspective it is argued that an even denominator FQH state is *only* found in the SLL due to a fortuitous modification of the short range interaction in this Landau level compared to the others. According to Read [61], this picture is supported phenomenologically by the observation that at half filling in the LLL (strong short range interaction) the system exists as a Fermi liquid [62], transitioning to an incompressible state at $\nu = \frac{5}{2}$ ($\frac{7}{2}$) in the SLL (moderate short range interaction) [28, 29, 36], and giving way to a stripe phase in higher LLs (weak short range interaction) [63].

In recent numerical work, Peterson *et al.* [58, 64] investigated the effect of varying the 2DEG thickness by examining corresponding variations in the Haldane pseudopotentials. They found that increasing the thickness of the 2DEG actually strengthens the $\frac{5}{2}$ state (and likewise the neighbouring $\frac{7}{3}$ state). This coincides with a corresponding weakening of the Coulomb interaction, which notably differs from the behaviour seen for the

odd-denominator FQH effect in the LLL where increasing the 2DEG thickness conversely destroys the states. Importantly, Peterson *et al.* showed that this contrasting behaviour between the Landau levels is revealed only when considering collectively the relative behaviour of *all* the pseudopotentials. At $\nu = \frac{5}{2}$, they further showed that the lowest order pseudopotentials do not dominate the physics as was implicitly assumed in the work of Morf (who examined the effect of varying $V_1$ only) and Rezayi and Haldane (who examined variations in $V_1$ and $V_3$).

### 2.2.6 Pfaffian versus anti-Pfaffian

In the absence of Landau level mixing, the Hamiltonian at $\nu = \frac{5}{2}$ is symmetric under particle-hole conjugation if one considers only two-body interactions. However, it was recently pointed out [65, 66] that, as first suggested by Greiter *et al.* [40] and later confirmed by Read and Rezayi [41], the Pfaffian is rather the exact ground state wavefunction for a *three-body* Hamiltonian that explicitly breaks this symmetry and so is not particle-hole symmetric. The Pfaffian ($Pf$) and its particle-hole conjugate, the "anti-Pfaffian" ($\overline{Pf}$) therefore must represent distinct phases. In the idealized two-body Hamiltonian the Pfaffian and anti-Pfaffian remain exactly degenerate. However, second-order perturbation theory from Landau level mixing gives rise to three-body interactions, and so is expected to break the $Pf - \overline{Pf}$ symmetry [65, 66]. Levin *et al.* [65] and Lee *et al.* [66] recently, and independently, suggested the Pfaffian is expected in regions of large LLM while at moderate to low LLM (such as that typically observed in experiment) the anti-Pfaffian may represent an alternate candidate wavefunction for the observed $\frac{5}{2}$ state. This may play an important role in understanding experimental data. The $Pf$ and $\overline{Pf}$ share many similarities including the predicted non-Abelian statistics. However, details in the edge transport differ including distinct thermal Hall conductance, and tunneling exponents in the edge state [65, 66]. Measuring these properties may allow future experiments to determine whether a Pfaffian or anti-Pfaffian describes the $\frac{5}{2}$ state and, importantly, may also allow us to determine the specific role played by Landau level mixing in the FQHE, which so far has remained not well understood.

### 2.2.7 Strong versus weak pairing

For the $\frac{5}{2}$ state to result from a Bose condensation of composite Fermions, an attractive coupling between the Fermions is necessary. Read [61] broadly categorizes this coupling into two regimes defined by a weak pairing and strong pairing phase. The weak pairing

regime (weak attractive coupling) corresponds to the Moore-Read state with $e/4$ fractionally charged excitations exhibiting non-Abelian statistics. On the other hand the strong pairing regime corresponds to strong attractive coupling. The strong coupling regime is expected to be related to the Halperin 331 phase and thus exhibit characteristics of the more usual Laughlin states, *i.e.* excitations that carry Abelian statistics. Aside from the corresponding quantum statistics, Read argued that these two regimes could be distinguished by experiments that examine tunneling into the edge. Read explicitly predicts that the exponent in the current-voltage relation (*i.e.* $I \sim V^{\alpha}$) should be $\alpha = 3$ in the weak-pairing (Moore-Read) phase and $\alpha = 8$ in the strong-pairing (Halperin 331) phase [61]

### 2.2.8   Theoretical support for the Moore-Read Pfaffian

Since the seminal work by Morf [47], substantial theoretical work has lent further support for the Moore-Read description, some of which is highlighted here. Shortly after Morf, Park *et al.* showed [67] that the MR Pfaffian is a lower energy ground state than both a fully-polarized and unpolarized Fermi-sea at $\nu = \frac{5}{2}$ and found evidence that the transition to a Pfaffian ground state may be favoured by increasing the thickness of the 2DEG. Using variational Monte Carlo to study paired states, Dimov *et al.* found [68] that at $\nu = \frac{5}{2}$ an incompressible ground state exhibits spontaneous ferromagnetism (*i.e.* fully spin polarized even in the absence of Zeeman energy), thereby favouring the MR Pfaffian (in comparison to Halperin's unpolarized 331 state). Using newly developed numerical methods, Feiguin *et al.* recently confirmed [69, 70] the ferromagnetic ordering at $\nu = \frac{5}{2}$. Peterson *et al.* found that increasing the 2DEG thickness away from the idealized zero thickness limit, *i.e.* mimicking the physical situation found in real samples, stabilizes the $\frac{5}{2}$ [58,64]. Importantly, in this work Peterson *et al.* additionally identified, for the first time, a topological degeneracy with the correct quantum numbers predicted for the Pfaffian state, and furthermore found this degeneracy only at finite thicknesses where overlap calculations with the MR wavefunction are maximum.

### 2.2.9   Observation of the 5/2 at high magnetic fields

Experimental investigations of the $\frac{5}{2}$ have yielded less conclusive results. While much of the experimental work is found to be consistent with the MR description, unequivocal experimental proof is still lacking. This is due in part to the stringent experimental requirements necessary to even observe the $\frac{5}{2}$ state, which has limited possible experiments. The $\frac{5}{2}$ is relatively fragile, appearing only in the very best samples, and requiring minimally invasive measurement schemes, *i.e.* ultra-low temperature, low noise etc. The $\frac{5}{2}$ was

27

first identified at relatively moderate B fields of ~5 T. Subsequent samples were generally grown with similar parameters (density, well construction etc.) therefore yielding a $\frac{5}{2}$ state at similar magnetic fields. In 2001, in an attempt to measure the spin polarization without resorting to tilted fields, Pan *et al.* studied a gated (variable density) sample that exhibited a $\frac{5}{2}$ state over a wide range of fields, from ~5 T up to more than 12 T [71]. Observation of the $\frac{5}{2}$ state at such a large B field represents further evidence in favour of a spin polarized state since if the state were unpolarized, one would expect larger Zeeman energy at these fields to destroy the state. For the same reasons, this finding also supported Morf's contention that the tilted field experiment of Eisenstein *et al.* [35, 36] probably was not due to a Zeeman interaction, but rather due to orbital coupling to the parallel field. However, the $\frac{5}{2}$ in this sample was not fully formed, *i.e.*, the minimum was not observed to go to zero in $R_{xx}$, and only a "developing plateau" was reported in $R_H$, and did not show true activated behaviour. Additionally, there appeared a gate induced mobility variation in the data, that was not fully accounted for in their analysis, making the conclusions of this experiment somewhat ambiguous.

### 2.2.10   Appearance of the stripe phase in tilted field experiments

After the initial work of Eisenstein *et al.* [35, 36], other tilted field experiments showed that the incompressible state at $\frac{5}{2}$ is not "simply" destroyed, but gives way to an anisotropic phase [72, 73]. This finding was in agreement with Morf's prediction [47] that under application of a parallel field, a MR Pfaffian ground state should give way to an charge density wave state (later confirmed by Rezayi and Haldane to be the stripe phase [51]).

In the context of the results from Morf [47] and Rezayi and Haldane [51], the transition from the $\frac{5}{2}$ state to a stripe phase indicates that the parallel magnetic field causes a softening (decrease) of the short range interactions, as defined by the Haldane pseudopotentials. This nicely reflects the symmetry discussed previously where in lower LL's (stronger short range interaction) the half filled state is a Fermi-sea while in higher LL's (weaker short range interaction) the half filled state is a stripe phase. However, a well known effect of coupling to the parallel field is to squeeze the 2DEG towards the ideal 2D limit. This should instead cause a hardening (increase) of the short range interactions and therefore a transition to the Fermi-sea state, rather than a stripe phase. Indeed, Peterson *et al.* found [58], as expected, that squeezing the wavefunction causes a universal increase in all pseudopotentials. However, in the same study, Peterson *et al.* showed that relative variations between all pseudopotentials, rather than arbitrary changes in only the first few, defines the physics. Peterson thus argues that both the work of Morf and Rezayi

and Read may be an oversimplification since varying only the $V_1$ (Morf) or $V_1$ and $V_3$ (Rezayi and Read) pseudopotentials does not reflect a real physical situation. This leaves the possibility that the transition to a stripe is not simply due to a variation in the lowest order pseudopotentials [51] but may result from a more complex interaction. Peterson *et al.* only reported on overlap calculations for the Moore-Read Pfaffian as a function of the 2DEG thickness, and did not investigate possible transitions to other states, *i.e.* whether it transitions to a stripe phase or a Fermi sea [74]. A full understanding of how the $\frac{5}{2}$ transitions to a stripe phase under tilt therefore remains an open question.

In spite of the remaining questions concerning its origin, the very appearance of a stripe phase is an important experimental result since it further questions the spin-unpolarized interpretation of Eisenstein's original tilted field data; *i.e.* it is unclear how Zeeman effects alone, if responsible for destroying the $\frac{5}{2}$ state, could give rise to the stripe phase.

### 2.2.11 Measurement of the $e/4$ fractional charge

Recent measurements of the shot noise [75] at $\nu = \frac{5}{2}$ and independent measurement of the tunneling spectra through a quantum point contact in the edge state [76] at $\nu = \frac{5}{2}$, both confirmed the predicted $e/4$ fractional charge. This represents a significant step towards verifying that the $\frac{5}{2}$ state results from a pairing of composite Fermions. However, other paired, Abelian, candidate wavefunctions are expected to also exhibit $e/4$ charged excitations, and so these results do not *on their own* verify the non-Abelian MR Pfaffian description [58, 61, 70].

## 2.3 Current Status of the 5/2

### 2.3.1 Known discrepancies with the Moore-Read theory

An important discrepancy that has yet to be resolved convincingly is the large difference between the calculated ground state energy gap based on MR description and the energy gaps measured experimentally. The $\frac{5}{2}$ gap is typically measured to be between 100 and 500 mK, which is up to twenty times smaller than theory predicts (1.5 to 2.5 K) for the Moore-Read Pfaffian [69, 77, 78]. By comparison, this discrepancy is much greater than in the well understood $\frac{1}{3}$ Laughlin state in the lowest Landau level, where there is near perfect agreement between theory and experiment [21, 77, 79]. The experimental disagreement with theory at $\nu = \frac{5}{2}$ needs to be addressed since, as Morf states, *"Such large discrepancies make one wonder whether the $\frac{5}{2}$ state has been correctly identified"* [78, 80]. This discrepancy is usually assumed to be due to disorder effects. However, so far there is

no microscopic theory that allows a full understanding of how the $\frac{5}{2}$ state is influenced by disorder.

Another important effect that needs to be more fully understood is Landau Level mixing (LLM). So far LL mixing has been included as a perturbation effect only. Recent theoretical work [65, 66, 80] has suggested LL mixing maybe be fundamentally necessary to understand the $\frac{5}{2}$ state, and may even affect the $\frac{5}{2}$ in a unique way, for example possibly causing a greater reduction in the activation energy gap than at other fractional states [80]. In general, Landau level mixing is expected to be stronger at weak magnetic fields, where the energy separation between LL's is smaller. The $\frac{5}{2}$ state is typically observed in regime of "moderate" LLM (*i.e.* $\sim$5 T), and so the validity of treating the effect in a perturbative way is largely unknown. Importantly, as Levin *et al.* [65] and Lee *et al.* [66] point out, the strength of the LLM may determine whether the Pfaffian, or anti-Pfaffian ground state is selected, with the possibility of a transition between the two as the size of the magnetic field is varied.

Finally, recent theoretical work has raised further questions regarding the MR description. In 2006, Toke and Jain [81] proposed that a fully spin-polarized $\frac{5}{2}$ state could be understood within the composite Fermion picture [18, 19] without appealing to the MR Pfaffian. They argue that residual interactions between composite Fermions could open an energy gap, and therefore yield an incompressible state, in a process that does not require electron pairing. They further argue that this approach addresses shortcomings of the MR Pfaffian description. For example, the MR Pfaffian claims to arise from instabilities in the composite Fermion sea, but the *"composite Fermion sea is not a limiting case of the MR Pfaffian"* [81]. However, so far Toke and Jain have not been able to construct a wavefunction in their theory [82]. Furthermore, recent measurement of the $e^* = e/4$ quasiparticle charge [75, 76] indicates a pairing mechanism is at play, in contrast to the theory of Toke and Jain in which the quasiparticle excitations are predicted to be unpaired composite Fermions. Toke and Jain note that the residual interactions in their picture *"may possibly induce pairing between composite Fermions"*, admitting however that it is not known how this would be established within their approach [81]. Much further work will be required before this approach can be considered a serious challenge to the Moore-Read wavefunction.

### 2.3.2   Needed experiments

Observation of non-Abelian statistics would, of course, provide strongest support for the MR Pfaffian. Several interferometry experiments have been proposed (see for example Refs. [83–85]) to probe the braiding statistics of the $\frac{5}{2}$ state. So far these experiments have

not been possible, owing mostly to the fragile nature of the $\frac{5}{2}$ state which tended to be destroyed by any modifications to the sample such as patterning and gating. An important step towards this effort however was recently realized by Miller *et al.* [86] and also by Willett *et al.* [87] who achieved patterning of a single quantum point contact while maintaining a robust $\frac{5}{2}$ state. In fact, the techniques developed in these studies directly lead to the recent measurements of the $e/4$ fractional charge [75, 76]. Interferometry experiments to measure the non-Abelian statics, which require a double quantum point contact, have not yet been forthcoming, but these advancements in sample fabrication represent a significant first step towards this effort. The existence of non-Abelian statistics so far remains a purely theoretical prediction, as no system exhibiting these characteristics has ever been observed. Thus, even if the required samples can be grown that will allow the proposed interferometry experiments to be carried out, there is no guarantee that the non-Abelian statistics will be observed *even* if the $\frac{5}{2}$ state truly emanates from a Moore-Read type pairing mechanism!

Aside from the predicted non-Abelian statistics, the single feature that distinguishes the MR Pfaffian from other candidate wavefunctions remains the spin polarization, with the MR Pfaffian corresponding to a fully spin polarized state, while all other, Abelian, wavefunctions describe a spin-unpolarized pairing. Determination of the electron spin polarization is therefore of fundamental importance in our attempt to understand this enigmatic state. The only two experiments that have attempted to directly measure the spin polarization, *i.e.* the first tilted field experiments by Eisenstein *et al.* [35, 36], and the gated variable density experiment by Pan *et al.*, yielded results that remain ambiguous. Measurement of the $\frac{5}{2}$ spin state therefore remains a fundamentally important experiment. Our attempts to carry out this measurement are described in the remainder of this thesis.

# References

[1] von Klitzing, K., Dorda, G., and Pepper, M. *Phys. Rev. Lett* **45**, 494 (1980).

[2] Prange, R. E. *Phys. Rev. B* **23**, 4802 (1981).

[3] Laughlin, R. B. *Phys. Rev. B* **23**, 5632 (1981).

[4] Das Sarma, S. and Pinczuk, A. *Perspectives in Quantum Hall Effects.* John Wiley and Sons, Inc., New York, (1997).

[5] Doucot, B., Duplantier, B., Pasquier, V., and Rivasseau, V. *The Quantum Hall Effect: Poincare Seminar 2004.* Birkhauser Verlag, Boston, (2004).

[6] Davies, J. H. *The Physics of Low-Dimensional Semiconductors: An Introduction.* Cambridge University Press, New York, (1998).

[7] Tsui, D. C., Stormer, H. L., and Gossard, A. C. *Phys. Rev. Lett.* **48**, 1559 (1982).

[8] Laughlin, R. B. *Phys. Rev. Lett.* **50**, 1395 (1983).

[9] Laughlin, R. B. *Rev. Mod. Phys.* **71**, 863 (1999).

[10] Clark, R. G., Mallett, J. R., Haynes, S. R., Harris, J. J., and Foxon, C. T. *Phys. Rev. Lett.* **60**, 1747 (1988).

[11] Kane, C. L. and Fisher, P. A. *Phys. Rev. Lett.* **72**, 724 (1994).

[12] de Picciotto, R., Reznikov, M., Heiblum, M., Umansky, V., Bunin, G., and Mahalu, D. *Nature* **389**, 162 (1997).

[13] Saminadayar, L., Glattli, D. C., Jin, Y., and Etienne, B. *Phys. Rev. Lett.* **79**, 2526 (1997).

[14] Haldane, F. D. M. *Phys. Rev. Lett.* **51**, 605 (1983).

[15] Halperin, B. I. *Phys. Rev. Lett.* **52**, 1583 (1984).

[16] Arovas, D., Schrieffer, J. R., and Wilczek, F. *Phys. Rev. Lett.* **53**, 722 (1984).

[17] Wilczek, F. *Phys. Rev. Lett.* **49**, 957 (1982).

[18] Jain, J. K. *Phys. Rev. Lett.* **63**, 199 (1989).

[19] Jain, J. K. *Phys. Rev. B* **41**, 7653 (1990).

[20] Leadley, D. R., Nicholas, R. J., Gee, P. J., Singleton, J., Harris, J. J., and Foxon, C. T. *22nd International Conference on the Physics of Semiconductors - Vol. 3* , 983 (1995).

[21] Du, R. R., Stormer, H. L., Tsui, D. C., Pfeiffer, L. N., and West, K. W. *Phys. Rev. Lett.* **70**, 2944 (1993).

[22] Du, R. R., Stormer, H. L., Tsui, D. C., Pfeiffer, L. N., and West, K. W. *Sol. Stat. Comm.* **90**, 71 (1994).

[23] Leadley, D. R., Nicholas, R. J., Foxon, C. T., and Harris, J. J. *Phys. Rev. Lett* **72**, 1906 (1994).

[24] Manoharan, H. C., Shayegan, M., and Klepper, S. J. *Phys. Rev. Lett* **73**, 3270 (1994).

[25] Du, R. R., Stormer, H. L., Tsui, D. C., Yeh, A. S., Pfeiffer, L. N., and West, K. W. *Phys. Rev. Lett.* **73**, 3274 (1994).

[26] Pan, W., Stormer, H. L., Tsui, D. C., Pfeiffer, L. N., Baldwin, K. W., and W.West, K. *Phys. Rev. Lett.* **90**, 016801 (2003).

[27] Chang, C.-C. and Jain, J. K. *Phys. Rev. Lett.* **92**, 196806 (2004).

[28] Willett, R. L., Eisenstein, J. P., Stormer, H. L., Tsui, D. C., Gossard, A. C., and English, J. H. *Phys. Rev. Lett.* **59**, 1776 (1987).

[29] Pan, W., Xia, J. S., Shvarts, V., Adams, D. E., Stormer, H. L., Tsui, D. C., Pfeiffer, L. N., Baldwin, K. W., and West, K. W. *Phys. Rev. Lett.* **83**, 3530 (1999).

[30] Xia, J. S., Pan, W., Vicente, C. L., Adams, E. D., Sullivan, N. S., Stormer, H. L., Tsui, D. C., Pfeiffer, L. N., Baldwin, K. W., and West, K. W. *Phys. Rev. Lett.* **93**, 176809 (2004).

[31] Pan, W., Xia, J. S., Stormer, H. L., Tsui, D. C., Vicente, C., Adams, E. D., Sullivan, N. S., Pfeiffer, L. N., Baldwin, K. W., and West, K. W. *Phys. Rev. B* **77**, 075307 (2008).

[32] Choi, H. C., Kang, W., Das Sarma, S., Pfeiffer, L. N., and West, K. W. *Phys. Rev. B* **77**, 081301 (2008).

[33] Haldane, F. D. M. and Rezayi, E. H. *Phys. Rev. Lett.* **60**, 956 (1988).

[34] Halperin, B. I. *Helv. Phys. Acta* **56**, 75 (1983).

[35] Eisenstein, J. P., Willett, R., Stormer, H. L., Tsui, D. C., Gossard, A. C., and English, J. H. *Phys. Rev. Lett.* **61**, 997 (1988).

[36] Eisenstein, J. P., Willet, R. L., STormer, H. L., Pfeiffer, L. N., and West, K. W. *Surf. Sci.* **229**, 31 (1990).

[37] Moore, G. and Read, N. *Nucl. Phys. B* **360**, 362 (1991).

[38] Bardeen, J., Cooper, L. N., and Schrieffer, J. R. *Phys. Rev.* **106**, 162 (1957).

[39] Bardeen, J., Cooper, L. N., and Schrieffer, J. R. *Phys. Rev.* **108**, 1175 (1957).

[40] Greiter, M., Wen, X., and Wilczek, F. *Phys. Rev. Lett* **66**, 3205 (1991).

[41] Read, N. and Rezayi, E. *Phys. Rev. B* **54**, 16864 (1996).

[42] Suen, Y. W., Engel, L. W., Santos, M. B., Shayegan, M., and Tsui, D. C. *Phys. Rev. Lett.* **68**, 1379 (1992).

[43] Eisenstein, J. P., Boebinger, G. S., Pfeiffer, L. N., West, K. W., and He, S. *Phys. Rev. Lett.* **68**, 1383 (1992).

[44] He, S., Das Sarma, S., and Xie, X. C. *Phys. Rev. B* **47**, 4394 (1993).

[45] Ho, T. L. *Phys. Rev. Lett.* **75**, 1186 (1995).

[46] MacDonald, A. H., Yoshioka, D., and Girvin, S. M. *Phys. Rev. B* **39**, 1989 (1989).

[47] Morf, R. H. *Phys. Rev. Lett.* **80**, 1505 (1998).

[48] Stopa, M. and Das Sarma, S. .

[49] Stopa, M. and Das Sarma, S. *Phys. Rev. B* **40**(14), 10048 (1989).

[50] Das Sarma, S. and Hwang, E. H. *Phys. Rev. Lett.* **84**, 5596 (2000).

[51] Rezayi, E. and Haldane, F. *Phys. Rev. Lett.* **84**, 4685 (2000).

[52] Read, N. and Moore, G. *Prog. Theo. Phys. Suppl.* **107**, 157 (1992).

[53] Read, N. and Rezayi, E. *Phys. Rev. B* **59**, 8084 (1999).

[54] Read, N. *arXiv:cond-mat/0010071v2* (2000).

[55] Kitaev, A. Y. *Ann. Phys.* **303**, 2 (2003).

[56] Das Sarma, S., Freedman, M., and Nayak, C. *Phys. Rev. Lett* **94**, 166802 (2005).

[57] Freedman, M., Nayak, C., and Walker, K. *Ann. Phys.* **73**, 245307 (2006).

[58] Peterson et al. *arXiv:0801.4819v1* (2008).

[59] Gervais, G., Engel, L. W., Stormer, H. L., Tsui, D. C., Baldwin, K. W., West, K. W., and Pfeiffer, L. N. *Phys. Rev. Lett.* **93**, 266804 (2004).

[60] Koulakov, A. A., Fogler, M. M., and Shklovskii, B. I. *Phys. Rev. Lett.* **76**, 499 (1996).

[61] Read, N. *Physica B* **298**, 121 (2001).

[62] Halperin, B. I., Lee, P. A., and Read, N. *Phys. Rev. B* **47**, 7312 (1993).

[63] Lilly, M. P., Cooper, K. B., Eisenstein, J. P., Pfeiffer, L. N., and West, K. W. *Phys. Rev. Lett.* **82**, 394 (1999).

[64] Peterson, M. R., Jolicoeur, T., and Das Sarma, S. *Phys. Rev. Lett.* **101**, 016807 (2008).

[65] Levin, M., Halperin, B. I., and Rosenow, B. *Phys. Rev. Lett.* **99**, 236806 (2007).

[66] Lee, S.-S., Ryu, S., Nayak, C., and Fisher, M. P. A. *Phys. Rev. Lett.* **99**, 236807 (2007).

[67] Park, K., Melik-Alaverdian, V., Bonesteel, N. E., and Jain, J. K. *Phys. Rev. Lett* **58**, 10167R (1998).

[68] Dimov, I., Halperin, B. I., and Nayak, C. *Phys. Rev. Lett.* **100**, 126804 (2008).

[69] Feiguin, A. E., Rezayi, E., Nayak, C., and Das Sarma, S. *Phys. Rev. Lett* **100**, 166803 (2008).

[70] Feiguin, A. E., Rezayi, E., Yang, K., Nayak, C., and Das Sarma, S. *arXiv:0804.4502v3* (2008).

[71] Pan, W., Stormer, H. L., Tsui, D. C., Pfeiffer, L. N., Baldwin, K. W., and West, K. W. *Sol. Stat. Comm.* **119**, 641 (2001).

[72] Lilly, M. P., Cooper, K. B., Eisenstein, J. P., Pfeiffer, L. N., and West, K. *Phys. Rev. Lett.* **83**, 824 (1999).

[73] Pan, W., Du, R. R., Stormer, H. L., Tsui, D. C., Pfeiffer, L. N., Baldwin, K. W., and West, K. W. *Phys. Rev. Lett.* **83**, 820 (1999).

[74] Peterson, M. R. private communication (2008).

[75] Dolev, M., Heiblum, M., Umansky, V., Stern, A., and Mahalu, D. *Nature* **452**, 829 (2008).

[76] Radu, I. P., Miller, J. B., Marcus, C. M., Kastner, M. A., Pfeiffer, L. N., and West, K. W. *Science* **320**, 899 (2008).

[77] Morf, R. H., d'Ambrumenil, N., and Das Sarma, S. *Phys. Rev. B* **66**, 075408 (2002).

[78] Morf, R. and d'Ambrumenil, N. *Phys. Rev. B* **68**, 113309 (2003).

[79] Dethlefsen, A. F., Mariani, E., Tranitz, H. P., Wegscheider, W., and Haug, R. J. *Phys. Rev. B* **74**, 165325 (2006).

[80] Wojs, A. and Quinn, J. J. *Phys. Rev. B* **74**, 235319 (2006).

[81] Toke, C. and Jain, J. K. *Phys. Rev. Lett.* **96**, 246805 (2006).

[82] Toke, C. and Jain, J. K. *Phys. Rev. Lett.* **98**, 036836 (2007).

[83] Fradkin, E., Nayak, C., Tsvelik, A., and Wilczek, F. *Nucl. Phys. B* **516**, 704 (1998).

[84] Stern, A. and Halperin, B. I. *Phys. Rev. Lett.* **96**, 016802 (2006).

[85] Bonderson, P., Kitaev, A., and Shtengel, K. *Phys. Rev. Lett.* **96**, 016803 (2006).

[86] Miller, J. B., Radu, I. P., Zumbuhl, D. M., Levenson-Falk, E. M., Kastner, M. A., Marcus, C. M., Pfeiffer, L. N., and West, K. W. *Nature* **3**, 561 (2007).

[87] Willett, R. L., Manfra, M. J., Pfeiffer, L. N., and West, K. W. *Appl. Phys. Lett.* **91**, 052105 (2007).

CHAPTER 3

# Apparatus and Measurement Techniques

Investigating the $\frac{5}{2}$ FQHE presents an experimental challenge since the state is so fragile; appearing in only the very best (high mobility) 2DEG samples, and even then only at very low temperatures (less than $\sim 100$ mK). In the following chapter, the methods and techniques we developed to meet these challenges are described. First I discuss the 2D electron gas samples used in our study. I then present an overview of the dilution refrigerator technique used to cool our samples, followed by a detailed description of the modifications made to our system. Finally, I discuss the measurement techniques used in our study of the $\frac{5}{2}$ state, including both a review of conventional methods and novel approaches developed through our studies.

## 3.1 Samples

### 3.1.1 GaAs Heterostructures and Quantum Wells

The materials of choice for investigating the quantum Hall effect in 2DEGs are GaAs/ AlGaAs heterostructures grown by molecular beam epitaxy (MBE), since these materials have exhibited the cleanest 2DEGs (*i.e.* highest measured mobility) ever observed. GaAs and AlGaAs are both crystalline semiconductors with nearly identical lattice spacing. Epitaxially growing AlGaAs onto crystalline GaAs therefore creates a nearly perfect (*i.e.* strain-free, defect-free) interface. Since GaAs and AlGaAs are both semiconductors, growing such a wafer alone would not yield a 2DEG as there are no free electrons. To introduce free electrons, the AlGaAs layer is grown with a layer of Si donors in a process referred to as *modulation doping* [1]. GaAs has a slightly larger electron affinity (lower free electron energy) than AlGaAs (upper panel of Fig. 3–1b) and so any free electrons
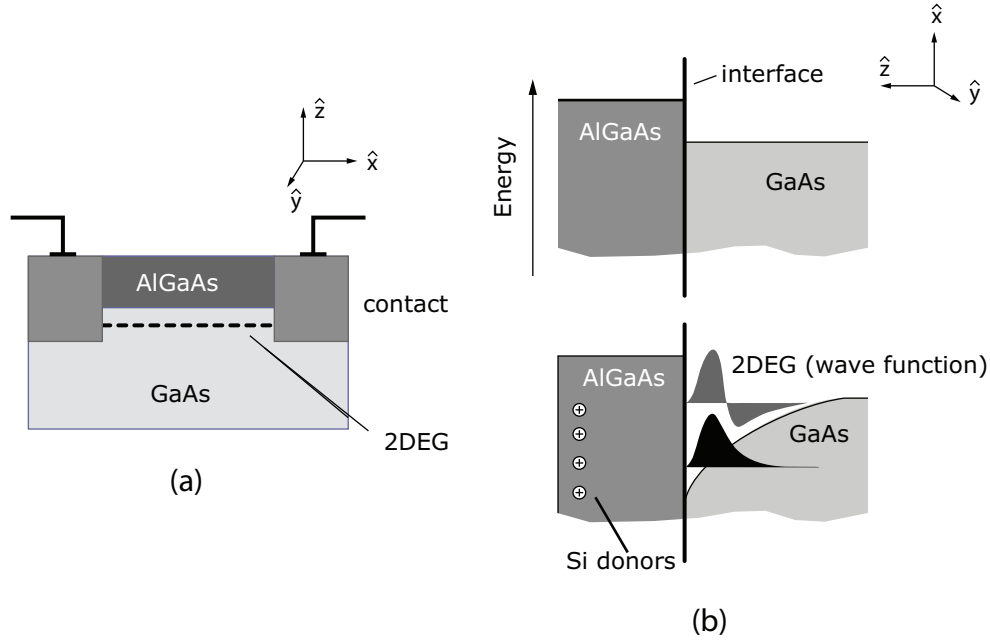
Figure 3–1: (a)Schematic drawing showing a typical GaAs/AlGaAs heterostructure substrate configuration. (b) The free energy of electrons is slightly higher in AlGaAs than GaAs (GaAs therefore has a larger electron affinity). Modulation doping with Si ions both donates free electrons electrons to the wafer and shapes the confinement quantum well where the 2DEG resides.

donated by the Si ions that wander to the GaAs/AlGaAs interface will fall over the edge and become trapped in the GaAs layer. The charged Si donor ions (positively charged after giving up their outer shell free electron) additionally create an attractive potential that modifies the energy band at the GaAs/AlGaAs interface resulting in an approximately triangular well potential (lower panel of 3–1b). At sufficiently low temperatures, the free electrons become trapped in this well, and since the well is limited in the $\hat{z}$ direction while effectively infinite in extent along the $\hat{x}$ and $\hat{y}$ directions (limited only by the macroscopic dimensions of the substrate), electrons in the well form a nearly ideal (*i.e.* zero thickness) 2DEG. The actual finite thickness of the 2DEG in the $\hat{z}$ direction is determined by the electron density and details of the confining potential [2, 3].

Since the GaAs/AlGaAs interface is essentially defect free, electrons in the 2DEG experience very little impurity scattering in the quantum well. Furthermore, the modulation doping technique which places the donor ions a relatively large distance away from the quantum well, allows scattering from the donor impurities to also be minimized. These two features of the GaAs/AlGaAs heterostructures are what give rise to the extremely high purity 2DEGs in comparison to other 2DEG samples.
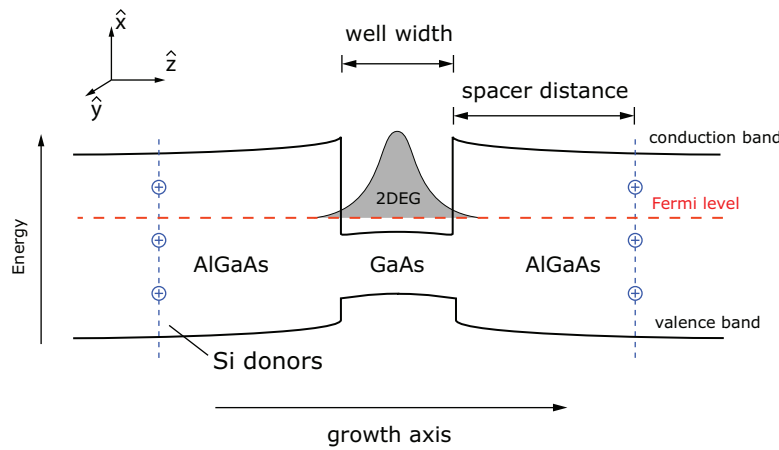
Figure 3–2: (a)Schematic drawing showing an AlGaAs/GaAs/AlGaAs square quantum well substrate configuration showing the resulting valence and conduction band energy profiles.

To achieve greater control over the shape (*i.e.* width) of the electron wavefunction, it has become customary to instead fabricate a square quantum well in GaAs by growing a symmetrically doped AlGaAs/GaAs/AlGaAs substrate. In this construction, shown in Fig. 3–2, the quantum well width is controlled by varying the layer thicknesses during sample growth. The shape of the resulting wavefunction, which is symmetric in the $\hat{z}$ direction, is calculated by solving the Schroedinger equation for the finite square well potential [2, 4].

In the experiments presented here samples from two very high purity, but different electron density, GaAs wafers were studied (all samples were provided by Loren Pfeiffer and Ken West at Bell Laboratories, Alcatel-Lucent Technologies, Inc.). The low density sample, is a symmetrically doped AlGaAs/GaAs/AlGaAs quantum well, with a specified well width of 40 nm and donor spacer distance of 160 nm. The high density sample, is a symmetrically doped AlGaAs/GaAs/AlGaAs quantum well, with a specified well width of 30 nm and donor spacer distance of approximately 100 nm. All samples studied from each wafer were cleaved to approximately 4 mm square, with 8 diffused Indium contacts around the perimeter in a van der Pauw geometry (see section 3.1.2). The density of the low density sample was typically measured to be $1.60 \pm 0.01 \times 10^{11}$ cm$^{-2}$ after treatment with a red LED. The mobility was measured to be $16.6 \pm 0.8 \times 10^6$ cm$^2$/Vs at base temperature. For the high density sample, the density was measured to be $3.04 \pm 0.08 \times 10^{11}$ cm$^{-2}$ and mobility $27 \times 10^6$ cm$^2$/Vs.

38
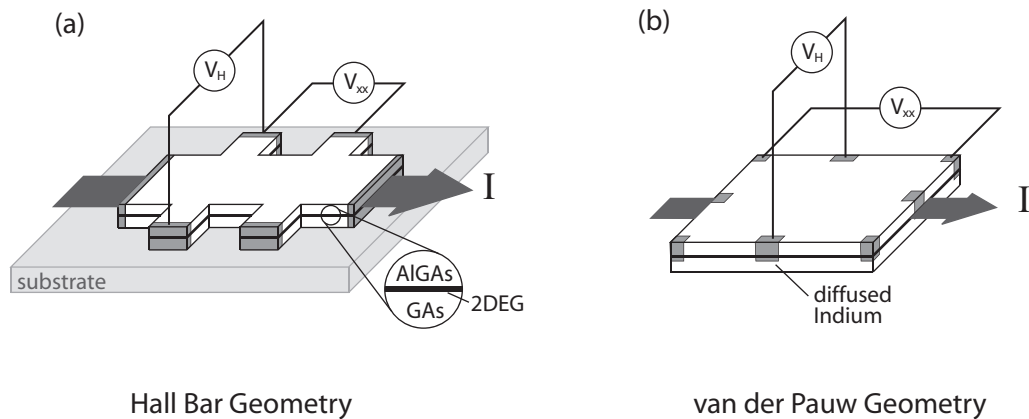
Figure 3–3: Schematic diagram showing a GaAs/AlGaAs substrate in a (a) Hall bar and (b) van der Pauw sample geometry.

### 3.1.2   Hall Bar versus van der Pauw

Quantum Hall measurements on GaAs 2DEG samples are traditionally performed by patterning the GaAs substrate into a Hall bar geometry, shown in the Fig. 3–3a. This has the advantage of ensuring the voltage is measured parallel (perpendicular) to the current flow when measuring the longitudinal resistance (Hall resistance). However, pattering the substrate can be difficult. Furthermore, when studying very high quality samples, patterning the sample can adversely affect the sample mobility, which could for example disturb observation of the fragile $\frac{5}{2}$ FQH state. An alternate technique therefore is to employ the so called van der Pauw geometry, where electrical contact is made to the 2DEG by diffusing indium into the GaAs at the edge of the wafer, as shown in Fig. 3–3b.

### 3.2   Ultra-Low Temperature Cryostat

In order to study the $\frac{5}{2}$ and other quantum Hall states it is necessary to be able to achieve very low temperatures (tens of mK) for lengthy time periods (days to months). All of our experiments were therefore performed on a continuous flow dilution refrigerator. We additionally face the difficult task of investigating the extremely fragile $\nu = \frac{5}{2}$ FQH state which requires high precision, low noise, and minimally invasive measurement techniques together with the ultra-cold environment and very large applied magnetic fields. In the following an overview of the dilution refrigerator technique is presented followed by a detailed description of our system including the performance of our fridge and the specific designs and modifications used in our focused effort to study the $\nu = \frac{5}{2}$ FQHE.
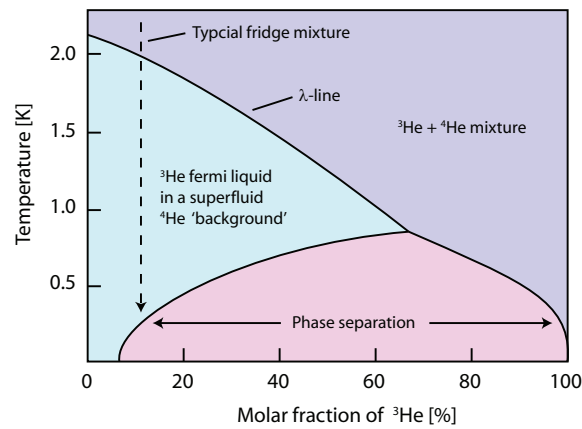
Figure 3–4: Phase diagram for liquid helium mixtures. Dashed line indicates a cooling curve for a typical mixture ratio used in a dilution refrigerator (10% $^3$He).

### 3.2.1   Dilution Refrigerator

A dilution refrigerator can reach temperatures extending below 10 mK with appreciable cooling power (typically on the order of tens of hundreds of micro-watts) and, when operated in continuous mode, can maintain a sample at these temperature indefinitely. Cooling is achieved by exploiting the entropy of mixing between the two isotopes of helium ($^4$He and $^3$He) in the liquid phase. Fig. 3–4 shows a schematic phase diagram of the liquid helium mixtures. In the figure, the dashed line corresponds to a typical mixture ratio used in the dilution process ($\sim$10% $^3$He disolved in $^4$He). As the temperature of the mixture is lowered the $^4$He component first undergoes a transition from a normal fluid to a superfluid. Further lowering the temperature eventually causes a second transition where the mixture abruptly phase seperates into a $^4$He-rich "dilute" phase with lighter $^3$He-rich "concentrated" phase floating on top. As the now phase-separated mixture is even further cooled towards the zero Kelvin limit, the concentrated phase approaches 100% $^3$He, while the dilute phase reaches a steady-state saturated concentration of 6.6% $^3$He disolved in $^4$He. Removing $^3$He from the dilute phase then results in a chemical potential gradient which draws $^3$He across the phase boundary from the concentrated phase to the dilute phase, maintaining the equilibrium 6.6% $^3$He concentration. In analogy to evaporative cooling where the liquid-to-gas phase transition absorbs energy, when $^3$He crosses the phase boundary, from the pure (concentrated) phase to the dilute phase, heat energy is absorbed. A full description of the thermodynamic process requires inclusion of the quantum properties of both the $^3$He (fermi-liquid) and $^4$He (bose-liquid) liquids [5]. Taking into account these considerations, the cooling power of a dilution fridge is given by

40
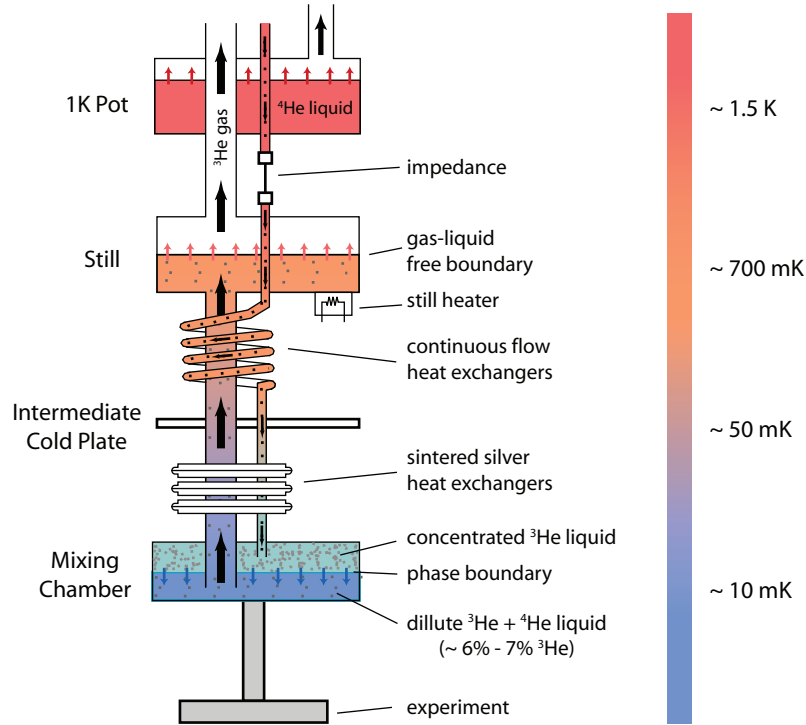
Figure 3–5: Schematic diagram showing the dilution refrigerator cooling process.

$$\dot{Q} = 84\dot{n}T^2 \tag{3.1}$$

where $T$ is the temperature of the mixture and $\dot{n}$ is the molar flow rate of $^3$He across the phase boundary.

**Continuous Mode:**

By pumping $^3$He out of the dilute phase and then recondensing it back into the concentrated phase $^3$He can be continuously drawn across the phase boundary, and therefore can provide constant cooling for indefinite time periods. Fig. 3–5 shows a schematic diagram of a typical dilution fridge construction. The phase boundary between the $^3$He rich concentrated phase, and the $^3$He + $^4$He dilute phase is confined to the *mixing chamber* (MC). From here a tube draws the dilute phase up to the *still* where the $^3$He is pumped out of the mixture. The still temperature, which is thermally isolated from the MC, will typically be cooled to ∼300 mK due to evaporative cooling by the mechanical pump. At these temperatures, the $^3$He vapour pressure is significantly larger (several orders of magnitude) than $^4$He ensuring that $^3$He is preferentially removed from the dilute phase. The

$^3$He gas pumped from the still is then returned to the concentrated phase in the mixture chamber. To ensure a continuous cooling cycle the mixture is circulated in a vacuum tight closed-circuit.

Before returning to the mixing chamber, the $^3$He gas is first re-condensed via a *1K pot* consisting of a bath of $^4$He evaporatively cooled by mechanical pumping. To ensure maximal condensation and cooling at the 1K pot a gas flow impedance, usually just a small diameter capillary, is placed in the $^3$He return line between the 1K pot and the still. The returning (now liquid) $^3$He is then further pre-cooled using a combination of counter-flow and pressed powder heat exchangers installed between the still and mixing chamber.

From Eqn. 3.1, the cooling power of the fridge is directly determined by the rate at which $^3$He crosses the phase boundary, which is in turn dictated by the rate at which $^3$He is pumped out of the dilute phase at the still. Since at typical operating temperatures the $^4$He component of the dilute phase is superfluid, the $^3$He can be readily drawn through the $^4$He background with little resistance. The limiting factor is therefore the pumping power of the still rotary pump. This can be improved by using a booster pump together with the rotary pump to achieve increased pumping rates. Additionally, a resistance heater is used to increase the mixture temperature in the still, raising its vapour pressure. As the still temperature (vapour pressure) is increased, the $^3$He circulation rate increases, and therefore the cooling power increases. There is however a peak circulation rate, beyond which the rate at which $^3$He is returned to the fridge is too fast to be sufficiently pre-cooled before reaching the mixing the chamber. This results in an additional heat-load on the mixing chamber that effectively decreases its cooling power.

The ultimate base temperature achievable by the fridge is determined by the cooling power (Eqn. 3.1) minus the thermal loads on the mixing chamber. Care is therefore taken to thermally isolate the various stages of the dilution fridge from each other and from the room temperature environment of the laboratory.

**Single Shot:**

Removing the heat load delivered to the mixing chamber by the returning $^3$He allows the system to achieve lower temperatures. Performing a *single shot* therefore involves diverting the $^3$He gas to a dump instead of returning it to the fridge. While this achieves a lower base temperature, single shot cooling will last only as long as a sufficient amount of $^3$He remains in the concentrated phase in the mixing chamber (typically tens of minutes).

Fig. 3–6 shows an example of a complete dilution system including the gas handling circuit. The fridge is operated inside of a vacuum can immersed in a liquid helium dewar.
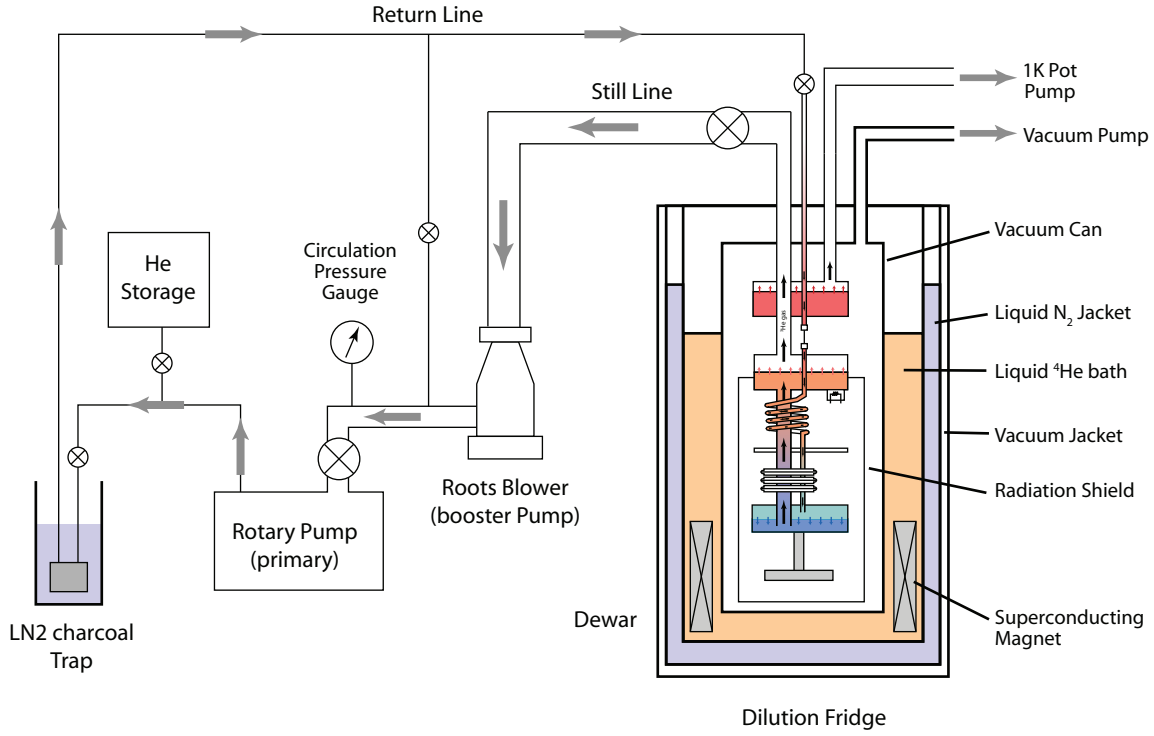
Figure 3–6: Example schematic of a complete dilution refrigeration system including a gas handling system. Arrows indicate gas flow during normal operation.

The dewar includes a vacuum jacket and liquid nitrogen jacket to minimize liquid helium boil off. The $^3$He-$^4$He mixture is circulated through the fridge via a rotary pump behind a mechanical booster pump. During continuous operation the mixture flows through a liquid nitrogen cold trap before returning to the fridge. The LN$_2$ is used to filter out any impurities (e.g. air) that could potentially freeze in the return line impedance, and prevent normal operation. The system is also equipped with a storage dump that is used to safely store the mixture when disconnecting the fridge from the circulation system.

### 3.2.2    Janis JDR-100 Dilution Refrigerator Specifications

Our refrigerator is a commercially built $^3$He-$^4$He dilution refrigerator system purchased from Janis Research Company, Inc. (model JDR-100-DP), with a specified base temperature of 17 mK, and cooling power of 150 $\mu$W at 100 mK. The system includes a high efficiency cryogenic dewar equipped with a 9 Tesla superconducting magnet (model 90-200D-10P) from Cryogenics Inc. The magnet is designed to achieve high stability near the field center, which is located 14.17" below the bottom plate of the mixing chamber.
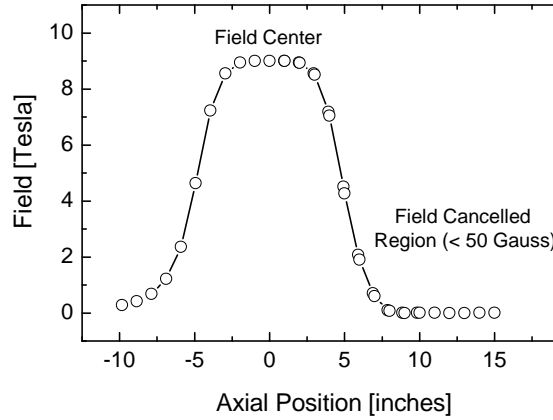
Figure 3–7: Field profile of the superconducting magnet (data was provided by Janis Research Company Inc.).

A second, field cancellation magnet coil is included to maintain zero field at the mixing chamber when the main magnet is turned on. The measured field profile along the center axis of the magnet, showing both the field center and field canceled region, is plotted in Fig. 3–7 (data was provided by Janis).

In order to isolate our experiments from unwanted extraneous RF radiation, the cryostat (fridge + dewar) is located inside a shielded room measured to give 100 dB attenuation at 1 GHz. All pumps are housed in a separate room to provide vibrational and acoustic noise isolation. Inside the shielded room, the still line is a 6" ID stainless tube, the 1K pot line is a 1.5" stainless tube and the return line is a 1/4" OD flexible copper tube. Outside the shielded room these mate to an 8" ID schedule 80 PVC plastic pipe (still line), 3" ID schedule 80 PVC plastic pipe (1K pot line) and a 1/4" flexible copper pipe (return line). An additional 1.5" ID schedule 80 PVC plastic pipe serves as a utility roughing line (both inside and outside the shielded room). Specially designed RF-tight vacuum feedthroughs connect all pumping lines from inside to outside the shielded room. All vacuum connections use the standard KF-style clamped o-rings.

All data acquisition and electronics control is performed by a computer located outside the shielded room via GPIB. To communicate with devices inside the shielded room while maintaining RF integrity of the room, all signals are transmitted through an optical fibre. Conversion between between electrical and optical signals is performed with a National Instruments 140A fibre optic GPIB extender both inside and outside the shielded room.

### 3.2.3   Wiring

The fridge is wired in 3 main stages: (i) Top of cryostat to 1K pot, (ii) 1K pot to mixing chamber, and (iii) Mixing chamber to cold plate. Six individual 32-pin vacuum tight feedthroughs, labeled A-F, are used to separately wire different devices within the fridge (*i.e.* thermometry, sample measurement, etc.). At each stage, the wiring material was specifically chosen to minimize electrical resistance while providing optimal thermal isolation. Between the top flange and 1K pot, all wires are insulated maganin wires in twisted pairs, thermally anchored at the 4K flange and terminating at individual breakout connectors at the 1K pot (1 32-pin breakout connector for each 32-pin feedthrough at the top of the cryostat). The only exception to this is feedthrough C, which was wired with twisted insulated copper pairs, allowing for the option of lower resistance leads (which could be also used to deliver higher currents). Between the 1K pot and mixing chamber all connections are made using NbTi superconducting wires (since superconductors exhibit zero thermal conductivity when in the superconducting state) with a braided stainless steel shield around each twisted pair. All wires are thermally anchored at the Still and ICP plates before terminating at the MC. Between the MC and experimental cold plate all connections are made with annealed silver wire. For detailed wiring schematics of each each feedthrough see Appendix A.

### 3.2.4   Experimental Tail

In order to perform experiments in the field center, an experimental tail was attached to the bottom plate of the mixing chamber. The tail was designed in order to optimize implementation of an NMR detection scheme. In this regard it was desirable to achieve maximal cooling of the sample while minimizing any unwanted magnetic sources that might introduce inhomogeneities to the magnetic field. The tail was therefore machined from a pure (99.9% purity) 0.5" OD silver rod swaged down to 0.25" OD to increase its mechanical stiffness, and then machined into a hexagonal profile. Silver was chosen since it offers one of the best low tempreature thermal conductivities among pure metals [5]. Additionally silver atoms have a very small magnetic moment (nearly 20 times smaller than copper for example) and therefore exhibit negligible magnetization even in the very strong applied fields ($\sim$10 T) and low tempereratures ($\sim$20 mK) typically used in our experiments [6, 7]. At the bottom of the tail the hex rod terminates at the experimental cold plate, a 0.185" thick round silver plate (1.325" OD) also machined from 99.9% pure silver.

The tail was designed to accommodate four samples simultaneously with two standard 8-pin sample headers mounted on the top side of the cold plate and two specially designed
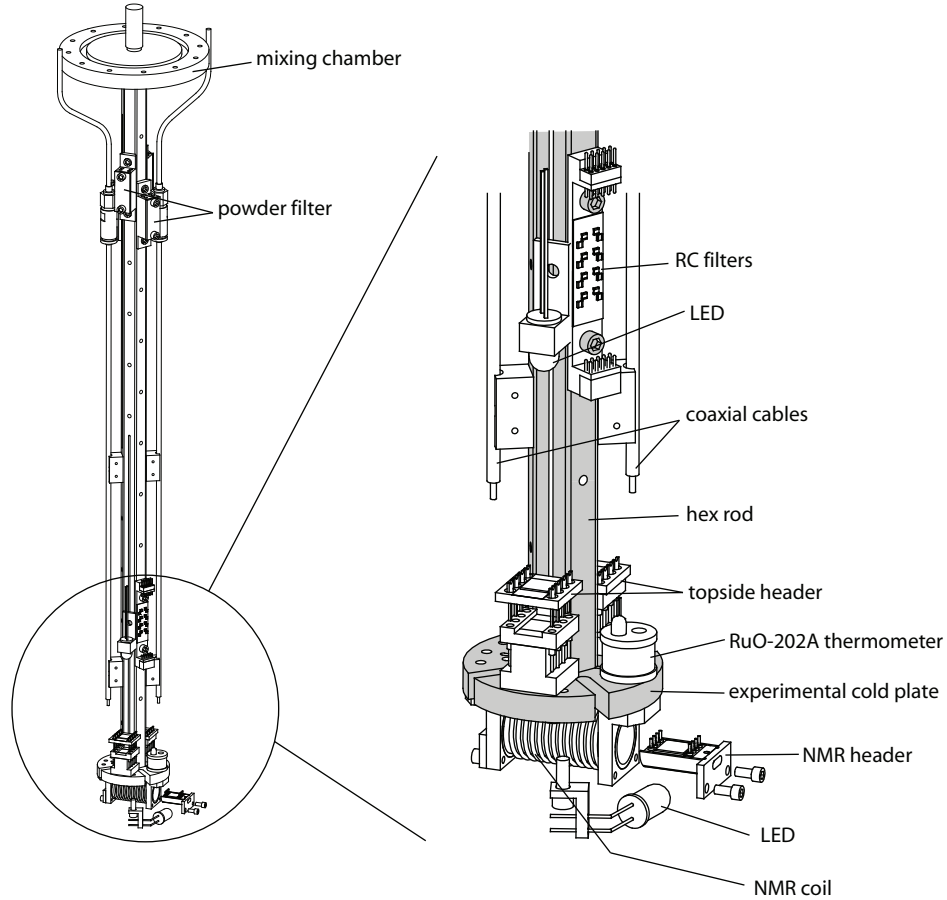
Figure 3–8: Drawing of the full experimental tail assembly equipped with the NMR coil. All measurement components are shown, however, wiring is omitted for clarity.

custom 8 pin headers mounted in an NMR coil assembly on the bottom side of the cold plate (see Fig. 3–8). The entire assembly was designed to place our samples (a few mm thick) at the exact field center when mounted inside the NMR coil, ensuring the maximum possible field homogeneity across the sample. To minimize eddy current heating, slots were cut through the hex-rod and cold plate where possible (see corresponding design drawings in Appendix B).

Fig. 3–8 shows a drawing of the full tail assembly (for clarity, the wiring is not shown). The four sample holders are distinguished by labeling them *alpha*, *beta*, *gamma*, and *delta*, with alpha and beta located in the NMR coil, while gamma and delta refer to the two top side headers. Starting at the mixing chamber the electrical leads for each header begins with a bundle of 4 twisted pairs (8 total wires) of 0.030" thick annealed silver wire, embedded

in a pressed silver powder. The pressed powder box acts both as a lossy RF filter [8] while simultaneously helping to heat sink the leads. The lead wires for headers alpha and beta additionally pass through an RC filter, designed for a 2 kHz cut-off frequency to further filter the sample from any unwanted RF radiation travelling down the lead wires. The lead wires then terminate at a double row strip socket near the cold plate designed to mate to two removable NMR coil sample headers.

By contrast, the gamma and delta leads terminate at a standard DIP IC socket with no additional filtering (0.004" thick annealed silver wires are used to connect the socket pins to the thicker lead wires). Each socket is epoxied to a G-10 mount which is secured to the cold plate by screws.

In addition to the headers + lead wires, the tail assembly includes two semi-rigid RF coaxial cables, two red LEDs, a RuO 2 k$\Omega$ thermometer and 8 free wires (4 twisted pairs) terminating near the cold plate. The two coaxial cables are labeled $^\#$1 and $^\#$2. Coax $^\#$1 terminates near the top of the cold plate. Coax $^\#$2 mates to a flexible RF coaxial cable via an mmcx connector, which is soldered at the other end to the NMR coil, and is therefore dedicated to delivering RF radiation to the NMR coil. To be able to deliver RF radiation at the mixing chamber (NMR experiments) with minimal attenuation, while additionally minimizing the heat-load placed on the fridge, a combination of several different semi-rigid coaxial cables were used. Details of each coax can be found in Appendix A.

### 3.2.5  Sample Rotation

We were additionally interested in utilizing a titled field geometry in order to probe the spin state of the electrons at $\nu = \frac{5}{2}$ (see Chapter 5). We therefore designed a removable rotator stage to achieve *in situ* sample rotation, shown in Fig. 3–9.

The stage is designed to mount onto the bottom the experimental cold plate by removing the NMR coil. Rotation is achieved by a spring-loaded paddle design where rotation results from pulling a string via a mechanical feedthrough operated at the top of the cryostat. Upon relaxing the string, the sample rotates back in the other direction via a spring under tension. The rotation stage was designed to accommodate samples mounted on both styles of custom headers (Fig. 3–10). When attached to the rotator, the sample is placed at the exact field center, and rotates about an axis along the middle of the sample surface. Our design allows for approximately $60^o$ full rotation, with the initial offset angle adjustable to any angle. Typically the range of the rotator is therefore set to between -$15^o$ to +$45^o$, with the negative offset allowing us to rotate through the zero point, in order to find the true zero *in situ*. The rotation angle, $\theta$, is defined as the angle between the 2DEG
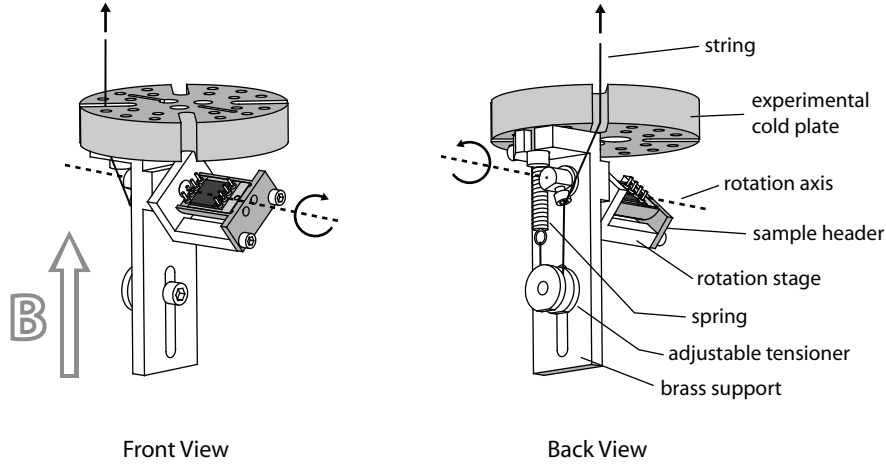
Figure 3–9: Schematic drawing of the sample rotator mounted on the experimental cold plate. Arrows indicate direction of rotation due to "pulling" the string. The direction of the applied magnetic field, B, is shown by the large white arrow.

normal and the direction of the applied magnetic field. The rotator was machined from brass, and attached to the cold plate via a screw. The string is a kevlar thread, and the spring is stainless steel.

### 3.2.6   Sample Cooling

In order to ensure maximal sample cooling we constructed custom sample headers for both the top-side and NMR coil headers. For each of the top-side headers (gamma and delta), the sample holder is a commercially purchased G-10 (garolite) header with 8 gold-plated pins designed to fit a standard 8-pin DIP socket. On to this we glued a 0.004" thick annealed silver foil (99.998% pure) attached to a 0.030" OD annealed silver wire (using a combination of solder for strength and silver paint for thermal conductivity) that can be thermally anchored to the cold plate (Fig. 3–10a). While the foil is intended to help heat sink the sample lattice, cooling the electrons of the sample 2DEG is achieved mostly through the leads [9], which are well thermally anchored to the silver hex rod.

The NMR coil sample holder, shown in (Fig. 3–10b), was designed to allow easy mounting/demounting of the sample from the NMR coil. Our design accommodates a permanent rigid coil as opposed to most other experiments performing resistively NMR in which the coil is formed by wrapping a thin wire around the sample substrate. Our design therefore allows us to place and remove the sample onto the fridge without solder-ing/desoldering the NMR coil connections, which helps to minimize variations in the RF coil characteristics from one run to the next. In order to maintain the highest possible
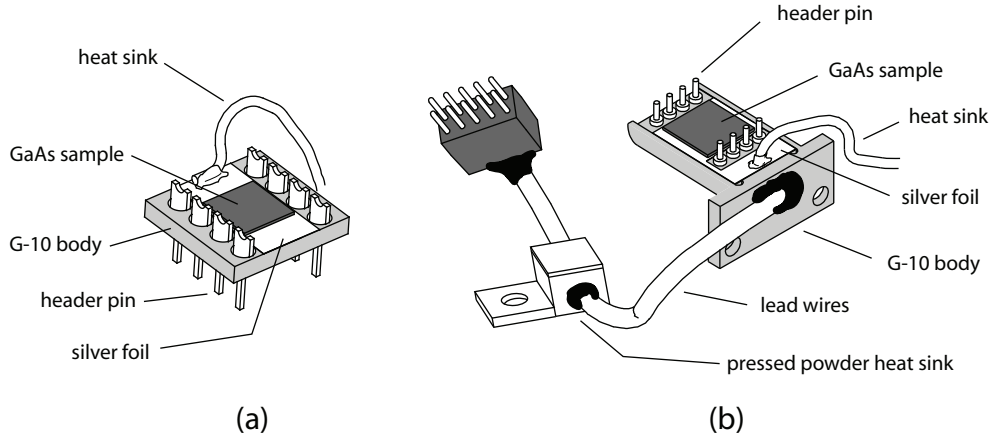
Figure 3–10: Schematic drawings of the custom sample holders constructed for both the top-side headers (a) and NMR coil (b).

field homogeneity at the sample, the NMR sample header consists of a G-10 body with all metal, including the wires, header pins, and substrate cooling foil (similar to that used in the top-side header) made from annealed silver. To further ensure optimal cooling of the sample leads, and therefore the 2DEG electrons, the lead wires in the removable sample holder were embedded in a pressed silver powder, contained in a silver box thermally anchored to the hex rod of the cold finger via a screw.

The NMR coil (shown in Fig. 3–8) is an approximately 8-turn coil, with a 0.372" cross-section radius. The coil is wrapped around a G-10 tube designed to mount to the bottom side of the experimental cold plate. The coil solders to a flexible coax terminating in an RF rated mmcx connector that mates with a semi-rigid coax. This allows the entire NMR coil to be removed from the cold plate in order to accommodate other experiments.

### 3.2.7   Thermometry

The fridge temperature is monitored with a combination of resistive, magnetization, and diode thermometers placed at several places on the cryostat. A list of each thermometer label, type, and location is given in Table 3–1.

All RuO resistors were purchased from Lakeshore Cryogenics. The Matsushita thermometer is a carbon resistor, supplied to us by Janis Research Inc.. The resistive thermometers (R1-R9) are all measured with a Lakeshore 370 AC resistance bridge, controlled by our data acquisition computer via GPIB. All thermometers are measured using a four-point probe configuration to eliminate the effect of lead resistance. In order to limit self heating, resistance is measured using the minimum excitation power that allows reliable

Table 3–1: List of Thermometers

| Label | Location | Type | Room Temp. Val. |
|-------|----------|------|-----------------|
| R1 | 1K Pot | RuO | 1.000 kΩ |
| R2 | Still | RuO | 1.000 kΩ |
| R3 | Intermediate Cold Plate | RuO | 1.000 kΩ |
| R4 | Mixing Chamber | RuO | 1.000 kΩ |
| R5 | Mixing Chamber | Matsushita Carbon Resistor | 50 Ω |
| R9 | Cold Plate | RuO-202A | 2.015 kΩ |
| Diode | 1K Pot | Si Diode | 300 Kelvin |
| CMN | Mixing Chamber | CMN magnetization therm. | — mH |
| FPD | Mixing Chamber | Fixed Point Device | — mH |
| Magnet | S.C. magnet | Carbon Resistor | 394.4 Ω |

measurement over the greatest temperature range. Typical excitation voltages are therefore set between 20 $\mu$V and 65 $\mu$V. Resistive oxide thermometers are highly sensitive from 4 K down to 50 mK. Below 50 mK, however, the temperature dependence begins to saturate making these thermometers less accurate at very low temperatures.

To extend our measurements to lower temperatures we employ a CMN magnetization thermometer. In this thermometry scheme, the mutual inductance between two small coils is measured with a paramagnetic salt pill (cerous magnesium nitrate) placed inside one of the coils. The mutual inductance is linearly dependent on the magnetic susceptibility, $\chi$, of the salt, which follows the well described 1/T Curie law temperature dependence. A measure of the mutual inductance versus inverse temperature therefore gives a linear relationship which can be calibrated to give very accurate temperature readings down to ∼6 mK. The CMN thermometer was purchased from Janis Research Company Inc., and calibrated by a nearby superconducting fixed point device (FPD), also supplied by Janis. The FPD is constructed similarly to the CMN but incorporates superconducting (SC) materials with well known transition temperatures. Owing to the Meissner effect, measurement of the mutual inductance of the coils in the FPD exhibits sharp jumps that coincide with the superconducting transition points. Since the SC transition temperature is a fundamental property of the corresponding material, these known values can be used to calibrate the CMN. Fig. 3–11a shows the measured inductance as a function of temperature for our FPD, with the superconducting transitions labeled in the plot. The CMN
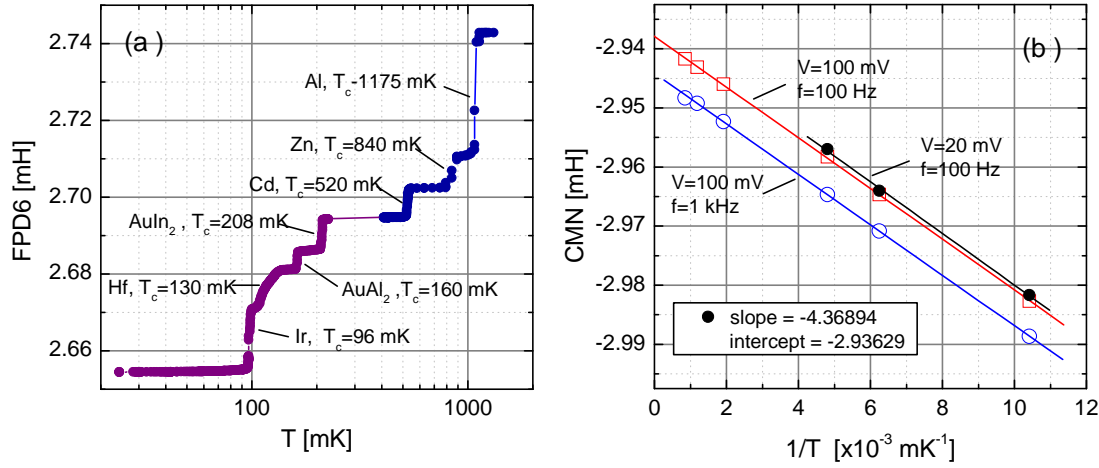
Figure 3–11: (a) Superconducting transition points in our fixed point device. (b) CMN calibration against the fixed point device. Open symbols represent calibration points performed by Janis Research Inc. Solid circles were performed in our lab after installing the fridge. CMN excitation parameters for each calibration are labeled in the figure.

calibration obtained by carefully measuring the inductance of the CMN at each transition point observed in the FPD is shown in Fig. 3–11b.

Table 3–2: Thermometer resistance values at cryo-temperatures.

|  | Room (300 K) | LN$_2$ (77 K) | LHe (4 K) |
|---|---|---|---|
| RuO | 1.000 k$\Omega$ | 1.033 k$\Omega$ | 1.38 k$\Omega$ |
| RuO-202A | 2.015 k$\Omega$ | 2.157 k$\Omega$ | 2.979 k$\Omega$ |
| Matsushita | 49.1 $\Omega$ | 55.2 $\Omega$ | 82.4 $\Omega$ |
| Magnet Thermometer | 394.4 $\Omega$ | 484.6 $\Omega$ | 5.71 k$\Omega$ |

The CMN and FPD are measured with a Hewlett Packard 4263B LCR meter, using a four point probe technique. Three separate calibration curves are shown in Fig. 3–11b, corresponding to different excitation parameters. To minimize self heating in the device we typically operate the CMN using a minimal excitation voltage of 20 mV, and frequency 100 Hz. A fit to the corresponding data in Fig. 3–11b (solid circles) gives the following temperature calibration

$$T[\text{mK}] = \frac{-4.36894}{\text{CMN[mH]} + 2.93629} \tag{3.2}$$
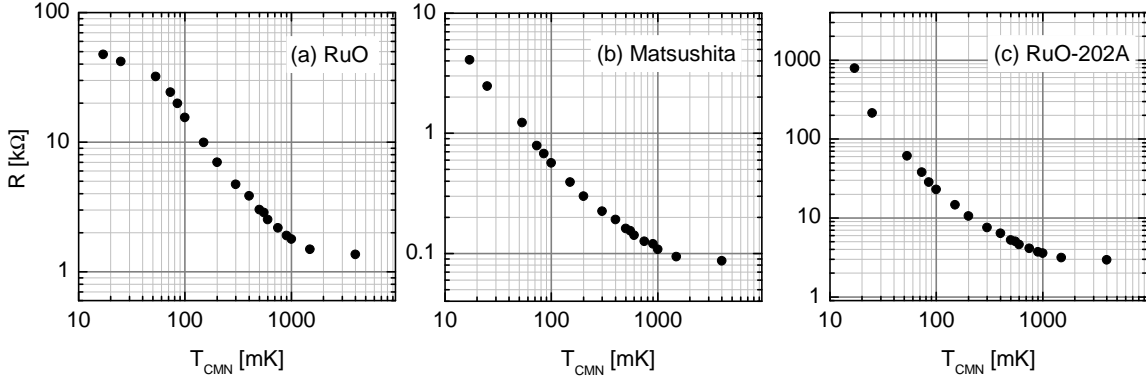
Figure 3–12: Resistive thermometers plotted against calibrated CMN temperature reading, acquired during continuous cooling from LHe to base temperature.

where the mutual inductance of the CMN is recorded in units miliHenry, and the resulting temperature is given in miliKelvin.

The CMN and FPD are located in the field-canceled region at the MC, and so are unaffected by the large magnetic fields applied in a typical experiment. Once calibrated, the CMN was used to in turn calibrate all other thermometers. Fig. 3–12 shows typical cooling curves of the RuO and Matsushita carbon thermometers acquired *dynamically* during a complete cool-down of the fridge from LHe to base temperature. All of our experiments are performed in the very low temperature regime, and so a more careful *static* calibration is shown in Fig. 3–13, where all thermometers were allowed to equilibrate before recording the measurement. The data in Fig. 3–13 was acquired with the magnetic field turned on (∼2.5 T). The RuO and Matsushita resistors are located in the field canceled region and so the field should have minimal effect. The RuO-202A thermometer however is located in the field center and so there may be an offset in the calibration curve owing to the influence of the magnetic field. Importantly, in both the dynamic temperature data (taken at zero field) and static temperature data, the RuO thermometer clearly saturates below 50 mK as expected. The matsushita and RuO-202A however continue to demonstrate a strong temperature dependence all the way down to our base temperature, indicating these resistors can both be used as good thermometers down to our lowest operating temperatures.
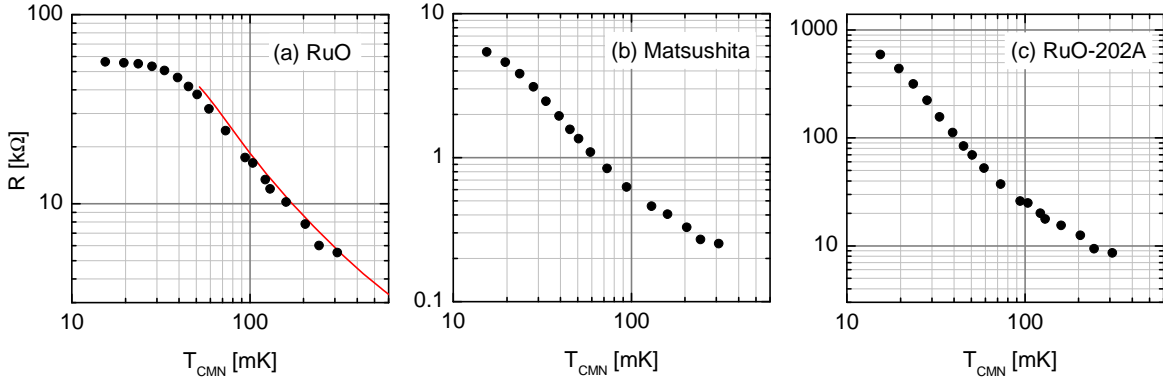
Figure 3–13: Resistive thermometers plotted against calibrated CMN temperature reading, acquired under equilibrium conditions in the low temperature regime (solid line in (a) is a standard RuO calibration curve provided by Janis Research Company Inc.).

### 3.2.8   Cooling Power

Fig. 3–14 shows the cooling characteristics of the dilution fridge. The cooling power was determined by applying a known power to the mixing chamber heater and then recording the mixing chamber temperature after allowing it to thermally equilibrate. The cooling power of a dilution refrigerator depends on the $^3$He circulation rate which in turn can be varied by applying heat to the still (see section 3.2.1). Fig. 3–14a shows the cooling power curves for several different values of current applied to the still heater. As expected, increased cooling power is observed when applying larger currents to the still heater.

The measured cooling power curves obtained when using only a rotary pump to circulate the mixture are indicated by the closed circles. Adding a booster pump to the front of the rotary pump allows us to further increase the circulation rate and, as shown by the open circles in Fig. 3–14, significantly improves the cooling power.

We have found the fridge can be safely operated with a current applied to the still heater between 0-12 mA with the upper value being limited by the rise in pressure observed at the return line pressure gauge. The fridge is typically operated with 5 mA applied to the still giving a measured base temperature of ∼16.5 mK as measured by the CMN and, according to Fig. 3–14, a cooling power of ∼100 $\mu$W at 100 mK.

Fig. 3–14 shows the result of operating the fridge in single shot mode with the maximum current of 12 mA applied to the still heater. The mixing chamber cooled from 16.4 mK to a minimum value of 8.4 mK in approximately 30 mins, after which it began to warm back up, suggesting the still had emptied.
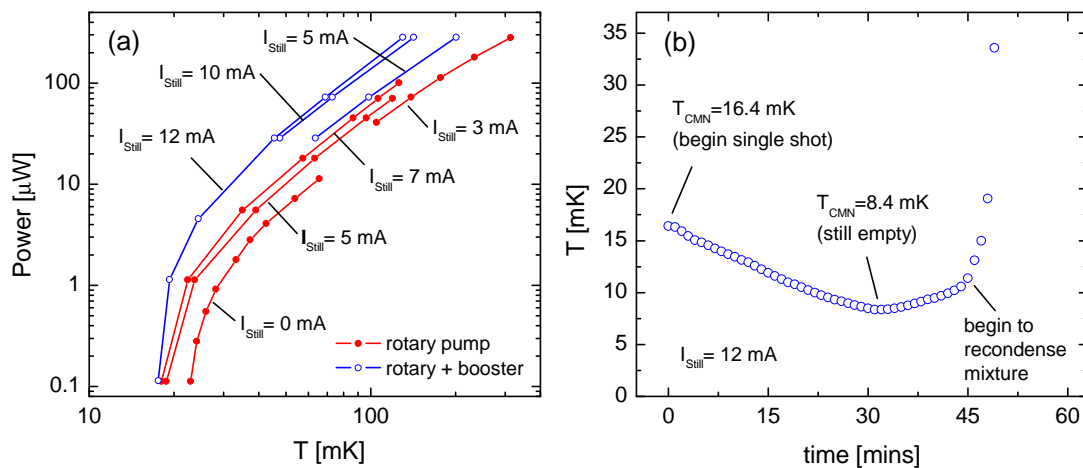
Figure 3–14: (a) Cooling power measured as a function of current applied to Still heater. Closed circles are data acquired by Janis using only a rotary pump to circulate the mixture. Open circles are data acquired by us using a booster pump together with the rotary pump. (b) Mixing chamber temperature versus time during single shot operation (data was acquired with maximal current of 12 mA applied to the still heater).

The cooling power and single shot measurements were performed before installing our experimental stage, and so any additional heat leaks caused by our added wiring etc. may reduce the performance of the fridge. However no significant change in the measured base temperature ($\sim$16-17 mK) was observed, suggesting our modifications have not introduced any substantial additional heat loads to the mixing chamber.

## 3.3 Transport Measurements

### 3.3.1 Two probe and Four probe I-V curves

Transport experiments, in spite of their simplicity, offer the most versatile tool with which to probe the physics of many systems, and the study of 2DEGs is no exception. In the most straightforward experiment, the resistance of a sample is determined by sourcing a voltage across the sample and measuring the resulting current drawn through the circuit (Fig. 3–15). Ohm's law relation, $V = IR$, then gives the resistance value of the sample. By varying the sample parameters (sample size, density, purity etc.) and environmental factors (temperature, pressure, etc.) and monitoring corresponding changes in the measured resistance, an incredible amount of information can be obtained.

The configuration shown in Fig. 3–15 has the limitation that the resistance of the measurement leads are included in the measurement since the current drawn through the circuit is determined by the total resistance (sample + leads). In most measurements the
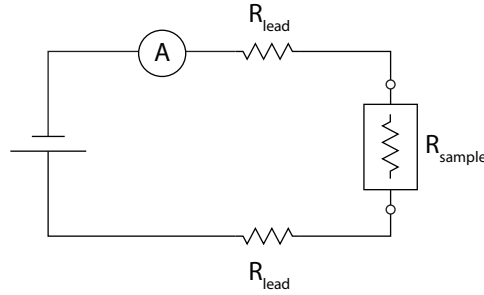
Figure 3–15: Circuit diagram showing a two-terminal I-V measurement. The total voltage drop through the circuit is set by the voltage source. The current is measured with an ammeter (A).

lead resistance is sufficiently small to be considered insignificant. However, if the sample resistance is also small, or if a highly accurate measurement is required, the influence of the lead resistance can be substantial. In this case it is desirable to use a four-terminal measurement, shown in Fig. 3–16. In this scheme, the current through the circuit is set and the resulting voltage drop across the sample is measured by a voltmeter using a second set of leads. Note that in the example circuit shown the current is determined by the large current sourcing resistor placed in series with the sample ($R_{source} \gg R_{sample}$). An ideal voltmeter has infinite input impedance (preventing any current through the voltmeter), and so only the voltage drop (and therefore resistance) across the contacts of the voltmeter leads is measured.
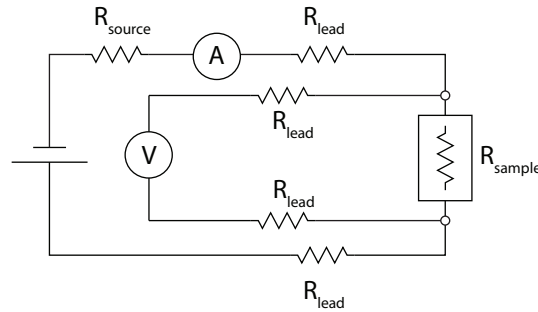


Figure 3–16: Circuit diagram showing a four-terminal V-I measurement. In this configuration the effect of the lead resistance is eliminated. The current sourced through the circuit is measured by an ammeter (A) and the resulting voltage drop across the sample measured by a voltmeter (V).

Power delivered to the sample is also an important consideration when choosing a transport measurement scheme. The power dissipation across a resistive sample is

$$P = I^2 R = \frac{V^2}{R} \tag{3.3}$$

where I and V are the current and voltage across the sample and R is the resistance of the sample. If the sample resistance is substantial, it is desirable to limit the voltage in order to minimize self heating. On the other hand if the sample resistance is small, limiting the current through the sample is desired.

### 3.3.2 Derivative dI/dV and dV/dI curves

To increase the measurement sensitivity we employ a standard AC lock-in measurement technique. In this scheme the sourcing voltage (current) is modulated at a known frequency. The resulting current (voltage) across the sample is then measured using a lock-in amplifier which filters out unwanted noise by only measuring time varying signals with the same frequency and phase as the sourcing signal. As with DC measurements, the AC measurement technique can use either a two-probe or four-probe configuration, depending on whether one sources the voltage or current. Fig. 3–17 and Fig. 3–18 show circuit diagrams used to perform a two-terminal dI-dV measurement and a four-terminal dV-dI measurement respectively.
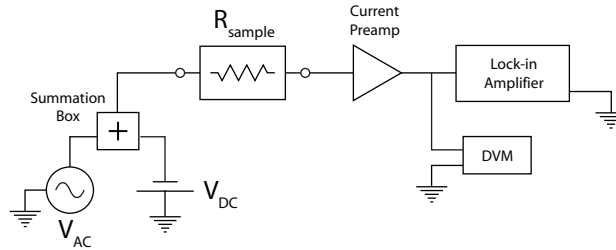


Figure 3–17: Circuit diagram showing a two-terminal dI-dV AC lock-in measurement.

The lock-in technique measures the derivative of an V-I (or I-V) curve, and therefore gives a measure of the change in resistance as a function of DC current (DC voltage). Performing the measurement at zero offset current (or voltage) with a small amplitude variation however gives us a direct measurement of the resistance given by

$$R = \left. \frac{dV}{dI} \right|_{V_{DC}=0, I_{DC}=0} \tag{3.4}$$

56
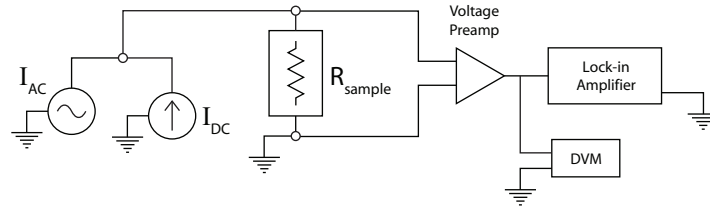
Figure 3–18: Circuit diagram showing a four-terminal dV-dI AC lock-in measurement.
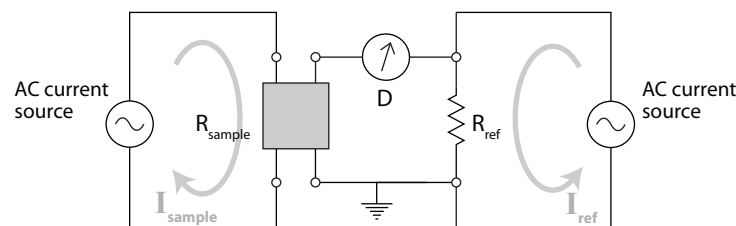


Figure 3–19: Schematic drawing showing the four-terminal AC bridge design. The null detector, D, measures zero voltage difference at the balance condition.

where typically we measure the RMS values of $dV$ and $dI$.

### 3.3.3   AC Bridge

In some experiments we are interested in monitoring the *change* in measured resistance in a quantum Hall state, while the background resistance value does not yield much useful information (see for example our discussion of the resistive NMR technique in Chapter 6). In this scenario, a resistance bridge technique can be very useful where we can null away the background signal allowing us to increase our measurement sensitivity. A 4-terminal AC resistance bridge was therefore developed for implementation in our dilution refrigerator. Detailed descriptions of several four-terminal resistance bridges designs can be found in literature. However, since for our purposes we are interested in measuring resistance *variations* with high sensitivity, we present here a modified, and significantly simplified bridge scheme.

Fig. 3–19 shows a schematic diagram of our four-terminal bridge, based on the "cryogenic current comparator" bridge design [10–14]. The bridge works as follows. A known current, $I_{sample}$, is sourced through the sample in the usual four point measurement configuration. A separate current, $I_{ref}$, is then sourced through a second, reference, resistor. The voltage drop across the sample is then compared to the voltage drop across the reference,

57
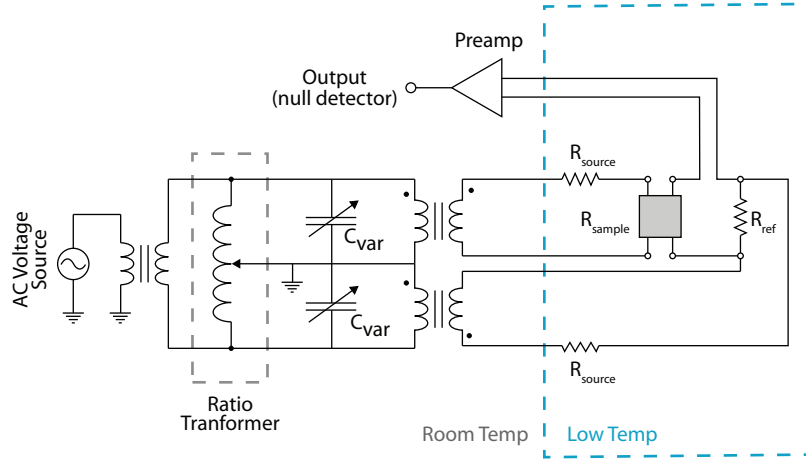
Figure 3–20: Complete circuit diagram for the four-terminal AC bridge (showing a room temperature preamp as the null detector).

and the current amplitude through one (or both) of the two resistors is varied until identical voltage drops are measured across each, as determined by the "null detector". Once balanced, any variation in the sample resistance disturbs this balance condition, which is measured by a fluctuation away from zero on the null detector.

The sensitivity of the bridge measurement is limited by the sensitivity of the null detector. For this reason, three different designs for the null detector were considered: (1) voltage preamp (cold or at room) + lock-in amplifier detector; (2) step-up (cold) transformer + lock-in detector; (3) SQUID current detector. Each of these designs are respectively expected to offer improved sensitivity. However, they also correspondingly provide increased experimental challenges in actual implementation. We therefore took a successive approach where first the theory of the bridge operation was tested using the "simplest" design, before working towards maximizing the bridge sensitivity. A discussion of our progress made in implementing and optimizing the bridge design is given in Chapter 6.

Fig. 3–20 shows the circuit diagram for configuration (1) of the bridge, where a voltage preamp is used as the null detector. All other configurations use the same sourcing circuit with the only difference being the null detector. To achieve precision control of the sourcing currents, a ratio transformer is used to divide AC voltage from a single source to each branch of the bridge circuit. Using the same signal generator to source both branches ensures the AC signals in each branch have identical frequencies; necessary when looking for the "null" measurement. The variable capacitors are used to fine tune the phase of each

signal in order to correct small phase shifts resulting from coupling to stray capacitance. In our implementation of the design, we set a fixed current through the sample and vary only the current through the reference resistor. This allows us to have precise control over the current through the sample throughout the experiment.

The bridge design is specifically optimized for integration into our dilution refrigerator in several ways. The reference resistor is thermalized to the LHe bath ($\sim$4 K) in order to minimize thermal noise contributions while additionally achieving good thermal stability. For reference resistors, we used metal thin film chip resistors ($2 \times 1.25 \times 0.4$ mm), which exhibit little response to temperature and magnetic field. Additionally, it was necessary to be able to switch *in situ* between a conventional 4-terminal measurement of the sample (for example to characterize the sample magnetoresistance and Hall resistance) and the AC bridge measurement. We therefore wired a complete set of leads from feedthrough "C" down to the experimental cold plate, where the termination at the experimental cold plate allows us to plug in one of the two custom NMR sample headers. A full schematic of the bridge wiring can be found in Appendix A. An additional bundle of leads is wired to two fixed value reference resistors ($R_1$=100 $\Omega$ and $R_2$=1 k$\Omega$) thermally connected to the 4K flange. Two reference resistors are included to allow us to use the bridge for a wider range of sample resistance values, since the bridge is optimized when the reference resistance is similar to the sample resistance. Finally, we constructed a special breakout box to mount directly onto the 32 pin connector at the top of the cryostat allowing us to attach the room temperature preamp directly at the cryostat, minimizing the distance the signal travels through the room temperature environment before being amplified.

### 3.3.4   Noise

In any transport measurement there is invariably noise present which limits the measurement sensitivity. Many external noise sources can be controlled by proper grounding and shielding. In our experimental set-up we therefore took special care to ensure there were no grounding loops, and to isolate all devices, wires, leads, etc. with grounded shielding where possible. Intrinsic noise however can be more limiting. For example, Johnson (or Nyquist) voltage noise results from thermal fluctuations of the charge carriers in the sample under test and therefore is temperature dependent

$$\delta V_{Johnson} = \sqrt{4k_B T R \Delta f} \tag{3.5}$$

where $T$ is the sample temperature, $R$ is the sample resistance, $k_B$ is Boltzmann's constant and $\Delta f$ is the frequency bandwidth of the detector used to measure the voltage across the resistor. Reducing Johnson noise is achieved by cooling the sample.

"$1/f$" noise results from resistance fluctuations and is proportional to the current flow through the device. $1/f$ noise is dictated by several factors including both the sample material and construction. The general form of $1/f$ voltage noise can be written as

$$\delta V_{1/f} = ARI\sqrt{\Delta f/f} \tag{3.6}$$

where $A$ is a dimensionless constant dependent on the sample, $R$ is the sample resistance, $I$ is the current, $\Delta f$ is the frequency bandwidth of the detector, and $f$ is the frequency at which the measurement is made. $1/f$ noise is therefore limited both by the sample and the measurement frequency.

Finally, "shot noise" is a current noise that results from the statistical fluctuations in the measurement of the charge carriers which are finite in nature. Shot noise is given by

$$\delta I = \sqrt{2q/I\Delta f} \tag{3.7}$$

where $q$ is the electron charge, $I$ is the RMS AC or DC current, and $\Delta f$ is the measurement bandwidth.

## 3.4  Disorder

### 3.4.1  Transport lifetime and electron mobility

Understanding the effect of disorder on the observed QHE is of fundamental importance since impurity scattering can have a significant and drastic effect on correlated electron behaviour. The disorder affecting a given 2DEG can be measured by two characteristic momentum relaxation lifetimes; $i$) the transport (or scattering) lifetime, $\tau_t$ and $ii$) the quantum (or single-particle) lifetime $\tau_q$ [15–18]. The transport lifetime results from short-range scattering, *i.e.* from atomic corrugation roughness in the quantum well, atomic dislocations, impurities in the 2DEG and phonon scattering, and determines the measured conductivity according to

$$\sigma = n\,e\,\mu \tag{3.8}$$

where $n$ is the electron density, $e$ the electronic charge and $\mu$ is the mobility, which is related to the transport lifetime, $\tau_t$, according to

$$R_A = \frac{V_{34}}{I_{12}} \qquad\qquad R_B = \frac{V_{31}}{I_{42}}$$
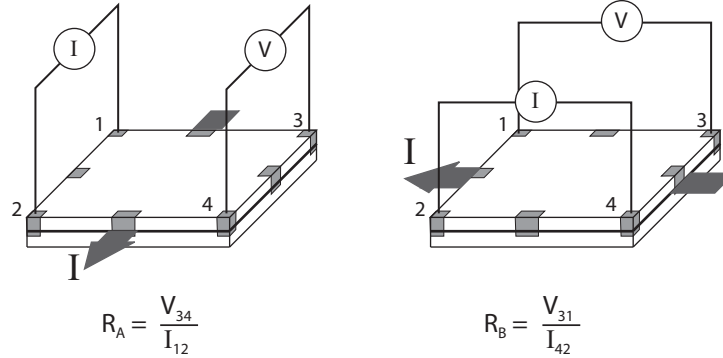
Figure 3–21: In the van der Pauw method, the resistivity of a 2D sheet of arbitrary shape can be measured by using a 4-point probe geometry to measure the resistance along two orthogonal directions.

$$\mu = \frac{e\,\tau_t}{m^\star} \tag{3.9}$$

where $m^\star$ is the electronic effective mass. The quantum lifetime on the other hand, while also determined by this short range scattering, is additionally sensitive to long range scattering (for example from the positive donor ions outside the 2DEG) and directly determines the quantum Landau level broadening. The two lifetimes can be very different, owing to the fact that the transport lifetime is insensitive to small angle (forward) scattering, whereas the quantum lifetime is determined by scattering in all directions.

The usual measure of disorder quoted in literature is the sample mobility. Mobility alone however is not a complete measure of the effective disorder since the mobility (transport lifetime) does not account for scattering off the donor ions, which in high mobility GaAs heterostructures is the dominant scatter mechanism [15,16]. Furthermore, the modulation doping technique in GaAs/AlGaAs forces much of this scattering to be forward scattering [15,16]. Nonetheless, the mobility remains a good measurement of relative disorder. For example, it has been found that the $\nu$=1 energy gap systematically scales with mobility even in the highest mobility samples [19]. The electron mobility therefore offers a useful benchmark by which to compare separate 2DEG samples.

The mobility is experimentally determined by measuring the zero-field sample resistance. To account for sample geometry, we use the van der Pauw technique for measuring resistance of a 2D sheet. In this technique a four-probe contact configurations is used to measure two separate resistance values, $R_A$ and $R_B$, obtained by sourcing the current along two orthogonal directions as shown in Fig. 3–21. In a square sample, the contacts are
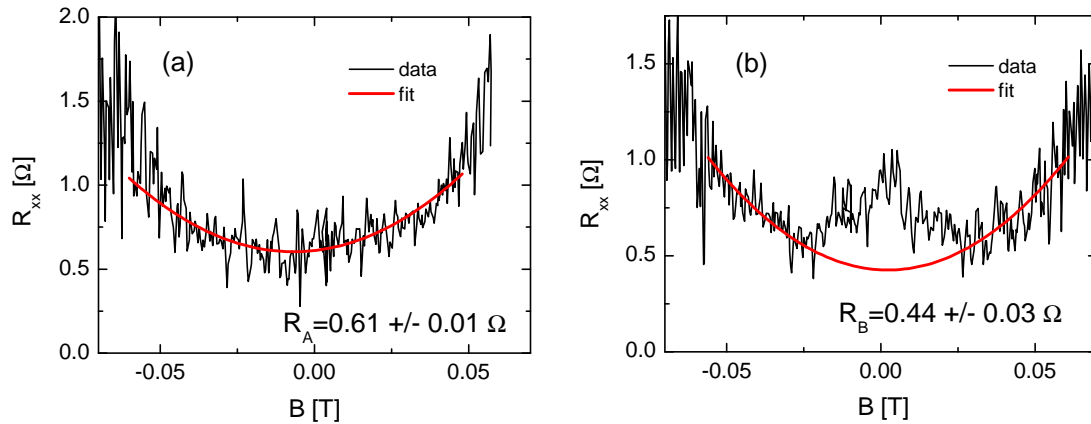
Figure 3–22: Magnetoresistance of our low density sample around zero field. (a) and (b) correspond to data acquired by sourcing the current along orthogonal directions. In (a) the zero field resistance was determined by fitting a parabola to the low field data. In (b) the local maximum at zero field was ignored in the fitting routine (see text). Data was acquired at a slow field sweep rate of 0.010 T/mins, and electron temperature of 17 mK. Despite the slow sweep rate there is a small hysteresis in the superconducting magnet, evidence by the displacement of the minimum $R_{xx}$ position away from B=0.

ideally placed at the corners. Van der Pauw showed [20] that from these two characteristic resistances, the 2D sheet resistance can be calculated by solving the relation

$$e^{\left(\frac{-\pi\,R_A}{R_S}\right)} + e^{\left(\frac{-\pi\,R_B}{R_S}\right)} = 1. \tag{3.10}$$

Knowing the sheet resistance then allows calculation of the bulk resistivity, $\rho = R_S t$, where t is the sample thickness. In a square 2D sample however, the sheet resistance and resistivity are equivalent, and therefore the conductivity can be written as $\sigma = 1/\rho = 1/R_S$. Finally, using this result together with Eqn. 3.8 gives the mobility equation

$$\mu = \frac{1}{n\,e\,R} \tag{3.11}$$

where $R$ is the sheet resistance determined from the van der Pauw equation. Note that it is customary to quote the density in units $cm^{-2}$, which gives the mobility in units $cm^2/V \cdot s$.

Fig. 3–22 shows an example mobility measurement taken from our low density sample. The field was slowly swept (0.010 T/mins) around the zero field value to find the true zero point in order to eliminate any magnet hysteresis or residual field in the superconducting magnet. The zero field resistance was then taken as the resistance value of the minimum, determined by fitting a parabola as shown in Fig. 3–22a. In the orthogonal contact

configuration (Fig. 3–22b), a local maximum is observed at zero field. The origin of this local resistance maximum is not known, but may be due to weak electron localization effects[1] . In this case the zero field resistance value was interpolated by applying the same parabolic fitting routine as used to find $R_A$ (Fig. 3–22a), but fitting only to the decreasing data on either side of the local maximum (*i.e.* effectively ignoring the maximum in the fit routine). The resulting resistance values ($R_A = 0.61 \pm 0.01\,\Omega$ and $R_B = 0.44 \pm 0.03\Omega$) were then used in Eqns. 3.10 and 3.11 to give a measured mobility for this sample of $16.6 \pm 0.8 \times 10^6$ cm$^2$/V·s, in excellent agreement with the mobility value specified by the sample grower ($16.7 \times 10^6$ cm$^2$/V·s). For comparison, if we instead take the peak value of the local maximum for $R_B$ (in this case $R_B \sim 0.86\ \Omega$), we calculate a much lower mobility of $\sim 11.8 \times 10^6$ cm$^2$V·s. This lends support to the accuracy of our fit routine shown in Fig. 3–22. Furthermore, the substantial difference in the calculated mobility (nearly 30%) resulting from a very small difference in measured zero-field resistance ($\sim$0.4 $\Omega$) emphasizes the importance of making very careful measurements when determining the mobility.

### 3.4.2   Quantum lifetime

As stated in the previous section, the quantum lifetime in GaAs/AlGaAs heterostructures gives a direct measure of the disorder induced Landau level broadening. This follows since the quantum lifetime is measured from the envelope shape of the low field Shubnikov de Haas oscillations which is directly related to the Landau level line width.

At low fields, in the onset region of the magnetoresistance oscillations, the longitudinal resistivity, $\rho_{xx}$, oscillates around the zero-field resistivity, $\rho_o$ (Shubnikov de Haas oscillations). Since the magnetoresistance oscillations are periodic in 1/B (Eqn. 2.14), the variation in the longitudinal resistance, $\Delta\rho$, can be expanded as a Fourier series. In the zero temperature limit, the amplitude of the fundamental oscillatory term yields the following expression for $\Delta\rho/\rho_o$ [15, 21]

$$\frac{\Delta\rho}{\rho_o} = Ae^{\frac{-\pi}{\omega_c \tau_q}} \tag{3.12}$$

where $\tau_q$ is the quantum lifetime and $\omega_c = eB/m$ is the cyclotron frequency. From this equation, plotting $\ln(\Delta\rho/\rho_o)$ versus 1/B (a so-called Dingle plot) gives a linear relation

---

[1] We note that the same feature was observed in a separate sample cut from the same wafer, but measured on a different cryostat.
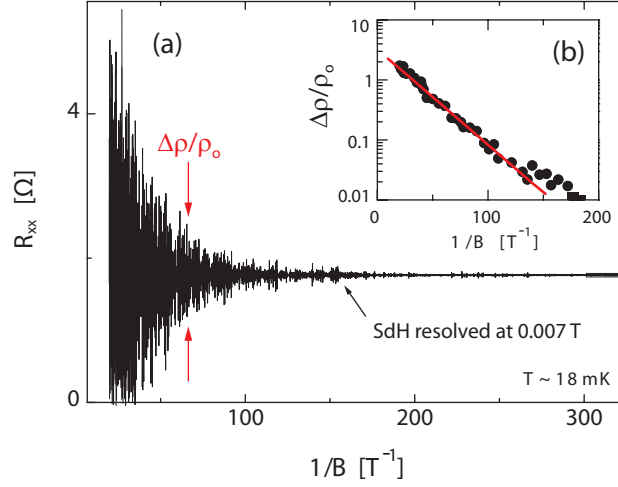
Figure 3–23: (a)Magnetoresistance in the low field regime of our low density sample plotted versus 1/B. The data was acquired at base temperature (18 mK) and at the lowest possible B field sweep rate (0.001 T/mins). The plotted data was filtered with a 2Hz wide band pass filter approximately centered on the SdH oscillation frequency (3.4 Hz). (b) Dingle plot of the envelope amplitude from (a). From the slope of the fitted line, the quantum lifetime was calculated to be $0.33 \pm 0.03$ ps, giving a LL broadening of $0.23 \pm 0.03$ K (see text).

whose slope can be used to extract the value of $\tau_q$. From the quantum lifetime, which is a measure of the collision scattering time, the disorder induced broadening of the Landau levels, $\Gamma$, can then be calculated according to

$$\Gamma = \frac{\hbar}{2\tau_q}. \tag{3.13}$$

Eqn. 3.12 results from assuming a Lorentzian shape for the Landau levels, however using a Gaussian gives a similar result (see Ref. [21]). The prefactor, A, in Eqn. 3.12 is a constant whose value is determined by the relation between the resistivity and density of states and is theoretically expected to be either 2 or 4, depending on whether the relation is linear or quadratic respectively [21]. It is important to note that the usual assumption is that level broadening determined is *field independent*, and so while the analysis is carried out on the low-field SdH oscillations (higher Landau levels), the measured broadening is expected to be the same for all Landau levels. Furthermore, the analysis outlined here is only valid in the low-field regime before Zeeman spin splitting is observed, and so attention must be paid when measuring the envelope amplitude to only include non-spin split Landau levels in the analysis.

64

Fig. 3–23 shows and example quantum life time measurement. The data plotted in figure Fig. 3–23a was first passed through a 2 Hz wide band pass filter, approximately centered on the SdH frequency (determined to by ~3.4 Hz by applying a Fourier transform to the raw data). The amplitude of the envelope function versus $1/B$ is shown in the inset dingle plot (Fig. 3–23b). From the slope of the fitted line, the quantum lifetime was calculated (Eqn. 3.12) to be $\tau_q = 33 \pm 3$ ps. Using Eqn. 3.13 this gives the (field independent) disorder induced LL broadening to be $0.23 \pm 0.03$ K. We can expect that the SdH are observable only once the cyclotron energy gap becomes larger than the LL width. Therefore, from the B field value where the SdH can first be resolved, we can approximately estimate the width of the LLs. From Fig. 3–23 the SdH oscillations are first observable at ~0.007 T which corresponds to a cyclotron gap of ~0.14 K. This therefore gives a very rough estimate for the LL broadening of 0.14 K which is similar (same order of magnitude) to the LL broadening calculated from the Dingle plot (0.23 K).

Using the sample mobility ($16.6 \pm 0.8 \times 10^6$ cm$^2$/V·s) together with Eqn. 3.9 gives the transport lifetime for the same sample to be $\tau_t = 640 \pm 30$ ps. The ratio of the transport lifetime to quantum lifetime is therefore $\tau_t/\tau_q \sim 19$, which is much greater than one, suggesting in our GaAs sample the dominant scatter mechanism is long range scattering from the remote donor impurities, as expected [15, 16].

## 3.5   Energy Gap Measurement

The appearance of both the integer and fractional quantum Hall states requires an energy gap in the electron density of states. This activation energy gap is measured experimentally from the temperature dependence of the magnetoresistance minimum of the quantum hall state. In the low temperature, zero disorder limit, the quantized Landau energy levels can be considered delta functions with zero width. Using a classical semiconductor model, the conductivity in the transport regime is proportional to the number of charge carriers, $n$, populating the excited level, *i.e.*

$$\sigma_{xx} \propto n \tag{3.14}$$

where $n$ is given by

$$n = \int_{E_F}^{\infty} f(E) \, D(E) \, dE \tag{3.15}$$

where $E_F$ is the Fermi energy, $D(E)$ is the density of states, and $f(E)$ is the Fermi-Dirac distribution given by

65

$$f(E) = \frac{1}{1 + e^{(E - E_F)/k_B T}} \tag{3.16}$$

where $k_B$ is the Boltzmann constant and $T$ is the electron temperature. Consider a two Landau level system such that at $T = 0$ the ground state, $E_o$, is completely filled and the excited state, $E_1$, is completely unfilled. If we assume the density of states is described by a $\delta$ function, then solving for Eqn. 3.15 gives the temperature dependent $(T \neq 0)$ population of the excited state to be

$$n = \int_{E_F}^{\infty} f(E)\, \delta(E_1)\, dE = \frac{1}{1 + e^{(E_1 - E_F)/k_B T}}. \tag{3.17}$$

Note however that since the Fermi energy is between the LLs, the energy gap, $\Delta = E_1 - E_o$, can be rewritten as $(\frac{1}{2})\Delta = E_1 - E_F$, which therefore gives

$$n = \frac{1}{1 + e^{\Delta/2k_B T}}. \tag{3.18}$$

In the low temperature limit where $\Delta \gg k_B T$ this approximates to

$$n \sim e^{-\Delta/2k_B T}. \tag{3.19}$$

Finally, the longitudinal resistivity is related to the conductivity according to the tensor relation

$$\sigma_{xx} = \frac{\rho_{xx}}{\rho_{xx}^2 + \rho_{xy}^2}. \tag{3.20}$$

In the high B field limit the Hall resistivity, $\rho_{xy}$, will be much larger than the longitudinal resistivity, $\rho_{xx}$, at the minimum such that we have the simple relation $\rho_{xx} \propto \sigma_{xx}$. Since in 2D $R_{xx} \propto \rho_{xx}$, then using this together with Eqn. 3.19 and 3.14 gives the resistance of the magnetoresistance minimum in the thermally activated transport regime to be

$$R_{xx} \propto e^{-\Delta/2k_B T}. \tag{3.21}$$

Plotting $R_{xx}$ versus inverse temperature (a so-called Arrhenius plot) therefore allows a determination of the gap from the slope of a straight line fit to the data.

# References

[1] Stormer, H. L. *Surf. Sci.* **132**, 519 (1983).

[2] Stern, F. and Das Sarma, S. *Phys. Rev. B* **30**(2), 840 (1984).

[3] Stopa, M. and Das Sarma, S. *Phys. Rev. B* **40**(14), 10048 (1989).

[4] Stopa, M. and Das Sarma, S. *Phys. Rev. B* **45**(15), 8526 (1992).

[5] Pobell, F. *Matter and Methods at Low Temperatures.* Springer-Verlag, New York, (1992).

[6] Linde, D. R., editor. *"Nuclear spins, moments, and other data related to NMR spectroscopy" in CRC Handbook of Chemistry and Physics, $88^{th}$ edition (internet version 2008).* CRC Press/Taylor and Francis, Boca Rayton, FL., (2008).

[7] Penner, G. H. and Liu, X. *Prog. NMR Spectrosc.* **49**, 151 (2006).

[8] Bladh, K., Gunnarsson, D., Hurfeld, E., Devi, S., Kristoffersson, C., Smalander, B., Pehrson, S., Claeson, T., and Delsing, P. *Rev. Sci. Instrum.* **74**(3), 1323 (2003).

[9] Hilke, M. private communication (2006).

[10] Rowlands, J. A. and Woods, S. *Rev. Sci. Instrum.* **47**(7), 795 (1976).

[11] Edmunds, D. L., Pratt, W. P., and Rowlands, J. A. *Rev. Sci. Instrum.* **51**(10), 1516 (1980).

[12] Delahaye, F. *IEEE Trans. Instrum. Meas.* **40**(6), 883 (1991).

[13] Witt, T. J. *Rev. Sci. Instrum.* **69**(8), 2823 (1998).

[14] Jeckelmann, B. and Jeanneret, B. *Meas. Sci. Technol.* **14**, 1229 (2003).

[15] Harrang, J. P., Higgins, R. J., Goodall, R. K., Jay, P. R., Laviron, M., and Delescluse, P. *Phys. Rev. B* **32**(12), 8126 (1985).

[16] Das Sarma, S. and Stern, F. *Phys. Rev. B* **32**(12), 8442 (1985).

[17] Gold, A. *Phys. Rev. B* **38**(15), 10798 (1988).

[18] Hwang, E. H. and Das Sarma, S. *Phys. Rev. B* **77**, 235437 (2008).

[19] Schmeller, A., ang L. N. Pfeiffer, J. P. E., and West, K. W. *Phys. Rev. Lett.* **75**(23), 4290 (1995).

[20] van der Pauw, L. J. *Philips Tech. Rev.* **20**, 220 (1958).

[21] Piot, B. A., Maude, D. K., Henini, M., Wasilewski, Z. R., Friedland, K. J., Hey, R., Ploog, K. H., Toropov, A. I., Airey, R., and Hill, G. *Phys. Rev. B* **72**, 245325 (2005).

# Intrinsic Gap of the $\nu = 5/2$ Fractional Quantum Hall Effect

W e present here a detailed analysis of the $\nu = \frac{5}{2}$ state for a sample with the lowest electron density reported to date (by nearly a factor of two). This allows the study of the fractional quantum hall effect (FQHE) in a regime where the cyclotron energy is smaller than the Coulomb interaction energy, *i.e.* in a regime of strong, possibly non-perturbative, Landau level coupling. We compare the measured energy gap with neighbouring FQH states in the second Landau level (SLL), and discuss these results in the context of previous studies. Finally, we experimentally determine the intrinsic energy gap of the $\frac{5}{2}$ state using three different methods and compare with theory. Our analysis shows that large discrepancies remain between theory based on a Moore-Read Pfaffian state and experiment at $\nu = \frac{5}{2}$ that cannot be attributed to disorder alone. In contrast, a similar analysis for the $\nu = \frac{1}{3}$ Laughlin state shows much better agreement with current models.

## 4.1  Experimental details

The sample used in this study was our low density GaAs/AlGaAs quantum well sample, with a measured density of $1.60(1) \times 10^{11}$ cm$^{-2}$ and mobility of $16.6(8) \times 10^6$ cm$^2$/V·s. Treatment with a red LED was used during the cooldown. Transport measurements were performed using a standard lock-in technique at $\sim$6.5 Hz and small excitation currents of 2-10 nA. The sample parameters can vary considerably from one cooldown to the next, and so to be able to make reliable comparisons between different quantum Hall states etc., we made all measurements during the same cooldown, except where noted.
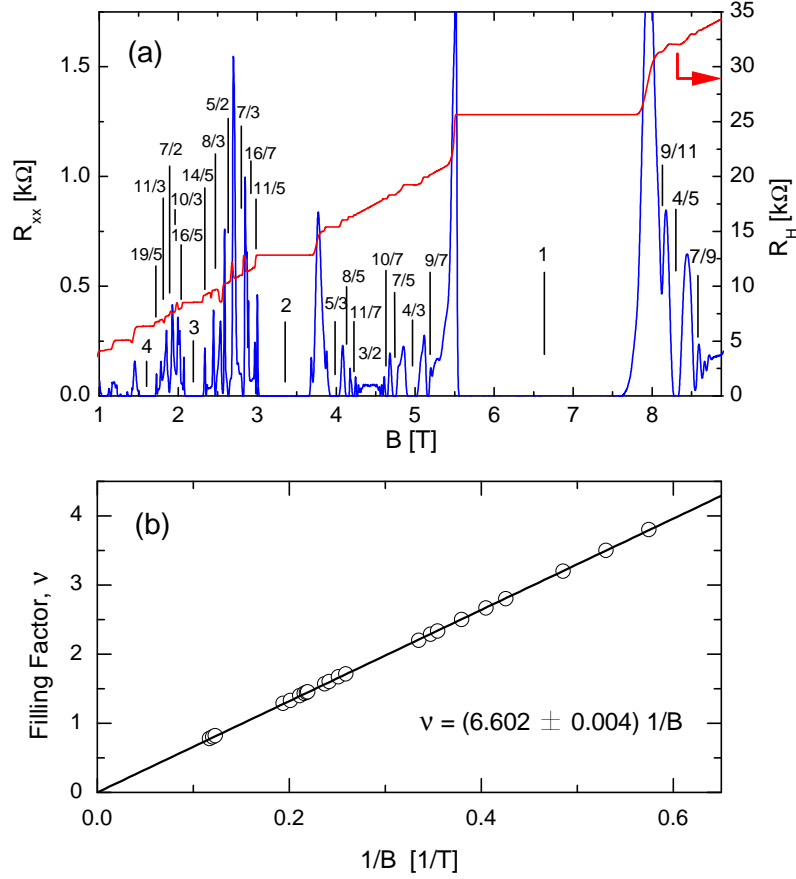
Figure 4–1: The B field position of the quantum Hall states labeled in (a) are used to extract the electron density from the slope of the fitted linear curve shown in (b).

## 4.2 Electron density

The electron density of a 2DEG can be determined directly from the quantum Hall effect since the value in magnetic field where a QHE state is observed, $B_\nu$, is determined only by the density and fundamental constants,

$$B_\nu = \frac{1}{\nu} \frac{n\,h}{e} \tag{4.1}$$

where $\nu$ is the filling fraction, $h$ is Planck's constant $(6.6261 \times 10^{-34}$ J·s), $e$ is the electronic charge $(1.6011 \times 10^{-19}$ C) and $n$ is the electron density. Plotting the filling factor, $\nu$, against the inverse field value where the corresponding QHE state is observed, $1/B_\nu$, therefore yields a straight line whose slope can be used to calculate the density according to
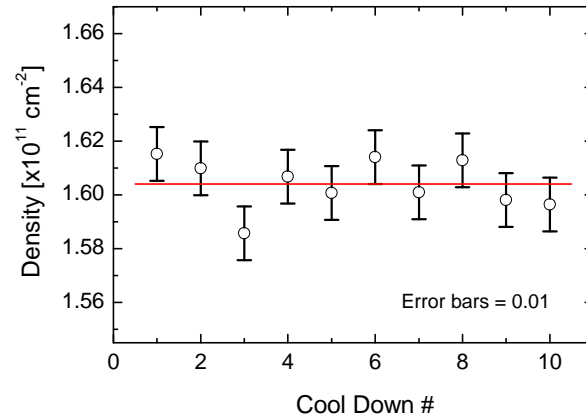
Figure 4–2: (a) Density values obtained from the same sample but during separate cooldowns. The scatter in the measured values is within the measurement uncertainty.

$$n = \text{slope} \cdot \frac{e}{h} \times \frac{1}{100^2}. \qquad (4.2)$$

The factor of $(1/100^2)$ in Eqn. 4.2 is included to give the density in units $\text{cm}^{-2}$, which is the notation conventionally reported in literature.

Fig. 4–1 shows an example density measurement obtained from our low-density sample. The data in the figure was acquired at base temperature (18 mK) while continuously sweeping the magnetic field from 9.0 to zero Tesla (0.113 T/mins). Using the slope in Fig. 4–1b the density is calculated from Eqn. 4.2 to be $1.60 \pm 0.01 \times 10^{11} \text{ cm}^{-2}$.

It is worth noting that the electron density can also be obtained from the slope of the Hall resistance versus magnetic field since the Hall resistance varies according to

$$R_H = \frac{B}{n\,e} \qquad (4.3)$$

where $B$ is the applied field. The quantized plateaus in $R_H$ coinciding with the quantum Hall effect however can make it difficult to achieve an accurate fit. Often therefore, the slope of the Hall resistance is measured in the low-field regime, before the onset of quantum Hall effect is observed. However, for the very high quality samples examined in this study the Shubnikov de Haas oscillations are resolved at as low as 0.007 T. In all of our studies the density was therefore determined from the longitudinal resistance oscillations as outlined above.

The electron density can vary from one cooldown to the next depending on variations in the LED treatment, cooling conditions etc. While we have indeed observed a slight scatter
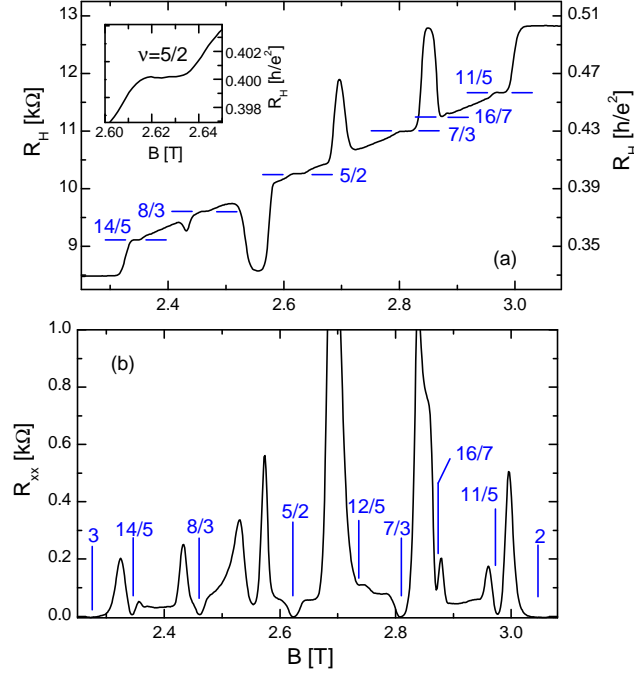
Figure 4–3: (a)Hall resistance and (b) corresponding magnetoresistance in the second Landau level of our low density, high mobility 2DEG (T=19 mK).

in the measured densities, shown in Fig. 4–2, the scatter is within the measurement error suggesting good consistency in our cooling procedure.

### 4.3    $\nu = 5/2$ at very low field

Fig. 4–3 shows the magnetoresistance ($R_{xx}$) and corresponding Hall resistance ($R_H$), taken around $\nu = \frac{5}{2}$ in the SLL at 19 mK. A vanishingly small magnetoresistance is observed at $\nu = \frac{5}{2}$, together with a wide plateau in the corresponding Hall trace, quantized to within 0.05% of $R_H = (\frac{2}{5})h/e^2$. The unambiguous $\frac{5}{2}$ state observed here occurring at $\sim$2.63 T represents the lowest magnetic field observation of the $\frac{5}{2}$ to date [1–15]. Strong FQHE minima are also observed at $\nu = \frac{14}{5}, \frac{8}{3}, \frac{7}{3}$, and $\frac{11}{5}$, each of which exhibit corresponding quantized plateaus in $R_H$. The four reentrant phases observed in the Hall trace on either side of the $\frac{5}{2}$ plateau (two peaks tending towards $R_H = (\frac{1}{3})h/e^2$ and two tending towards $R_H = (\frac{1}{2})h/e^2$) together with the observation of a $\nu = \frac{16}{7}$ minimum, and the hint of an emerging minimum at $\nu = \frac{12}{5}$, are all signatures of an extremely high quality sample [7,9,10,14]. The deep $R_{xx}$ minima appearing in the reentrant insulating phase at $\sim$2.55 T (Fig. 4–3b) is similar to that observed elsewhere upon lowering the electronic temperature to a regime where the reentrant state is fully formed [10,13,15].
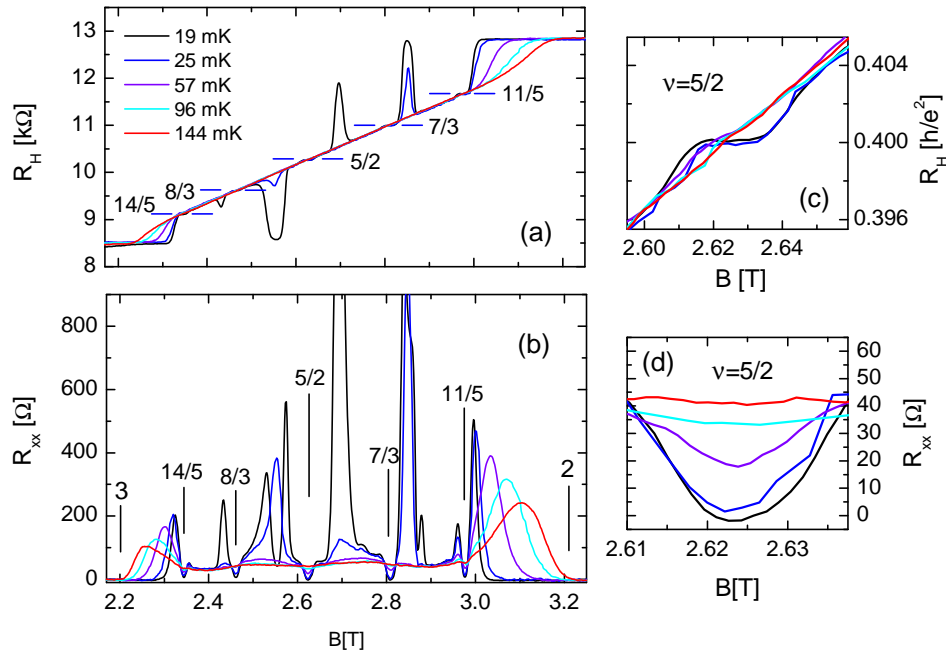
Figure 4–4: (a) Hall resistance and (b) corresponding magnetoresistance in the SLL around $\nu = \frac{5}{2}$ as a function of temperature. (c) and (d) shows an enlarged view of the $\frac{5}{2}$ $R_H$ plateaus and $R_{xx}$ minimum, respectively.

## 4.4 Activation energy gaps in the SLL

Fig. 4–4 shows the magnetoresistance in the SLL at several different temperatures. The sample temperature was varied by applying current to a resistive wire heater thermally contacted to the dilution fridge mixing chamber. The reported temperatures were measured by a CMN thermometer also mounted on the mixing chamber. As expected, the quantum hall states all diminish as the temperature is increased. We also note that the anomalous peaks in $R_H$ associated with the reentrance phase are rapidly destroyed with temperature, in agreement with previously published observations [11,15][1] . Fig. 4–5 shows a plot of the $\nu = 3$ zero-resistance minimum in $R_{xx}$ as a function of mixing chamber temperature, which we used to track our electron temperature. In Fig. 4–5b, the width versus temperature follows a well behaved linear trend (plotted on a log scale) all the way down to our base

---

[1] In these previous studies, the abrupt low-temperature behaviour was interpreted as evidence that the reentrance phase is associated with the formation of an exotic electron solid phase (bubble phase).
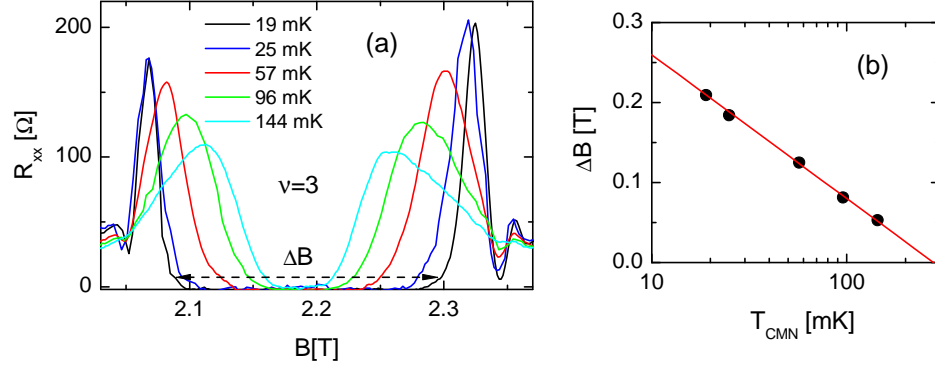
Figure 4–5: (a) Width of the $\nu = 3$ magnetoresistance minimum, $\Delta B$, at various temperatures. (b) Plotting $\Delta B$ versus temperature shows a linear behaviour (plotted on a log scale) down to our base temperature.
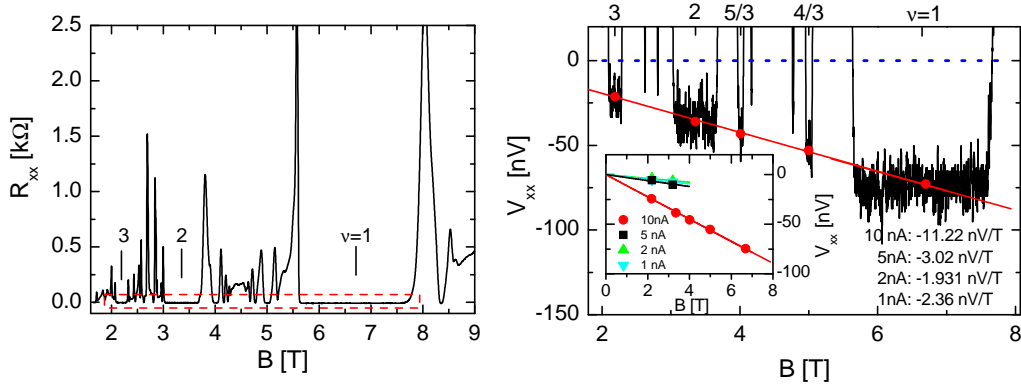


Figure 4–6: (a) Magnetoresistance of our low density sample (T=19 mK, $I_{AC}$=10 nA). (b) Enlarged view of the longitudinal voltage around zero (dashed box in (a)), showing a small offset that varies linearly with B. Inset shows the offset versus B measured at different sourcing currents.

temperature of 19 mK. We take this as evidence that the electrons are well thermalized since otherwise saturation in the width would be observed at some temperature. We therefore consider our thermometry to accurately reflect the electron temperature. The "width" plotted in Fig. 4–5b was measured as the B field separation, $\Delta B$, between the high and low field flank on either side of the $\nu = 3$ minimum taken at an arbitrary but small $R_{xx}$ value, indicated by the dashed arrow in Fig. 4–5a (measuring the width at larger $R_{xx}$ values, *i.e.* higher in the flank, showed the same linear behaviour).

The activation energy gaps of the FQH states in the SLL were measured from the temperature dependence of the corresponding magnetoresistance minimum. In the thermally activated transport regime, the resistance value of the minimum is given by
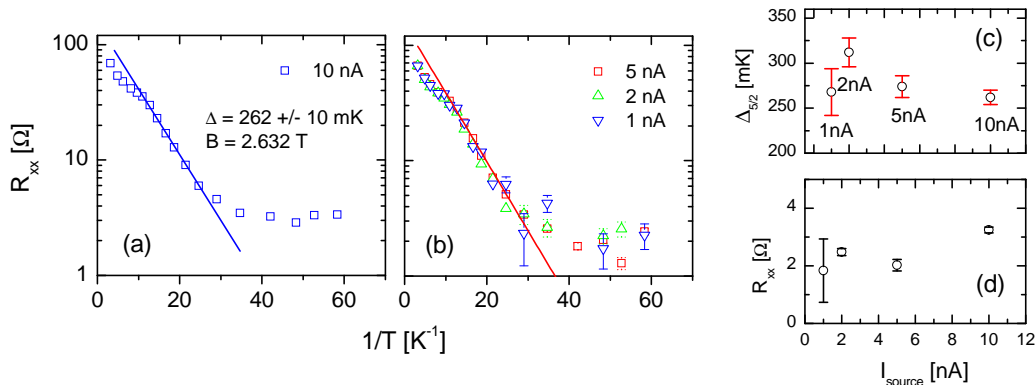
Figure 4–7: (a)-(b) Arrhenius plots showing activated behaviour at $\nu = \frac{5}{2}$ measured at different sourcing currents. (c) Gap values measured at each current. (d) Magnetoresistance in the low-temperature tail off region measured at each current.

$$R_{xx} \propto e^{-\Delta/2k_B T}. \tag{4.4}$$

where $\Delta$ is the activation energy gap, $k_B$ is the Boltzmann constant and $T$ is the electron temperature. Plotting $R_{xx}$ versus inverse temperature (a so-called Arrhenius plot) therefore allows a determination of the gap from the slope of a straight line fit to the data.

We often observe a small zero-offset in the measured magnetoresistance. In Fig. 4–6b, an enlarged view around zero voltage from a typical magnetoresistance measurement is shown. Importantly, this measured offset varies linearly with the magnetic field and also varies with the amplitude of the sourcing current. We therefore believe the offset results from a mixing of the Hall resistance and magnetoresistance, which is common when using a van der Pauw measurement configuration where it is difficult to ensure the contacts are perpendicular. When measuring the activation energy gap it is important to account for this offset since the corresponding error can influence the gap measurement by a significant amount (up to nearly 100 mK in cases). To correct for this, we determined the deviation from "true zero" as a function of B field by fitting a linear curve to the measured zero at the center of several well defined and clearly formed quantum hall minima (shown inset in Fig. 4–6).

Fig. 4–7a shows an Arrhenius plot of the $\frac{5}{2}$ gap measurement using a 10 nA sourcing current compared with smaller 5, 2, and 1 nA sourcing currents shown in Fig. 4–7b. Smaller current causes less self heating, but increases uncertainty in the corresponding voltage measured across the sample. This translates into increased error in the gap measurement. As shown in Fig. 4–7c the error, determined from the goodness of the linear fit,
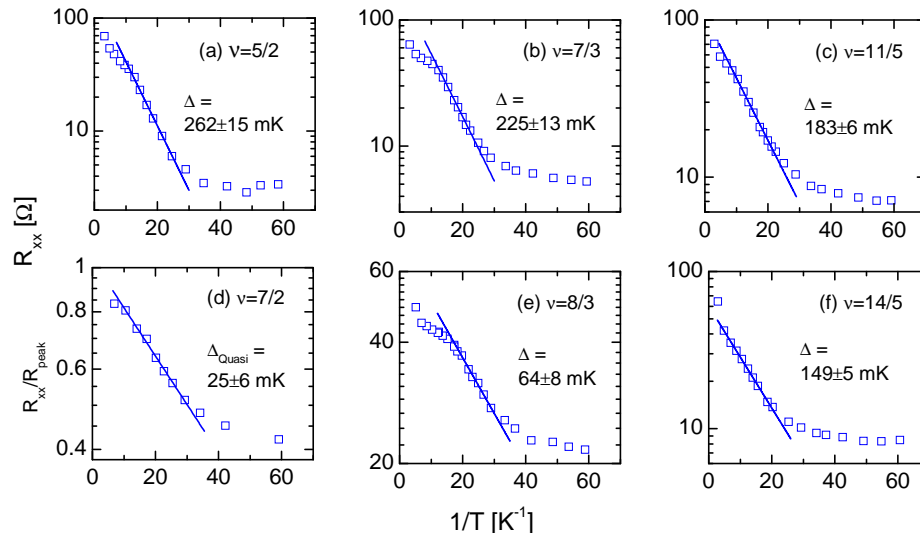
Figure 4–8: Arrhenius plots showing activated temperature behaviour in the second Landau level. All plots show the resistance value of the corresponding FQH minimum plotted versus inverse electron temperature except (d) which shows a "quasi-gap" measurement for $\nu = \frac{7}{2}$ (see text).

is systematically larger when sourcing smaller currents. The gap value between the measurements however is approximately the same. Furthermore, the resistance value measured in the low temperature tail-off region does not vary significantly (less than $\sim 1 \ \Omega$) between the different source currents (Fig. 4–7d). Together with the data in Fig. 4–5 this indicates the self heating at 10 nA is less than our fridge temperature (at base). This is consistent with a systematic study of the current heating at low temperatures by Pan *et al.* [7] and also Gammel *et al* [3] where in both studies it was reported (using a lower temperature fridge than ours) that using a source current as large as 20 nA at $\nu = \frac{5}{2}$ raised the electron temperature to only $\sim 15$ mK. We therefore used a 10 nA source current for all of our activation energy gap measurements.

Fig. 4–8 shows the activation energy gap measured for all of the FQHE states in the SLL. All data was acquired at fixed magnetic field in order to avoid heating effects caused by varying fields, and only after allowing the temperature to stabilize. Stable thermal equilibrium was determined by monitoring all four thermometers mounted on the mixing chamber (CMN, Matsushita, RuO and RuO-202A), and also by measuring the magnetoresistance of the quantum Hall state as a function of time. The gap error quoted on each plot was estimated from the goodness of the linear fit.

A characteristic "s" shape [16] is seen in each of the plots in Fig. 4–8. Since from the above discussion (Figs. 4–5 and 4–7) we believe the electrons are well thermalized to
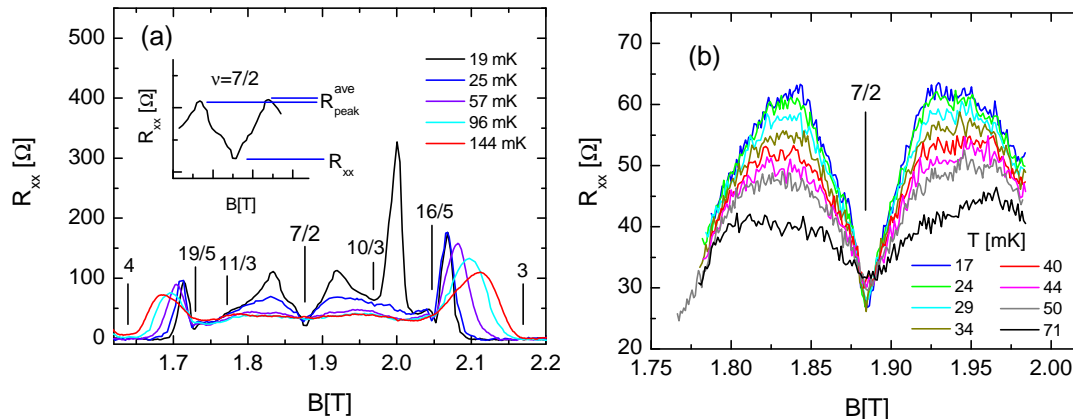
Figure 4–9: (a) Magnetoresistance in the SLL around $\nu = \frac{7}{2}$ as a function of temperature. Inset shows an enlargement of the $\frac{7}{2}$ minimum defining the parameters used in to estimate the "quasi-gap". (b) Slow B field sweeps around the seven half minimum (0.001 T/mins) at various temperatures.

the mixing chamber over the full temperature range, the low temperature tail-off likely does not reflect a saturation in the electronic temperature. Instead, it may indicate a transition from activated conduction to hopping conduction [16], and/or could result from the energy dependent Landau level broadening due to disorder [17]. In the $\frac{7}{3}$, $\frac{5}{2}$, and $\frac{8}{3}$ states (Fig. 4–8a,b,e), there is also a deviation from activated behaviour at high temperature whose onset temperature scales with the corresponding gap value. Furthermore we note that around these temperatures a clear minimum in $R_{xx}$ is no longer observed (see for example Fig. 4–4d). The high temperature saturation therefore likely results from $k_B T$ approaching the gap value, where the gap is not well formed and Eqn. 4.4 is no longer valid. Interestingly, the same deviation is not observed in the $\frac{11}{5}$ and $\frac{14}{5}$ FQH states, which have lower measured gaps than the $\frac{7}{3}$ and $\frac{5}{2}$ states. Recent work has suggested the $\frac{11}{5}$ and $\frac{14}{5}$ to be Laughlin states, while the $\frac{7}{3}$ and $\frac{8}{3}$ are proposed to possibly be non-Laughlin [14, 18, 19], which may be related to the different behaviours. Another contributing factor may be competing effects with the insulating regime around the $\frac{7}{3}$, $\frac{5}{2}$, and $\frac{8}{3}$ states, which exhibits complex temperature dependence (such as the reentrance phase) that may affect the FQHE behaviour when the states are only weakly formed.

The $\nu = \frac{7}{2}$ state (the electron-hole conjugate of $\nu = \frac{5}{2}$) appears at magnetic field less than 2 T (Fig. 4–9), however in the cooldown shown here the $\frac{7}{2}$ state was only weakly formed. Owing to a competition between the weak $\frac{7}{2}$ and rapidly emergent neighbouring reentrant states, the $R_{xx}$ minimum did not fall significantly with temperature near base
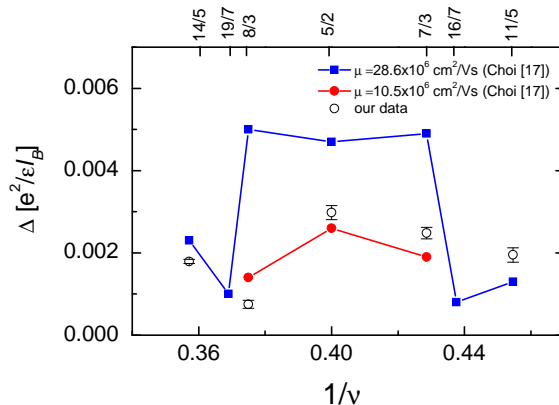
Figure 4–10: Energy gaps for the FQH states, plotted in Coulomb energy units. Open circles are our data. Solid squares and circles, respectively, are the "high mobility" and "low mobility" data in reference [14].

making it difficult to obtain the same thermal gap measurement . A "quasi-gap" measurement was therefore performed by measuring the depth of the $\frac{7}{2}$ minima with respect to the average resistance of the two neighbouring peaks ($R_{peak}$) [2, 3, 8]. The resulting Arrhenius plot, which indicates activated behaviour (Fig. 4–8d), gives an estimate for the $\frac{7}{2}$ gap value of $\sim$25 mK. A "true" gap measurement from a better formed $\frac{7}{2}$ state (resulting from a separate cooldown) is given in the next chapter. The value measured there ($\sim$35 mK) is in good agreement with this quasi-gap measurement.

In Fig. 4–10, the gap values are plotted in Coulomb energy units, $e^2/\epsilon l_B$, where $l_B = \sqrt{\hbar/eB}$ is the magnetic length, and $\epsilon = 12.9$ is the dielectric constant for GaAs. Results from recent gap measurements in the SLL by Choi *et al.* [14] are also shown for comparison. The Choi *et al* "low mobility" sample (filled circles) had a similar mobility ($\mu_B = 10.5 \times 10^6 \mathrm{cm}^2/\mathrm{Vs}$) to ours , while the Choi *et al* "high mobility" sample (filled squares) had nearly twice the mobility ($\mu_B = 28.3 \times 10^6 \mathrm{cm}^2/\mathrm{Vs}$) than ours. The densities of the two Choi samples were similar to each other, and both roughly twice ours ($2.8 \times 10^{11} \mathrm{cm}^{-2}$, and $3.2 \times 10^{11} \mathrm{cm}^{-2}$ respectively). From the figure it can be seen that the gap energies follow a nearly identical trend between the three data sets.

The excellent agreement between our data set and that of the Choi *et al* 'low mobility' sample is surprising given the factor of two difference in electron densities between the two samples. Simple dimensional considerations imply that the interaction energy, and hence the FQH gap, should scale as $\sqrt{B}$, which would predict a $\sim$40% enhancement in the gap between the low density (ours) and the high density (Choi *et al.*) samples. Our finding that the gap is almost the same for the two samples with similar mobility (independent of

Table 4–1: Measured gap energies shown in Fig. 4–8 expressed in both mK and Coulomb energy units.

| | fraction ($\nu$) | | | | | |
| | 7/2 | 14/5 | 8/3 | 5/2 | 7/3 | 11/5 |
| --- | --- | --- | --- | --- | --- | --- |
| $\Delta$ [mK] | 25±6 | 149±5 | 64±8 | 262±10 | 225±13 | 183±6 |
| $\Delta$ [$\frac{e^2}{\epsilon l_B}$] | 0.0004 | 0.0018 | 0.0008 | 0.0030 | 0.0025 | 0.0020 |

density), while significantly enhanced in samples with higher mobility (Choi *et al.* "high mobility"), suggests that disorder more strongly affects the gap than the applied magnetic field [20].

## 4.5 Intrinsic energy gap of the $\nu = 5/2$ state

The $\frac{5}{2}$ energy gap measured for our sample ($\sim$260 mK) is similar to other measurements found in literature, which range from $\sim$100 mK to $\sim$500 mK. This value however is in significant disagreement with the theoretical gap based on a Moore-Read type Pfaffian wave-function which is predicted to be $\sim$2 K at 2 T [21, 22]. The conventional approach to account for the large discrepancy between the theoretical and experimental gap measured at $\nu = \frac{5}{2}$ is to assume the difference is due to disorder induced broadening of the Landau levels. Using a simple semiconductor model, the contribution from disorder broadening to the measured gap is usually described by

$$\Delta^{exp} = \Delta^i - \Gamma \qquad (4.5)$$

where $\Delta^{exp}$ is the experimentally measured activation energy gap, $\Delta^i$ is the intrinsic energy gap (*i.e.* the gap that would be observed in the absence of disorder), and $\Gamma$ is the disorder induced LL broadening (assumed to be independent of filling fraction). From the low-field Shubnikov de Haas (SdH) oscillations we measured the quantum lifetime to be $\tau_q = 33\pm3$ ps in our sample. This gives a direct experimental measure of the LL broadening to be $\Gamma = 0.23\pm0.03$ K (see section 3.4.2). Using our measured energy gap and level broadening in Eqn. 4.5 gives an experimental measurement for the intrinsic gap from our sample of $\Delta^i = \Delta^{exp} + \Gamma \cong 500$ mK. Including LL broadening in our gap measurement therefore still remains well below the theoretical gap ($\sim$2 K) even if theory is corrected for finite width and LL mixing effects ($\sim$1.5 K) [21–23].

We compared our result against all other $\frac{5}{2}$ gap measurements found in the literature. While in our experiment we measured the LL broadening from the SdH oscillations, most
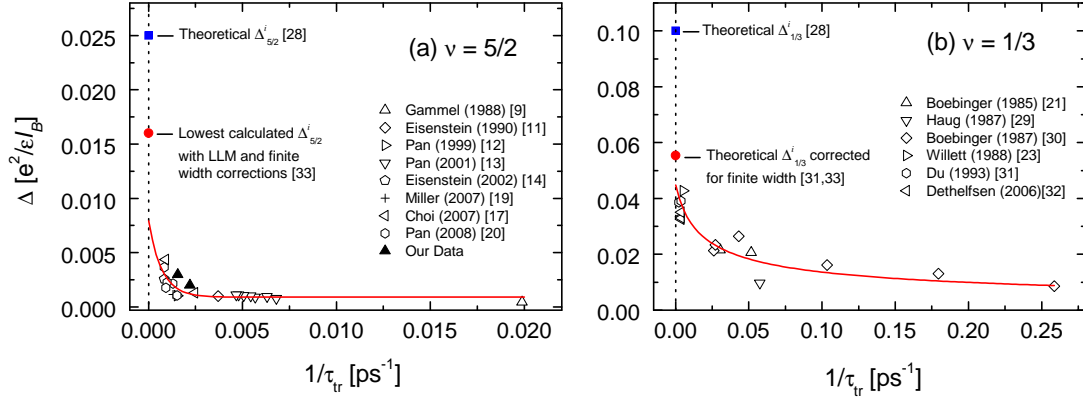
Figure 4–11: (a) Comparison of the measured $\nu = \frac{5}{2}$ gap energy with values found in literature (open symbols). Solid triangles represent our data (the two data points result from two different mobilities measured on separate cooldowns). Solid square is the theoretically calculated intrinsic gap energy [21, 22] and the solid circle includes corrections for Landau level mixing, and finite width. Solid curve is a guide to the eye. (b) Same plot as in (a), but for $\nu = \frac{1}{3}$ energy gap values reported in the literature. The horizontal scales are very different between the two plots reflecting that the $\frac{5}{2}$ gap is very small ($\sim$ hundreds of mK) and so can only be observed in very high mobility (low disorder) samples. By contrast the $\frac{1}{3}$ gap is very strong ($\sim$1.5 mK) and thus observable in much lower mobility samples.

other studies did not make this measurement but instead indicated the disorder in their samples by reporting the sample mobility. The mobility does not give a direct measure of the LL broadening, however this quantity does allow us to make qualitative comparisons of relative disorder. In Fig. 4–11a, we show a plot of all the $\frac{5}{2}$ gap values (in Coulomb energy units) from literature versus the inverse transport lifetime, $\tau_{tr}^{-1}$ [3, 4, 7–9, 13–15]. The transport lifetime was deduced from the reported mobilities according to Eqn. 3.9 such that in the figure $\tau_{tr}^{-1} = 0$ corresponds to the infinite mobility (*i.e.* zero disorder) limit. In spite of the large spread in the $\frac{5}{2}$ data, owing to wide ranging differences in sample parameters, *i.e.* dopant, well width, etc., a clearly discernible trend (indicated by the solid curve as a guide-to-the eye) is observed pointing towards a disorder-free intrinsic gap value in the range of $\Delta_{\frac{5}{2}}^{i} \sim 0.005\text{-}0.010$ e$^2/\epsilon l_B$. It is important to note that the solid line "fit" in the figure is merely meant as a guide-to-the-eye and that the actual functional form has no obvious physical interpretation other than indicating the measured gap increases as the disorder is reduced (as expected from (4.5)). The range quoted for the extrapolated intrinsic gap value comes from attempting to fit several different functions which all gave values of the same order. The intrinsic gap estimated by our extrapolation from an ensemble of $\frac{5}{2}$ measurements to the zero-disorder limit (0.006-0.010 e$^2/\epsilon l_B$), is in good agreement with the intrinsic gap deduced for our sample from the measured LL
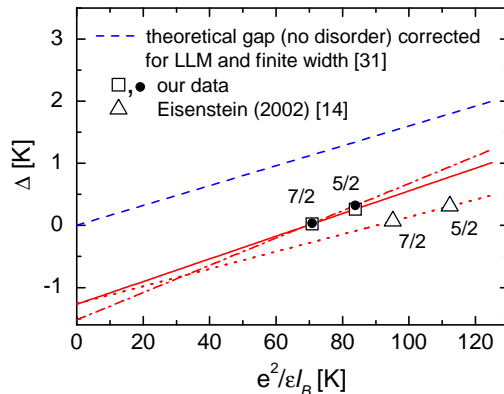
Figure 4–12: Intrinsic gap energy at $\nu = \frac{5}{2}$ from particle-hole paired states [23] (see text). Dashed line indicates a theoretical gap with no disorder. Open squares and solid circles are the gaps for the $\frac{7}{2}$ and $\frac{5}{2}$ FQH states from our sample but measured on two separate cooldowns. Open triangles are data taken from Ref. [9], for comparison. Solid, dash-dot, and dotted red lines are linear fits to the data.

broadening ($\sim$0.005 e$^2$/$\epsilon l_B$ in Coulomb energy units). Furthermore, these two results are also in good agreement with a similar extrapolation ($\sim$0.006 e$^2$/$\epsilon l_B$) reported very recently by Pan *et al.* [15]. However, while the experimentally measured intrinsic gap values at $\nu = \frac{5}{2}$ obtained by these two methods are in agreement with each other, they remain well below, by a factor of three to five, the theoretical intrinsic gap ($0.016 - 0.025$ e$^2$/$\epsilon l_B$) [21–23]. A similar plot of experimentally measured gap values versus sample mobility is shown for the well understood $\nu = \frac{1}{3}$ Laughlin state in Fig. 4–11b [16, 24–28]. Performing the same extrapolation as above gives the $\frac{1}{3}$ energy gap determined with this procedure to be $\Delta^i_{1/3} \sim 0.045$ e$^2$/$\epsilon l_B$, which is in good agreement with theory ($\sim 0.055$ e$^2$/$\epsilon l_B$) [21, 27]. We take this as further validation of our extrapolation procedure. Moreover, this excellent agreement between theory and experiment at $\frac{1}{3}$ compared with the large disagreement at $\frac{5}{2}$ points toward a discrepancy in our theoretical understanding of the $\frac{5}{2}$ FQH state.

$\qquad$Morf *et al.* proposed [23] that the level broadening, $\Gamma$, is filling fraction dependent, so that the experimentally measured gap is better described by

$$\Delta^{exp}(\nu) = \Delta^i(\nu) - \Gamma(\nu) \tag{4.6}$$

where $\nu$ is the fractional filling and $\Delta^i(\nu) = \delta(\nu)E_c$ is the intrinsic gap with $\delta(\nu)$ termed the intrinsic gap parameter, and $E_c$ the Coulomb energy. However, according to Morf both $\delta(\nu)$ and $\Gamma(\nu)$ are expected to be approximately equal for FQH states corresponding to particle-hole conjugate pairs. Morf therefore suggested that plotting the experimental gaps

for conjugate pairs as a function of their corresponding Coulomb energy ($E_c = e^2/\epsilon l_B$), gives a linear relationship where the slope, $\delta(\nu)$, provides a direct measure of the intrinsic gap, and the intercept gives the level broadening. Fig. 4–12 shows the $\frac{5}{2}$ and $\frac{7}{2}$ gap values obtained in our low electron density sample (open squares and solid circles) together with those from Ref. [9] (open triangles) which Morf used to apply his theory. The open squares are from the data shown in Fig. 4–8 where at $\nu = \frac{7}{2}$ a 'quasi-gap' measurement was performed. The solid circles were acquired from a separate cooldown where the $\frac{5}{2}$ and $\frac{7}{2}$ states were slightly better formed allowing a "true" gap measure for both states. The dashed line shows the predicted trend for a disorder free gap but corrected for finite width and LL mixing effects. The slope extracted from a linear fit gives the intrinsic gap for our sample to be $\sim$0.018 e$^2/\epsilon l_B$ and $\sim$0.021 e$^2/\epsilon l_B$ from the two data sets, which is in reasonable agreement with the data from ref. [9] ($\sim$0.014) and also in agreement with the theoretical value corrected for finite width and LL mixing ($\sim$0.016) [23]. This however disagrees with the intrinsic gap determined experimentally both from our sample, and from the extrapolation towards the infinite mobility limit. Furthermore, the Landau Level broadening deduced from Fig. 4–12 implies a rather large value for our sample ($\sim$1.25-1.5 K) that is an order of magnitude larger than determined experimentally from the SdH oscillations ($\sim$0.23 K). Finally, the model proposed by Morf *et al.* presumes the $\frac{5}{2}$ gap scales with the Coulomb energy, which we find may not be true.

Deducing the intrinsic gap by comparing the gap energies measured at $\frac{5}{2}$ and $\frac{7}{2}$ (as proposed by Morf *et al.*) gives good agreement with theory, but in our sample significantly overestimates, by an order of magnitude, the disorder induced LL broadening we actually measured. On the other hand, using our measured LL broadening and activation energy gap (in Eqn. 4.5) gives an intrinsic gap value that, while in poor agreement with theory, is in excellent agreement with the intrinsic gap deduced by extrapolating all measurements found in literature to the zero disorder limit. As of today, it remains unclear how to reconcile this discrepancy between experiment and theory.

While there is substantial theoretical evidence in support of a spin-polarized $\nu = \frac{5}{2}$ state described by the Moore-Read Pfaffian wavefunction, we emphasize that experimental support for the theory is still lacking. Furthermore, questions remain concerning the finite width and LL mixing corrections at $\frac{5}{2}$. For example, finite width corrections, assumed to result from a softening of the Coulomb interaction as the 2DEG width increases away from zero [21,23], gives very good agreement between theory and experiment for the $\nu = \frac{1}{3}$ Laughlin state [21,26,27]. Recent theoretical work by Peterson *et al* [29,30] however showed that a non-zero thickness of the 2DEG actually stabilizes (*i.e.* strengthens) the $\frac{5}{2}$ state in

81

contrast to the $\frac{1}{3}$ Laughlin state where increasing the finite thickness destroys the state [21]. Applying finite width corrections to the $\frac{5}{2}$ state by using the same approach that has been successful in studying Laughlin states ($\nu = \frac{1}{3}$) might therefore need to be reconsidered. Additionally, LL mixing has so far been treated approximately, as a perturbation to the main theory. Up to now the $\frac{5}{2}$ state has been studied at sufficiently high fields that the LL mixing has been considered moderate [31, 32], and so treating Landau level mixing perturbatively may have been justified. By contrast, in our sample we measure the $\frac{5}{2}$ gap in a low field region (2.63 T) where the LL mixing is expected to be strong since the cyclotron energy is smaller than the Coulomb energy at this field by nearly a factor of 2. Furthermore, recent theoretical work by Wojs and Quinn [33] has suggested LL mixing more severely affects the $\frac{5}{2}$ state than, for example, the Laughlin states in the lowest LL. They argue that Landau level mixing may have a larger effect on the $\frac{5}{2}$ than previously thought, which might account for the existing discrepancy between theory and experiment [33]. Again however, attempts to accurately quantify the effect have been limited. To fully understand the influence of Landau level mixing on the $\frac{5}{2}$ state, it may be necessary to include non-perturbative LL mixing in the theory, which so far has not been possible.

Including the effects of disorder into theory has also been problematic. In the simplest approximations, it is usually assumed that disorder affects all integer and fractional quantum hall states equally. However, this may not be true, perhaps especially for the $\nu = \frac{5}{2}$ state which is particularly unique because it is believed to be a *paired* state. In addition to broadening the quantized energy levels, disorder may also adversely affect the pairing mechanism. Importantly, so far no microscopic theory currently exists that is able to quantitatively include the effects to disorder into the theory [23]. Clearly more theoretical work is necessary to resolve these issues.

## 4.6   Energetics of our low density 5/2 FQH state

Finally, we summarize the energetics of our low-density $\frac{5}{2}$ FQH state. At the observed field of 2.63 T the cyclotron energy is 52 K, the Coulomb interaction ($e^2/\epsilon l_B$) energy is 81 K, and the Zeeman energy (assuming the GaAs band g-factor) is 0.75 K. The level broadening in our sample was measured to be ∼0.23 K and the mobility broadening ∼0.006 K (the large difference between the mobility and level broadening arises from the modulation doping which forces much of the scattering to be forward scattering [34, 35]). Also important is the suppression of the ideal two-dimensional FQH excitation gap due to the finite width $d = 40$ nm of our quasi-2D square well sample. For our $\frac{5}{2}$ FQH gap, this is only about 15%

(using our sample parameters in [21]). Taking all of these energies into account we conclude: *i)* our measured gap value of 0.262 K is a factor of 3-5 lower than the ideal 2D theoretical $\frac{5}{2}$ excitation gap ($\sim$2 K at 2.6 T), even if corrected in the usual way for finite width and level broadening suppression ($\sim$1.5 K); *ii)* the cyclotron gap, *i.e.* the Landau level separation, is smaller than the interaction energy in our system, suggesting considerable non-perturbative inter-Landau level coupling, which has not so far been included in the theory and may be important in understanding the $\frac{5}{2}$ FQH state; *iii)* the Zeeman energy at 2.6 T is extremely small compared to the Coulomb energy. The observation of such a strong $\frac{5}{2}$ gap in this low field (small Zeeman) regime might suggest that the $\frac{5}{2}$ FQHE is spin-unpolarized. However, in this scenario we would expect the state to be destroyed at larger fields where the Zeeman interaction becomes much stronger forcing a spin polarized state. By contrast, the $\frac{5}{2}$ FQHE has been observed in magentic fields as large as 12 T [8], where the system would most likely be spin-polarized, without much affecting the gap. Therefore, unless a quantum phase transition occurs between a low-field spin-unpolarized state and a high field spin-polarized state, our low density, low field experiment, when considered in the context of existing $\frac{5}{2}$ measurements rather points towards a spin-polarized state at $\nu = \frac{5}{2}$. Our strong gap measured in the low-field (small Zeeman energy) regime further suggests the $\frac{5}{2}$ state is spin-polarized even in the zero-field limit, consistent with the Moore-Read Pfaffian wave function.

## 4.7   Summary

The $\frac{5}{2}$ energy gap was measured for a sample with an electron density nearly two times smaller than previously observed, and was found to be comparable to samples with higher densities, and similar mobilities (disorder). Extrapolating the experimentally measured energy gap values at $\nu = \frac{5}{2}$ to the zero disorder limit yields an estimate for the intrinsic gap which remains well below the theoretical value. By contrast, a similar extrapolation for the $\frac{1}{3}$ Laughlin state is in much better agreement with theory. Our study suggests that the large discrepancies observed between theory and experiment at $\nu = \frac{5}{2}$ cannot simply be attributed to disorder, but rather may indicate that our knowledge of electron-electron interactions for the $\nu = \frac{5}{2}$ FQH state remains incomplete. Based on the fact that the Coulomb interaction energy scale for our low density $\frac{5}{2}$ FQH state is larger than the cyclotron energy, we speculate that the non-perturbative aspects of Landau level mixing (as well as disorder), not considered in the theoretical literature, may play an important role in the understanding of the enigmatic $\frac{5}{2}$ FQH state.

# References

[1] Willett, R. L., Eisenstein, J. P., Stormer, H. L., Tsui, D. C., Gossard, A. C., and English, J. H. *Phys. Rev. Lett.* **59**, 1776 (1987).

[2] Eisenstein, J. P., Willett, R., Stormer, H. L., Tsui, D. C., Gossard, A. C., and English, J. H. *Phys. Rev. Lett.* **61**, 997 (1988).

[3] Gammel, P. L., Bishop, D. J., Eisenstein, J. P., English, J. H., Gossard, A. C., Ruel, R., and Stormer, H. L. *Phys. Rev. B* **38**, 10128 (1988).

[4] Eisenstein, J. P., Willet, R. L., STormer, H. L., Pfeiffer, L. N., and West, K. W. *Surf. Sci.* **229**, 31 (1990).

[5] Sajoto, T., Suen, Y. W., Engel, L. W., Santos, M. B., and Shayegan, M. *Phys. Rev. B* **41**, 8449 (1990).

[6] Pan, W., Du, R. R., Stormer, H. L., Tsui, D. C., Pfeiffer, L. N., Baldwin, K. W., and West, K. W. *Phys. Rev. Lett.* **83**, 820 (1999).

[7] Pan, W., Xia, J. S., Shvarts, V., Adams, D. E., Stormer, H. L., Tsui, D. C., Pfeiffer, L. N., Baldwin, K. W., and West, K. W. *Phys. Rev. Lett.* **83**, 3530 (1999).

[8] Pan, W., Stormer, H. L., Tsui, D. C., Pfeiffer, L. N., Baldwin, K. W., and West, K. W. *Sol. Stat. Comm.* **119**, 641 (2001).

[9] Eisenstein, J. P., Cooper, K. B., Pfeiffer, L. N., and West, K. W. *Phys. Rev. Lett.* **88**, 076801 (2002).

[10] Xia, J. S., Pan, W., Vicente, C. L., Adams, E. D., Sullivan, N. S., Stormer, H. L., Tsui, D. C., Pfeiffer, L. N., Baldwin, K. W., and West, K. W. *Phys. Rev. Lett.* **93**, 176809 (2004).

[11] Csathy, G. A., Xia, J. S., Vicente, C. L., Adams, E. D., Sullivan, N. S., Stormer, H. L., Tsui, D. C., Pfeiffer, L. N., and West, K. W. *Phys. Rev. Lett.* **94**, 146801 (2005).

[12] Willett, R. L., Manfra, M. J., Pfeiffer, L. N., and West, K. W. *Appl. Phys. Lett.* **91**, 052105 (2007).

[13] Miller, J. B., Radu, I. P., Zumbuhl, D. M., Levenson-Falk, E. M., Kastner, M. A., Marcus, C. M., Pfeiffer, L. N., and West, K. W. *Nature* **3**, 561 (2007).

[14] Choi, H. C., Kang, W., Das Sarma, S., Pfeiffer, L. N., and West, K. W. *Phys. Rev. B* **77**, 081301 (2008).

[15] Pan, W., Xia, J. S., Stormer, H. L., Tsui, D. C., Vicente, C., Adams, E. D., Sullivan, N. S., Pfeiffer, L. N., Baldwin, K. W., and West, K. W. *Phys. Rev. B* **77**, 075307 (2008).

[16] Boebinger, G. S., Change, A. M., Stormer, H. L., and Tsui, D. C. *Phys. Rev. Lett.* **55**, 1606 (1985).

[17] Usher, A., Nicholas, R. J., Harris, J. J., and Foxon, C. T. *Phys. Rev. B* **41**, 1129 (1990).

[18] Bonderson, P. and Slingerland, J. K. *arXiv:0711.3204v1* (2007).

[19] Simion, G. J. and Quinn, J. J. *arXiv:0712.1222v1* (2007).

[20] Very recently R. R. Du (unpublished) has studied a 10M mobility sample with a density of 6.2, where the 5/2 gap was measured at 9 T to be only ∼160 mK. This is further evidence that the gap does not scale with B field as expected.

[21] Morf, R. H., d'Ambrumenil, N., and Das Sarma, S. *Phys. Rev. B* **66**, 075408 (2002).

[22] Feiguin, A. E., Rezayi, E., Nayak, C., and Das Sarma, S. *Phys. Rev. Lett* **100**, 166803 (2008).

[23] Morf, R. and d'Ambrumenil, N. *Phys. Rev. B* **68**, 113309 (2003).

[24] Haug, R. J., v. Klitzing, K., Nicholas, R. J., Maan, J. C., and Weimann, G. *Phys. Rev. B* **36**, 4528 (1987).

[25] Boebinger, G. S., Stormer, H. L., Tsui, D. C., Chang, A. M., Hwang, J. C., Cho, A. Y., Tu, C. W., and Weimann, G. *Phys. Rev. B* **36**, 7919 (1987).

[26] Willett, R. L., Stormer, H. L., Tsui, D. C., Gossard, A. C., and English, J. H. *Phys. Rev. B* **37**, 8476 (1988).

[27] Du, R. R., Stormer, H. L., Tsui, D. C., Pfeiffer, L. N., and West, K. W. *Phys. Rev. Lett.* **70**, 2944 (1993).

[28] Dethlefsen, A. F., Mariani, E., Tranitz, H. P., Wegscheider, W., and Haug, R. J. *Phys. Rev. B* **74**, 165325 (2006).

[29] Peterson et al. *arXiv:0801.4819v1* (2008).

[30] Peterson, M. R., Jolicoeur, T., and Das Sarma, S. *Phys. Rev. Lett.* **101**, 016807 (2008).

[31] Levin, M., Halperin, B. I., and Rosenow, B. *Phys. Rev. Lett.* **99**, 236806 (2007).

[32] Lee, S.-S., Ryu, S., Nayak, C., and Fisher, M. P. A. *Phys. Rev. Lett.* **99**, 236807 (2007).

[33] Wojs, A. and Quinn, J. J. *Phys. Rev. B* **74**, 235319 (2006).

[34] Das Sarma, S. and Stern, F. *Phys. Rev. B* **32**(12), 8442 (1985).

[35] Harrang, J. P., Higgins, R. J., Goodall, R. K., Jay, P. R., Laviron, M., and Delescluse, P. *Phys. Rev. B* **32**(12), 8126 (1985).

# Contrasting Behaviour of the 5/2 and 7/3 Fractional Quantum Hall Effect in a Tilted Field

$S$upport for the Moore-Read description [1] of the even denominator $\nu = \frac{5}{2}$ FQHE continues to be mostly theoretical [2–9] with unequivocal experimental proof still lacking. Very recent observation of the $e^* = e/4$ quasi-particle charge [10, 11] is an important measurement in this regard since it indicates the formation of a paired electron state and therefore is fully consistent with the Moore-Read Pfaffian pairing wavefunction (or equivalently its particle-hole conjugate, the so-called antiPfaffian [12, 13]). However, these measurements do not, on their own, validate the Moore-Read theory, in part due to other possible candidate paired-states, such as the (abelian) Halperin 331 state [14], which could in principle also be realized at $\nu = \frac{5}{2}$.

A key feature of the Moore-Read Pfaffian that distinguishes it from other proposed wavefunctions is its fully spin-polarized electron polarization [2,5,7], and consequently the non-zero angular momentum of its $p_x + \imath p_y$ pairing, very similar to the $A_1$-phase of superfluid $^3$He. In the following chapter we therefore investigate the $\frac{5}{2}$ spin polarization, by measuring the activation energy gap of the $\frac{5}{2}$ (and particle-hole conjugate $\frac{7}{2}$) and neighbouring $\frac{7}{3}$ state in a tilted field geometry where, in addition to the perpendicular field ($B_\perp$), a parallel field ($B_{//}$) is applied in the plane of the 2DEG. Two important aspects distinguish our work from previous tilted field experiments in the second Landau level (SLL) [15–19]. First, we examine a strong $\frac{5}{2}$-state occurring at lower magnetic field than previously observed, owing to our low density sample [20]. Secondly, we study the FQH energy gap in a sample with a relatively wide 2D quantum well so that under tilt the magnetic length associated with $B_{//}$ becomes of order or smaller than the well width, allowing us to study the effect
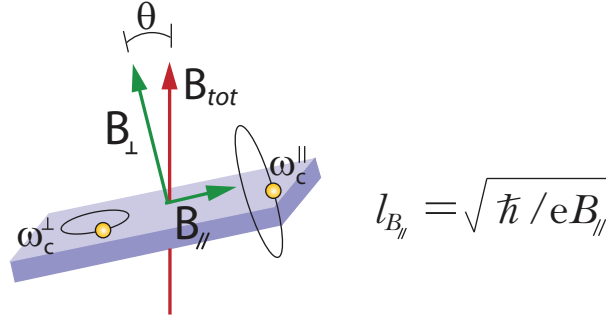
Figure 5–1: Rotating the 2DEG in a fixed field allows us to vary the Zeeman energy (depends on $B_{tot}$) while keeping the Coulomb energy (depends on $B_\perp$ only) constant. At sufficiently large parallel fields, the parallel magnetic length, $l_{B_{//}}$, can become smaller than the size of the well width.

of orbital coupling to the parallel field. Comparing the even-denominator $\frac{5}{2}$ with the odd-denominator $\frac{7}{3}$, we find that the in-plane magnetic field induces dramatically, and qualitatively, different behaviour in the two activation gaps. This is a particularly surprising result since current theoretical models that interpret the decreasing $\frac{5}{2}$ gap under tilt in the context of orbital coupling to the parallel field, suggest the same gap suppression should be seen in the neighbouring $\frac{7}{3}$ state [2,8]. The unexpected experimental finding presented here, in direct contradiction to theory, implies that our understanding of the FQHE in the second landau level is incomplete

## 5.1 Experimental details

The following data was acquired from our low density GaAs/AlGaAs quantum well sample, with a measured density of $1.60(1) \times 10^{11}$ cm$^{-2}$ and mobility of $16.6(8) \times 10^6$ cm$^2$/Vs. Treatment with a red LED was used during the cooldown. The tilted field geometry was achieved by rotating the sample *in situ* in a static field (*see* sction 3.2.5 for details concerning the sample rotator). All transport measurements were performed using a standard lock-in technique at ∼6.5 Hz and small excitation current, $I_{exc}$ = 2 - 10 nA. All data was taken within the same cooldown, however, we present two data sets corresponding to slightly different sample conditions resulting from a complete power shut down in the lab, where the sample was temporarily warmed to ∼4 K. After the power shutdown we observed a slight decrease in the sample density and "quality", indicated by smaller measured activation gaps at $\nu = \frac{5}{2}$ and $\nu = \frac{7}{3}$ and a less developed minimum in R$_{xx}$ at $\nu = \frac{7}{2}$.

## 5.2   Tilted Field Geometry

Rotating the sample in a fixed field causes a change in the electron Zeeman energy, since the Zeeman energy depends on the total applied field

$$E_Z = \mu_B g^* \mathbf{B} \cdot \mathbf{S} \tag{5.1}$$

where $\mathbf{B}$ is the total magnetic field vector, and $\mathbf{S}$ is the electron spin. However, the Coulomb energy remains unchanged (at a specified filling factor) under tilt, since it depends only on the perpendicular component of the magnetic field

$$E_C = \frac{e^2}{\epsilon l_B} \tag{5.2}$$

where $l_B = \sqrt{\hbar/\epsilon B_\perp}$ is the magnetic length, $B_\perp$ is the perpendicular magnetic field, and $\epsilon$ is the dielectric constant.

In the simplest approximation, the activation energy gap can be written as [21]

$$\Delta = \Delta_o - \mu_B \, |g| \, \mathrm{B}_{tot} \Delta S \tag{5.3}$$

where $\Delta_o$ includes all contributions to the energy gap that depend only on the perpendicular component of the magnetic field, such as the Coulomb energy, and therefore does not vary for a given quantum Hall state as the sample is rotated [22]. The second term in the above equation is the Zeeman energy, written to emphasize that the g-factor in GaAs is negative (g=-0.44 for bulk GaAs), where $\mu_B = 0.67$ K/T is the Bohr magneton, $B_{tot} = \sqrt{(B_\perp)^2 + (B_{//})^2}$ is the total applied magnetic field and $\Delta S$ is the change in spin resulting from excitation of quasielectron-quasihole pairs. If we assume the only effect of adding an in-plane magnetic field is to alter the Zeeman energy,[1]   then measuring the activation energy gap under rotation (*i.e.* varying the ratio of Zeeman to Coulomb energy) can be used to probe the spin nature of a QHE state.

In Fig. 5–2 we consider three scenarios. i) *Ground state and excited states are fully spin polarized*: If electrons are excited from a fully spin polarized ground state to a fully spin-polarized excited state then $\Delta S = 0$ so that as we vary the size of the parallel field (tilt the sample) we expect to see no change in the Zeeman energy and therefore no change

---

[1] This is only strictly valid for the ideal 2D case where the 2DEG has zero thickness in the transverse direction.

(a) spin polarized ground state          (b) spin unpolarized ground state
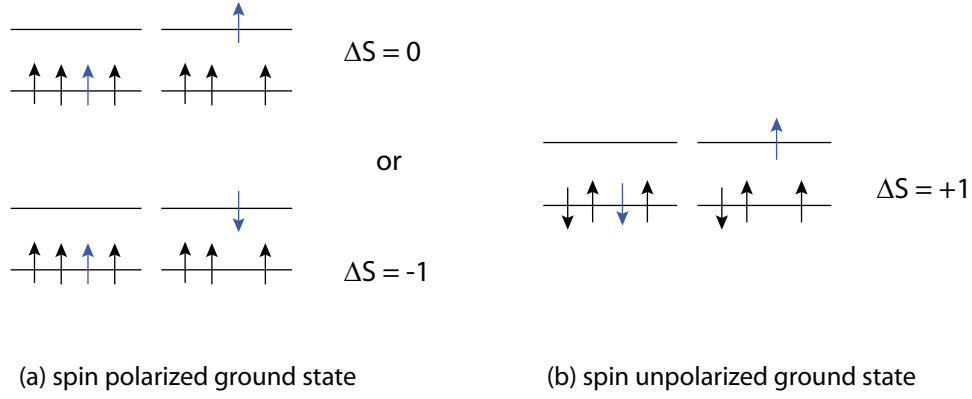
Figure 5–2: Spin excitations from a spin polarized (a) and spin unpolarized (b) ground state.

in the activation energy gap. ii) *Ground state is spin polarized and excited state is spin unpolarized*: Excitations from a polarized ground state that involve single spin flips yields a net spin change of $\Delta S = -1$ with each excited electron, and since $g < 0$ this gives an increasing Zeeman energy as $B_{//}$ ($B_{tot}$) is increased, and thus we would expect to measure an *increasing* energy gap as we rotate the sample away from zero. iii) *Ground state is spin un-polarized*: An unpolarized ground state can be distinguished from the previous two scenarios if excitations involve a spin reversal giving $\Delta S = +1$. In this case, an overall negative increase in the Zeeman energy with increasing $B_{//}$ results and therefore we would expect to measure a *decreasing* energy gap as the sample is rotated. Note that in this analysis it is not possible to distinguish between a fully un-polarized and partially polarized ground state. Importantly however a fully polarized ground state can not yield a decreasing gap versus tilt, if the only affect of the parallel field is coupling to the electron spins through the Zeeman energy. Observation of a decreasing gap would therefore suggest the FQH state is not fully spin polarized.

## 5.3  Activation gaps under tilted fields

Eisenstein *et al.* first used the tilted field technique to study the $\frac{5}{2}$ FQH state shortly after its discovery [15, 16]. He found an approximately linear decay of the $\frac{5}{2}$ gap with increasing total B field whose slope gave the electron g-factor to be 0.56, in reasonable agreement with the excepted value of 0.44 for GaAs [16]. Initially this was interpreted as evidence that the $\frac{5}{2}$ ground state is spin unpolarized in accordance with the Zeeman interaction picture outlined above [16]. Subsequent theoretical work by Morf [2] however showed that a fully spin polarized wavefunction at $\nu = \frac{5}{2}$ has a lower ground state energy,

calling into question this interpretation. He further argued that the observed gap suppression under tilt [15, 16] could be understood in terms of coupling between the parallel field and orbital dynamics of the 2DEG in the perpendicular direction (possible due to its finite thickness), rather than simply resulting from Zeeman coupling to the electronic spins. Morf additionally predicted that such an interaction would eventually give rise to a charge density wave state [2, 23] (identified as the stripe phase in further numerical work by Rezayi and Haldane [4]) as the parallel field is increased, which was later verified in experiments on higher quality samples and utilizing larger tilt angles. [17, 18].

Morf's proposed explanation for the $\frac{5}{2}$ gap suppression due to magneto-orbital coupling to the parallel field results from a corresponding modification of the short range many-body electron interaction potential. In this scenario, he further argued a similar suppression would be expected for the neighbouring $\frac{7}{3}$ state [2]. Rezayi and Haldane subsequently showed [4] by numerics that a modification of the short range interaction potential could be driven by a variation of the 2DEG thickness. More recently, Peterson and Das Sarma [8, 9] reported in a detailed numerical study that both the $\frac{5}{2}$ and $\frac{7}{3}$ states are strengthened by thickening the 2DEG [8]. In agreement with Morf [2] and Rezayi and Haldane [4], they therefore concluded that orbital coupling to a parallel field, whose effects include squeezing the wavefunction towards the ideal 2D limit, is likely responsible for the $\frac{5}{2}$ destruction under tilt, and furthermore is expected to similarly destroy the $\frac{7}{3}$ state. In all of these studies a Pfaffian was used for the $\frac{5}{2}$ wavefunction whereas a Laughlin wavefunction was taken for the $\frac{7}{3}$. The theoretical predictions therefore follow despite the two states being described by radically different ground states. Taken together, all of this theoretical work indicates that if indeed magneto-orbital coupling to the parallel field is responsible for the observed destruction of the $\frac{5}{2}$ gap under tilt rather than Zeeman interaction, the same effect should be manifest in the neighbouring $\frac{7}{3}$ state, which is widely expected to also be spin polarized. Importantly, no systematic experimental study has examined these predictions [15–19]. Where qualitative observations have been made concerning the $\frac{7}{3}$, they appear inconsistent with, for example, the state reported to strengthen [15], weaken [2, 16], and/or 'stay robust' [19] under tilt.

Fig. 5–3 shows the magnetoresistance in the SLL at various tilt angles, $\theta$, measured on our low density sample. The behaviour of the $\frac{5}{2}$ minima as a function of tilt (*i.e.* increasing $B_{//}$) is dramatically different from the neighbouring, odd-denominator, $\frac{7}{3}$ and $\frac{8}{3}$ states. As emphasized in the inset of Fig. 5–3a, the $\frac{5}{2}$ minimum clearly diminishes while the $\frac{7}{3}$ and $\frac{8}{3}$ strengthen under tilt.
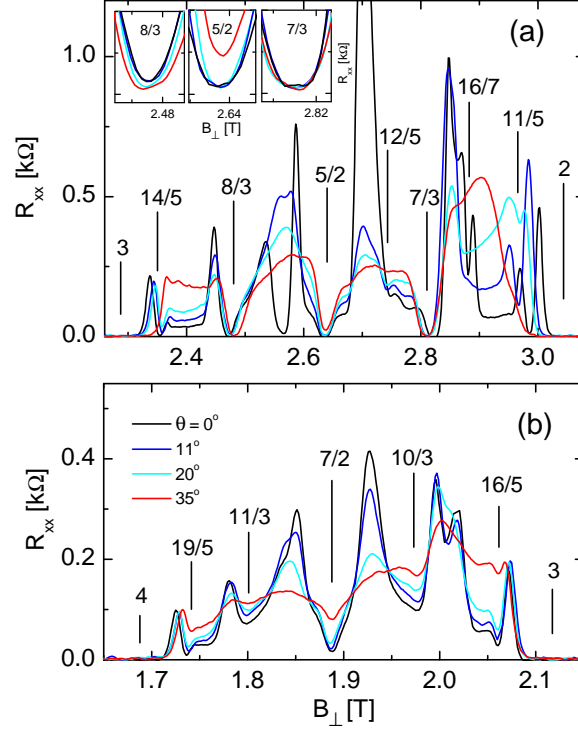
Figure 5–3: Magnetoresistance under tilt in the second Landau level around (a) $\nu = \frac{5}{2}$ and (b) $\nu = \frac{7}{2}$ plotted versus perpendicular field (T=19 mK). Inset: enlargement showing the trend of the $\nu = \frac{8}{3}, \frac{5}{2}$, and $\frac{7}{3}$ FQHE minima versus tilt.

The qualitatively opposite trends between the $\frac{5}{2}$ and $\frac{7}{3}$ seen here is in stark contradiction to theory which predicts the two states should behave the same. We therefore performed a detailed comparative study of the two states by measuring the corresponding activation gap energies versus applied parallel field (tilt angle). The aim of this study was both to attempt to probe the spin nature of the $\frac{5}{2}$ FQH state, and also to fully investigate the mechanism causing destruction of the $\frac{5}{2}$ state under tilt.

## 5.4 Decreasing 5/2 gap under tilt

Fig. 5–4 shows the activation energy gap as a function of tilt angle for both the $\frac{5}{2}$ and $\frac{7}{2}$ FQH states. The energy gap, $\Delta$, was determined from the temperature dependence of the FQHE resistance minima in the thermally activated regime where $R_{xx} \propto e^{-\Delta/2k_B T}$. Example activation curves are shown in the left panel for several tilt angles, with the corresponding energy gap plotted versus total $B$ field shown in the right panels in Fig. 5–4. Improved sample conditions resulting from thermal cycling allowed us to perform a standard measurement of the $\frac{7}{2}$ gap rather than the quasi-gap reported in the previous

Figure 5–4: (a)Ahhrenius plot showing activated behaviour at $\nu = \frac{5}{2}$ for various tilt angles. (b) Activation gaps measured from (a) plotted versus total magnetic field. (c),(d) same plots as in (a),(b) but measured at $\nu = \frac{7}{2}$. In (b) two data sets are shown corresponding to measurements performed on the same sample but with the open symbols corresponding to a slightly smaller density and mobility than the solid symbols resulting from a change in the sample condition (see text). Dotted lines in (b) and (d) are linear fits used to estimate a value for the g-factor (see text). Solid curves in (b) are a guide to the eye. Open symbol in (d) was taken from an already destroyed gap.

chapter. Consistent with the qualitative trend seen in Fig. 5–3, the gap measured at $\frac{5}{2}$ and $\frac{7}{2}$ both diminish rapidly with tilt (Fig. 5–4b and 5–4d respectively).

Varying the measurement configuration in our sample did not show any evidence of anisotropy at $\nu = \frac{5}{2}$ up to the highest tilt angle investigated ($\theta = 44^o$). In Fig. 5–5 we show the magnetoresistance in the SLL around $\nu = \frac{5}{2}$ taken at a tilt angle of $44^o$. As seen in the figure there appears no discernible difference in the $\frac{5}{2}$ minimum between measurements obtained by sourcing the current along three different directions; the small variation in $R_{xx}$ at the $\frac{5}{2}$ minimum is similar to that measured at zero tilt. This is in contrast to Refs. [17, 18] where under tilt a large maximum appeared in the magnetoresistance at $\frac{5}{2}$ when sourcing current parallel to the direction of the in plane field. The lack of anisotropy

92
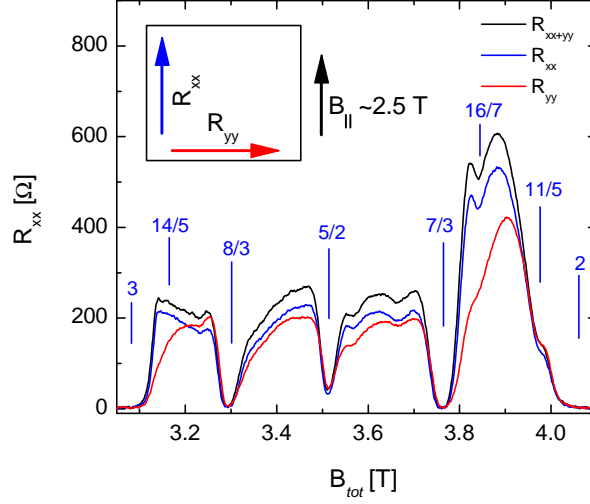
Figure 5–5: Magnetoresistance in the SLL around $\nu = \frac{5}{2}$ at $\theta = 44^o$ measured along several directions. There is no evidence of the emergence of a stripe phase (ie resistance anisotropy) at $\nu = \frac{5}{2}$ at this tilt angle.

in our data might simply be due to the limited parallel field imposed in our study owing to our lower density (smaller perpendicular field) sample. Curiously, however, in Ref [18] the anisotropy is evident at quite small tilt angles, with a difference in $R_{xx}$ of a few hundred Ohms measured at a similar parallel field to that shown in Fig. 5–5 ($B_{//} \sim 2.5$ T), where we observe no anisotropy. Comparisons between different samples should be made cautiously due to the wide variety of other potentially important sample parameters such as disorder, well width, crystal defects etc. It thus appears necessary to examine our sample under much higher tilt, *i.e.* larger parallel field, in order to explore the possible transition to an anisotropic stripe phase more fully.

In a perfectly 2D system, *i.e.* with a vanishing quantum well width, applying an in-plane field by sample rotation should only couple to the electron spin through the Zeeman energy. As such, the most obvious interpretation of our observed weakening FQHE with tilt is that the $\frac{5}{2}$ (and $\frac{7}{2}$) state is spin-unpolarized. A spin-unpolarized $\frac{5}{2}$ state however would be in conflict with extensive theoretical evidence in favor of a fully spin-polarized state, most likely described by the Moore-Read Pfaffian wave function [2,5,7]. In a single-particle Zeeman picture, a reduction of the $\frac{5}{2}$ gap induced by spin coupling alone should furthermore yield a universal slope in a plot of activation gap versus $B_{tot}$, determined by the effective g-factor whose commonly accepted value in GaAs is $g^* = -0.44$. Extracting the g-factor from our $\frac{5}{2}$ and $\frac{7}{2}$ gaps, we obtain differing values of 0.47±0.06 and 0.31±0.03 respectively, compared with the value 0.56 reported in the work of Eisenstein *et al.* [16].
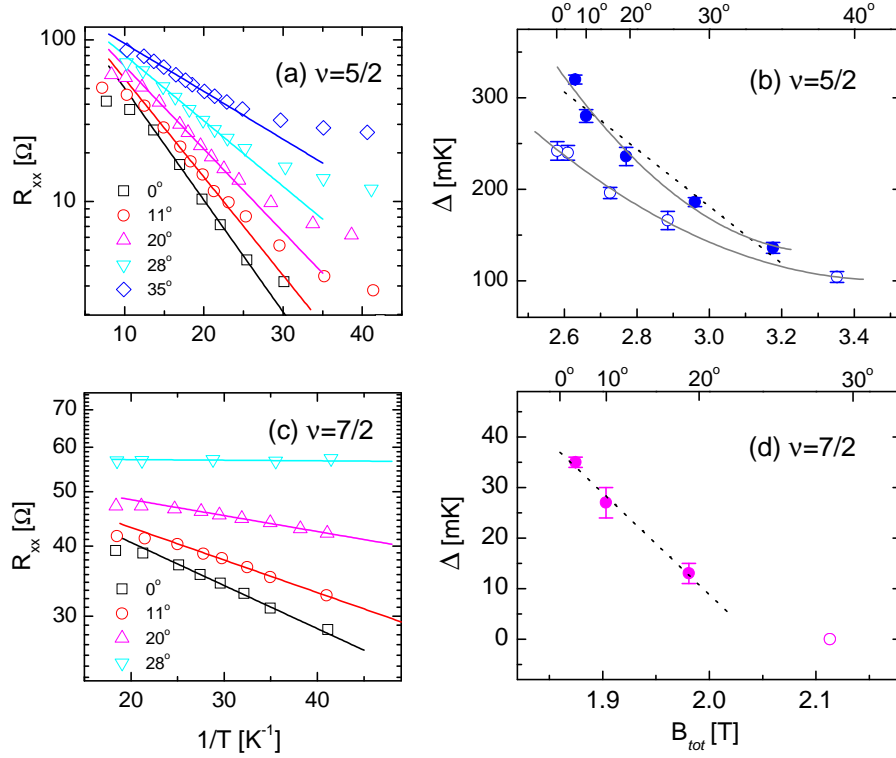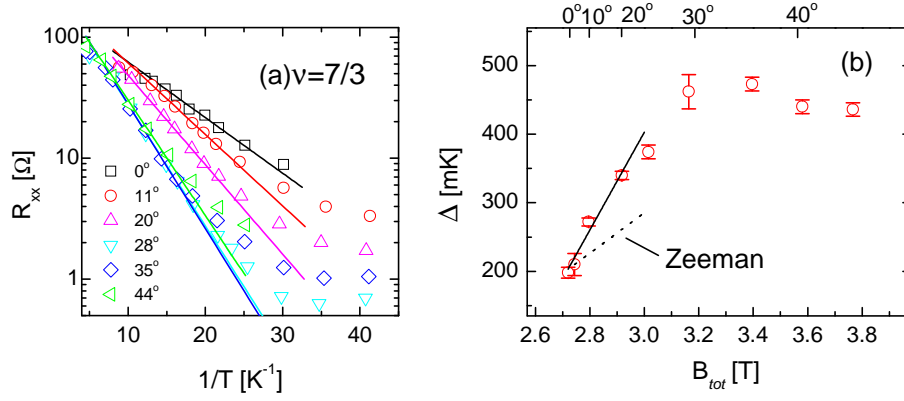
Figure 5–6: (a)Ahhrenius plot showing activated behaviour at $\nu = \frac{7}{3}$ for various tilt angles. (b) Activation gaps measured from (a) plotted versus total magnetic field. A fit to the lowest $B$-field data (solid line) is shown for comparison to the theoretical trend (dotted line) expected for a single particle Zeeman interaction (see text).

Additionally, closer inspection of the $\frac{5}{2}$ data (Fig. 5–4b) suggests a linear trend (dotted line) does not fit the data well over the entire range, but rather the data is non-linear (solid curve guide to the eye), raising further doubts about the spin-induced gap suppression in a spin-unpolarized FQHE interpretation. In our view, the non-linear behaviour in $B_{tot}$, together with the scattered g-factors, is indicative of a gap suppression not driven by Zeeman coupling, but rather by another mechanism. In a real 2DEG sample with finite thickness, orbital coupling between the in-plane field and the transverse electron dynamics becomes possible when the parallel field magnetic length becomes of order or less than the quantum well width. In this case, a spin-polarized $\frac{5}{2}$ state can also be suppressed with increasing $B_{//}$ [2,4,8] since the activation gap is no longer determined by Zeeman coupling alone. At $B_{//}$=1 T, the parallel magnetic length $l_{B_{//}}=\sqrt{\hbar/eB_{//}}$ is only 26 nm, already nearly half the width of our quantum well, making it plausible for magneto-orbital effects to play an important role in our experiment, even under modest tilting.

## 5.5 Increasing 7/3 gap under tilt

The parallel field magneto-orbital coupling that is believed to destroy the $\frac{5}{2}$ state under tilt is also expected to destabilize the $\frac{7}{3}$ state in a similar way [2, 4, 8]. In Fig. 5–6, the activation energy gap at $\nu = \frac{7}{3}$ is shown, measured at several different tilt angles. In stark contrast to the $\nu = \frac{5}{2}$ and $\frac{7}{2}$ states the $\frac{7}{3}$ state does not diminish with tilt as expected but instead shows a remarkable enhancement, producing a gap larger by more than a factor of two at only $\theta \sim 35°$. If we again consider the only effect of the parallel field to be coupling

to the electron spins through the Zeeman energy, an increasing gap under tilt suggests the $\frac{7}{3}$ ground state is spin polarized.

We note however that the gap increase in Fig. 5–6b is non-linear, with the low-tilt regime exhibiting a slope (solid line) of nearly $\sim 2.5$ times *larger* than expected by single-particle Zeeman coupling alone (dashed line). The growth of the $\frac{7}{3}$ gap at a greater rate than predicted by single-particle Zeeman interaction alone suggests a non-trivial excitation spectrum, perhaps involving a spin texture similar to the skyrmion excitations observed at $\nu = \frac{1}{3}$ in the lowest landau level [24,25]. The formation of skyrmions is characterized by the interplay between Zeeman and Coulomb energies, with skrymionic spin-reversal excitations existing only below some critical value of the ratio $\eta = \frac{E_Z}{E_C}$. In our sample $\eta \sim 0.01 - 0.013$ at $\nu = \frac{7}{3}$, well below the critical value of $\eta_c = 0.022$ at $\nu = 1$ [26] and similar to the value of $\eta_c = 0.01$ at nu=1/3 [24]. It is therefore possible that our observed $\frac{7}{3}$ behavior arises from the existence of small skyrmions involving two to three reversed spins.

## 5.6    Contrasting behaviour

In Fig. 5–7 the gap values from Figs. 5–4 and 5–6 are replotted versus the parallel field, $B_{//}$, and normalized to their zero-tilt values (the data is vertically offset for clarity). Whereas the $\frac{5}{2}$ gaps appear to vary non-linearly with changing total field, $B_{tot}$, (Fig. 5–4), they follow a remarkably linear trend versus $B_{//}$. We also note in the $\frac{5}{2}$ data (open and closed squares) a range in low $B_{//}$ distinct from the high $B_{//}$ where the gap is unmodified for tilt up to $\sim 10°$. Interestingly, a similar trend is also observed when replotting the data from reference [16] (closed circles). The onset of the gap suppression for the $\frac{5}{2}$ state occurs in all data set at a parallel field strength of $B_{//} \sim 0.5$ T, corresponding to a transverse magnetic length $l_{B_{//}}=36$ nm. This is remarkably close to the width of our quantum well and is therefore consistent with magneto-orbital coupling effects becoming relevant when the transverse magnetic length approaches the size of the quantum well. Importantly, a constant gap value is not observed in the $\frac{7}{3}$ data at low tilt. We take this as a further indication that the $\frac{5}{2}$ gap suppression and the $\frac{7}{3}$ gap enhancement originate from distinct mechanisms. We show in the inset of Fig. 5–7 our measured $\frac{5}{2}$ gap data versus $B_{//}$ against the theoretical trend expected for a Zeeman energy variation associated with a total spin change $\Delta S = -1, 0$ (dashed increasing, flat line), and $\Delta S = +1$ (decreasing dashed line), expected for a spin-polarized and spin-unpolarized ground state, respectively. While, within the resolution of our experiment, we cannot distinguish whether the low $B_{//}$ data better fits the trend for a spin-polarized or unpolarized ground state, the gap suppression of the $\frac{5}{2}$ state following a linear behaviour in $B_{//}$, and departing from the
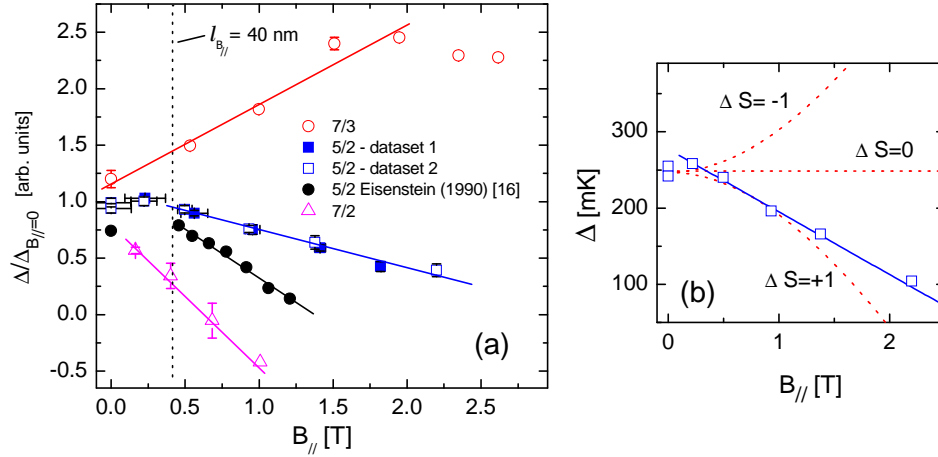
Figure 5–7: Normalized gap values under tilt versus parallel field (data is vertically offset for clarity). All data is replotted from Figs. 5–4 and 5–6 except the solid circles which are replotted from ref. [16]. (b) Experimental activation gap versus $B_{//}$ at $\nu = \frac{5}{2}$ (open squares) compared with the theoretical Zeeman interaction for single spin flips (dashed lines, see text).

$\Delta S = +1$ curve at field $B_{//} \gtrsim 1.5$T, is further evidence for a gap suppression driven by a mechanism other than Zeeman coupling.

We note that the actual effect of the in-plane field is quite complex as it not only reduces the effective well width through orbital dynamics [4, 8, 9], it also anisotropically enhances the 2D effective mass [9, 27], and increases the level broadening by inducing intersubband scattering through Landau level-subband coupling [28, 29] as the electron motion becomes effectively three-dimensional when the magnetic length associated with the parallel field becomes smaller than the well-width. A full theoretical treatment of the complex electron dynamics in the presence of a strong in-plane field is well beyond the scope of our experimental work. However, we note that all of these effects are expected to affect both the $\frac{5}{2}$ and $\frac{7}{3}$ in the same way, at least qualitatively, and so on their own cannot explain the opposite trends under tilt that we observe.

With the $\frac{5}{2}$ and $\frac{7}{3}$ states appearing so closely together in magnetic field, having nearly the same energetics and Landau level coupling when $B_{//}=0$, we speculate that the contrast in behaviour between the $\frac{5}{2}$ and $\frac{7}{3}$ states may require some fundamentally new theoretical insight. One possibility is that this difference arises, not from a ground state spin-polarization difference between these two states, but rather from a difference in the excited states. If we consider both the $\frac{5}{2}$ and $\frac{7}{3}$ states to be spin polarized, then the decreasing $\frac{5}{2}$ gap compared to the increasing $\frac{7}{3}$ gap could be explained by the $\frac{7}{3}$ trend resulting from a

96

combination of spin-reversed excitation (gap enhancement) and finite width (gap suppression) whereas the $\frac{5}{2}$ state does not experience spin reversal and so is suppressed purely as a result of magneto-orbital coupling. In this picture, the $\frac{7}{3}$ gap would presumably increase with increasing $B_{tot}$ but with a smaller slope than if spin effects alone were present. The saturation of the $\frac{7}{3}$ gaps at high tilt is evidence for a possible crossover taking place between a spin-dominated and orbitally-coupled regime. Another possibility is that if the $\frac{5}{2}$ FQH state truly emanates from a Moore-Read Pfaffian wavefunction with $p_x + \imath p_y$ pairing, it may experience non-trivial coupling to the in-plane field owing to the intrinsic angular momentum $l = 1$ of paired electrons. We view this scenario as plausible in analogy with that observed in other $p_x + \imath p_y$ systems such as the A-phase of superfluid $^3$He. A word of caution is, however, in order with the $^3$He analogy since it is the spin unpolarized (abelian) (3,3,1) strong-pairing state which is thought to be akin to the A-phase with the Pfaffian state being analogous to the $A_1$-phase. Considering the paired nature of the Moore-Read state it may also be possible, for reasons presently unknown, that disorder more strongly affects the $\frac{5}{2}$ than the (non-paired) Laughlin state, by specifically interfering with the fragile pairing mechanism. Our analysis is admittedly highly speculative, since from our experiment alone it is difficult to conclude with certainty why the two states behave oppositely under a titled field, owing in large part to limitations in existing theory that make it difficult to account for the many complex and interrelated interactions that occur when the quasi-2D electron gas couples to an in plane field. We therefore conclude that more experimental work, such as examining the tilted field behaviour in samples with a variety of well widths and densities, and at higher tilt angles, together with further numerical work will be required to fully address this behaviour.

We emphasize that the naive direct explanation of our data, namely that the $\frac{5}{2}$ ($\frac{7}{3}$) FQH state is spin-unpolarized (polarized) although believed to be unlikely for reasons discussed above, cannot be compellingly ruled out. Most importantly, the principal motivation [2] for accepting the spin-polarized description of the $\frac{5}{2}$ was based on an assumed universal similarity in the behaviour of the $\frac{5}{2}$ and $\frac{7}{3}$ states in a tilted field. Our experimental finding that the two states behave qualitatively differently fundamentally undermines this assumption and so in our view may necessitate a rethinking of the nature of the $\frac{5}{2}$ FQHE. In this context, it is interesting to mention that several recent theoretical papers [30–32] have indeed raised questions regarding the nature of the $\frac{5}{2}$ state, and if further investigations proved it to be non spin-polarized, it would unlikely be a Moore-Read non-Abelian Pfaffian state.

## 5.7    Summary

We performed the first ever simultaneous activation gap measurement of both the $\frac{5}{2}$ and neighbouring $\frac{7}{3}$ FQH states under tilt. We find completely opposite behaviour between the two states, with the $\frac{5}{2}$ found to weaken under tilt while the $\frac{7}{3}$ actually strengthened. This is in startling contradiction to theory, which predicts the two states should behave the same in the presence of an applied parallel field. Theoretical foundation for this prediction is based on i) the $\frac{5}{2}$ being described by the Moore-Read Pfaffian wavefunction, while the $\frac{7}{3}$ is presumed to be Laughlin state, and ii) the widely held belief that the $\frac{5}{2}$ destruction under tilt is due to magneto-orbital coupling to the parallel field and does not result from Zeeman interaction. Our observed parallel-field induced linear suppression of the $\frac{5}{2}$ gap, as well as its in-plane field threshold supports the existing belief that the $\frac{5}{2}$ destruction under tilt is due to orbital coupling to the parallel field, rather than Zeeman coupling. The opposite behaviour of the $\frac{7}{3}$ state however is contradictory, since magneto-orbital coupling is expected to destroy the $\frac{7}{3}$ state in the same way. On the other hand, the large enhancement of the $\frac{7}{3}$ gap shows evidence for the existence of small (2-3 electron spin) reversed-spin skyrmions, suggesting the different behaviours may be due to differences in the corresponding excitation spectra, rather than in their ground state properties. Our identification of a non-trivial excitation spectrum in the $\frac{7}{3}$ state (possibly involving skyrmions) is the first such observation in the second Landau level.

Our findings do not allow us to convincingly address the question of the spin nature of the $\frac{5}{2}$ state since our results are both consistent with the view that the $\frac{5}{2}$ state is described by the spin-polarized Moore-Read Pfaffian wavefunction, but also can not rule out that the $\frac{5}{2}$ state is rather spin unpolarized. Our data in the low tilt, possibly Zeeman dominated, regime suggests that studying an even lower density sample, where the low parallel field effect can be examined in even finer detail, may help answer this question.

The contrasting dichotomy between the two states observed in our study is of considerable importance. This result calls into question the prevailing theoretical belief that they should behave similarly if both are spin-polarized and therefore challenges the foundational argument on which initial support for the Moore-Read Pfaffian description at $\nu = \frac{5}{2}$ was built. While we interpret the behavior of the $\frac{7}{3}$ gap in our experiment to be arising from the formation of skyrmions, the suppression of the $\frac{5}{2}$ state in the presence of even a modest parallel field remains an open question.

# References

[1] Moore, G. and Read, N. *Nucl. Phys. B* **360**, 362 (1991).

[2] Morf, R. H. *Phys. Rev. Lett.* **80**, 1505 (1998).

[3] Park, K., Melik-Alaverdian, V., Bonesteel, N. E., and Jain, J. K. *Phys. Rev. Lett* **58**, 10167R (1998).

[4] Rezayi, E. and Haldane, F. *Phys. Rev. Lett.* **84**, 4685 (2000).

[5] Dimov, I., Halperin, B. I., and Nayak, C. *Phys. Rev. Lett.* **100**, 126804 (2008).

[6] Feiguin, A. E., Rezayi, E., Nayak, C., and Das Sarma, S. *Phys. Rev. Lett* **100**, 166803 (2008).

[7] Feiguin, A. E., Rezayi, E., Yang, K., Nayak, C., and Das Sarma, S. *arXiv:0804.4502v3* (2008).

[8] Peterson et al. *arXiv:0801.4819v1* (2008).

[9] Peterson, M. R., Jolicoeur, T., and Das Sarma, S. *Phys. Rev. Lett.* **101**, 016807 (2008).

[10] Dolev, M., Heiblum, M., Umansky, V., Stern, A., and Mahalu, D. *Nature* **452**, 829 (2008).

[11] Radu, I. P., Miller, J. B., Marcus, C. M., Kastner, M. A., Pfeiffer, L. N., and West, K. W. *Science* **320**, 899 (2008).

[12] Levin, M., Halperin, B. I., and Rosenow, B. *Phys. Rev. Lett.* **99**, 236806 (2007).

[13] Lee, S.-S., Ryu, S., Nayak, C., and Fisher, M. P. A. *Phys. Rev. Lett.* **99**, 236807 (2007).

[14] Halperin, B. I. *Helv. Phys. Acta* **56**, 75 (1983).

[15] Eisenstein, J. P., Willett, R., Stormer, H. L., Tsui, D. C., Gossard, A. C., and English, J. H. *Phys. Rev. Lett.* **61**, 997 (1988).

[16] Eisenstein, J. P., Willet, R. L., STormer, H. L., Pfeiffer, L. N., and West, K. W. *Surf. Sci.* **229**, 31 (1990).

[17] Lilly, M. P., Cooper, K. B., Eisenstein, J. P., Pfeiffer, L. N., and West, K. *Phys. Rev. Lett.* **83**, 824 (1999).

[18] Pan, W., Du, R. R., Stormer, H. L., Tsui, D. C., Pfeiffer, L. N., Baldwin, K. W., and West, K. W. *Phys. Rev. Lett.* **83**, 820 (1999).

[19] Csathy, G. A., Xia, J. S., Vicente, C. L., Adams, E. D., Sullivan, N. S., Stormer, H. L., Tsui, D. C., Pfeiffer, L. N., and West, K. W. *Phys. Rev. Lett.* **94**, 146801 (2005).

[20] Dean, C. R., Piot, B. A., Hayden, P., Das Sarma, S., Gervais, G., Pfeiffer, L. N., and West, K. W. *Phys. Rev. Lett.* **100**, 146803 (2008).

[21] Das Sarma, S. and Pinczuk, A. *Perspectives in Quantum Hall Effects.* John Wiley and Sons, Inc., New York, (1997).

[22] . In general $\Delta_o$ is quite complex and unknown, including for example Coulomb energy, spin-orbit coupling, hyperfine interaction etc. In this simple model however it assumed that $\Delta_o$ depends only on $B_\perp$, and so remains fixed under tilt [21].

[23] Koulakov, A. A., Fogler, M. M., and Shklovskii, B. I. *Phys. Rev. Lett.* **76**, 499 (1996).

[24] Leadley, D. R., Nicholas, R. J., Maude, D. K., Utjuzh, A. N., Portal, J. C., Harris, J. J., and Faxon, C. *Phys. Rev. Lett.* **79**, 4246 (1997).

[25] Dethlefsen, A. F., Mariani, E., Tranitz, H. P., Wegscheider, W., and Haug, R. J. *Phys. Rev. B* **74**, 165325 (2006).

[26] Schmeller, A., ang L. N. Pfeiffer, J. P. E., and West, K. W. *Phys. Rev. Lett.* **75**(23), 4290 (1995).

[27] Stopa, M. and Das Sarma, S. .

[28] Stopa, M. and Das Sarma, S. *Phys. Rev. B* **40**(14), 10048 (1989).

[29] Das Sarma, S. and Hwang, E. H. *Phys. Rev. Lett.* **84**, 5596 (2000).

[30] Toke, C. and Jain, J. K. *Phys. Rev. Lett.* **96**, 246805 (2006).

[31] Toke, C. and Jain, J. K. *Phys. Rev. Lett.* **98**, 036836 (2007).

[32] Wojs, A. and Quinn, J. J. *Phys. Rev. B* **74**, 235319 (2006).

CHAPTER 6

# Resistively Detected NMR

An important question regarding the $\nu = \frac{5}{2}$ FQH state continues to be its spin-polarization. The spin nature of the $\frac{5}{2}$ remains a distinguishing feature of the proposed non-Abelian Moore-Read Pfaffian description versus other, Abelian, candidate wavefunctions. However, attempts to experimentally measure the 5/2 spin, which according to the the Moore-Read theory should be fully spin polarized, have so far yielded inconclusive results. Resistively detected nuclear magnetic resonance (RDNMR) is a recently developed technique that allows us to, among other things, probe *directly* the spin polarization in the quantum Hall regime. Conventional nuclear magnetic resonance (NMR) is by now a well understood and widely used standard tool to probe spin systems. However, conventional NMR is limited in application to "bulk" systems since typical sensitivities require $\gtrsim 10^{16}$ nuclear spin particles to obtain measurable signals. It has therefore not been possible to apply traditional NMR techniques to quantum systems that contain "too few spins", such as quantum dot structures ($10^6$-$10^{10}$ spins), carbon nanotubes ($\lesssim 10^3$ $^{13}$C atoms per tube), and GaAs/AlGaAs 2DEGs ($\lesssim 10^{15}$ for a 30 nm quantum well). The RDNMR technique overcomes this problem by exploiting spin-interactions between transport electrons and the surrounding nuclei to detect the resonance condition in the electron resistivity, allowing substantial improvements in measurement sensitivity. We therefore implemented an RD-NMR measurement scheme in our dilution refrigerator with the ultimate aim of using this technique to probe the spin state at $\frac{5}{2}$ fractional filling. In the following chapter I first give a review of the RDNMR measurement technique. I then present our investigation of the RDNMR response signal where we studied in detail the anomalous response signal around filling fraction $\nu = 1$. Finally, at the end of this chapter I present our recent observation of an RDNMR response measured near the $\nu = \frac{5}{2}$ FQH state. I then discuss our efforts to further optimize the technique in order to fully explore the $\frac{5}{2}$ spin state.

## 6.1   Theory of resistively detected NMR

### 6.1.1   Nuclear Zeeman interaction

When placed in a magnetic field a particle with non-zero spin interacts with the field according to the Zeeman interaction,

$$\hat{H} = -\boldsymbol{\mu} \cdot \mathbf{B} \tag{6.1}$$

where $\mathbf{B}$ is the applied field and $\boldsymbol{\mu}$ is the magnetic moment, defined by

$$\boldsymbol{\mu} = \gamma \, \mathbf{J} \tag{6.2}$$

where $\mathbf{J}$ is the total quantum spin number and $\gamma$ is the *gyromagnetic ratio*. Classically, the gyromagnetic ratio is defined for a rotating charge as the ratio of the magnetic dipole to its angular momentum. The equivalent quantum mechanical definition for a spin particle is simply the ratio of the magnetic moment to the angular momentum associated with its spin, as above. For a nuclear spin this can be written as

$$\gamma_N = g_N \frac{e}{2m_p} = g_N \frac{\mu_N}{\hbar} \tag{6.3}$$

where $e$ is the electron charge, $m_p$ is the proton mass, $\mu_N = e\hbar/2m_p$ is the nuclear magneton, and $g_N$ is the dimensionless nuclear g-factor. Using these definitions and solving the Schrodinger equation for the Hamiltonian in Eqn. 6.1 gives the Zeeman energy for a nuclear spin

$$E_{Z_N} = -\gamma_N \, \hbar \, B \, m_J = -g_N \, \mu_N \, B \, m_J \tag{6.4}$$

where $m_J$ is the magnetic quantum number, restricted to allowed values $m_J = J, J - 1, .., -J + 1, -J$. The Zeeman energy is quantized in units $\hbar m_J$ where $m_J$ represents the spin-projection along the direction of the applied B field. Fig. 6–1a shows the possible energy states for a spin-3/2 particle as an example. In this case there are four possible spin orientations ($m_J = 3/2, 1/2, -1/2, -3/2$) where each spin state corresponds to a different Zeeman energy according to Eqn. 6.4. Note that in each case the magnetic moment precesses about the z-direction at the Larmor frequency. In Fig. 6–1b the energy level splitting caused by the Zeeman interaction is shown for a spin-3/2 nucleus. The energy gap, $\Delta$, between each level is calculated simply from Eqn. 6.4
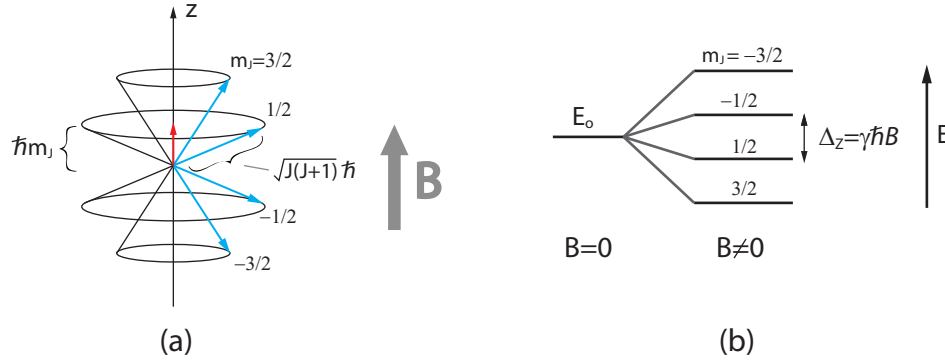
Figure 6–1: (a) In the presence of a magnetic field, a quantum particle with spin angular momentum J has only 2J+1 allowed states corresponding to projections along the direction of the applied field quantized in units $\hbar m_J$ where $m_J = J, J-1, ..., -J$. Shown here is an example for J=3/2. (b) Energy level diagram showing the corresponding Zeeman splitting (possible allowed energy spin states) for a spin-3/2 particle.

$$\Delta_{Z_N} = \gamma_N \, \hbar \, B \tag{6.5}$$

where we see the gap is identical between each level, depending only on the gyromagnetic ratio and the size of the B field.

From Eqn. 6.4 the lowest energy state occurs when the maximum nuclear spin projection ($m_J = J$) is aligned to the applied B field. This is true at zero temperature, however, if the nucleus is in contact with a thermal bath at non-zero temperature it can be excited to one of the higher energy levels. If there are $n$ allowable energy spin states, the probability of the nuclear spin being in the $j^{th}$ energy state, $E_j$, when in thermodynamic equilibrium with a bath at temperature T is given by the Boltzmann distribution

$$p(E_j) = \frac{e^{-E_j/k_B T}}{\sum_i^n e^{-E_i/k_B T}} \tag{6.6}$$

where $k_B$ is the Boltzmann constant. If instead of a single nuclear spin we consider a large system containing $N$ nuclear spins per unit volume, the Boltzmann probability distribution directly gives the fraction of spins occupying a particular energy state

$$p(E_j) \equiv \frac{N_j}{N} \tag{6.7}$$

where $N$ is the total number of nuclei and $N_j$ is the number of nuclei in the $E_j$ energy state. Because the nuclear Zeeman energy is related to the direction of the nuclear spin relative to the direction of the applied B field, the Boltzmann distribution among the allowable

energy states defines the overall polarization, *i.e.* the average net direction of the nuclear spins. For example, consider for simplicity a system of $N$ spin 1/2 nuclei. There are only two available states for each spin: aligned to the field with energy $E_{1/2}$, or anti-aligned with energy $E_{-1/2}$. The overall polarization is therefore defined by the number of polarized (aligned) versus the number of anti-polarized (anti-aligned) spins. From Eqn. 6.6 this can be described by the ratio

$$\frac{N_{1/2}}{N_{-1/2}} = e^{-(E_{1/2}-E_{-1/2})/k_B T} = e^{\gamma_N \hbar B/k_B T} \tag{6.8}$$

The thermal distribution thus varies from fully polarized (all nuclear spins aligned) in the limit that $T \to 0$, to fully-unpolarized (equal number of up and down spins) in the limit $T \to \infty$.

In general, for a system of particles with spin J, the average net polarization is calculated from the expectation value of the Boltzmann distribution. Substituting the Zeeman energy (Eqn. 6.4) into the Boltzmann distribution (Eqn. 6.6) and calculating the expectation gives the polarization to be

$$P = B_J(x) = \frac{(2J+1)}{2J}\coth\left(x\frac{(2J+1)}{2J}\right) - \frac{1}{2J}\coth\left(x\frac{1}{2J}\right) \tag{6.9}$$

where $B_J$ is called the Brillouin function with $x = Ng_N\mu_N JB/k_B T$ and $J$ is the total nuclear spin. The resulting, measurable, nuclear *magnetization* is then given by

$$M = M_S P \tag{6.10}$$

where $M_S = Ng_N\mu_N J$ is the saturation nuclear magnetization, and $P$ is the nuclear polarization defined above. The Brillouin function varies between 1 when $B/T \to \infty$, and 0 when $B/T \to 0$. Therefore, at T=0 only the lowest energy state is occupied and all the spins are aligned giving maximum magnetization ($M = M_S$). On the other hand when T is large all of the possible energy states become equally populated and the net magnetization (polarization) goes to zero.

In the high temperature/low B field limit where $\mu B << k_B T$ the Brillouin form of the magnetization reduces to the experimentally measured Curie Law given by

$$M = \frac{N\mu_N^2 g_N^2 J(J+1)}{3k_B}\frac{B}{T} = \frac{N\mu^2}{3k_B}\frac{B}{T} \tag{6.11}$$
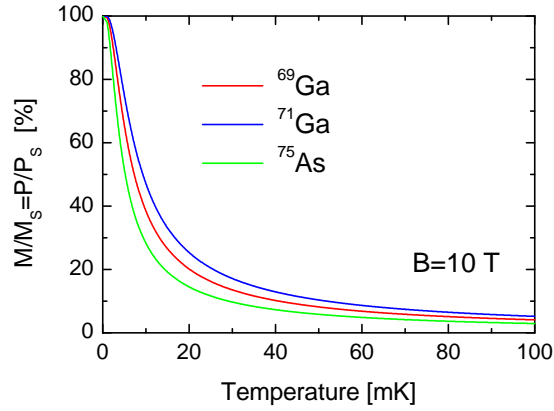
Figure 6–2: Percent nuclear magnetization (or equivalently nuclear polarization) as a function of temperature calculated from the Brillouin function for the $^{69}$Ga, $^{71}$Ga, and $^{75}$As isotopes in GaAs

where $B$ is the applied field and $T$ is the nuclear temperature. Note that in typical experiments the $\mu B << k_B T$ condition is almost always satisfied since the nuclear magneton is so small. The Curie law is therefore generally a very good approximation [1].

In Fig. 6–2 the percent magnetization, $M/M_S$ (or equivalently the percent polarization, $P/P_S$) is shown as a function of temperature at 10 T for the three nuclear isotopes ($^{69}$Ga, $^{69}$Ga and $^{69}$As) found in GaAs/AlGaAs quantum well structures. As seen in the figure, the magnetization is rapidly diminished with temperature. For example, at 50 mK there is only about 10% polarization at 10 T. This makes apparent the need for operating in the ultra-low temperature limit and at high magnetic fields when maximal nuclear polarization is desired.

Table 6–1: Properties of the GaAs/AlGaAs nuclear isotopes. All values are taken from Ref. [2]

| Isotope | I | Abundance* [%] | Magnetic moment, $\mu$ [$\mu_N$] | Gyromagnetic ratio, $\gamma/2\pi$ [MHz/T] |
|---------|-----|----------|---------|---------|
| $^{69}$Ga | 3/2 | 60.108 | 2.01659 | 10.2478 |
| $^{71}$Ga | 3/2 | 39.892 | 2.56227 | 13.0208 |
| $^{75}$As | 3/2 | 100 | 1.43947 | 7.3150 |
| $^{27}$Al | 5/2 | 100 | 3.64151 | 11.1031 |

### 6.1.2  Nuclear magnetic resonance

To avoid confusion, the nuclear spin angular momentum is usually labeled $I$ and the electron spin $S$. The nuclear Zeeman energy is therefore written as

$$E_{Z_N} = -\gamma_N \, \hbar \, B \, I_z \tag{6.12}$$

where $I_z = I, I - 1, .., -I$ is the spin projection along the quantization axis.

By applying a transverse magnetic field oscillating with frequency[1] $f$, the sample can be irradiated with photons carrying energy $hf$. If the frequency of the transverse field is properly tuned so that the photon energy exactly matches the Zeeman splitting in the nuclear energy spectrum

$$hf = \gamma \hbar B \tag{6.13}$$

transitions between the energy states can be induced by photon absorption. Rewriting the above equation for the frequency gives

$$f_L = \frac{\gamma}{2\pi} B \tag{6.14}$$

where $f_L$ is the Larmor frequency in units Hz. Note that the gyromagnetic ratio has units $rad/s/T$. In NMR however it is often more convenient according to Eqn. 6.14 to quote the entire factor $\gamma/2\pi$ in units MHz/T. Values of the gyromagnetic ratio for the GaAs isotopes are given in Table 6–1 .

The effect of forcing these energy transitions via photon absorption is to disturb the equilibrium Boltzmann distribution. If sufficient power is delivered by the transverse oscillating field all transitions can be saturated and the net polarization in a sample completely destroyed. Any polarization between these two extremes (including a complete inversion of the initial polarization) can be achieved by varying the time over which the transverse oscillating field is turned on.

If at time $t = 0$, the transverse oscillating field is turned *off*, the system will return to its equilibrium magnetization according to

$$M_z(t) = M_o - [M_o - M_z(0)] \, e^{-t/T_1} \tag{6.15}$$

where $M_o$ is the equilibrium magnetization, and $T_1$ is the characteristic *spin-lattice relaxation time*. The spin-relaxation time is dominated by interactions with the surrounding

---

[1] Throughout the frequency in Hz is labeled $f$ so as to avoid confusion with the filling factor denoted by $\nu$.
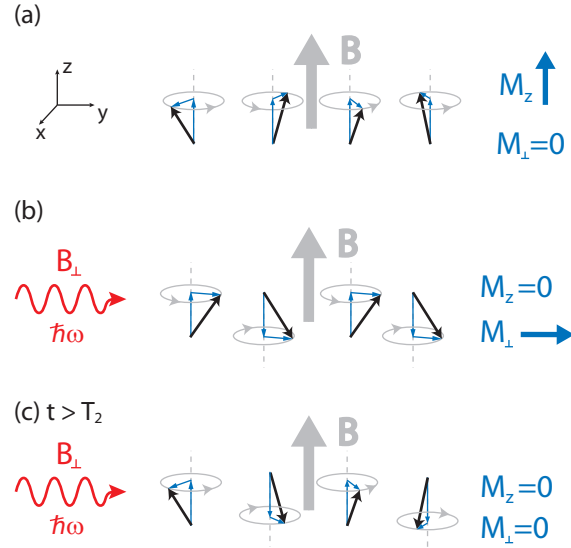
Figure 6–3: Cartoon picture of NMR. In (a) four spins are shown all aligned to the externally applied B-field giving net magnetization $M = M_z$. The total spin vector (black arrow) rotates about the B-field direction at the Larmor frequency but since the spins are in general out of phase the net transverse magnetization, $M_\perp$, is zero. (b) A continuous transverse oscillating field, tuned to the Larmor frequency, is applied. This saturates the aligned/anti-aligned population reducing the magnetization in the z-direction to zero. However, the transverse radiation initially imparts a phase coherence between the spins momentarily giving a non-zero transverse magnetization in the x-y plane that precesses around the z-axis. (c) Dephasing between the spins resulting from variations in the local environment causes the net transverse magnetization to decay to zero with characteristic time $t = T_2$ (see text).

lattice that mediate the spin flip process, in this case allowing the nuclei to relax back to their equilibrium state. However, at very low temperatures where there are no phonons, the relaxation mechanism relies mostly on spontaneous photon emission giving very long $T_1$ times, on the order of minutes to hours (or even days) [3, 4].

The nuclei all precess at the same Larmor frequency under application of the B field ($\omega = \gamma B$). However, the nuclei are in general out of phase with each other so that averaging over all nuclei there is no net magnetization in the transverse direction. Application of the transverse radiation can momentarily impart a phase coherence between the nuclear spins, causing a component of the net polarization to point in the x-y plane (perpendicular to the direction the large static B field), but precessing around the z-axis (parallel to the static B field). However, dephasing between the spins due to decoherence effects causes the transverse component of the magnetization, $M_\perp$, to quickly decay to zero. This decoherence time is given by

107

$$M_\perp(t) = M_\perp(t=0)e^{-t/T_2} \qquad (6.16)$$

where $T_2$ is the *spin-spin relaxation time.* The decoherence results from interactions with other atoms in the local environment of each nuclear spin, but is also due to inhomogeneities in the applied polarizing B field. The measured spin-spin relaxation time is therefore labeled $T_2^*$ where

$$\frac{1}{T_2^*} = \frac{1}{T_2} + \frac{1}{T_2^{inhomo.}} \qquad (6.17)$$

where $T_2$ is the contribution from pure spin-spin interactions and $T_2^{inhomo.}$ is the contribution from inhomogeneities in the applied magnetic field.

Both equations 6.15 and 6.16, describing respectively the $T_1$ and $T_2$ ($T_2^*$) relaxation times, are derived from the macroscopic Bloch equations; a set of time dependent differential equations describing the *macroscopic* nuclear magnetization averaged over all the individual nuclei.

### 6.1.3   Classical view of NMR

It can often be more physically intuitive to consider a classical analogy to the nuclear magnetic resonance phenomenon. In the classical view each atom is again considered a magnetic moment, precessing about the applied field at the Larmor frequency. This is similar to the quantum solution depicted in Fig. 6–1. However, whereas the Schrodinger equation indicates the projection of the magnetic moment along the B-field direction can only take on quantized values, in the classical view the moment can be oriented along any arbitrary direction. From Eqn. 6.1 the classical nuclear Zeeman energy is therefore $E_{Z_N} = -\mu\, B \cos(\theta) = -\gamma_N \hbar\, B\, I_z$ where now the spin projection along the B field direction is $I_z = I\, cos\theta$. If we consider a single spin particle only, the classical view does not agree with the quantum picture. However, in NMR experiments we are usually concerned with measuring the magnetization averaged over a large ensemble of spin particles. The ensemble average over a large number of quantum spin particles versus classical spin particles gives the same behaviour in the thermodynamic limit and so the classical view in many cases is valid.

In Fig. 6–4 the effect of shining a transverse radiation in the classical picture is shown. When tuned exactly to the Larmor frequency, the incident photons can "tip" the spin away from the equilibrium polarization direction by rotating the magnetic moment through an angle $\theta$ relative to the z-axis (direction of the applied B field). The angle through which
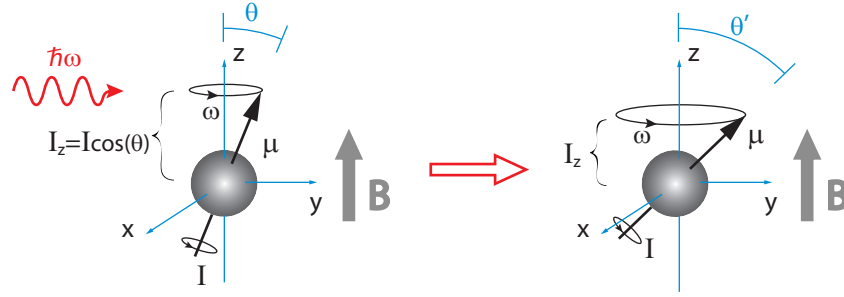
Figure 6–4: In the classical view the transverse radiation can tip the direction of the magnetic moment away from its equilibrium position when the frequency of the incident photons exactly matches the resonant Larmor frequency.

the polarization vector is rotated depends on how long the transverse oscillating field is applied according to

$$\theta = 2\pi\gamma_N\,\tau\,B_\perp \tag{6.18}$$

where $\tau$ is the pulse time and $B_\perp$ is the magnitude of the transverse field. If the magnetization vector is initially aligned along the z-axis a $\pi/2$-pulse rotates the vector into the x-y plane whereas a $\pi$-pulse rotates the vector by 180º, completely inverting the polarization along the negative z-direction. After a $\theta$-pulse the characteristic time for the magnetization to return to the equilibrium value along the z-direction is again given by $T_1$ according to Eqn. 6.15. Similarly, the characteristic time for the average transverse magnetization to be destroyed (due to phase decoherence between the individual precessing spins in the x-y plane) is given by the spin-spin relaxation time, $T_2^*$.

### 6.1.4  Continuous Wave mode

In continuous wave (CW) mode the transverse radiation is shone continuously such that $\tau \to \infty$. The nuclear polarization therefore rotates continuously through $\theta = 0$ to $2\pi$ at a frequency defined by the Rabi-frequency. However, dephasing between the nuclei quickly leads to a decoherence in the signal and in the long time average CW radiation destroys the mean nuclear polarization.

### 6.1.5  Electrons in a magnetic field

The same analysis as above applies equally to electrons interacting with an applied magnetic field. However, one important difference is that for electrons the direction of

109

the spin magnetic moment is opposite to the direction of its spin. This gives the relation between the g-factor, $g_e$, and gyromagnetic ratio, $\gamma_e$, for electrons to be

$$\gamma_e = -g_e \frac{\mu_B}{\hbar} \tag{6.19}$$

where $\mu_B = e/2m_e$ is the Bohr magneton. From Eqn. 6.4 this therefore gives the Zeeman energy for electrons in a magnetic field to be

$$E_Z = g^* \, \mu_B \, B \, S_z \tag{6.20}$$

where $S_z$ is the projection of the electron spin ($=\pm 1/2$), and $g^*$ is the effective g-factor. In free space the g-factor for electron is $g \sim 2$. Because the electron g-factor is positive the lowest energy state in a magnetic fields is realized when the electron spin is *anti-aligned* to the applied field. In a semiconductor the g-factor is modified due to spin-orbit coupling giving an effective g-factor, $g^*$, determined both by the size of the semiconductor band gap and by the spin-orbit coupling in the valence band. In GaAs $g^*$ is reduced so much that it is negative, measured to be $g^* = -0.44$ in bulk GaAs [5].

### 6.1.6   Resistively detected NMR

It was first shown by Dobers *et al.* [6], nearly twenty years ago, that the electron/nuclear spin interactions in the quantum Hall regime could be observed in the longitudinal magnetoresistance, $R_{xx}$. Their study was performed at $\sim$4 K and so to achieve sufficient nuclear polarization they employed a dynamic nuclear polarization technique via electron spin resonance. Kronmuller *et al.* then applied this resistively detected interaction to study the anomalous huge magnetoresistance peak that appears around filling factor $\nu = \frac{2}{3}$ in very thin quantum well samples [7]. By resistively detecting the NMR resonance and measuring the corresponding relaxation times, they were able to directly probe the electron/nuclear spin interactions in the FQHE regime. Finally, Desrat *et al* found [8] that by examining the QHE at much lower temperatures, where nuclear polarization is significantly enhanced according to the Boltzmann distribution (see Fig. 6–2), resistively detected NMR could be performed without having to first dynamically polarize the nuclei. This allows the RDNMR technique to be applied throughout the integer and fractional quantum Hall regime with minimal disturbance of the equilibrium QH states, and importantly allows application of the technique in the ultra-low temperature limit, where FQH states with small excitation gaps (such as the $\frac{5}{2}$) are revealed.

Electrons in a solid can couple to the nuclear spins of the surrounding atoms via the contact hyperfine spin interaction. If the solid is placed in a magnetic field the nuclear spins can exhibit an average net polarization along the field direction as outlined above. The electronic contact hyperfine interaction energy is then given by

$$E_{HF} = A \langle I_z \rangle S_z \tag{6.21}$$

where $S_z$ is the electron spin along the field direction, $\langle I_z \rangle$ is the mean nuclear spin polarization seen by each electron, and $A$ is the hyperfine coupling constant

$$A = \frac{2\mu_o}{3}(g_e\mu_B)(g_N\mu_N)\left|\psi(0)\right|^2 \tag{6.22}$$

where $|\psi(0)|$ is the electron probability density at the nuclear site. In the presence of an external magnetic field, $B$, the Zeeman energy in a solid includes both the normal Zeeman effect and the hyperfine interaction giving the *total* electronic Zeeman energy

$$E_Z = g^*\mu_B B S_z + A \langle I_z \rangle S_z. \tag{6.23}$$

We can rewrite this equation as

$$E_Z = g^*\mu_B(B + B_N)S_z \tag{6.24}$$

where $B_N = A \langle I_z \rangle /g^*\mu_B$ defines an additional effective nuclear magnetic field seen by the electrons and is termed the Overhauser shift.

In the thermally activated regime, the longitudinal magnetoresistance, $R_{xx}$, is given by

$$R_{xx} \propto e^{-\Delta/2k_B T} \tag{6.25}$$

where $\Delta$ is the energy gap in the density of states. At odd filling fraction the energy gap is just the Zeeman gap plus exchange energy due to electron-electron interactions; $\Delta_{odd} = \Delta_Z + \Delta_{exch.}$. Similarly, at even filling, the energy gap is $\Delta_{even} = \hbar\omega_c - (\Delta_Z + \Delta_{exch.})$ where $\hbar\omega$ is the cyclotron energy gap. In general therefore, the energy gap includes a contribution from the Zeeman gap, $\Delta_Z = g^*\mu_B(B + B_N)$, so that we can rewrite Eqn. 6.25 as

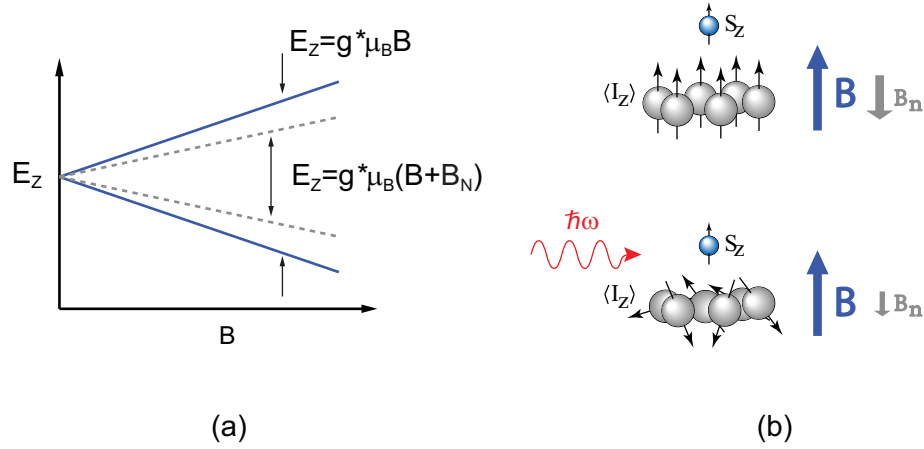$$R_{xx} \propto e^{-g^*\mu_B(B+B_N)/2k_B T}. \tag{6.26}$$

Figure 6–5: (a) The effective magnetic field resulting from contact hyperfine interaction, $B_N$ reduces the total Zeeman energy. (b) Destroying the nuclear polarization by shining RF radiation reduces the effective nuclear field $B_N$ therefore increasing the Zeeman energy

In this way we see that the longitudinal resistance is determined, in part, by the hyperfine interaction coupling, and is therefore sensitive to variations in the nuclear polarization.

Since the effective g-factor in GaAs is negative ($g^* = -0.44$), the effective nuclear field, $B_N$, is *opposite* to the applied field, $B$, and therefore reduces the Zeeman energy (Fig. 6–5). Applying transverse radiation at resonance destroys the nuclear polarization (*i.e.* destroying $B_N$), and therefore increases the effective Zeeman gap. At odd filling factor, for example, where $\Delta$ varies directly with the Zeeman gap, this results in a corresponding decrease in the measured $R_{xx}$, and thereby give a resistance minimum. This therefore provides a means to *resistively detect* the nuclear magnetic resonance condition.

It is important to stress that $B_N$ is an *effective* field arising from the contact hyperfine interaction. Changing $B_N$ by varying the nuclear polarization therefore does not influence the cyclotron motion (*i.e.* filling factor) of the electrons, which remains set by the externally applied magnetic field. Also, there exists an additional exchange energy contribution to the spin gap arising from electron-electron interactions. In the simplest theoretical approach this exchange term does not depend on the nuclear polarization and so in principle is not affected at the resonance condition and therefore does not contribute to measured RDNMR response.

### 6.1.7   Knight Shift

In discussing the Overhauser effect we considered the effective nuclear field seen by each electron resulting from interactions with the surrounding polarized nuclei. If we instead

consider a single nucleus in a bath of polarized electrons, the electron polarization likewise gives rise to an effective magnetic field, via the hyperfine interaction, seen by each the nuclear spin. This analogue of the Overhauser shift, but for nuclei, is termed the Knight shift. Recall that the nuclear resonant frequency is dependent on the applied magnetic field according to Eqn. 6.14. Including the hyperfine interaction gives the modified nuclear resonant frequency in the presence of a sea of polarized electrons to be

$$ f = \frac{\gamma}{2\pi}(B + B_e) \tag{6.27} $$

where $B_e = -A \langle S_z \rangle /g_N \mu_N$ is the effective electronic magnetic field with $\langle S_z \rangle$ the mean electron polarization seen by each nuclear spin. The resonant frequency Knight shift, $K_s = \gamma B_e/2\pi$, varies directly with the electron polarization. Measurement of the Knight shift in nuclear resonance experiments therefore gives a tool to directly probe the polarization state of the surrounding electrons [3]. Several experiments have demonstrated measurement of the Knight shift in quantum Hall structures using resistively detected NMR [9, 10] establishing this as an effective method to measure the spin polarization in FQHE states.

### 6.1.8 $T_1$ relaxation times

Another important NMR tool in the effort to study electron behaviour in the QHE regime is measurement of the $T_1$ relaxation times. While Knight shift measurements allow us to probe the electron spin polarization state, $T_1$ can give insight into the electron excitation spectrum. Once the transverse radiation is turned off the nuclear system relaxes to the equilibrium polarization state via a nuclear spin flip process. At very low temperatures however there are few energy exchange mechanisms available. Nuclear spins are coupled to the electron spins via the hyperfine interactions and so spin-exchange can occur through a nuclear flip-electron flop process [8]. However, the Zeeman gap for electrons is much larger than for the nuclei, i.e. $\gamma_e \sim 1000\gamma_N$ in GaAs. The probability of a spontaneous flip-flop exchange is therefore very low. Near filling factor $\nu = 1$ however the ground state exhibits Skyrmion excitation (a crystalline spin wave texture) with charged spin-reversal excitations [3, 8, 11, 12]. These low-lying energy excitations readily couple of the nuclei greatly enhancing the relaxation time. Conventional NMR experiments on multi-well structures [3] and more recently RDNMR experiments on single quantum well samples [8, 13, 14] have observed a drastic reduction in $T_1$ around $\nu = 1$, lending considerable support to the proposed formation of Skyrmions at these filling factors.

## 6.2   Investigation of the anomalous RDNMR lineshape near $\nu = 1$

The resistively detected NMR technique allows us to probe the many fascinating 2D electronic phenomena (crystalline spin texture, quantum transport dynamics, composite boson/fermion particle formation) in a novel way. However, while RDNMR offers the potential to gain new insight into a wide range of interesting many body electron physics, several features of the measured signal remain unexplained [8–10, 14–17]. According to the hyperfine interaction picture, at odd filling fraction the RDNMR signal is predicted to coincide with a reduction in the magnetoresistance at the resonance condition. While such a minimum is indeed measured at nearly all integer and fractional filling factors in GaAs/AlGaAs quantum hall samples [8], in the vicinity of $\nu = 1$ an anomalous "dispersive" lineshape is observed, where on resonance the usual resistance minimum is followed by a secondary resistance peak at slightly higher RF frequency [8,14,16]. Several attempts have been made to understand the origin of the dispersive lineshape. Desrat *et al.* argued that the anomalous signal near $\nu = 1$ could be related to the formation of the spin-reversal Skyrmions [8, 14]. However, a similar dispersive lineshape has since been observed at higher fields near filling fractions $\nu = \frac{2}{3}$ and $\frac{1}{3}$ [9] and also near $\nu = \frac{2}{9}$ and $\frac{1}{5}$ [15] where the formation of Skyrmions is unlikely. Combining RDNMR with conventional NMR, Stern *et al.* argued that the dispersive signal might be related to the existence of spin domains in the electron system, however, they could not account for their observation that around both $\nu = \frac{2}{3}$ and $\frac{1}{3}$ the dispersive shape appeared on the high-filling factor side of the state only with a minimum-only observed on the low-filling side [9]. More recently Tracy *et al.* [16] argued that the dispersive shape could be due to a variation in the electron temperature around the resonant frequency with the peak (minimum) indicating a mechanism causing electron heating (cooling). However, the mechanism responsible for electron cooling/heating remains unclear. With still no consensus as to the origin of the anomalous signal, we performed a detailed study of the resonance lineshape near $\nu = 1$ under a variety of RF and sample conditions.

### 6.2.1   Experimental details

We examined two different 2DEG samples using resistively detected NMR. First we studied the low density sample described in the previous chapters. This sample is a 40 nm wide modulation-doped GaAs/AlGaAs quantum well structure with a mobility of $16.6(8) \times 10^6$ cm$^2$/Vs and electron density of $1.60(1) \times 10^{11}$ cm$^{-2}$. The low electron density allows us to observe the $\nu = 1$ QHE state within the range of our 9 T magnet. The second sample
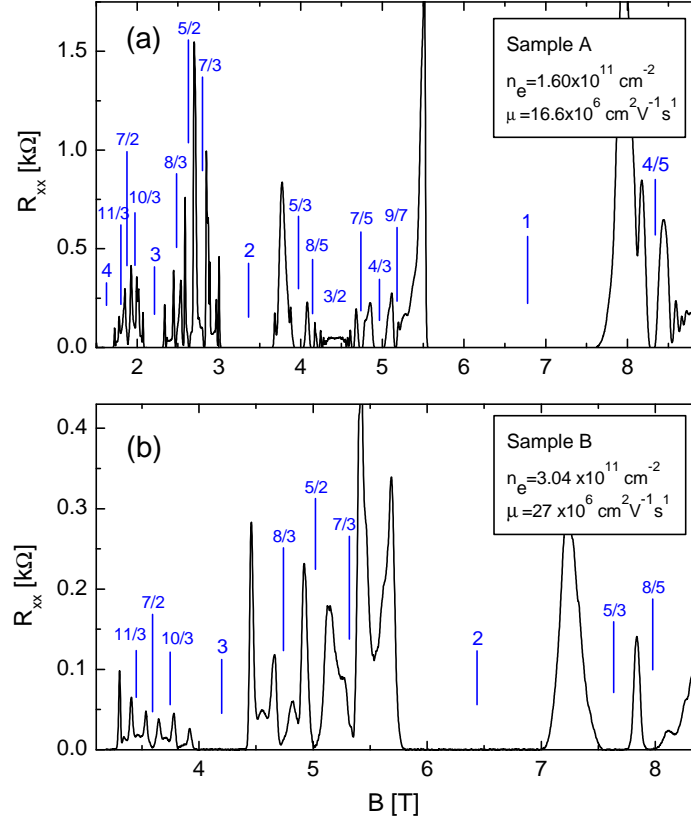
Figure 6–6: Longitudinal resistance, $R_{xx}$ versus applied B field for (a) sample A and (b) sample B used in the RDNMR experiments. Sample A was used to study the anomalous RDNMR signal lineshape around $\nu = 1$. Both sample A and B were then used to apply the RDNMR technique to probe the $\frac{5}{2}$ state.

is 30 nm wide GaAs/AlGaAs quantum well. Importantly this sample has both a higher electron density, $n_e = 3.04(1) \times 10^{11}$ cm$^{-2}$, and higher mobility, $\mu = 27 \times 10^6$ cm$^2$/Vs. The enhanced mobility is expected to give a better developed, *i.e.* more robust, $\nu = \frac{5}{2}$ state. Additionally the increased density causes the $\frac{5}{2}$ state to appear at nearly twice the magnetic field. According to the hyperfine picture the magnitude of the RDNMR response signal increases with the degree of nuclear polarization, $\langle I_z \rangle$, and therefore is expected to increase with increasing B field. The higher density sample therefore should give an enhanced RDNMR response around $\nu = \frac{5}{2}$. The two samples are distinguished as the "low density" and "high density" samples in the remainder of this chapter.

Fig. 6–6 shows the magnetoresistance, $R_{xx}$, measured from each sample. As can be seen, both samples are very high quality, with both exhibiting a strong, well developed, minimum at $\nu = \frac{5}{2}$ at base temperature. While our primary interest is to study the $\frac{5}{2}$,
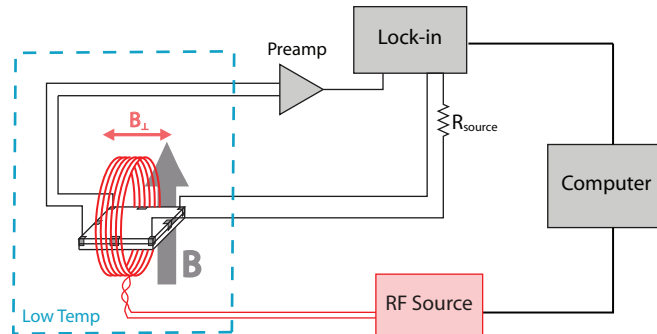
Figure 6–7: Circuit diagram of the resistively detected NMR measurement scheme. The large grey arrow indicates the large static B field (typically $B \sim$ a few Tesla). The small red arrow indicates transverse RF field ($B_\perp \sim$ a few $\mu$T).

we first devoted our efforts to characterizing the RDNMR signal. Using our low density sample we studied extensively the anomalous dispersive lineshape reported around $\nu = 1$ [8,10,14,16]. While investigating the effects of varying RF and sample conditions conditions on the dispersive RDNMR signal around $\nu = 1$ we learned how to better optimize our signal. We then applied the RDNMR technique to probe the $\nu = \frac{5}{2}$ state in both the low density and high density samples

In all studies the sample was cooled in our a dilution refrigerator. Treatment with illumination from a red LED was used during the initial cool down. Resistance measurements were performed under quasi-dc conditions, $f < 15$ Hz, using a standard lock-in technique, with small excitation currents, $I_{AC} = 10 - 100$ nA. NMR measurements were performed at fixed field with the RF frequency swept through resonance at constant RF power (CW mode). RF radiation was applied transverse to the static B field using an 8 turn coil around the sample (details of the NMR coil and sample headers are given in Chapter 3). Fig. 6–7 shows a circuit diagram for our RDNMR measurement scheme. RF sweep and data acquisition was automated and controlled remotely by a computer. Throughout this chapter RF power amplitude is quoted by a decibel scale where for our setup a 0 dBm source corresponds to a 440 mV$_{pk-pk}$ sine wave applied to the top of the cryostat. The RF conditions (sweep rate, amplitude, etc.) and transport measurement parameters (sourcing current, lock-in time constant, etc.) were adjusted for each experiment as required. As a benchmark however, in 'a ''typical" RDNMR measurement we would shine a -13 dBm RF signal (which we estimate gives a few $\mu T$ field radiated at the sample) at an RF sweep rate of 300 MHz/3 s while monitoring the transport using 10 nA sourcing current and a 1 s measurement time constant on the lock-in.
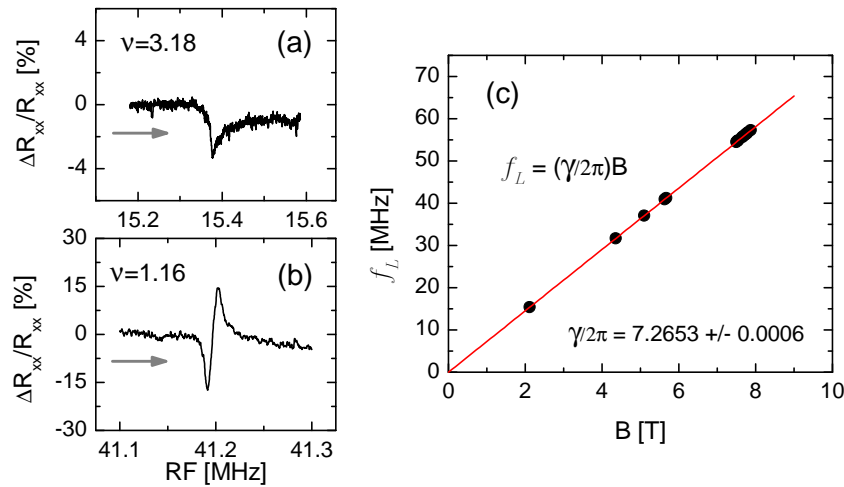
Figure 6–8: (a) RDNMR resonance at $\nu = 3.18$, in the flank of the $\nu = 3$ minimum. This represents an example of the "minimum-only" RDNMR signal measured at most filling factors. (b) Near $\nu = 1$ an anomalous dispersive lineshape is measured with a significantly enhanced response. The signal shown here was obtained at $\nu = 1.16$. Grey arrows indicate the frequency sweep direction of the transverse RF field. (c) Determination of the gyromagnetic ratio, $\gamma$, from the $^{75}$As resonance frequency measured at various B fields (filling fractions).

### 6.2.2   Anomalous signal near $\nu = 1$

Fig. 6–8a shows a typical "minimum-only" RDNMR response, measured in the flank of the $\nu = 3$ QHE minimum. The lineshape closely resembles the RDNMR signal reported in previous studies [8,14], with the minimum corresponding to the nuclear resonance condition as predicted by the hyperfine interaction picture. The lineshape shown here is strongly asymmetric with a sharp minimum first observed, followed by a long tail in the sweep direction. This lineshape is due to the frequency sweep rate being faster than the $T_1$ relaxation time where the sharp minimum corresponds to the resonance condition and the tail results from the exponential relaxation to the equilibrium magnetization away from the resonance condition.[2]   Using slow sweep rates (not shown), or under similar RF conditions and sweep rate, but at filling factors where the $T_1$ time is reduced (*i.e.*

---

[2] By sweeping the RF frequency in the so-called "adiabatic fast passage" [18] regime, where the frequency sweep is much faster than $T_1$, it is possible to not only destroy the nuclear polarization at resonance but to cause a complete inversion of the nuclear polarization if the duration of the sweep through resonance is appropriately tuned. This is analogous to the application of a $\pi$-pulse in pulsed NMR techniques.

at $\nu = 0.84$ in Fig. 6–9), a Lorentzian lineshape is observed, similar to that reported in Ref. [8]. Also consistent with other studies we were able to observe the RDNMR resonance response throughout the quantum Hall regime, at both integer and fractional quantum Hall states. In all NMR experiments described in the remainder of this chapter the $^{75}As$ nuclear resonance was chosen since this is the most abundant isotope in GaAs and thus gives the strongest signature [8]. In Fig. 6–8c the measured resonance frequency, $f_L$, is plotted against the corresponding magnetic field for several different filling factors. According to Eqn. 6.14, the slope of a fitted line gives the gyromagnetic ratio, which we find to be $\gamma_{75As} = 7.2653 \pm 0.0006$ MHz/T. This is slightly smaller than the accepted value found in literature of 7.3150 MHz/T [2]. Interestingly however our value is in close agreement with that reported in similar RDNMR experiments by Desrat *et al* who measured $\gamma_{75As} = 7.259$ MHz/T [8]. The discrepancy with the accepted value is small, less than 1%, and so could simply be due to miscalibration in the superconducting magnet/power supply. Alternatively, the measured error in $\gamma$ might be caused by the Knight shift since the RDNMR technique is only sensitive to atoms in close proximity to electrons in the 2DEG, *i.e.*, strongly coupled to the 2DEG electrons via the hyperfine interaction [3]. The Knight shift may explain why in both ours and in the study by Desrat *et al* the measured $\gamma$ is lower than expected since in the QH regime the electrons are expected to be either spin unpolarized, partially spin polarized or fully spin polarized, and not for example "anti"-spin polarized.

Near $\nu = 1$ we observed the previously reported "dispersive" lineshape [8–10, 14–16]. An example is shown in Fig. 6–8b where the usual resistance minimum is followed by a well defined "peak" in $R_{xx}$ at higher frequency. Additionally, the anomalous lineshape near $\nu = 1$ is found to be significantly enhanced compared with other filling factors under similar RF conditions. For example, when we observed a minimum-only, the resistance deviation at resonance was typically measured to be $\Delta R_{xx}/R_{xx} < 5\%$, whereas around $\nu = 1$ the response routinely gives up to 20% or more deviation in $R_{xx}$ at resonance.

Fig. 6–9 shows the evolution of the dispersive lineshape away from $\nu = 1$. In the left panel of Fig. 6–9, the filling factors where the RDNMR signals were measured are indicated by labeled dots on the magnetoresistance trace. It is important to note that application of the RF radiation induces non-resonant heating that changes the shape of the magnetoresistance. By comparing the values of $R_{xx}$ with the RF on but away from resonance, with values of $R_{xx}$ measured by heating the sample with the RF off, we can deduce the amount of non-resonant heating caused by the RF. A full analysis of the RF non-resonant heating is given in section 6.2.4. According to our calibration in Fig. 6–14,
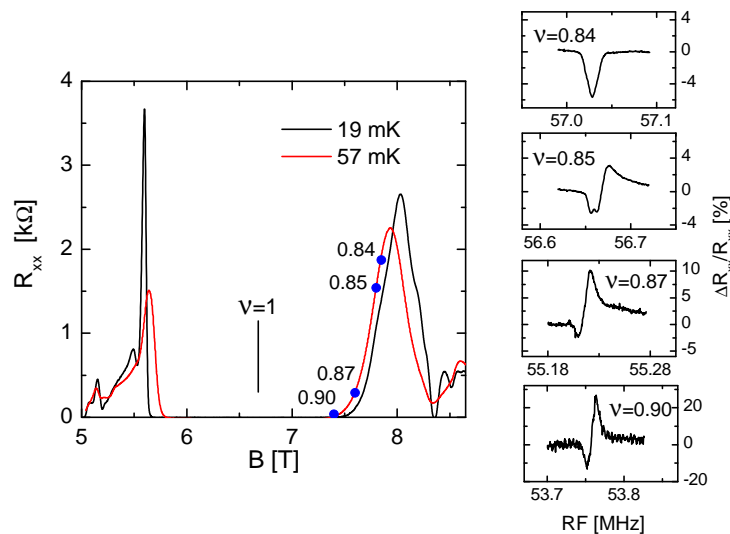
Figure 6–9: RDNMR lineshape as a function of filling fraction around $\nu = 1$. The lineshape continuously evolves from a dispersive shape near $\nu = 1$ to a minimum-only as the filling fraction is decreased. Left panel indicates (blue dots) where in the magnetoresistance the signals were measured.

a -13 dB RF signal corresponds to $\sim$40 mK heating above base, consistent with the data shown Fig. 6–9a.

In the right panel of Fig. 6–9, the crossover from a dispersive line shape near $\nu = 1$ to a minimum-only response away from $\nu = 1$ is shown. In agreement with a similar study by Kodera *et al.* [14] a continuous evolution between the two signal shapes is observed. However, whereas Kodera *et al* report a dispersive shape persisting all the way to $\nu = 0.82$ in our sample the signal already shows a Lorentzian shaped pure minimum by $\nu \sim 0.84$. Differences between the two studies might be sample dependent, as our 2DEG has a significantly higher mobility ($16.6 \times 10^6$ cm$^2$/Vs) compared with their sample ($1.8 \times 10^6$ cm$^2$/Vs). However this is more likely attributable to differences in the experimental conditions. For example, we found that increasing the RF power can change the resonance from a minimum to dispersive shape, with the RF amplitude where this transition occurs dependent on the filling factor. We also found the RDNMR lineshape to vary significantly with sample temperature. Our investigation of the temperature and RF effects on the dispersive lineshape is presented in detail in the following.

### 6.2.3   Temperature dependence

Fig. 6–10 shows the magnetoresistance around $\nu = 1$ as a function of sample temperature. As the temperature increases the minimum collapses causing the resistance peaks on
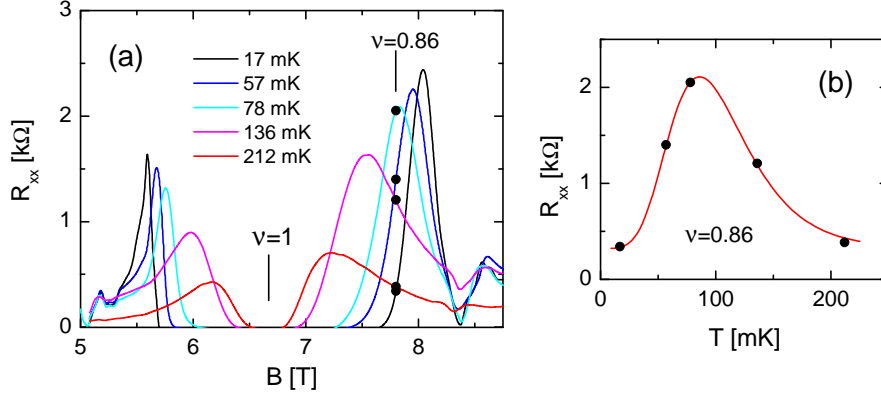
Figure 6–10: (a)$R_{xx}$ versus temperature around $\nu = 1$ (b) Example of the variation in $R_{xx}$ at fixed filling factor ($\nu = 0.86$) as the temperature is varied.

either side of the minimum to converge. In Fig. 6–10b an example is shown of the corresponding change in $R_{xx}$ at a fixed fraction in the flank of the initial minimum. As seen in the figure the resistance first increases with temperature ($dR_{xx}/dT > 0$), but then crosses over to a regime where the resistance decreases with further temperature ($dR_{xx}/dT < 0$). In general the behaviour is complex with no specific theory available to predict the functional dependence on temperature (the solid curve in Fig. 6–10 is a "guide-to-the-eye") [16].

Fig. 6–11 shows the evolution of the dispersive lineshape with temperature at fixed filling factor. The data in Fig. 6–11a was acquired at $\nu = 0.85$, and at an applied RF power -17 dB. Fig. 6–11b shows a second data set acquired on a separate cooldown at $\nu = 0.86$ and at a much lower RF power of -25.5 dB. The temperatures reported are the electron temperature, corrected for non-resonant electron heating due to the applied RF radiation (see section 6.2.4 ). Despite the differences in the experimental conditions the two figures show similar qualitative behaviour. Both the minimum and peak responses diminish with increasing sample temperature. Interestingly, the anomalous peak seemingly disappears before the minimum even though the peak response is initially much stronger.

In Fig. 6–12 the percent deviation at resonance is plotted versus temperature. "Dataset 1" corresponds to the data in Fig. 6–11a while "Dataset 2" corresponds to Fig. 6–11b. Both the normalized minimum ($\Delta R_{xx}^{min}/R_{xx}$) and peak ($\Delta R_{xx}^{peak}/R_{xx}$) responses rapidly diminish with increased temperature. In the lower panels of Fig. 6–12 the corresponding variation of the background, off-resonance, resistance is also shown. Tracy *et al* recently argued that near $\nu = 1$ [16] the RDNMR response is essentially proportional to $dR_{xx}/dT$, pointing out that signals become very weak in regions where $|dR_{xx}/dT| \rightarrow 0$. Therefore,
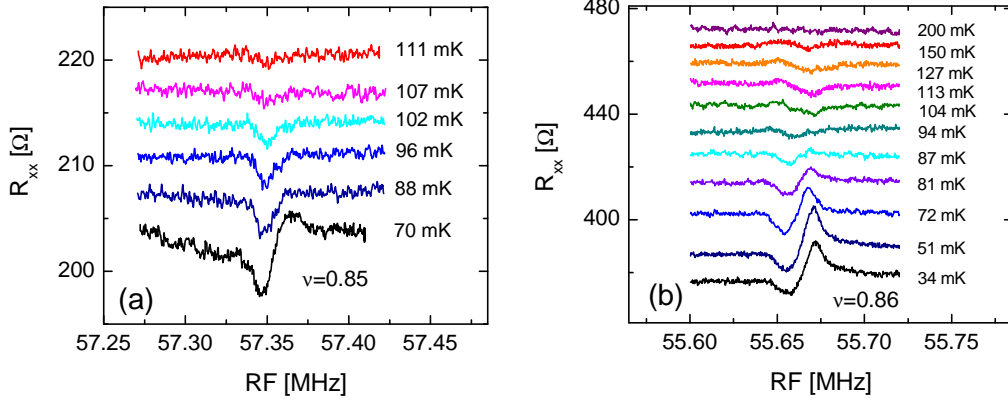
Figure 6–11: (a)Evolution of the RDNMR dispersive lineshape with increasing sample temperature. Temperatures quoted are the electron temperature, corrected for electron heating ($\nu = 0.85$, RF=-17 dB) (b) Similar data as in (a) but acquired on a separate cooldown ($\nu = 0.86$, RF=-25.5). In both (a) and (b) the vertical offset is adjusted arbitrarily for ease of comparison.

while the destruction of the RDNMR response with temperature could be due to a thermal destruction of the nuclear polarization (*i.e.* Fig. 6–2), it could also be correlated with $dR_{xx}/dT$ going to zero. The data in Fig. 6–12b was taken over a large temperature range where $dR_{xx}/dT$ transitions from $dR_{xx}/dT > 0$ to $dR_{xx}/dT = 0$ to $dR_{xx}/dT < 0$. Importantly, the signal does not recover in the negative $dR_{xx}/dT$ regime, where at base temperature we are readily able to observe an RDNMR signal (see for example Fig. 6–17). This might suggest that the destruction of the signal is due to a thermal reduction in the nuclear polarization ($B_N$), rather than due to variations in $R_{xx}$.

Recall that in the thermally activated regime the longitudinal resistance varies as $R_{xx} \propto e^{-g^* \mu_B (B+B_N)/k_B T}$. At resonance the nuclear polarization is destroyed causing $B_N$ to decrease by $\delta B_N$. The measured decrease in $R_{xx}$ is therefore given by

$$
\begin{aligned}
\Delta R_{xx} &= R_{xx} - R_{xx}^{'} &(6.28)\\
&\propto e^{g^* \mu_B (B+B_N)/2k_B T} - e^{g^* \mu_B (B+B_N-\delta B_N)/2k_B T}\\
&= e^{g^* \mu_B (B+B_N)/2k_B T}\left(1 - e^{-g^* \mu_B \delta B_N/2k_B T}\right)\\
&= R_{xx}\left(1 - e^{-g^* \mu_B \delta B_N/2k_B T}\right).
\end{aligned}
$$

In the low RF power limit where $\delta B_N$ is small ($<< B_N$) such that $g^* \mu_B \delta B_N << 2k_B T$ this gives
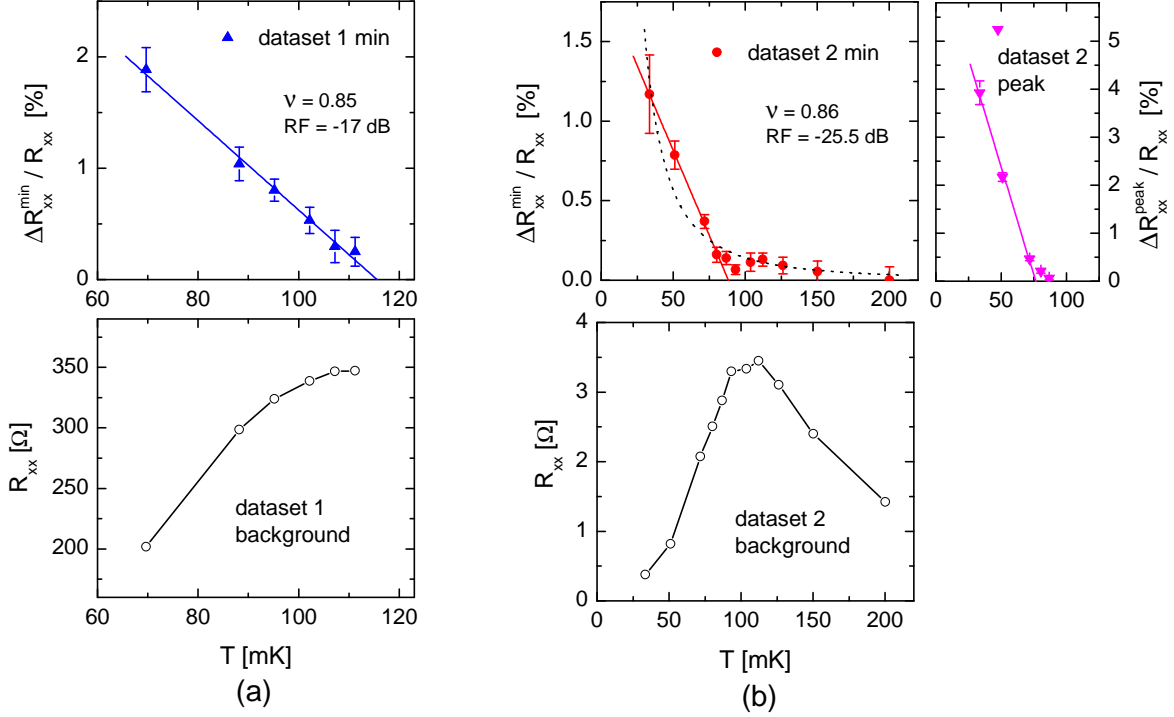
Figure 6–12: Normalized RDNMR response amplitude for both the minimum ($\Delta R_{xx}^{min}/R_{xx}$) and peak ($\Delta R_{xx}^{peak}/R_{xx}$) features in the dispersive lineshape. (a) Dataset 1 corresponds to the data in Fig. 6–11a. (b) Dataset 2 corresponds to the data in Fig. 6–11b. The lower panel in both (a) and (b) shows the corresponding variation in the off-resonant background resistance with temperature. Solid lines in the upper panels are linear fits to the data over a limited range. The dashed line in (b) is a fit of $\alpha/T^2$ showing good agreement in the high temperature regime, but poor agreement at low temperatures.

$$\Delta R_{xx}/R_{xx} \propto \frac{g^* \mu_B \delta B_N}{2 k_B T}. \tag{6.29}$$

If $\delta B_N$ is a small fraction of $B_N$, then we might expect $\delta B_N$ to remain constant with temperature. On the other hand, if the RF power is sufficient to completely destroy the nuclear polarization, the maximum possible variation to the Zeeman energy would correspond to $\delta B_N = B_N$. In this case $\delta B_N = B_N \propto \langle I_z \rangle$ where $\langle I_z \rangle$ is the mean nuclear polarization, which varies with the inverse temperature (from the Curie law, $M \propto 1/T$ where $M \propto \langle I_z \rangle$ is the magnetization). To first order therefore, we would expect the RDNMR response to vary with inverse temperature

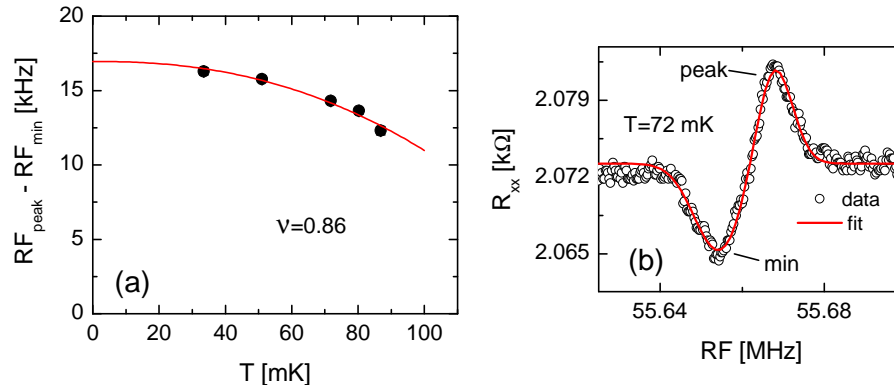$$\Delta R_{xx}/R_{xx} \propto \frac{1}{T^p} \tag{6.30}$$

Figure 6–13: (a) Temperature dependence of the resonant frequency shift between the peak and minimum in the dispersive RDNMR signals in Fig. 6–11b ($\nu = 0.86$ at low RF power (-25.5 dB)). The shift was extrapolated by fitting Gaussians to the data. An example is shown in (b) for the $T = 72$ mK signal.

where p is either 1 (low RF power) or 2 (high RF power). However, in Fig. 6–12a and 6–12b both the minimum and peak appear to decay *linearly* with temperature, consistent with a similar temperature dependence of the minimum-only signal reported previously by Zhang *et al.* [19]. In figure 6–12b we attempted to also fit a $\alpha(1/T^p)$ curve to the data. Allowing both $\alpha$ an $p$ to vary, no good fit could be found over the entire temperature range. However, setting $p = 2$ and and allowing only the coefficient, $\alpha$, to vary gave an excellent fit to the data in the "high-temperature" range (dashed line in the figure), with the low-temperature regime deviating from the trend. The temperature dependence therefore appears to initially exhibit a linear decay with increasing temperature, crossing over to power-law decay at higher temperatures. The power law regime may reflect sufficient thermal depolarization of the nuclei at these temperatures such that Eqn. 6.30 is a valid description. However, it should be stressed that the 1/T dependence predicted in Eqn. 6.30 was derived from Eqn. 6.28, which is only strictly valid in the thermally activated regime, *i.e.* in the low $R_{xx}$ tails of the LL. The data in Fig. 6–12 was acquired high on the flank of the $\nu = 1$ minimum and at high temperatures where it is not known how the DOS varies with temperature. The reason for a linear decay with temperature in the "low-temperature regime" is not known. This might be the result of an interplay involving both the thermal destruction of the nuclear polarization and the variation in the electron DOS with increased temperature.

In a recent investigation combining RDNMR with conventional NMR on GaAs single quantum well samples, Stern *et al.* reported evidence that the minimum in the dispersive

lineshape near $\nu = 1$ is Knight shifted due to nuclear interactions with polarized electrons in the 2DEG [9]. The peak however was found to coincide with *non-Knight shifted* resonant frequency position, *i.e.*, indicative of nuclear interactions with a fully unpolarized 2DEG. This suggests the two features of the dispersive signal results from distinct domains in the 2DEG consisting of polarized (RDNMR minimum) and un-polarized (RDNMR peak) regions. More recent studies by Kawamura *et al.* [10] involving dynamically polarized RDNMR measurements of the Knight shift have found further evidence in favour of two distinct spin-polarizations in the 2DEG. Prior to the development of the RDNMR technique, Barrett *et al.* examined the electron polarization around $\nu = 1$ using optically pumped NMR on a multiple quantum well GaAs sample [3]. They found a well defined Knight shift in the conventional NMR spectrum near $\nu = 1$ that decreased with increasing temperature. In Fig. 6–13 the difference in the frequency position of the peak and minima from our data in Fig. 6–11b is plotted as function of the corresponding electron temperature. The data shows a clear trend, indicating a decreasing separation between the features with increasing temperature. If we assume that the separation corresponds to the Knight shift, as suggested by Stern *et al.* [9], then the data in Fig. 6–13 suggests a decreasing Knight shift with increasing temperature, in qualitative agreement with the findings of Barrett *et al.* Furthermore, extrapolating our data to the $T = 0$ limit suggests a saturated Knight shift (*i.e.* saturated electron spin polarization) at $\nu = 0.86$ of 16-17 kHz, which is similar to the value of ∼12 kHz reported by Barret *et al.* at this filling fraction in a sample with similar 2DEG parameters (the Barrett quantum well width was 30 nm with electron density $n_e = 1.4 \times 10^{11}$ cm$^2$). In this interpretation, our data suggests a strong temperature dependence for the Knight shift in the low temperature limit. By contrast, Barrett *et al.* reported a saturation in the Knight shift at $\nu = 0.98$ for temperatures below ∼2 K. On the other hand, at lower filling fraction ($\nu = 0.88$) they did not observe saturation in the Knight shift down to their lowest temperature of 1 K, which may be consistent with our finding. In a later study, Melinte *et al.* performed a similar measurement as Barrett, on a multiple quantum well sample but at lower temperatures where optical pumping enhancement of the nuclear polarization was not required [20]. They found a similar saturation in the Knight shift with decreasing temperature, with only a small variation (a few kHz) observed between 0.1 K and 1 K at $\nu = 1$. However, they did not study the temperature dependence away from $\nu = 1$, where deviation away from full spin polarization (Skyrmions) is expected. A more thorough examination of the temperature dependence in the peak-min frequency separation will be necessary to confirm whether this relative shift is indeed related to the Knight shift.
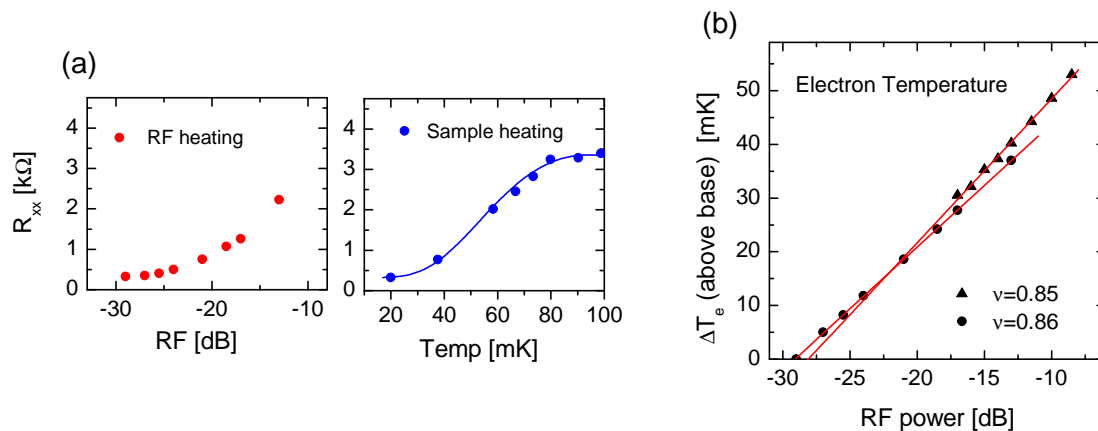
Figure 6–14: Determination of the electron temperature due to non-resonant RF heating. (a) Variation in $R_{xx}$ caused by varying the RF power (left) compared with similar variation (right) caused by heating the sample with no RF applied ($\nu = 0.86$). (b) Calibration of the electron heating above base temperature as a function of applied RF power. Two datasets are shown acquired on separate cooldowns with solid red circles acquired at $\nu = 0.86$ (corresponding data is shown in (a)) and solid blue circles acquired at $\nu = 0.85$. Solid lines are linear fits to the data.

### 6.2.4    RF power dependence

The magnitude of the RDNMR response, $\Delta R_{xx}/R_{xx}$, is determined by the variation in nuclear polarization on resonance ($\delta B_N \propto \langle I_z \rangle$) which in turn is dependent on several factors including: the nuclear polarization at thermal equilibrium (*i.e.* away from resonance); the $T_1$, and $T_2$ relaxation times; and the magnitude of the applied transverse RF radiation. The nuclear polarization and nuclear relaxation times are intrinsic properties of the sample that in general can not be tuned other than by varying the sample temperature, or employing a dynamic pumping technique. On the other hand increasing the RF amplitude should more effectively destroy the nuclear polarization on resonance and therefore yield a larger response. However, shinning RF radiation on the sample can also cause non-resonant heating and as discussed in the previous section, sample heating can rapidly destroy the RDNMR signal. In order to maximize the RDNMR response, as well as to have accurate knowledge of the electron temperature in our RDNMR experiments, is important to determine the RF induced electron heating.

To measure the non-resonant RF heating we can correlate variations in the off-resonance magnetoresistance, $R_{xx}$, for different applied RF powers, to similar variations in $R_{xx}$ observed when varying the fridge temperature but with the RF turned off. An example is shown in Fig. 6–14a, acquired at $\nu = 0.86$. The solid circles (left panel in Fig. 6–14a) shows the result of varying the RF power while keeping the fridge at base temperature, and the
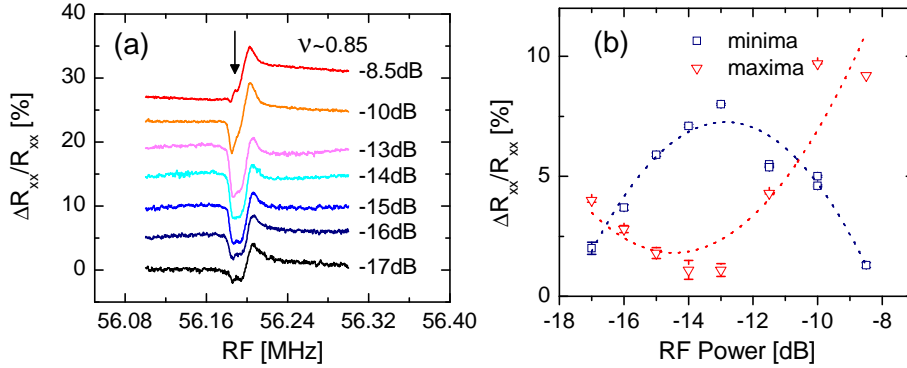
Figure 6–15: (a)RDNMR response versus applied RF power. Data is vertically offset for comparison ($\nu = 0.85$). Black arrow indicates the appearance of a second peak in the spectrum at large RF powers. (b) Normalized minimum and peak responses plotted versus RF power. The minimum first grows and then diminishes to zero. By comparison the peak first diminishes to zero and then grows stronger. Dotted lines are a guide-to-the-eye.

solid circles (right panel in Fig. 6–14a) corresponds to varying the fridge temperature with the RF turned off. Comparing the two plots gives a calibration for the electron heating. In Fig. 6–14b the deduced electron heating (relative to base temperature) is plotted versus applied RF power. The solid circles correspond to the data shown in Fig. 6–14a. The solid triangles are from a second data set (taken at $\nu = 0.85$), acquired on a separate cooldown and extending to higher RF powers. Both data sets show a clear linear relation between the applied RF power and resulting electron heating, with the slope and y-intercept determined by fitting a straight line (solid curve) similar between the two data sets. Averaging together the fitted curves in Fig. 6–14 gives an approximate general relation between the applied RF power and electron heating

$$\Delta T_e = (2.4 \pm 0.2) RF_{power} + (71 \pm 4) \qquad (6.31)$$

where $\Delta T_e$ is the electron heating above base temperature. This relation was found to hold true at other filling fractions around $\nu = 1$.

Fig. 6–15 shows the effect of varying the RF power on the dispersive lineshape. In Fig. 6–15b the normalized minimum and peak responses are plotted versus applied RF power. Surprisingly the two features behave oppositely. The minimum first increases with RF power and then decreases as the power is further increased. The most obvious explanation for this behaviour is that the initial increase in the RF power enhances the RDNMR response at resonance, *i.e.*, by destroying a larger fraction of the polarized nuclei. As the RF power is further increased however, non-resonant heating may begin to cause a
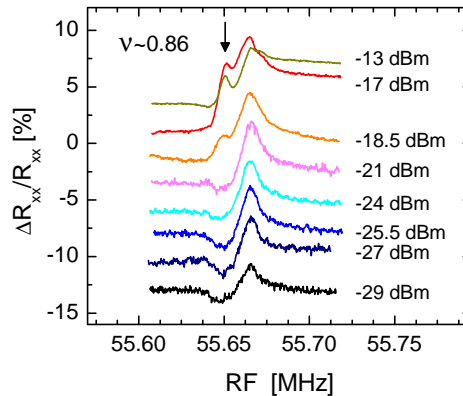
Figure 6–16: (a) Similar RDNMR versus RF power data as presented in Fig. 6–15 but acquired on a separate cooldown and slightly different filling factor ($\nu = 0.86$). Data shows similar behaviour with again a second peak emerging in the spectrum at large RF powers (indicated by the black arrow).

reduction in the equilibrium nuclear polarization, thus weakening the RDNMR response. In contrast, the peak response initially diminishes with increasing RF power but then grows dramatically. The reason for this opposite behaviour of the peak response, compared with the minimum, is not understood. The enhancement of the peak is especially mysterious considering the temperature dependence examined in the previous section where both the peak and minimum were found to rapidly diminish with temperature, and with the peak seemingly more sensitive (*i.e.* diminishing rapidly) to temperature effects. It should be stressed that the peak response cannot be explained by the usual hyperfine interaction description of the RDNMR signal, which predicts a minimum-only response. The opposite, and contradictory, behaviour of the peak response versus the minimum with varying RF power may indicate the two features result from very different mechanisms.

Another intriguing feature in the RF dependence in Fig. 6–15 is the emergence of second peak in the RDNMR spectrum (indicated in the figure by an arrow) at higher RF powers. Fig. 6–16 shows a second study of the RF power dependence acquired during a separate cooldown. Again, the second peak emerges upon increasing the RF power. In both figures the appearance of the second peak seems to coincide with a very long tail that does not decay back to the equilibrium $R_{xx}$ within the scan time (all scans are swept from low to high frequency), suggesting this secondary peak exhibits a lengthy $T_1$ relaxation time. The origin of the second peak is unknown. This peak could possibly be a satellite of the main peak, resulting from the quadrupole splitting. However, the peak-to-peak separation is $\sim$10 kHz, which is more than 2 times smaller than the quadrupolar splitting reported
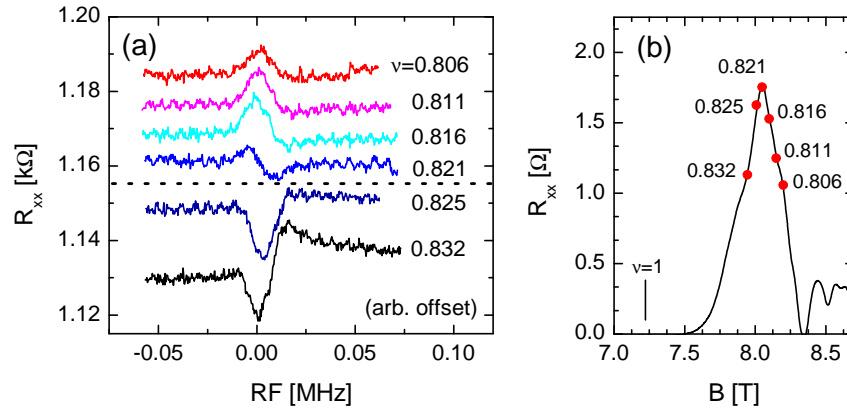
Figure 6–17: (a) RDNMR signal versus filling fraction in the high field flank of the $\nu = 1$ minimum showing lineshape inversion. Dashed line separates the "normal" signal (below the line) from the inverted signal (above the line). For ease of comparison the signals are shifted along the horizontal and vertical axis. (b) Magnetoresistance trace in the $\nu = 1$ flank. Filled circles label the NMR signals measured in (a).

previously for As in GaAs quantum well samples [8, 21]. Furthermore, it is unclear why the quadrupole satellite would coincide with a significantly enhanced $T_1$ relaxation time[3] .

### 6.2.5   Current induced lineshape inversion

In an effort to understand the origin of the peak in the dispersive lineshape, Tracy *et al.* argued in a recent study that the lineshape could be understood from the perspective of electronic temperature [16]. They found that as the filling factor was changed through a region where $dR_{xx}/dT$ changes sign, the shape of the signal undergoes an inversion. Since the lineshape inversion closely tracks the change of sign in $dR_{xx}/dT$, it was argued the signal results from a cooling of the electron gas on the low frequency side of the resonance, followed by a heating on the high frequency side. However, the mechanism causing cooling versus heating around the resonance could not be explained.

In Fig. 6–17 we reproduce the basic results of Tracy *et al.* where we observe a similar inversion of the lineshape when varying the filling factor through a region where $dR_{xx}/T$ changes from positive to negative. Comparing the lineshapes at different filling factors by

---

[3] The apparent increase in $T_1$ together with the emergence of the second peak could be a coincidence. For example, the increasing $T_1$ time could result from increased nuclear depolarization at higher RF powers, while the appearance of the second peak is related to some other, unknown, RF power dependence.
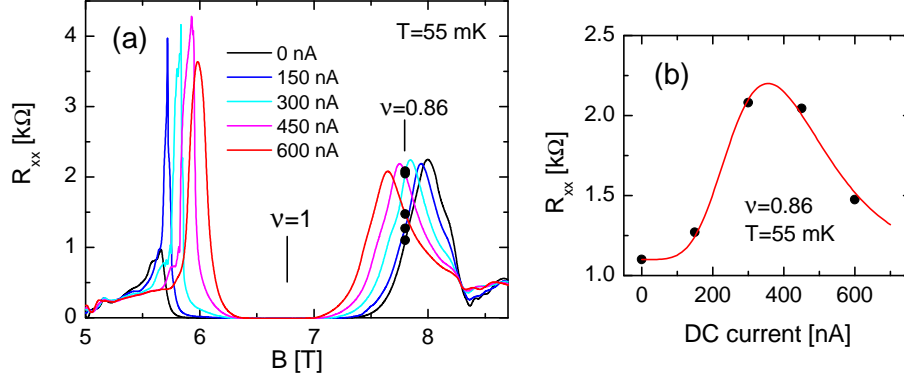
Figure 6–18: $R_{xx}$ versus temperature around $\nu = 1$ (b) Example of the variation in $R_{xx}$ at fixed filling factor ($\nu = 0.86$) as the temperature is varied. Both (a) and (b) indicate nearly identical behaviour with the temperature dependence shown in Fig. 6–10

varying the B field has the disadvantage of altering other important parameters, such as the coulomb interaction strength, which can confuse the data. We therefore looked for evidence of the same inversion but at fixed filling factor.

One effect of applying a DC current bias to a quantum hall sample is to heat the 2DEG. Fig. 6–18 shows the magnetoresistance around $\nu = 1$ as a function of applied DC current. In Fig. 6–18b the magnetoresistance, $R_{xx}$, versus the applied DC current is plotted for $\nu = 0.86$, which shows a nearly identical trend with the temperature dependent trace taken at the same filling filling factor in Fig. 6–10. By comparing current induced variations of the magnetoresistance with temperature induced changes in the resistance (*i.e.* with no DC current applied), the electron temperature resulting from the applied DC current can be determined [22–25]. Importantly, this suggests there is a direct relationship between the sign of the current dependence of the magnetoresistance ($dR_{xx}/dI_{DC}$) and sign of the temperature dependence ($dR_{xx}/dT$). Applying a DC current therefore gives us a means to directly vary the electron temperature and thereby tune $dR_{xx}/dT$ at a *fixed* filling factor. Since at the ultra-low temperatures of our experiments the electrons are effectively thermally decoupled from the lattice [9] heating the electron 2DEG directly should not significantly affect the lattice temperature, and therefore should not disturb the nuclear polarization. In principle therefore, sweeping the DC current should allow us to tune $dR_{xx}/dT$ at fixed filling factor with less reduction of the RDNMR signal than would be caused by heating the entire sample (*i.e.* by raising the fridge temperature).

Fig. 6–19 shows the RDNMR signal as a function of applied DC current at fixed filling factor ($\nu \sim 0.84$). The data was acquired by stepping the $I_{DC}$ in regular intervals
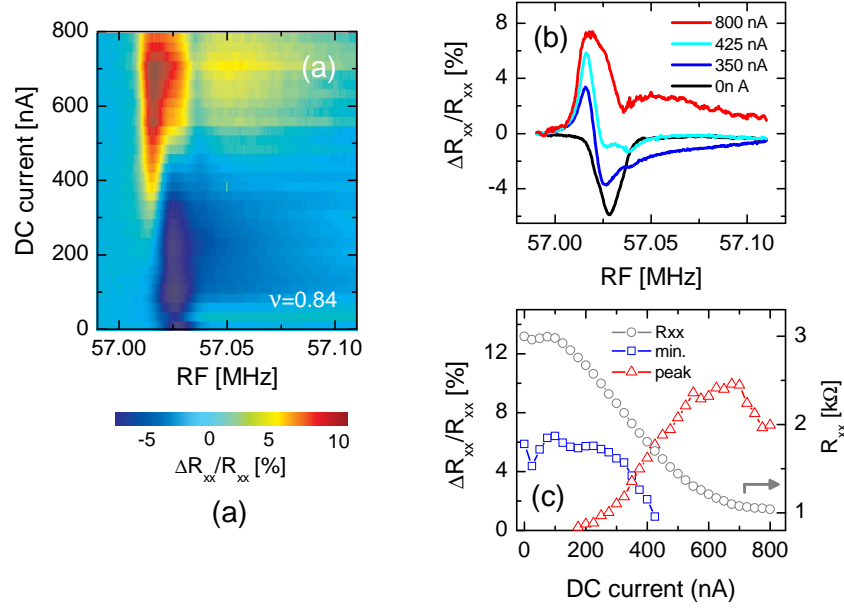
Figure 6–19: 2D contour map of the RDNMR lineshape versus DC current bias at $\nu = 0.84$ (RF = -13 dBm, $T_e \sim 60$ mK at $I_{DC} = 0$ nA). (b) Selected traces from the contour plot in (a). (c) Normalized min. (open squares) and peak (open triangles) versus applied Current, plotted along with the corresponding off-resonant background resistance (open circles). As the DC current is increased the signal transitions from a minimum-only to peak-only signal.

and sweeping the RF frequency through resonance at each DC current value. All DC current biased contour maps presented in the remainder of this chapter were acquired in the same way. In each case the RF frequency scan rate was 300 Hz/3 s with a 10-15 mins pause between increasing the DC current and beginning the RF sweep to allow the system to stabilize. The DC current step-size was chosen to give a total scan time of $\sim$10 hrs. During the scan the magnet was held in persistent mode with the magnet power supply turned off. Comparison between RDNMR signals acquired on a similar time scale without changing any RF or sample parameters allowed us to estimate the NMR frequency shift due to magnet drift to be less than $\sim$400 Hz/hr. Importantly this is significantly less than the width of the RDNMR signal which we typically measured to be $\sim$10 kHz.

The RDNMR signal at $I_{dc} = 0$ nA in Fig. 6–19 is the same "minimum-only" signal shown in Fig. 6–9. As the DC current is increased the initial minimum-only signal transitions to an inverted dispersive signal before becoming a "peak-only" response at large current values. In Fig. 6–19b it appears that the position in frequency of the inverted peak does not coincide with the initial minimum, being shifted downwards by $\sim$10 kHz. This is supported by the 2D map in Fig. 6–19a which shows that the down-shifted peak develops

alongside the minimum, giving a dispersive lineshape over a range of nearly 200 nA DC current (centered around $\sim$400 nA) until at higher current the minimum disappears and only the peak remains. In Fig. 6–19c the magnitude of the normalized minimum ($\Delta R_{xx}/R_{xx}$ - open squares) and peak (open triangles) is plotted together with the off-resonant background resistance ($R_{xx}$ - open circles). As can be seen, the current induced signal inversion occurs in a region, near $\sim 400$ nA, where $dR_{xx}/dI_{DC}$ (and we assume therefore $dR_{xx}/dT$) is always negative. The inversion therefore does not seem to coincide *directly* with the sign change in $dR_{xx}/dI$ ($dR_{xx}/dT$). Since the data was acquired at constant field (fixed filling fraction) the resonance condition is expected to remain unchanged. The sizable shift in the position of the resonance, together with the evolution from a minimum-only, to dispersive, to peak-only lineshape, suggests that the lineshape inversion is not a direct "flip" of the initial minimum, but instead the result of a more complex process, possibly involving two distinct mechanisms.

Despite the significant heating caused by the applied DC current (the electronic temperature at $I_{dc} = 800$ nA was estimated to be $\sim$200 mK) the NMR signal remains surprisingly strong, with the $\Delta R_{xx}/R_{xx}$ measured at $I_{DC} = 800$ nA nearly 1.5 times larger than at $I_{dc} = 0$ nA. This compares with Fig. 6–11 where at similar filling factors and RF conditions, the RDNMR signal was completely destroyed at these temperatures. This is possibly consistent with the current-induced heating predominantly affecting the electron temperature without much changing the nuclear temperature. Alternatively, the observed *enhancement* of the down-shifted peak compared with the initial minimum might indicate that the DC current enhances the nuclear polarization, consistent with recent reports of DC current-induced dynamic nuclear polarization (DNP) near $\nu = 1$ by Kawamura *et al.* [10, 19, 26].

Fig. 6–20 shows the result of repeating the same measurement but at $\nu = 0.896$. At this higher filling fraction (lower field) $dR_{xx}/dI_{DC}$ ($dR_{xx}/dT$) is positive over the same range of DC current values as in Fig. 6–19. Interestingly, the lineshape remains dispersive at all DC current values with no inversion. With increasing current the signal initially diminishes but then reemerges showing a strong minimum even in the flat region where $dR_{xx}/dI_{DC} \rightarrow 0$. This behaviour is again consistent with the DNP interpretation where initially the signal diminishes (possibly due to $dR_{xx}/dI$ becoming small), but then strengthens at higher current as the nuclei are dynamically polarized.

We again performed the same DC current bias experiment, but at intermediate filling fraction, $\nu = 0.863$, where the signal again shows an initially dispersive lineshape.
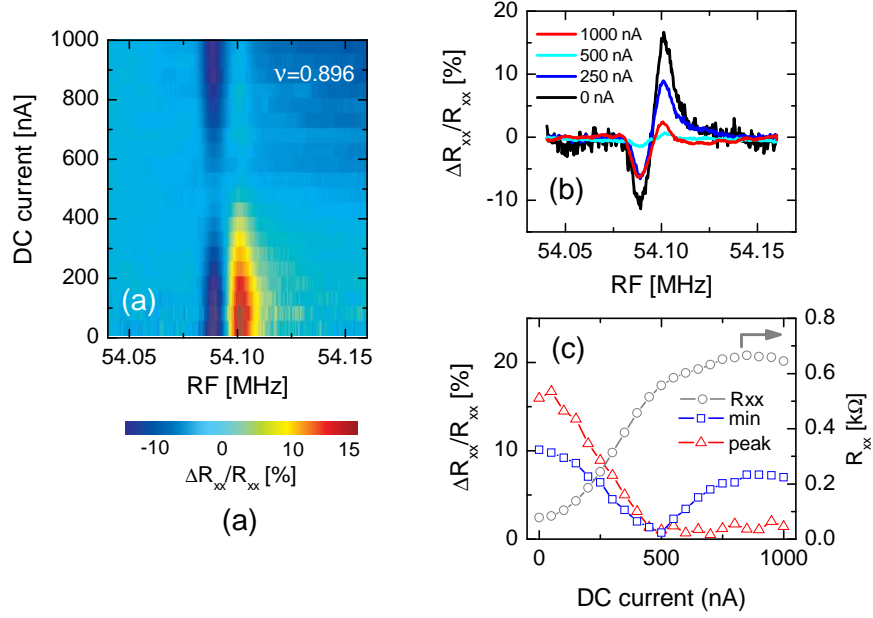
Figure 6–20: (a) 2D contour map of the RDNMR lineshape versus DC current bias at $\nu = 0.896$ (RF = -25.5 dBm, $T_e = 34$ mK at $I_{DC} = 0$ nA). (b) Selected traces from the contour plot in (a). (c) Normalized min. (open squares) and peak (open triangles) versus DC current bias, plotted along with the corresponding off-resonant background resistance (open circles). No signal inversion is observed over the DC current range shown here

However, at this filling fraction and RF parameters and background, off-resonance, resistance was sufficiently high in the flank (with no DC current applied) that collapse of the $\nu = 1$ minimum by current heating allowed us to probe both the $dR_{xx}/dI_{DC} > 0$ and $dR_{xx}/dI_{DC} < 0$ regimes within the limitations of our $I_{DC}$ scan range. Fig. 6–21a shows the corresponding 2D contour plot. As with the previous two scans the RDNMR signal initially disappears with applied current. As $I_{DC}$ is further increased the minimum re-appears giving a minimum-only lineshape for a several hundred nA range around 400 nA. Finally, at large current a second peak (labeled "peak 2" and indicated in the figure by a black arrow) appears but on the low frequency side of the minimum, similar to what was seen in Fig. 6–19. In short, complete inversion of the lineshape is observed, occurring by a process where the peak on the high side of the minimum first disappears, and then re-emerges on the low frequency side. Consistent with the data in Fig. 6–19 this suggests the lineshape inversion is not a simple "flip" of the minimum and peak; rather the peak shifts from the high frequency side to the low frequency side. Interestingly, there is no indication that the peak "crosses" the minimum, *i.e.* we do not observe a systematic reduction in the frequency separation of the minimum and peak as the DC current is increased from zero,
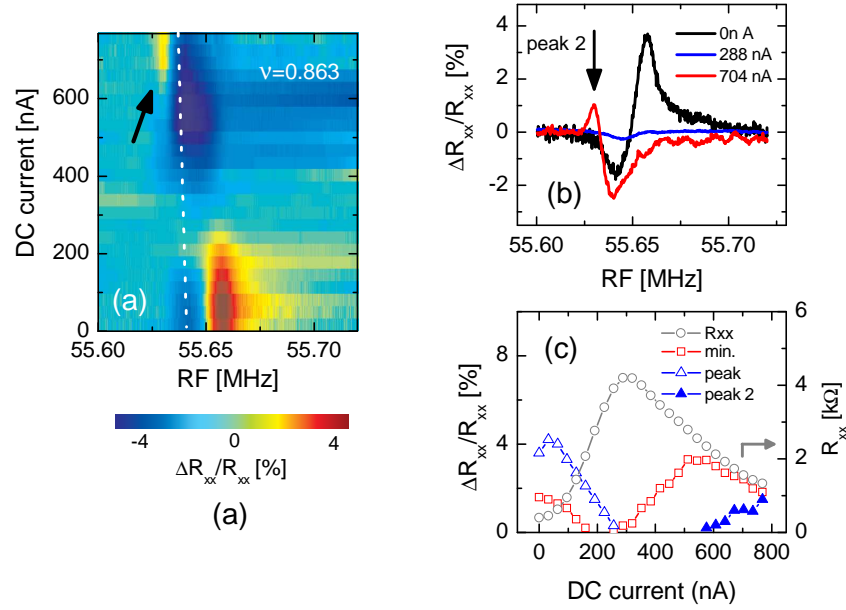
Figure 6–21: (a) 2D contour map of the RDNMR lineshape versus DC current bias at $\nu = 0.863$ (RF = -25.5 dBm, $T_e \sim 34$ mK at $I_{DC} = 0$ nA). Dotted line indicates the expected frequency shift over the time of the scan due to the magnet drift. (b) Selected traces from the contour plot in (a). (b) Normalized min. (open squares) and peak (open triangles) versus DC current bias, plotted along with the corresponding off-resonant background resistance (open circles). "Peak2" (closed triangles) labels the down-shifted peak, indicated in (a) and (b) by a black arrow. As the DC current increases, the initial peak on the high frequency side of the dispersive lineshape disappears and then re-emerges on the low frequency side. By contrast the min. initially disappears, and then re-emerges at the same frequency.

at least within the resolution of our current steps. We also note that in both Fig. 6–19 and Fig. 6–21 the lineshape inversion appears well into the negative $dR_{xx}/dI_{DC}$ ($dR_{xx}/dT$) region and so does not appear to coincide directly with a change in sign of $dR_{xx}/dI_{DC}$. Importantly, we never observed signal inversion in a region of positive $dR_{xx}/dI_{DC}$ when varying the DC current.

Finally, we examined the lineshape evolution under similar parameters as in Fig. 6–21 ($\nu = 0.863$, RF=-25.5 dB) but where we varied the sample temperature by varying the fridge temperature. A 2D contour map of the resulting data is shown in Fig. 6–22. Like in the previous $I_{DC}$ experiments the RDNMR signal initially diminishes when heating the sample. However, unlike in the previous experiments the signal does not recover to its initial strength with continued heating. This is further evidence that the signal enhancement seen at large DC current likely results from a DNP mechanism. Closer examination of the high-temperature curves (Fig. 6–22b) reveals that the signal *does* persist to high temperature
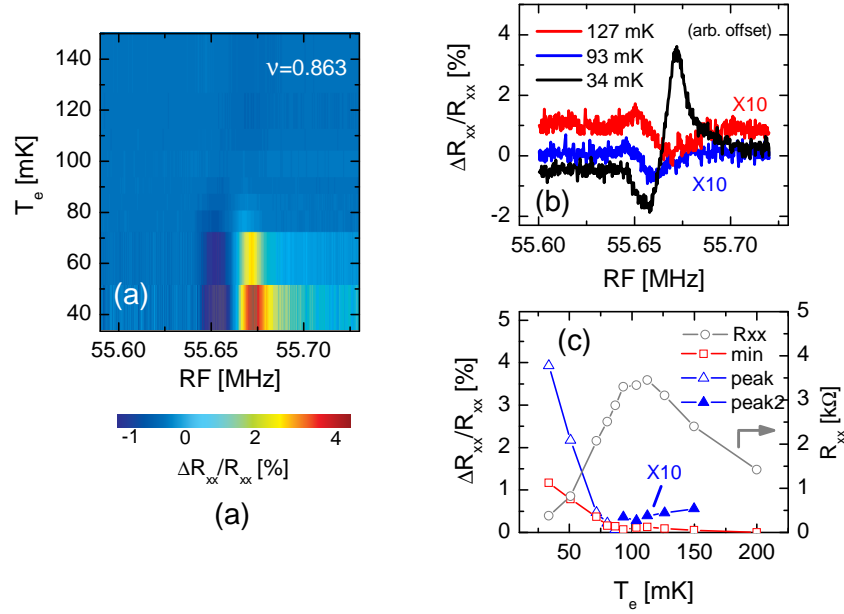
Figure 6–22: (a) 2D contour map of the RDNMR lineshape versus sample temperature ($I_{DC} = 0$) at $\nu = 0.863$ (RF = -25.5 dBm, $T_e \sim 34$ mK at base fridge temperature). (b) Selected traces from the contour plot in (a) (data is vertically offset for clarity).(c) Normalized min. (open squares) and peak (open triangles) versus DC current bias, plotted along with the corresponding off-resonant background resistance (open circles). As the temperature increases, an inversion in the lineshape is observed, similar to that seen in Fig. 6–21.

but is very small, barely perceptible above the background noise. Importantly we can clearly discern an inverted dispersive lineshape in the high temperature curves (the 93 mK and 127 mK traces in Fig. 6–22b are multiplied by a factor of ten and offset vertically for comparison with the initial base-temperature signal). Fig. 6–22c shows the temperature evolution of the minimum and the two peaks together with the the background resistance. In contrast to the current induced inversion discussed previously, the purely temperature-induced inversion begins to appear before $dR_{xx}/dT$ becomes negative, *i.e.*, the down-shifted peak first emerges in the region where $dR_{xx}/dT$ appears flat and then continues to grow in the negative $dR_{xx}/dT$ region. It is unclear why the down-shifted peak should appear sooner when varying the sample temperature compared with DC induced heating. It might be that the sizable minimum seen in this same region in the DC current bias data (which we believe results from DNP) simply obscures the initial appearance of a down-shifted peak. We also note that the minimum in the high temperature traces does not appear at the same frequency as in the initial dispersive signal. This might result from a decrease in the Knight shift at elevated temperatures as described in Fig. 6–13. We caution however

that the temperature dependent data given in Fig. 6–22 was acquired over the course of several days. On such a long time scale, small variations in the sample features including apparent shift in the density and changes in the $R_{xx}$ peak height in the insulating regime are not uncommon. A more careful study of the temperature induced lineshape inversion is therefore necessary to investigate the apparent frequency shift in the minimum more fully.

### 6.2.6  Summary

In summary we have studied the anomalous dispersive lineshape near filling fraction $\nu = 1$ under a variety of sample and RF conditions. In all cases the peak appears to behave quite differently than the minimum, which suggests the peak and minimum possibly arise from distinct mechanisms. For the first time we report observation of a lineshape inversion resulting from application of a DC current bias. The inversion is not found to be a simple peak-to-minimum flip and vice versa. Instead the inversion proceeds by the peak first decaying to zero on the high frequency side of the minimum and then re-emerging on the low-frequency side, with the minimum frequency position remaining relatively unchanged. A similar inversion is observed under identical RF conditions but by varying the sample temperature with no current DC applied. This suggests the inversion is primarily due to current-induced heating. We observe the inversion to occur in regions where $dR_{xx}/dT$ is positive *and* negative. This suggests the $\nu = 1$ anomalous lineshape may not be entirely determined by the sign of $dR_{xx}/dT$ as previously reported by Tracy *et al.* [16]. Finally, application of the DC current appears to enhance the RDNMR minimum signal, possibly by increasing the nuclear polarization through DNP. It might therefore be possible to enhance the RDNMR response at other filling factors by a similar application of DC current. However, the DC current also alters the lineshape and so might actively alter the electronic state. Further investigation of the DC current biased RDNMR technique is required to explore this possibility.

From our temperature dependent study we speculate that the peak and minimum separation corresponds to the Knight shift. This is consistent with previous work where combining RDNMR in the 2DEG with with conventional NMR on the bulk it was suggested that the anomalous peak coincides with the non-Knight shifted resonant frequency [9]. Our data could be taken as further evidence of two distinct spin-polarization domains around $\nu = 1$ with the minimum response corresponding to nuclear interactions with a fully or partially polarized electron state, while the peak indicates a fully unpolarized electron spin domain. However, it should be cautioned that there is no theory at present that indicates a resistance peak should be observed for a spin unpolarized electron state. Furthermore,

it is difficult to account for the current-induced signal inversion in this model since it is unclear how the peak signal, if arising due to an unpolarized regime, could be shifted to the low frequency side of the minimum. If for example the DC current caused the unpolarized electron regime to become polarized, this could explain the frequency shift (Knight shift) but then we would likely expect the signal to become a minimum, much like the initial (polarized) minimum. If on the other hand the applied current caused a complete inversion of the spin polarization (becoming anti-polarized) the peak position would rather shift in the other direction, *i.e.* towards even higher frequencies. Furthermore, the dispersive lineshape becomes stronger as the filling fraction is varied towards $\nu = 1$, where the system is expected to be fully spin polarized.

While our data shows distinct differences between the behaviour of the minimum and peak features in the dispersive lineshape, the origin of the peak remains unknown. Most likely the minimum can be understood by the hyperfine interaction picture, whereas the peak appears to be specific to the sample condition and filling factor. Importantly, several studies have observed the dispersive lineshape and also a peak-only signal at higher fields (lower filling fraction) [9, 15, 17]. Understanding the origin of the "anomalous" peak in the RDNMR tool therefore remains an important question; one that will likely lead to new insight into the often subtle details of the quantum Hall effect.
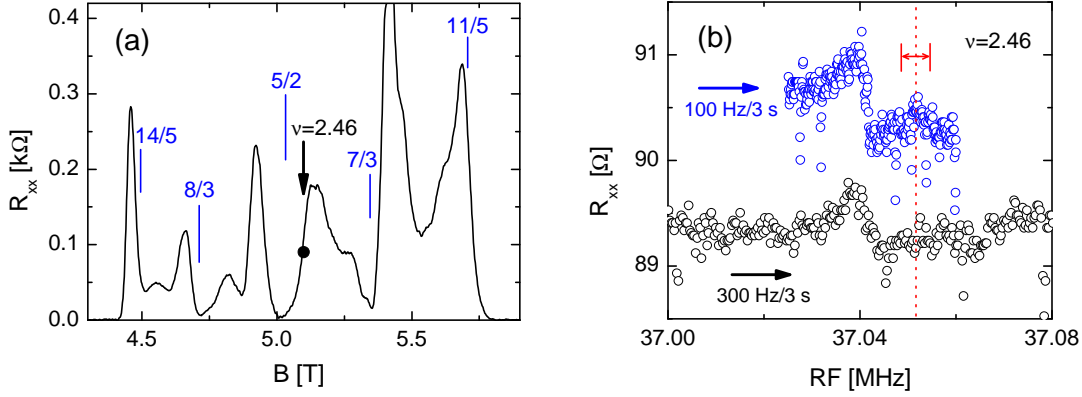
Figure 6–23: Measurement of an RDNMR response at $\nu = 2.46$, in the flank of the $\frac{5}{2}$ minimum. (a) Magnetoresistance trace around $\nu = \frac{5}{2}$ at base temperature ($T = 19$ mK). Black arrow/dot indicates position where RDNMR signal is measured. (b) RDNMR response showing a weak but discernible response (RF=-17 dB, $I_{AC} = 100$ nA). Lower scan was performed at 300 Hz/3 s. Upper scan was a performed several hours later at 1/3 the scan speed, 100 Hz/3 s. Vertical dashed line indicates the expected resonance position based on the gyromagnetic ratio deduced from Fig. 6–8

## 6.3   Resistively detected NMR at $\nu = 5/2$

### 6.3.1   Measurement of RDNMR signal near $\nu = 5/2$

In the final section of this chapter I discuss our efforts to apply the RDNMR technique to probe the $\frac{5}{2}$ FQH state. Despite extensive efforts by several researchers, so far no one has reported measurement of an RDNMR response at $\nu = \frac{5}{2}$. There is no reason to believe, in principle, that quantum hall 2DEG should not yield a response at $\frac{5}{2}$ fractional filling, since the signal has been observed throughout the quantum Hall regime, at both integer and fractional filling [8], and also at half filling in the LLL [9, 17]. We therefore tried to measure a $\frac{5}{2}$ RDNMR response by examining both of our very high quality 2DEGs, under a wide variety of RF and sample conditions. Recently we were able to observe a weak, but clearly discernible signal in the high field flank of the $\frac{5}{2}$ minimum in our high density sample (Fig. 6–23). The two RDNMR scans shown in Fig. 6–23b were acquired at $\nu = 2.46$ using a fairly moderate RF power of -17 dB, but using a relatively large AC current amplitude of 100 nA. Fig. 6–23 shows the corresponding position in the magnetoresistance trace where the RDNMR response was obtained (indicated in the figure by a black arrow/dot). The two RDNMR measurements were taken several hours apart, with the upper scan acquired at 1/3 the frequency scan speed (100 Hz/3 s) of the lower scan (300 Hz/3 s).

Both scans shown in the figure clearly show a resonance signal variation, however we note that within our resolution it is difficult to resolve the lineshape. Interestingly, the

resonance position is down-shifted from the expected frequency, based on our measurement of the gyromagnetic ratio (vertical dashed line in the figure). The down-shift in frequency could indicate a Knight shift in the resonance, which would be consistent with a fully spin-polarized $\frac{5}{2}$, as predicted by the Moore-Read Pfaffian description. However, we caution that the dashed line in Fig. 6–23 does not represent a true non-zero Knight shifted frequency position, since this is calculated from our measurement of the the gyromagnetic ratio in the same system, which is already biased by spin interactions between the nuclei and the 2DEG. A more complete study of the lineshape around the $\frac{5}{2}$ is required to further explore its interpretation, including an accurate measurement of the true non-shifted resonance frequency.

### 6.3.2   Improving the RDNMR signal with a resistance bridge

The signal response at $\frac{5}{2}$ in Fig. 6–23 is very small with $\Delta R_{xx}/R_{xx}$ less than 1%. Furthermore, this very weak signal was acquired at a relatively large AC current amplitude, which is known to significantly degrade the $\frac{5}{2}$ by electron heating. To be able to fully characterize the RDNMR signal around $\nu = \frac{5}{2}$ therefore requires that we either develop methods to enhance the signal response or improve the measurement signal-to-noise. Unfortunately, most paramater changes that could increase the RDNMR response, such as increasing RF power, AC current amplitude, etc. also lead to increased electron heating which can destroy the fragile $\frac{5}{2}$. We therefore designed a resistance bridge measurement scheme in an attempt to improve our signal-to-noise measurement sensitivity. Details of the four-terminal bridge design are given in section 3.3.3.

As a first proof-of-principle test we implemented the bridge scheme on the fridge, but with the same room-temperature preamp used in our conventional lock-in measurement scheme. Fig. 6–24 shows an example obtained by measuring the RDNMR resonance in the flank of the $\nu = 3$ QHE minimum. The conventional lock-in measurement (blue curve) and the bridge measurement (red curve) show a nearly identical response. The measurement was taken at a background resistance of $R_{xx} \sim 130$ $\Omega$ with the two traces taken within a few hours of each other. For comparison the signal-to-noise is plotted with the lock-in response shifted in the vertical direction to coincide with the bridge signal.

The bridge scheme should allow us to introduce low-temperature signal preamplification where nulling the signal around zero with the bridge will allow us to optimize the signal gain without saturating the amplifier. The benefit of a low temperature preamplifier is to significantly reduce the noise introduced by the amplifier itself. For example, we typically employ a Stanford Research SR560 low-noise room-temperature preamplifier which has a
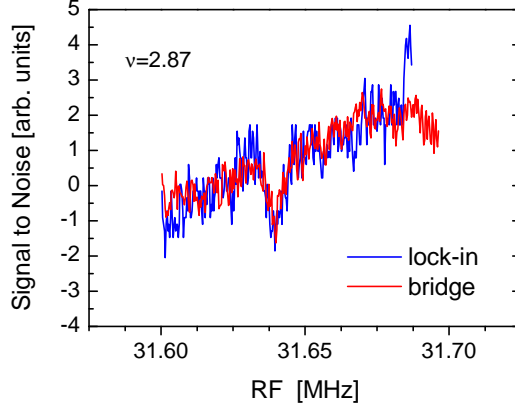
Figure 6–24: RDNMR response signal measured in the flank of the $\nu = 3$ using the 4-terminal bridge design (red line) compared with the standard lock-in measurement (blue line). The signal-to-noise is plotted for comparison. The bridge measurement depicted here does not include low temperature amplification, which is expected to further enhance the signal-to-noise.

voltage noise of $\sim 4$ nV/$\sqrt{\text{Hz}}$ at T=290 K. This is at least several hundred times larger than the thermal Johnson noise from our sample at typical magnetoresistance values. For example, if we consider a sample resistance of 100 $\Omega$ at 50 mK, the Johnson thermal noise is only $\delta V_{rms} = \sqrt{4kTRB} \sim 17$ pV/$\sqrt{\text{Hz}}$. As an optimal goal we would like to be able to resolve an RDNMR response corresponding to a $\sim 1\%$ resistance variation on resonance near the mininum in a well formed $\frac{5}{2}$ state. If we therefore consider a $R_{xx} \sim 10$ $\Omega$ resistance with a low sourcing current of 10 nA, a 1% variation in resistance (0.1 $\Omega$) gives only a 1 nV voltage response, which is below the noise figure of our preamp. Reducing the preamp noise by implementing a cold preamp would significantly improve the situation. However, operating a low-power preamp in a dilution refridgerator is challenging. Furthermore, we are interested in working at low frequencies, where a JFET preamp is optimal (low 1/f noise) but JFET's can not be operated below $\sim 77$ K [27]. An alternative approach is to use a low temperature step-up transformer. Since the step-up transformer is passive it is comparatively easy to implement in the dilution fridge. We recently acquired and have begun testing a low-temperature step-up transformer from *Cambridge Magnetic Refrigeration*, which is specifically designed for low noise cryomeasurements. While we have not yet introduced the step-up transformer into our cryostat, performance testing on a test circuit cooled to LHe temperatures has already allowed observation of a less than a 1 nV variation on a 100 $\Omega$ sample with a 100 nA sourcing current. Implementation of this measurement scheme into our system, together with other improvements in measurement sensitivity such

as signal averaging, will no doubt lead to improved measurement of the RDNMR signal around $\frac{5}{2}$ and ultimately a better understanding of its spin state.

# References

[1] Pobell, F. *Matter and Methods at Low Temperatures.* Springer-Verlag, New York, (1992).

[2] Linde, D. R., editor. *"Nuclear spins, moments, and other data related to NMR spectroscopy" in CRC Handbook of Chemistry and Physics, 88$^{th}$ edition (internet version 2008).* CRC Press/Taylor and Francis, Boca Rayton, FL., (2008).

[3] Barrett, S. E., Dabbagh, G., Pfeiffer, L. N., West, K. W., and Tycko, R. *Phys. Rev. Lett.* **74**, 5112 (1995).

[4] Smet, J. H., Deutschmann, R. A., Ertl, F., Wegscheider, W., Abstreiter, G., and von Klitzing, K. *Nature* **415**, 281 (2002).

[5] Weisbuch, C. and Hermann, C. *Phys. Rev. B.* **15**, 816 (1977).

[6] Dobers, M., von Klitzing, K., Schneider, J., Weimann, G., and Ploog, K. *Phys. Rev. Lett.* **61**, 1650 (1988).

[7] Kronmuller, S., Dietsche, W., von Klitzing, K., Denninger, G., Wegscheider, W., and Bichler, M. *Phys. Rev. Lett.* **82**, 4070 (1999).

[8] Desrat, W., Maude, D. K., Potemski, M., Portal, J. C., Wasilewski, Z. R., and Hill, G. *Phys. Rev. Lett* **88**, 256807 (2002).

[9] Stern, O., Freytag, N., Fay, A., Dietsche, W., Smet, J. H., von Klitzing, K., Schuh, D., and Wegscheider, W. *Phys. Rev. B* **70**, 075318 (2004).

[10] Kawamura, M., Takahashi, H., Masubuchi, S., Hashimoto, Y., Katsumoto, S., Hamaya, K., and Machida, T. *Phys. E* **40**, 1389 (2008).

[11] Sondhi, S. L., Karlhede, A., and Kivelson, S. A. *Phys. Rev. B* **47**, 16419 (1993).

[12] Fertig, H. A., Brey, L., Cote, R., and MacDonald, A. H. *Phys. Rev. B* **50**, 11018 (1994).

[13] Gervais, G., Stormer, H. L., Tsui, D. C., Kuhns, P. L., Moulton, W. G., Reyes, A. P., Pfeiffer, L. N., Baldwin, K. W., and West, K. W. *Phys. Rev. Lett.* **94**, 196803 (2005).

[14] Kodera, K., Takado, H., Endo, A., Katsumoto, S., and Iye, Y. *Phys. Stat. Sol.* **3**, 4380 (2006).

[15] Gervais, G., Stormer, H. L., Tsui, D. C., Moulton, W. G., Kuhns, P. L., Reyes, A. P., Baldwin, K. W., West, K. W., and Pfeiffer, L. *Phys. Rev. B* **72**, 041310 (2005).

[16] Tracy, L. A., Eisenstein, J. P., Pfeiffer, L. N., and West, K. *Phys. Rev. B* **73**, 121306 (2006).

[17] Tracy, L. A., Eisenstein, J. P., Pfeiffer, L. N., and West, K. W. *Phys. Rev. Lett.* **98**,

086801 (2007).

[18] Abragam, A. *Principles of Nuclear Magnetism.* Oxford University Press, New York, (1961).

[19] Zhang, X. C., Scott, G. D., and Jiang, H. W. *Phys. Rev. Lett.* **98**, 246802 (2007).

[20] Melinte, S., Freytag, N., Horvatic, M., Berthier, C., Levy, L., Bayot, V., and Shayegan, M. *Phys. Rev. B* **64**, 085327 (2001).

[21] Schreiner, M., Pascher, H., Denninger, G., Studenikin, S. A., Weimann, G., and Losch, R. *Sol. Stat. Comm.* **102**, 715 (1997).

[22] Wei, H. P., Tsui, D. C., Paalanen, M. A., and Pruiskin, M. A. A. *Phys. Rev. Lett.* **61**(11), 1294 (1988).

[23] Wei, H. P., Engel, L. W., and Tsui, D. C. *Phys. Rev. B* **50**(19), 14609 (1994).

[24] Scherert, H., Schweitzert, L., Ahlerst, F. J., Bliekt, L., Loscht, R., and Schlapp, W. *Semicon. Sci. Technol.* **10**, 959 (1995).

[25] Chow, E., Wei, H. P., Girvin, S. M., and Shayegan, M. *Phys. Rev. Lett.* **77**, 1143 (1996).

[26] Kawamura, M., Takahashi, H., Sugihara, K., Masubuchi, S., Hamaya, K., and Machida, T. *Appl. Phys. Lett* **90**, 022102 (2007).

[27] Engel, L. private communication (2007).

CHAPTER 7

# Conclusion And Future Work

## 7.1 Conclusion

### 7.1.1 $\nu = \frac{5}{2}$ FQHE

We have investigated the $\nu = \frac{5}{2}$ FQHE in very high quality samples and at lower density (by nearly a factor of two) than previously observed. We measure a similar activation gap as previous studies on samples with similar mobility, but larger densities. Examining the role of disorder on the $\frac{5}{2}$ state, we find that a large discrepancy, by a factor of 3-5, remains between theory based on the Moore-Read Pfaffian and experiment for the intrinsic gap, extrapolated from the infinite mobility limit. This disagreement is viewed as especially problematic when compared with similar studies of the $\frac{1}{3}$ Laughlin state where there is near perfect agreement between experiment and theory. The origin of the discrepancy remains unknown, due in part to to limitations in theory that cannot, for example, provide a microscopic theory of how disorder effects the $\nu = \frac{5}{2}$ FQHE, or accurately predict the role played by LL mixing. The large difference in experimental versus theoretical gaps indicates our theoretical description of the $\frac{5}{2}$ state remains incomplete, and could possibly point towards the Moore-Read Pfaffian not being the correct wavefunction. On the other hand, our strong $\frac{5}{2}$ FQH state in the low field regime exhibits a similar energy gap as $\frac{5}{2}$ states measured up to fields as high as 12 T. Taken together, a well formed minimum over such a large B range points towards a fully spin polarized state, consistent with the Moore-Read Pfaffian, which so far is the only candidate wavefunction describing a spin polarized paired state at $\frac{5}{2}$.

Using a titled field geometry we found the $\frac{5}{2}$ gap to decay linearly in the presence of the of an applied in-plane magnetic field. By contrast, the neighbouring $\frac{7}{3}$ state shows a remarkable enhancement. This finding is in startling contradiction to theory, which

predicts the two states should behave the same in the presence of an in-plane field (under tilt). Modifications to the $\frac{5}{2}$ state resulting from magneto-orbital coupling to the in-plane field, in addition to variations in the Zeeman energy resulting from the corresponding change of the total applied field, makes it difficult to interpret our tilted field results in terms of the spin nature of the $\frac{5}{2}$. However, the observed contrasting behaviour between the $\frac{5}{2}$ and $\frac{7}{3}$ states represents an important experimental finding since the early theoretical foundation in support of the Moore-Read interpretation assumed a universal similarity in the behaviour of the two states in a tilted field. The opposite behaviour of the two states may therefore necessitate a fundamental reassessment of the nature of the $\frac{5}{2}$ FQHE.

The questions raised by our experimental observations concerning our theoretical understanding of the $\frac{5}{2}$ FQH state, emphasize the urgency to understand, unambiguously, the origin of the $\frac{5}{2}$ FQHE. A remaining question of fundamental importance continues to be the spin state of the $\frac{5}{2}$ FQHE, which, despite nearly twenty years of experimental effort, still has not been determined convincingly. While it has been hopeful that the newly developed resistively detected NMR technique would allow a means to directly measure the $\frac{5}{2}$ spin, results have not yet been forthcoming. We have made significant progress towards this effort by measuring for the first time an RDNMR signal near $\nu = \frac{5}{2}$. However, the signal remains very weak with a less than 1% deviation observed on resonance when sourcing large currents. To be able to study the $\frac{5}{2}$ spin using this technique will require that we find ways to enhance the signal and/or increase the RDNMR measurement sensitivity. Our development of a four terminal resistance bridge in combination with the RDNMR scheme will undoubtedly lead to improvements in this regard.

### 7.1.2   Anomalous RDNMR lineshape near $\nu = 1$

We studied extensively the anomalous dispersive RDNMR lineshape near $\nu = 1$ filling fraction. We found that the lineshape depends in an interrelated way on the filling factor, sample temperature, and on the strength of the applied transverse RF field. We further show that at fixed filling factor the lineshape can be inverted by applying a large DC current bias without loss of signal strength. The signal inversion is also observed by direct sample heating, but with significant loss in the signal strength. This indicates the current induced inversion likely results from electron heating, with the strong signal strength possibly indicating the applied current also acts to enhance the nuclear polarization through dynamic nuclear pumping

By studying the signal inversion at fixed filling, we find evidence that the inversion is not a simple flip of the minimum and peak, rather the peak on the high frequency side of

the minimum is first destroyed and then reemerges on the low frequency side. The origin of the dispersive lineshape, much less the signal inversion observed here, remains unknown. However, our results suggest the anomalous shape is likely not determined by the sign of $dR_{xx}/dT$ alone, as has been suggested previously. Furthermore, the different behaviour between the peak and minimum under variations in a number of different parameters may suggest the two features result from distinct mechanisms.

## 7.2 Future Work

### 7.2.1 Combining RDNMR with conventional NMR

The primary interest in applying RDNMR to the $\frac{5}{2}$ FQHE is to probe its electron spin polarization state. The most direct way to do this is to measure the corresponding Knight shift, which is maximum for a fully polarized electron state and zero if the electrons are fully unpolarized. To measure the Knight shift however requires a precise measurement of the non-Knight shifted resonance frequency as a reference. The most accurate way to accomplish this is by combining conventional NMR together with the resistive NMR scheme. Since the RDNMR measurement relies on interactions between the nuclei and electrons in the 2DEG, this technique only measures the resonant frequency of atoms in the 2DEG quantum well. On the other hand conventional NMR measures the nuclear resonance in the bulk which mostly does not interact with electrons in the 2DEG and so do not experience a Knight shift. Since we have demonstrated that the RDNMR signal can be found near $\frac{5}{2}$ state, preliminary work on implementing a complimentary conventional NMR probe into our system has already begun.

### 7.2.2 RDNMR as a function of $\nu$ around the 5/2 state

In the absence of a true non-Knight shifted NMR reference, it may still be possible to infer the polarization state at $\frac{5}{2}$. Our tilted field experiment indicates the possible existence of spin-reversed Skyrmion excitations at the neighbouring $\nu = \frac{7}{3}$ state. If the $\frac{5}{2}$ state is truly described by the spin polarized Moore-Read Pfaffian we may be able to find evidence of a continuous transition from an unpolarized electron state adjacent to the $\frac{5}{2}$ to a fully spin polarized state at exactly $\frac{5}{2}$ fraction filling. This would be observable by a continuous increase in the Knight shift as we approach the $\frac{5}{2}$ state, similar to what has been observed by conventional NMR around $\nu = 1$. A simple way to observe this might be by using the resonance frequency far away from $\nu = \frac{5}{2}$ as a pseudo-marker to predict the non-Knight shifted resonant frequency at filling factors very near $\nu = \frac{5}{2}$. The ability to make this measurement is however limited by our ability to resolve the RDNMR response.

Since at other filling fractions we typically measure a lineshape width of less than $\sim$10 kHz, which is at least a factor of two smaller than the Knight shift measured on similar samples ($\sim$25 kHz) such a measurement is plausible.

### 7.2.3   Current induced lineshape inversion near $\nu = 1$

The origin of the anomalous dispersive lineshape near $\nu = 1$ remains unknown. Since this lineshape has now been observed at several other filling factors, including our observation of a possible inverted dispersive lineshape near $\nu = \frac{5}{2}$, the mechanism causing a peak versus minimum response is an important open question. Our observation and characterization of the current-induced lineshape inversion offers clues that the minimum and peak result from distinct mechanisms. However, we still do not have a clear understanding of these mechanisms. From our temperature dependence studies, we found evidence that the separation in frequency between the minimum and peak signals (in the 'normal dispersive' case) may correspond to the Knight shift. However this experiment was performed only at a single filling factor. To further explore this possibility the temperature dependence of the dispersive lineshape should be examined at several filling factors around $\nu = 1$ on both sides of the $\nu = 1$ minimum, and in both the normal and inverted signal regimes. In this context it would also be useful to make a detailed measurement of the peak-minimum frequency separation as a function of filling factor. If the peak/minimum truly emanate from distinct spin unpolarized/polarized regimes then the frequency separation (Knight shift) should systematically increase towards exact filling at $\nu = 1$.
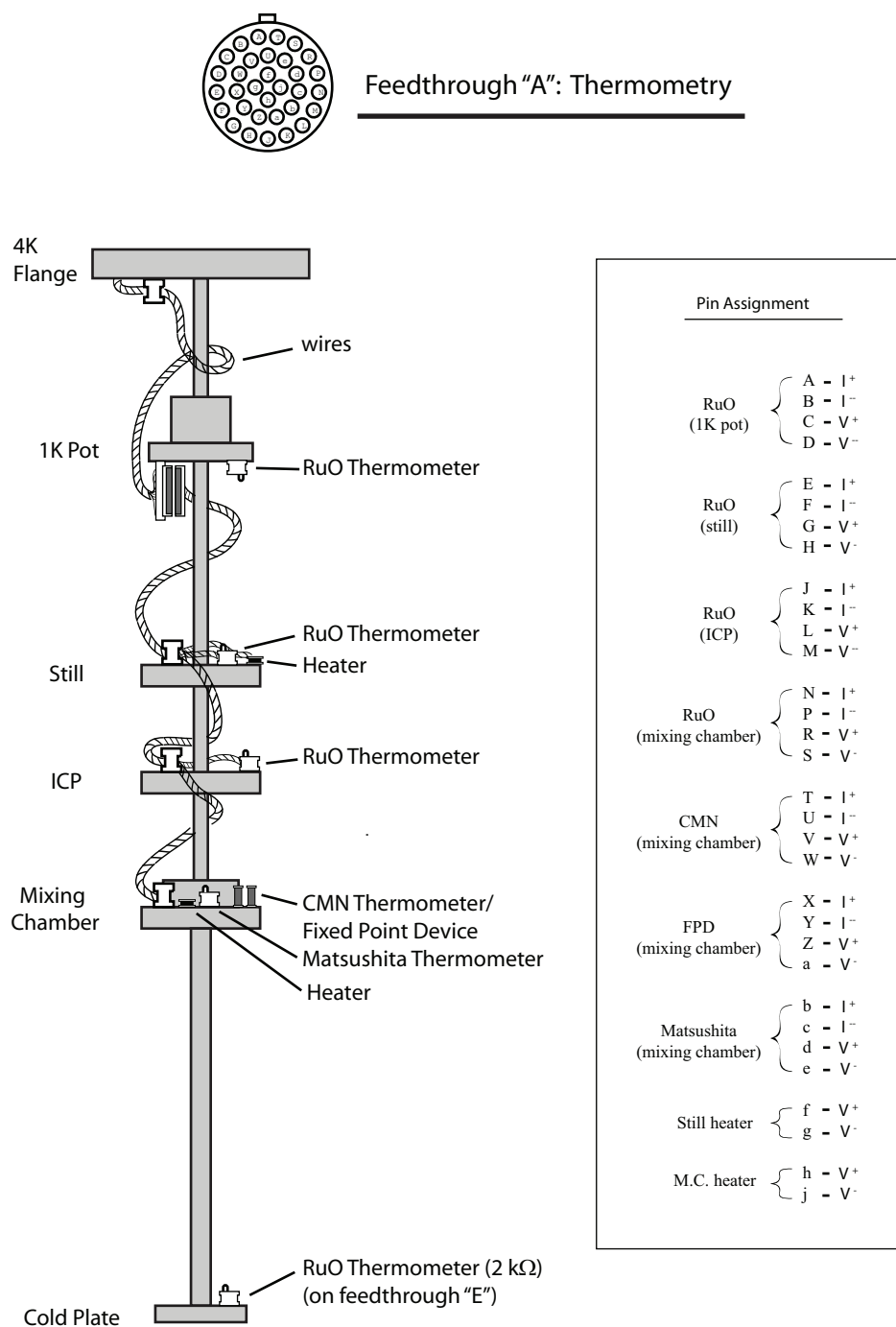
# Wiring Schematics

Feedthrough "A": Thermometry

Figure A–1: Feedthrough "A" wiring schematic and pin-out
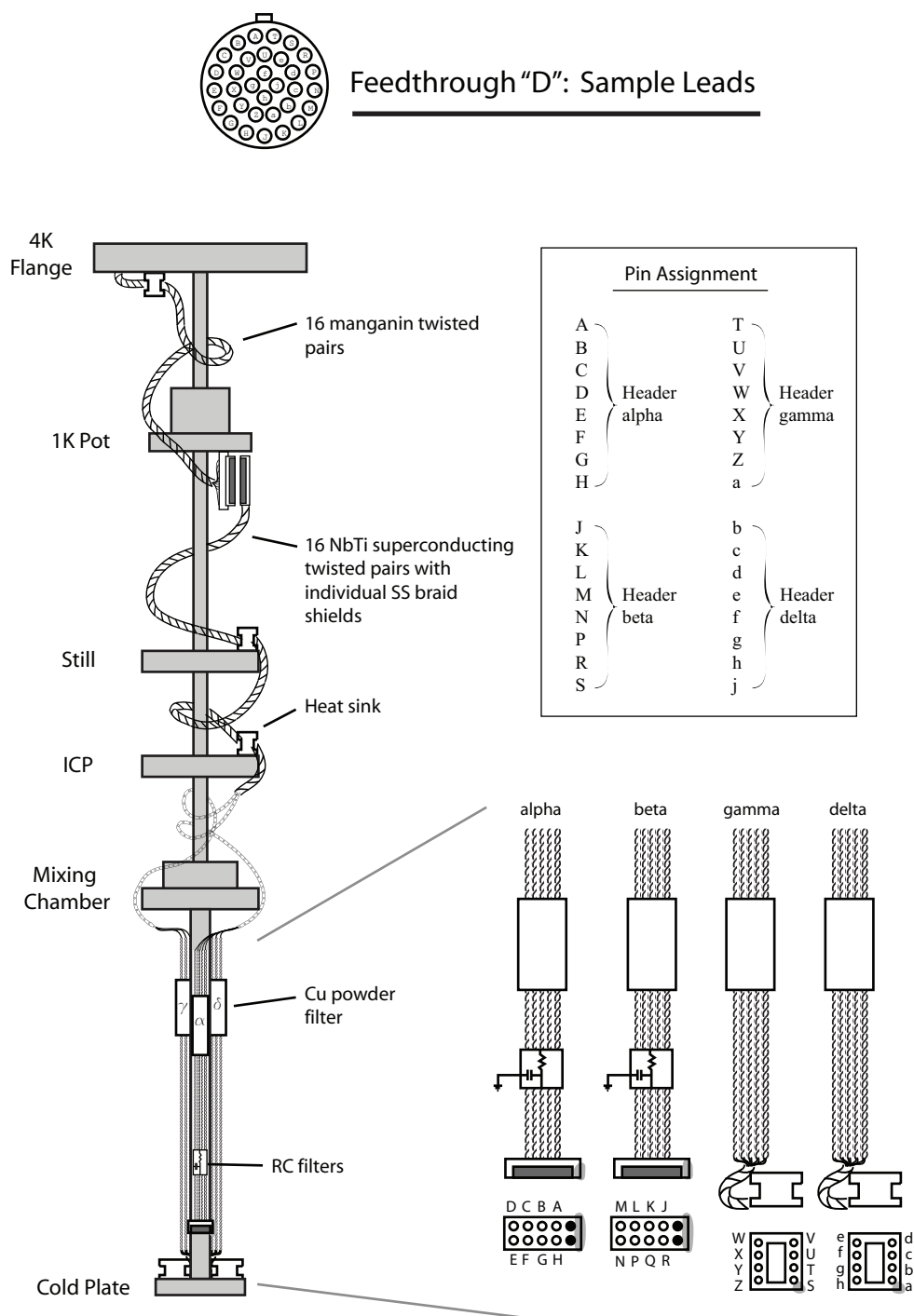
Feedthrough "D": Sample Leads

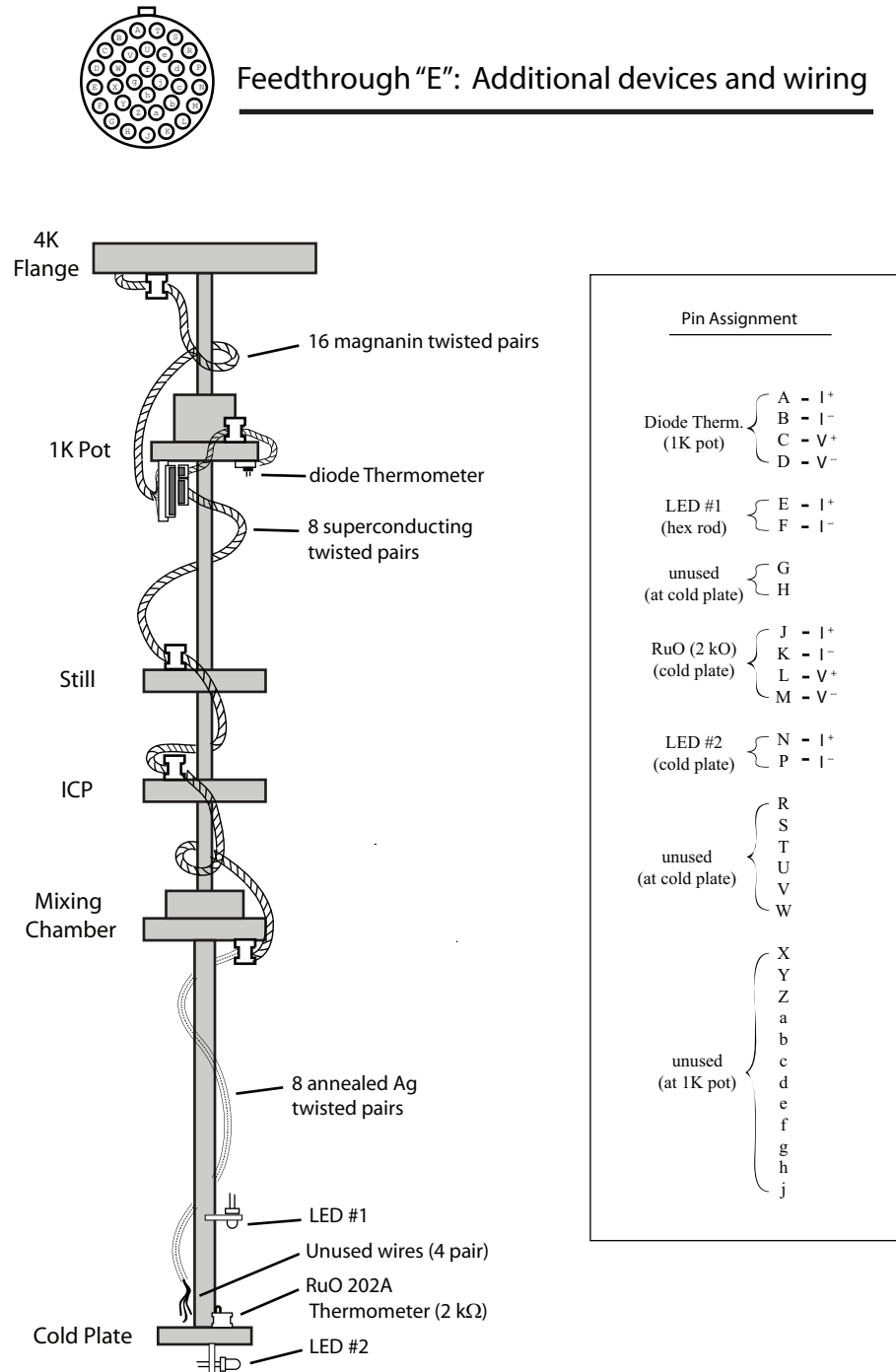Figure A–2: Feedthrough "D" wiring schematic and pin-out

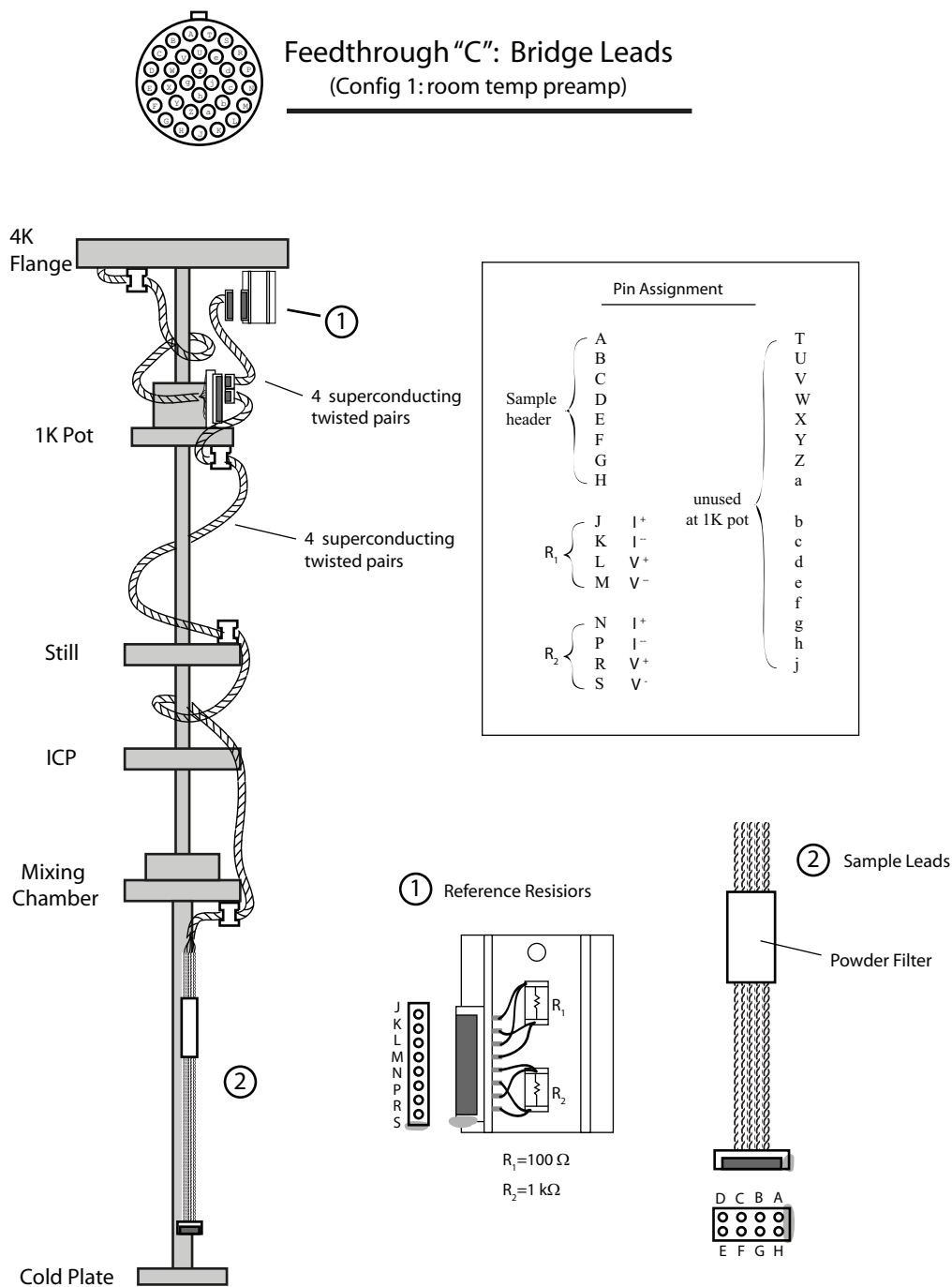Figure A–3: Feedthrough "E" wiring schematic and pin-out

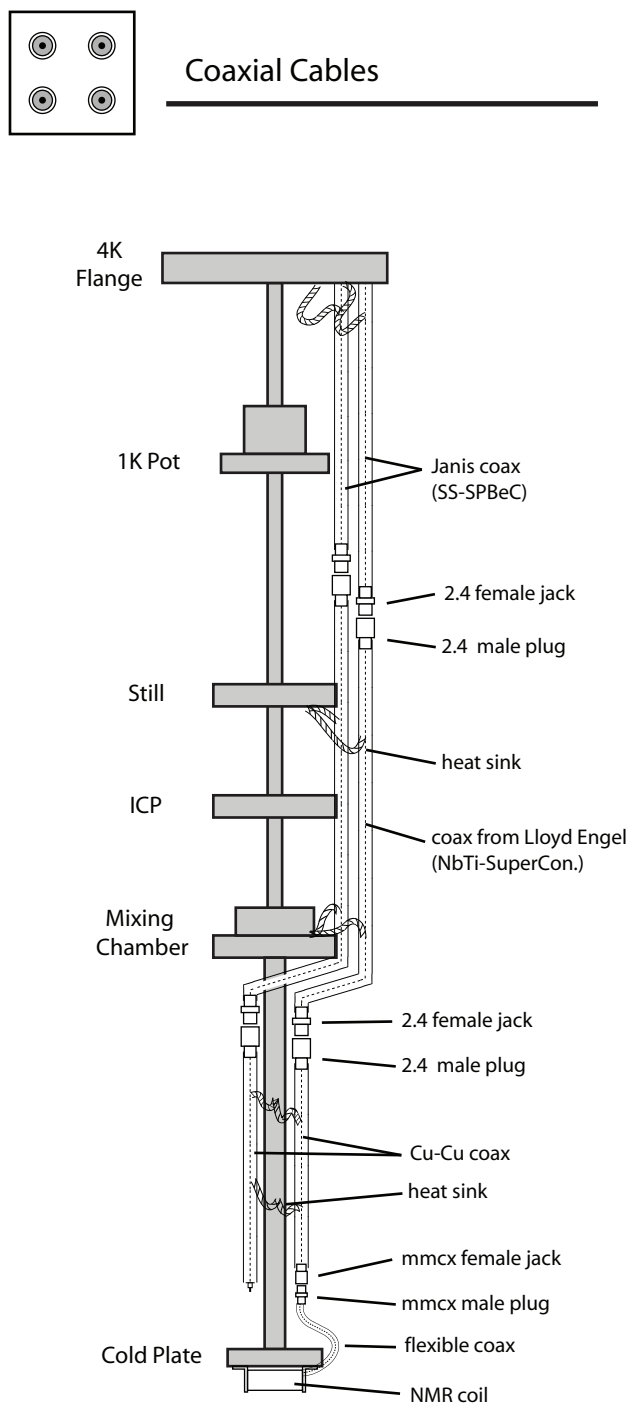Figure A–4: Feedthrough "C" wiring schematic and pin-out

Figure A–5: Schematic drawing of the coxiale cables installed on the dilution fridge
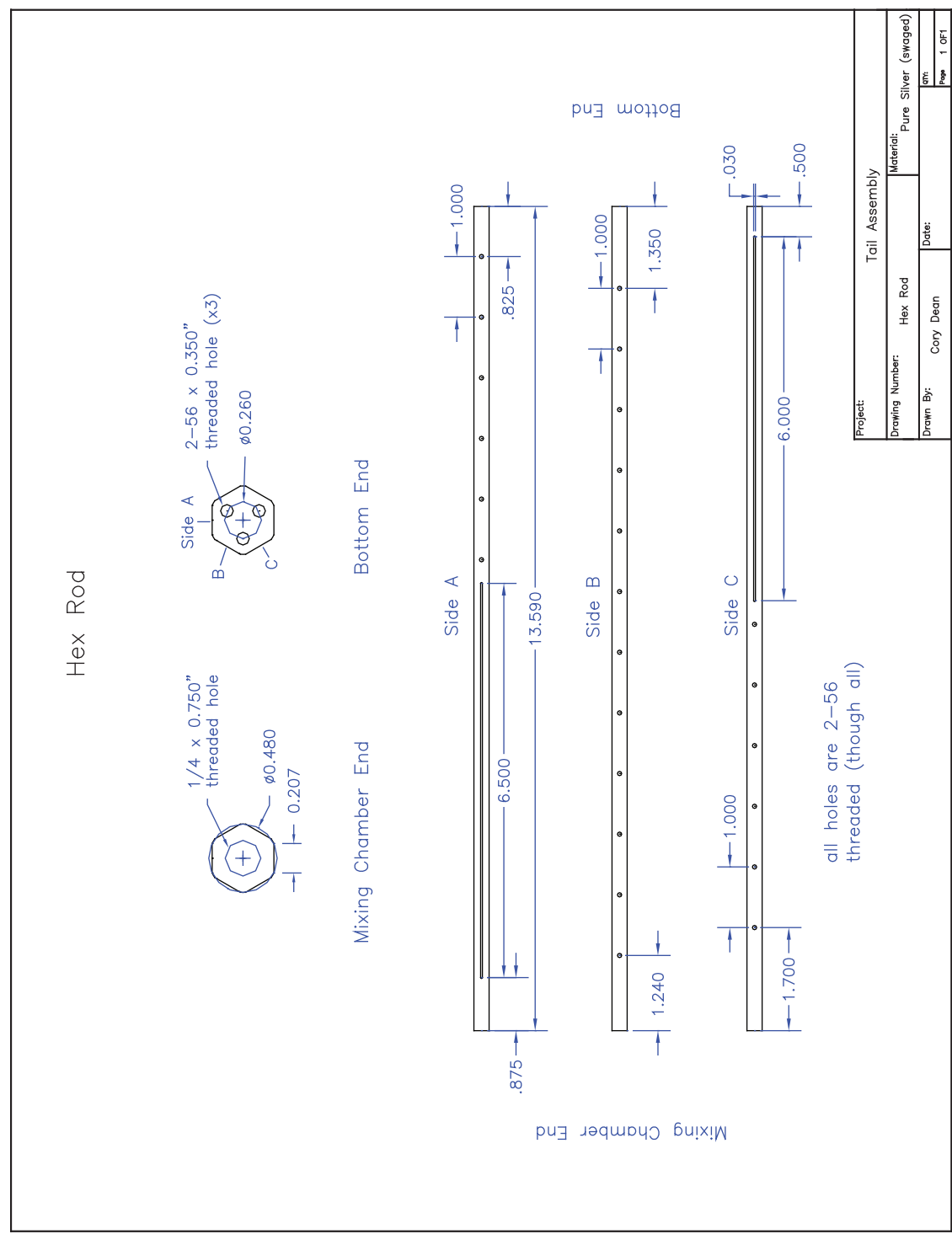
APPENDIX B

# Design Drawings

Hex Rod

Side A
2-56 x 0.350"
threaded hole (x3)
ⵁ0.260

B
C

Bottom End

1/4 x 0.750"
threaded hole
ⵁ0.480
0.207

Mixing Chamber End

Side A
13.590
6.500
.825
1.000
.875

Side B
1.000
1.350
1.240

Side C
.030
.500
6.000
1.000
1.700

all holes are 2-56
threaded (though all)

Bottom End

Mixing Chamber End

Tail Assembly

Material: Pure Silver (swaged)

Project:

Drawing Number: Hex Rod

Drawn By: Cory Dean

Date:

Qty.

Page 1 OF1

Figure B–1: Hex Rod for Tail Assembly

154
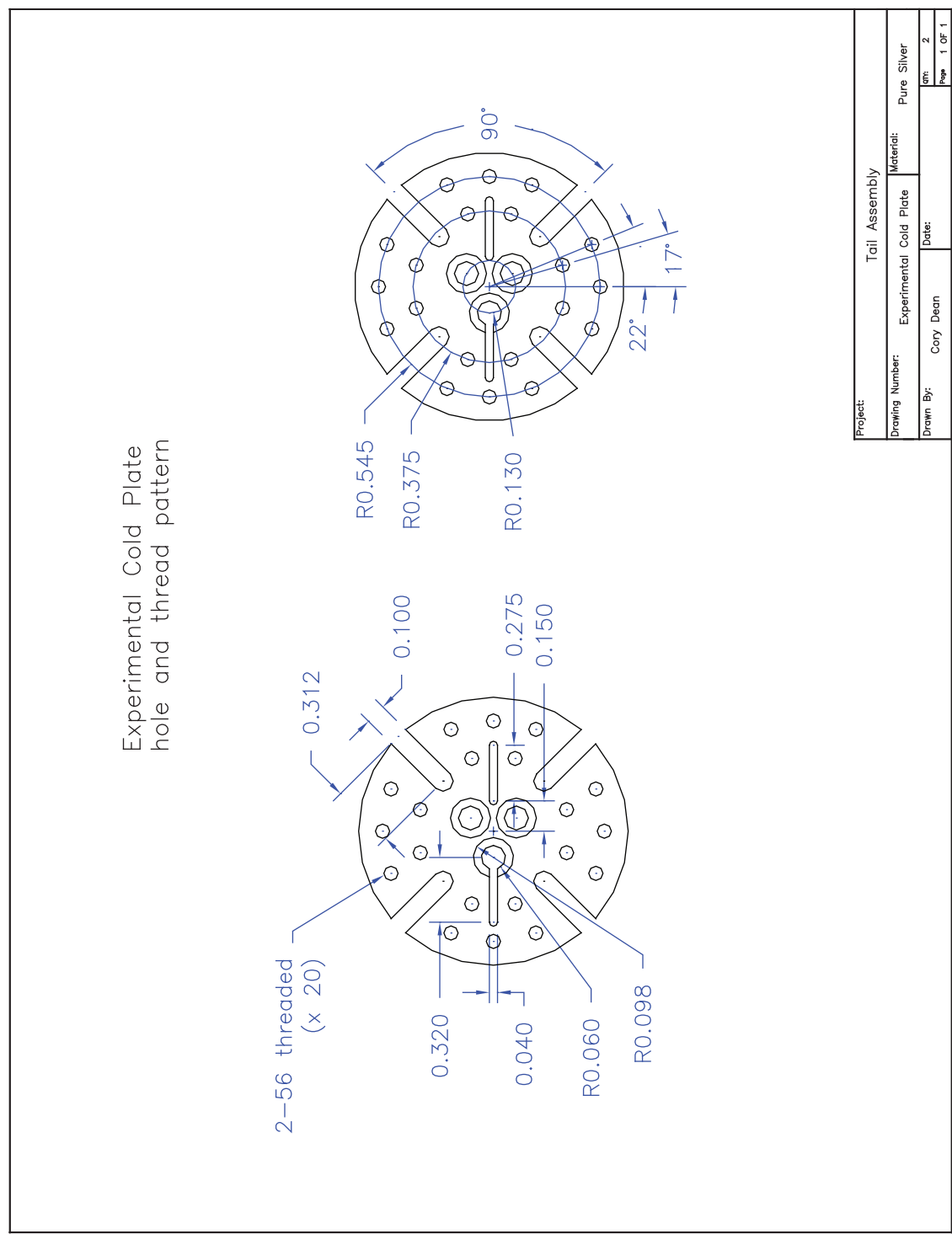
Figure B–2: Experimental Cold plate hole and thread pattern
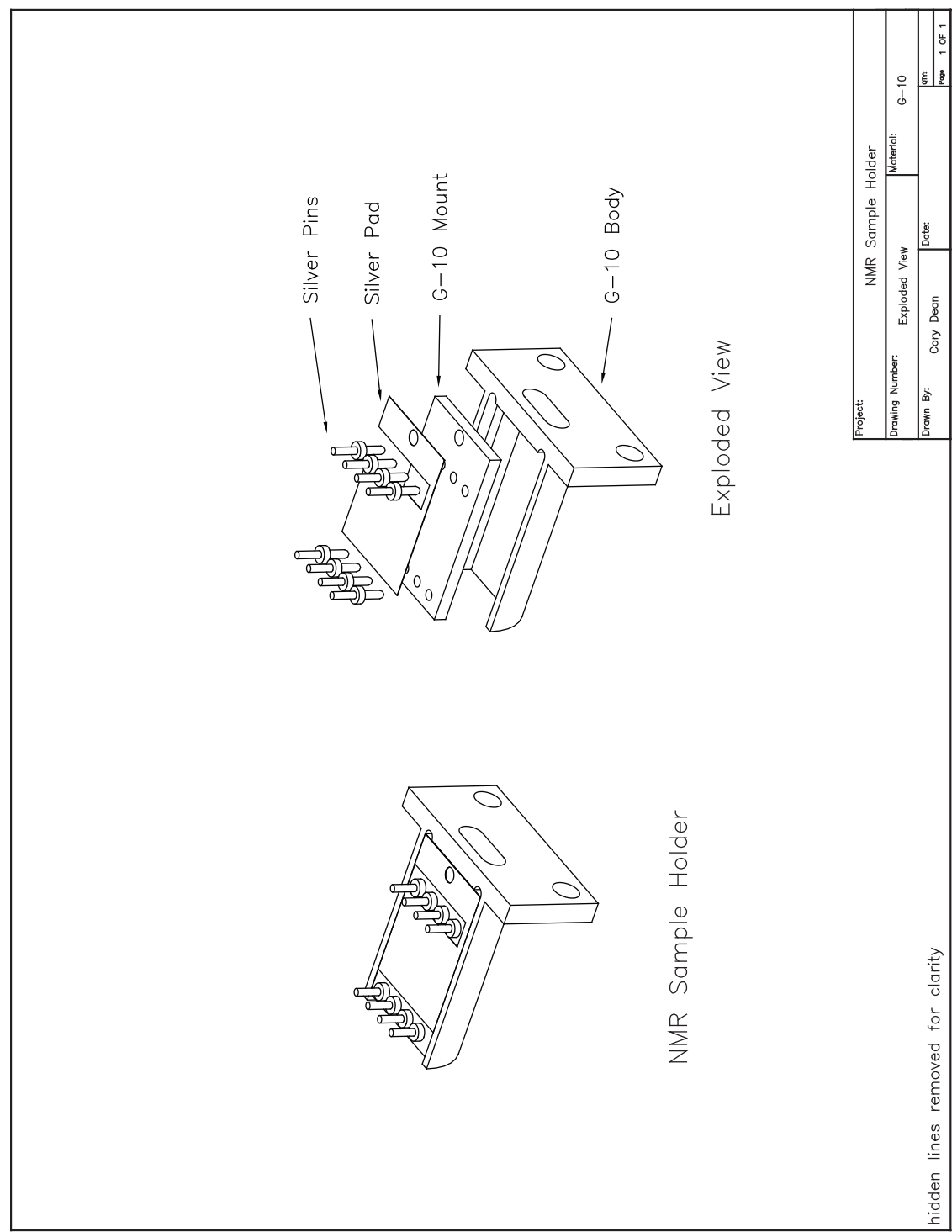
Figure B–3: NMR sample holder

NMR Sample Holder Body

Perspective View

Front View

Side View

0.031
0.091
0.055
0.055
0.200
0.260
R0.150
R0.030
0-80 clearance
(x2)

0.480
0.445
0.495
0.300

0.445
0.495

hidden lines removed for clarity

Project:                    NMR Sample Holder
Drawing Number:  Body        Material:  G-10
Drawn By:     Cory Dean      Date:
                                          Qty:
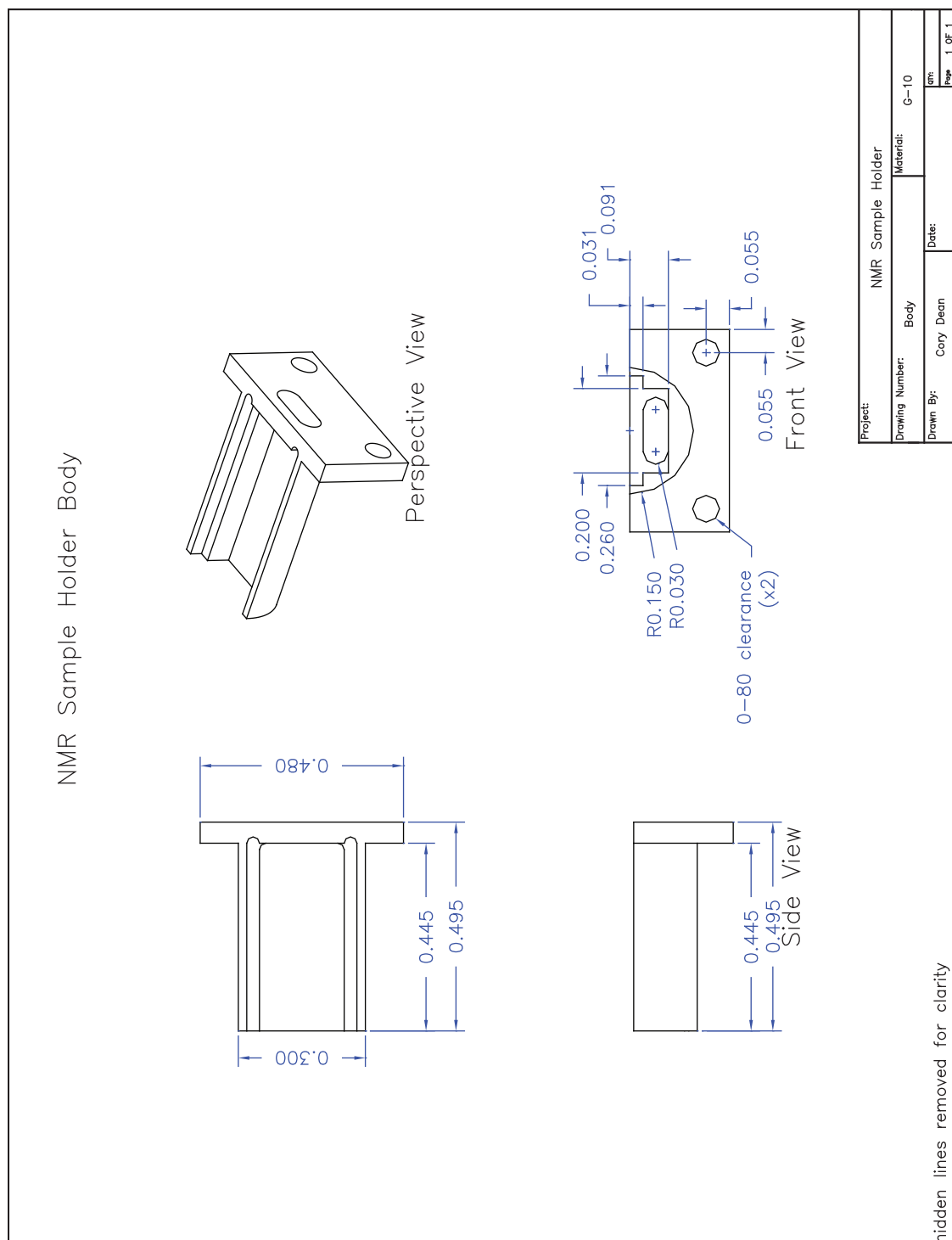                                          Page    1 OF 1
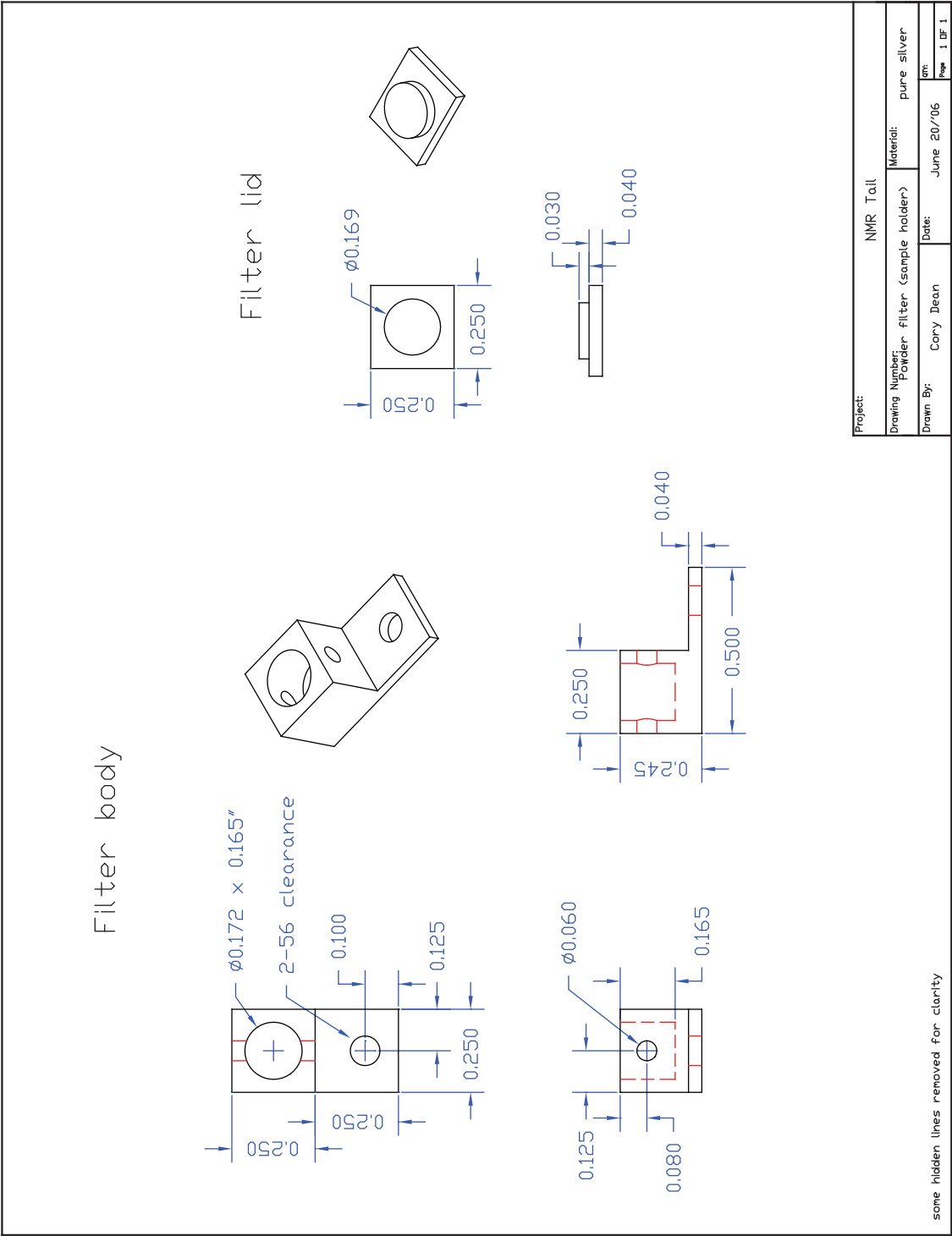
Figure B–4: NMR sample holder; G-10 body dimensions

Figure B–5: Powder filter for NMR sample holder